Doctorate Dissertation
博士論文

Study of Optical System of the Ultra-Cold Neutron
with High Intensity Pulsed-Beam at J-PARC for
Discovery of Neutron Electric Dipole Moment
（中性子電気双極子能率の発見のための
J-PARC における大強度パルスビームを用いた
超冷中性子の光学系の研究）

A Dissertation Submitted for Degree of Doctor of Philosophy
December 2017
平成 29 年 12 月博士（理学）申請

Department of Physics, Graduate School of Science,
The University of Tokyo
東京大学大学院理学系研究科 物理学専攻

Ryo Katayama
片山 領

Abstract

The neutron electric dipole moment (EDM) is sensitive to new physics beyond the standard model (BSM). Currently, the best upper limit of neutron EDM, obtained at Institute Laue-Langevin (ILL), is 3×10^{-26} e · cm (90% CL). Many BSM models, such as supersymmetric models, predict 1 to 2 orders of magnitude larger EDM that can be detected by experimental techniques that can be developed today, which motivates a more precise measurement of neutron EDM. Generally, neutron EDM can be measured most precisely by confining ultracold neutrons (UCN) in a storage container to which electric and magnetic fields are applied. Today, the sensitivity of this measurement is mainly limited by statistics, while it is expected to be drastically improved by the super-thermal method that can produce UCNs effectively. Therefore, new EDM experiments adopting the super-thermal method are being planned all over the world. Recently, a new EDM experiment has been proposed at J-PARC (J-PARC P33 experiment). This experiment uses a unique experimental technique to make pulsed UCNs re-bunched on the measurement cell, and is expected to be a strong candidate of next-generation experiment.

This thesis describes the first basic study for the neutron EDM experiment based on P33 concept. For the J-PARC P33 experiment, there was a problem that the experimental capability was not evaluated because it was particularly difficult to understand effects of the reflection loss and the non-specular reflection on the statistical sensitivity. Therefore, in this study, first of all, the dependence of the statistical sensitivity on such reflection performances was tried to be quantitatively investigated by a full simulation that can deal with an experimental system and entire procedures based on J-PARC P33 concept. Neutron optical theory and micro-roughness model were used to represent the reflection loss and the non-specular reflection. Total reflection energy, V_F, and UCN loss probability coefficient, η, were used for controlling the reflection loss, which were chosen to be in the range from 91 neV $\sim$ 210 neV and $8 \times 10^{-5} \sim 5 \times 10^{-4}$. On the other hand, RMS roughness b was used to handle the non-specular reflection, which was chosen to be in the range from 0 to 3 nm. As a result, it was shown that the statistical sensitivity was changed by 8 times according to the difference of reflection performances.

Full simulation study showed that the development of reflection materials is the key to improving the sensitivity. Hence, high efficient neutron mirrors, Nickel Molybdenum alloy (NiMo) and Diamond-Like Carbon (DLC), were developed. NiMo was prepared by the binary vapor deposition, and DLC was fabricated by methods of Filtered Arc Ion Plating Deposition (FAIPD) and Ionized Evaporation Method (IEM) and Plasma Based Implantation Deposition (PBIID). These reflectors were evaluated by surface analyses; the neutron reflectometry showed that V_F was 228 neV (NiMo), 243 neV (IEM), 264 neV (FAIPD), and 193 neV (PBIID); η was evaluated to be 3.6×10^{-4} (NiMo) and 3.4×10^{-4} (PBIID) by the UCN storage experiment, and b was evaluated to be 0.3 nm (IEM) and 0.49 nm (FAIPD) by AFM.

Finally, with the above-evaluated reflection performances along with the systematic error evaluated in a similar manner as the ILL experiment, the experimental sensitivity for the measurement duration of 2.3 years was estimated to be $(\pm 1.6(\text{stat}) \pm 2.5(\text{syst})) \times 10^{-27}$ e·cm. This is the first comprehensive evaluation of the experimental capability based on J-PARC P33 concept including the reflection performance, which provides a reliable basis for future experiment design.

Contents

List of Tables

List of Figures

iv

Chapter 1

Introduction

This thesis deals with the first basic study of the proposed experiment for searching the neutron electric dipole moment using ultracold neutrons produced by the J-PARC pulsed proton beams of the world's highest instantaneous luminosity.

The neutron electric dipole moment (EDM) is one of the most sensitive physical quantities to probe the CP symmetry violation. In general, an intrinsic non-zero neutron EDM implies that time reversal symmetry is violated, and the CPT theorem guarantees that the time reversal symmetry violation is equivalent to CP symmetry violation. Therefore, the source of CP violation can be effectively searched by the precise neutron EDM measurement. In the standard model, only second-order interaction from the weak interaction shown in Figure 1.1 contributes to CP symmetry violation, and thereby EDM about 10^{-31} e $\cdot$ cm appears. This is so small that it cannot be detected with current experimental techniques. On the other hand, many of BSM models introduce first-order interaction as shown in Figure 1.2, and thereby the signal is possible to be detected even with current experimental techniques. Therefore, we can search for the existence of BSM effectively by precise measurement of neutron EDM, which can be the key to solving problems in elementary particle physics. For example, the hierarchy problem in the standard model may be solved by the framework of a BSM model such as supersymmetric models (SUSY). In addition, the violation of a large amount of CP symmetry supplied by BSM is also necessary to explain the origin of the baryon asymmetry in the universe, which is an unsolved problem of elementary particle physics [1]. Therefore, a new experiment to precisely measure the neutron EDM is well motivated as it can probe two fundamental problems such as the existence of BSM physics and the baryon asymmetry in the universe.

The current most tight experimental upper limit is 3×10^{-26} e $\cdot$ cm (90 % CL) [2], which was performed at Institute Laue-Langevin (ILL) in France. In this experiment, the statistical uncertainty was dominant and its anticipated value was 1.34×10^{-26} e $\cdot$ cm [2]. In this thesis, the neutron EDM experiment performed at Institute Laue-Langevin is referred to as the ILL experiment hereafter. The detail of the experiment is described in chapter 3.2. Many of BSM models, such as SUSY, which is one of the most promising models of new physics, predict larger EDM values that can be detected by current experimental techniques. For reference, a history about the precision of neutron EDM measurement is shown in Figure 1.3. The precision is improved year by year, and it comes to the stage reaching 10^{-26} e $\cdot$ cm which is predicted by multi-Higgs models. Therefore, with the improvement of one or two orders of magnitude in
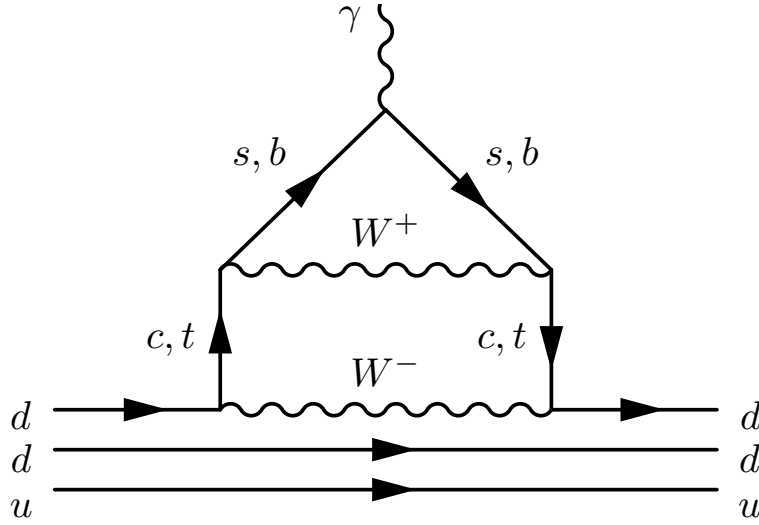
Figure.1.1 Feynman diagram of weak interaction for standard model that can break CP symmetry
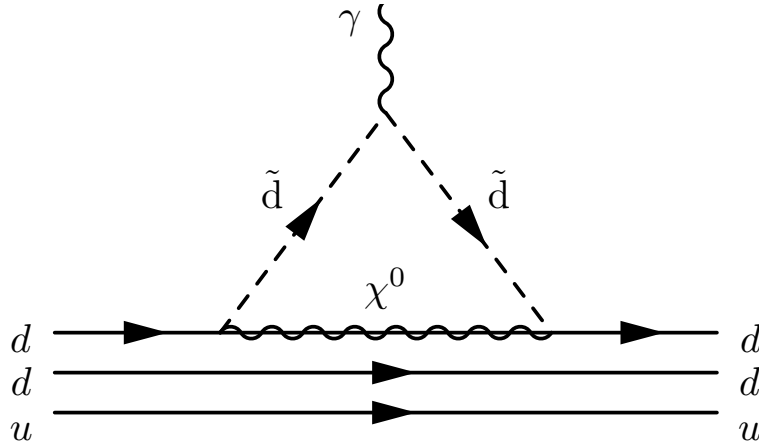
Figure.1.2 Feynman diagram of the interaction for supersymmetry model that can break CP symmetry

the precision, many of BSM models can be effectively searched by the precise neutron EDM measurement, and there is a possibility that the neutron EDM experiment can prove BSM.

Today, the most precise neutron EDM measurement is possible by using low energy neutrons of 300 neV or less, which is referred to as Ultra Cold Neutron (UCN). In general, UCNs can reflect from the material surface, which makes the neutron EDM have the property of becoming parallel (or antiparallel) to the neutron spin and precess in the electric field. Therefore, the neutron EDM can be detected through the phase shift due to the spin precession occurring in UCNs confined in a container to which an electric field is applied. In an actual measurement, a magnetic field is also used, and the electric field is applied parallel/antiparallel to the magnetic field.

The current neutron EDM experiment is mainly limited by the statistical precision. Therefore, a more intense UCN source is desired. Conventionally, the production method that neutrons emitted from a
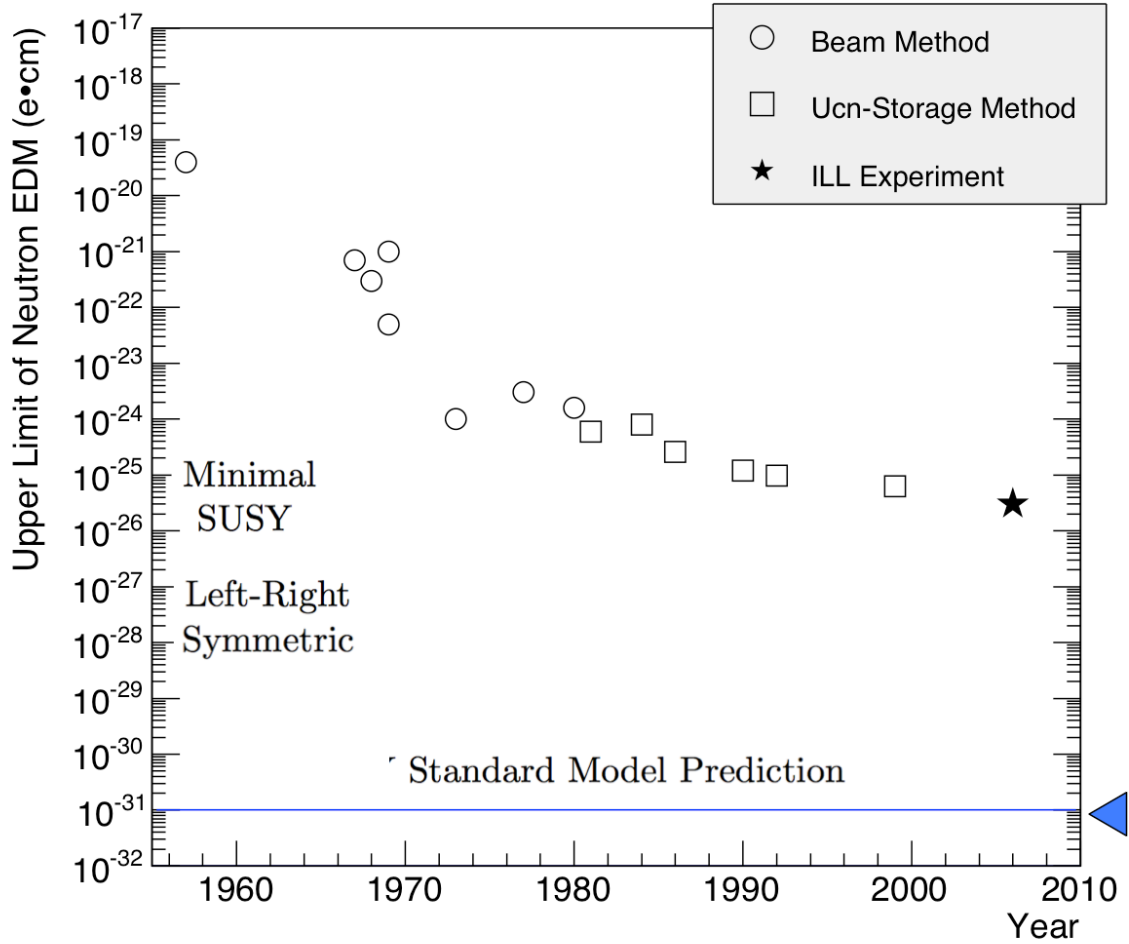
Figure.1.3 The history in the precision of neutron EDM measurement. History of precision of neutron EDM measurement. The vertical axis is precision and the horizontal axis is the measurement year. At present, the precision of neutron EDM measurement reaches 10^{-26}e · cm. [3, 4, 5, 6, 7, 8, 9, 10, 11, 12, 13, 14, 15]

nuclear reactor are decelerated by reflection with a mirror has been used. This method is called the Doppler Shift method. In recent years, a new production method that cools fast neutrons to ultracold neutrons by inelastic scattering of quasiparticles in a substance has been developed and put into practice. This method is called the super-thermal method [16]. Thanks to the super-thermal method, the statistical precision is expected to be improved. Accordingly, a lot of neutron EDM experiments adopting super-thermal method are being planned all over the world. In particular, there is significant progress at PSI in Switzerland and TRIUMF in Canada, and they announced that it has prospected to improve one or more order of magnitude from the ILL experiment. Both groups produce fast neutrons using an accelerator, and it is cooled by liquid helium or solid deuterium.

At Japan Accelerator Research Complex (J-PARC), an experimental facility located in Tokai, Japan, new neutron EDM experiment has been proposed which has the following quite unique characteristics [17, 18, 19]:

1. To produce fast neutron beams by nuclear spallation reaction with J-PARC pulsed proton beam with the world's highest instantaneous intensity.
2. To produce high intensity pulsed UCN beams by cooling via elastic scattering on heavy water and liquid deuterium and inelastic scattering on phonons in a solid deuterium converter.
3. To extract and transport the high-intensity pulsed UCN beams to the storage container for the neutron EDM experiment.
4. To refocus pulsed UCN to the shutter position in front of the storage container by decelerating high velocity component with the magnetic field interaction to avoid the UCN bunches diffused in the transportation.
5. To accumulate the refocused UCN in the storage container by the managing shutter opening/closing time to prevent back-flow.
6. To perform the EDM measurement when the UCN density is around the maximum.

This procedure was proposed in the 33rd proposal submitted to J-PARC. In this thesis, the experiment adopting the above procedure is called as the J-PARC P33 experiment. In addition, the above technique to refocus pulsed UCNs is called "rebunch", and the above method to take refocused UCNs into the container with preventing back-flow is referred to as "rebunch storage" hereafter. For reference, a table showing the difference between the J-PARC P33 experiment and the ILL experiment is given below.

	J-PARC P33	ILL Experiment
UCN Production	Super-Thermal Method	Doppler Shift Method
Fast Neutron Production	Nuclear Spallation	Nuclear Fission
Fast Neutron Beam Structure	Pulsed Beam	Continuous Beam
UCN Beams Structure	Refocused Beam	Continuous Beam

With the above J-PARC P33 experimental procedure, the world's most intense pulsed beam at J-PARC can be efficiently transmitted into the storage container, and the statistical precision is expected to be significantly improved. Also, due to the pulsed beam characteristics, there is a merit that the heat load to the ultracold neutron source can be greatly reduced.

This thesis describes the first basic study for the neutron EDM experiment using the J-PARC facility based on P33 concept. For J-PARC P33 concept, there was a problem that the experimental capability had not been evaluated. Thereby, the experimental sensitivity expected at the present time could not be evaluated, and any optimization studies to improve the sensitivity could not be done. In this experiment, the sensitivity greatly depends on a lot of factors such as the experimental setup, the experimental procedure, the magnetic field structure of the rebuncher, the performance of the ultracold neutron source, the storage and transport efficiency of UCNs. In particular, it was difficult to understand the storage and transport efficiency that depend on the performance of the reflective material used in the neutron EDM experiment. Therefore, in this study, for solving this problem, the dependence of the

statistical sensitivity on such reflection performances was tried to be quantitatively investigated by a full simulation that can deal with an experimental system and entire procedures based on J-PARC P33 concept. Details of this content are described in chapter 4. The J-PARC P33 simulation results showed that the experimental sensitivity greatly varied depending on all of the total reflection energy, the non-specular reflection probability, and the loss probability of the reflector. Therefore, in this study, a highly functional reflective material, which is the key to improving the experiment sensitivity, was developed. The content of this study is described in chapter 5. In evaluating the reflection characteristics, various surface analyses were needed. However, it was extremely difficult to determine only the UCN loss probability because its value is only about 10^{-4} for one bounce. Therefore, the author constructed a dedicated experimental facility at J-PARC to perform the UCN storage experiment that enables us to directly determine the UCN loss probability. Details of this experiment are described in chapter 6. Finally, the sensitivity of the J-PARC P33 experiment expected at the present time was evaluated by performing J-PARC P33 simulation with the information of the performance of the reflective material along with the systematic error evaluated in a similar manner as the ILL experiment. As a result, the problem that existed initially in the evaluation of J-PARC P33 experiment is solved, which gives a solid basis on this experimental concept. This content is described in chapter 7.

In particular, the purposes of this study are as follows:

1. Numerical evaluation of the effects of non-specular reflection along with UCN loss on the experimental sensitivity.
2. Development of reflective materials that are actually expected to be used for the experiment.
3. Performing the first UCN storage experiment at J-PARC, which establishes the solid basis for the further development.
4. Performance evaluation of reflective materials using various surface analysis methods related to 3.
5. Estimating final experimental sensitivity and feasibility by conducting full simulation using the results obtained from the above 1-4.

The author's contribution in this thesis is described below. Regarding the basic concept of this experiment, it was proposed as a J-PARC P33 experiment, and I am a co-researcher. In the J-PARC P33 experiment, we proposed a system called rebuncher to refocus high-intensity pulse neutrons, and this concept is also explained in this thesis. The author's contribution to this study is following:

1. Development of dedicated tools to simulate the entire experimental system incorporated with non-specular refection and the rebuncher system.
2. Performing first full simulation study of J-PARC P33 experiment.
3. Development of reflective materials expected to be used for the experiment.
4. Performing the first UCN storage experiment at J-PARC.
5. Estimating the final experimental sensitivity and its feasibility.

It is noted that although development of a highly precise magnetometer is an important subject in the neutron EDM experiment, this thesis does not deal with it.

This thesis is organized as follows. Chapter 1 is an introduction. In chapter 2, the basic neutron

interaction and experimental techniques are explained. In chapter 3, an overview of the neutron EDM experiments is presented, which deals with the sensitivity of the experiment and the details of the experimental procedure. Chapter 4 deals with the evaluation of the dependence of the statistical precision on the storage efficiency and transport efficiency. Chapter 5 deals with the development of reflective materials that is key to the highly precise neutron EDM experiment. Chapter 6 explains the details of the UCN storage experiment for directly measuring the loss probability coefficient. In chapter 7, assuming the performance of the reflector evaluated in chapters 5 and 6, the full simulation was performed in the same manner as chapter 4 in order to evaluate the sensitivity of the J-PARC P33 experiment using the reflector developed in this study. Finally, this study is summarized in chapter 8.

Chapter 2

Neutron Interaction and Basic Experimental Techniques

2.1 Interaction for UCN Physics

2.1.1 Strong Interaction

Neutrons with kinetic energy less than 300 neV, whose velocity is less than ~ 7.6 m/s, is called as ultracold neutron (UCN). A material wavelength of UCN is longer than 50 nm. It is very long compared to the atomic arrangement scale of 0.1 nm. Thus, when UCNs are incident on a substance, neutrons feel at once the repulsive force from the nucleon near the surface. This potential is referred to the Fermi potential and represented as a step function V_F according to the following equation.

$$V_F = 2\pi\hbar^2/m_n Nb \tag{2.1}$$

where m_n is the mass of the neutron, N is the number of atoms per unit volume, and b is the coherent forward scattering length, respectively.

UCNs have the property that can be confined in a material container, which can be used in experiments to measure the fundamental neutron properties, such as lifetime and electric dipole moment. In general, nickel is regarded as a standard material to evaluate the Fermi potential because of its excellent reflection performance. The mirror which can reflect neutrons with a wavelength $1/N$ times the Fermi potential of nickel is called mN mirror.

The Fermi potential of a substance consisting of n kinds of elements $i(i = 0, 1, ..., n)$ is represented as follows:

$$V_F = \frac{2\pi\hbar^2}{m_N} \sum_{i=0}^{n} N_i b_i \tag{2.2}$$

where N_i is the nuclear density of element i, b_i is the scattering length of element i, and m_N is the neutron mass.

Strong interactions not only lead to reflection between the UCN and the substance but also induce loss and absorption. The effect of absorption and loss is expressed as Fermi potential with an imaginary part as follows:

$$V_F = V - iW \tag{2.3}$$

It is possible to calculate the reflectivity / transmissivity of the substance by solving the Schrödinger equation assuming the one dimension wall potential.

$$-\frac{\hbar^2}{2m_n}\triangledown^2\psi + [E - V_F]\psi = 0 \tag{2.4}$$

We obtain the following neutron reflectivity $|R|^2$ as the solution of the Schrödinger equation of 2.4.

$$|R|^2 = 1 - \mu(E, \theta) \tag{2.5}$$
$$= 1 - 2\eta\left(\frac{E_\perp cos^2\theta}{V - E_\perp cos^2\theta}\right) \tag{2.6}$$

where the second term is the UCN loss probability. If the second term of the right side of the formula (2.6) is zero, the reflectivity becomes unity.

In addition, the following relation is satisfied for the expression (2.6).

$$\eta = \frac{W}{V} = \frac{\sigma_{\text{loss}}m_n v}{4\pi\hbar b} \tag{2.7}$$

where σ_{loss} is the total sum of the cross-section due to interactions that lead to UCN loss and absorption, m_n represents the neutron mass, and v denotes the neutron velocity.

Although the reflectivity of UCN is expressed using the parameter η and can be theoretically calculated like expression (2.6), in practice there is a large discrepancy between the theoretical prediction and experimental result. In general, the theory predicts 10^{-5} to 10^{-6}, but 10^{-3} to 10^{-4} is observed in the experiment.

2.1.2 Other Interaction

The scales of gravity potential and kinetic energy of UCN are the same for the neutron. Specifically, the contribution of the gravity potential is given below.

$$V_g \sim 1 \text{ (neV/cm)} \tag{2.8}$$

The neutron decays at ~ 880 s through weak interaction [20].

$$n \rightarrow p + e^- + \overline{\nu}_e \tag{2.9}$$

The neutron lifetime is one of the fundamental parameters to test Big Bang nucleosynthesis and it is an important physical quantity that affects the ratio of the light element in the universe. However, the precise value is not fixed because there is now a large discrepancy between two different major methods. In addition, the neutron lifetime is a parameter that determines the maximum time that UCN can be stored in a container.

The neutron has a magnetic moment μ, so it interacts with magnetic fields. Under an external magnetic field, neutrons cause spin precession. The main components of spin precession are represented as follows:

$$\omega = -\gamma_n B \tag{2.10}$$

γ_n is the gyromagnetic ratio, which is related to $\gamma = 2\mu/\hbar$. For neutrons, $\gamma_n \sim 2\pi \times 29.164702 \text{Hz}/\mu\text{T}$.

Generally, time evolution of the spin precession of particles moving in an electric field follows the Bargmann–Michel–Telegdi (BMT) equation [21][22].

$$\frac{d\vec{s}}{dt} = \vec{s} \times \left[\left(\frac{g_n}{2} - 1 + \frac{1}{\gamma} \right) \vec{B} - \left(\frac{g_n}{2} - 1 \right) \frac{\gamma}{\gamma+1} (\vec{\beta} \cdot \vec{B}) \vec{\beta} - \left(\frac{g_n}{2} - \frac{\gamma}{\gamma+1} \right) \vec{\beta} \times \frac{\vec{E}}{c} \right], \qquad (2.11)$$

where $\vec{s}$ is the spin of UCN, $\vec{E}$ and $\vec{B}$ are electric and magnetic fields, g_n is the neutron g factor, β is the ratio of the UCN speed to the speed of light, and γ is $1/\sqrt{1-\beta^2}$. The first term of the expression (2.11) represents a non-relativistic effect, and the second and third terms represent relativistic effects. Assuming a typical UCN maximum speed 7 m/s, the contribution of the second term is negligibly small compared to the third term. Therefore, in this study, the outer product vector of the third term can be regarded as relativistic transverse magnetic field: B_v.

If UCNs rotate with the frequency ω_r in a cylindrical container to which an electric field is applied, the relativistic fields also rotate. Then, the UCN spin rotation frequency changes as the following formula (2.12):

$$\omega_{xy} = \omega_0 + \frac{1}{2} \frac{(\omega_{\mathrm{rel}})^2}{(\omega_0 \mp |\omega_r|)}, \qquad (2.12)$$

where ω_0 is the Larmor frequency of the neutron, and $\mp|\omega_r|$ represents the angular velocity of counter-clockwise/clockwise rotation. Further, ω_{rel} is $-\gamma_n B_v$, where γ_n and B_v correspond to the gyromagnetic ratio of neutrons and the third term of the equation (2.11), respectively.

For magnetic potential U, a contribution of a magnetic field is expressed as follows.

$$U = \pm 60 \text{ neV/T} \qquad (2.13)$$

where $\pm$ sign represents whether the neutron spin is parallel/anti-parallel to magnetic fields.

Considering that the magnetized foil has an internal magnetic field, the neutrons passing through it feels an additional potential as follows:

$$V_F = \frac{2\pi\hbar^2}{m_n} Nb \pm \mu B \qquad (2.14)$$

where B is the magnetic field inside the material, and $\pm$ correspond to the two spin states. In general, a spin polarizer of UCN is realized by using a thin magnetized foil of ferromagnetic materials.

2.2 Inelastic Scattering

The reaction of the inelastic scattering that excites neutrons is called up-scattering, and the reverse is called down-scattering. In general, the up-scattering process causes a loss of UCN, while the down-scattering can produce UCN. This section describes these two important interactions for UCN experiments.

In general, up-scattering occurs when phonons and angular momentum are exchanged between UCN and a molecule. In the J-PARC P33 experiment, up-scattering process has a serious effect on the performance of UCN production, and its cross section is greatly different between ortho-deuterium and para-deuterium. The calculation result of the up-scattering cross section of the solid deuterium of 0

and 1 phonon exchange is given in Figure 2.1, where the blue line corresponds to 1-phonon exchange for ortho-deuterium, the red line corresponds to 1-phonon exchange for para-deuterium, and the green line corresponds to angular momentum change. In this calculation, the up-scattering cross section of the document [23] and the phonon density of Figure 2.2 are used. Obviously, it is found that there is a large difference between ortho and para-deuterium. In this study, the up-scattering cross section of the Figure 2.1 and solid deuterium of ortho 95% of 5 K are assumed to indicate the performance of the ultracold neutron source. It is noted that both the ortho-para ratio of 95 % and temperature of 5 K are enough feasible.
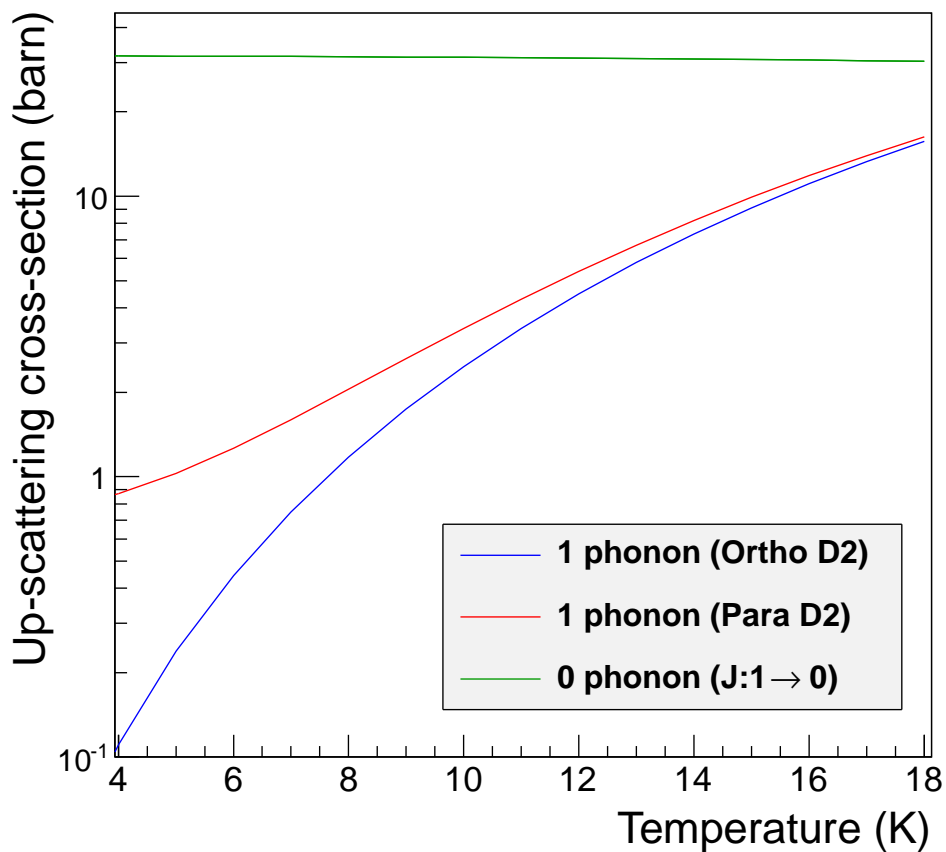
Figure.2.1   Temperature dependence of up-scattering cross-section of solid deuterium. The vertical axis represents the up-scattering cross section, and the horizontal axis represents the temperature of solid deuterium. The green line represents the process of up-scattering due to angular momentum change and the blue and red line represent the cross section of the process where up-scattering occurs due to the sum of inelastic scattering and angular momentum change.

Generally, the UCN loss probability that the neutron optical theory predicts is 1 to 2 orders of magnitude higher than the actual observation. This discrepancy is suspected to be caused by hydrogen having
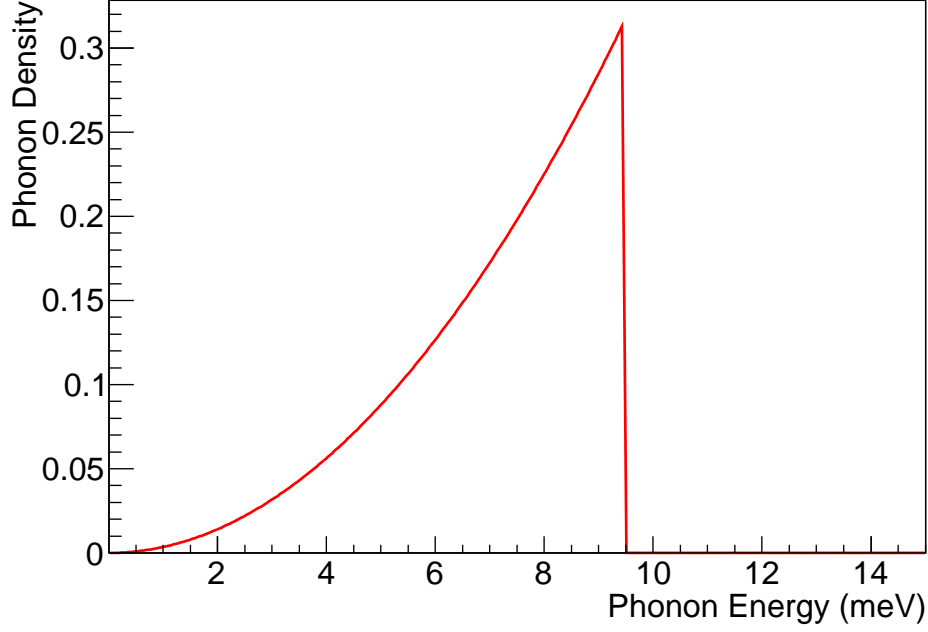
Figure.2.2 Phonon density of solid deuterium. The density of phonon contained in 5 K solid deuterium calculated by using Debye model. The total sum of the spectrum of phonon density is normalized to 1. The vertical axis represents phonon density, and the horizontal axis represents phonon energy.

a large up-scattering cross section. Golub and his colleagues have derived the up-scattering cross section caused by hydrogen film forming on the material surface as follows [24]:

$$\sigma_{\text{ie}}(E) = 4\pi b^2 \int e^{-2W(T)} G(\omega) n(\omega, T) \sqrt{\frac{\omega}{E}} d\omega \tag{2.15}$$

$$2W(T) = \int_0^{\omega_{max}} \frac{G(\omega')}{\omega'} \coth(\frac{\omega'}{2T}) d\omega' \tag{2.16}$$

$$\eta_{\text{film}} = 2\sigma_{\text{ie}}(E) A_{\text{H}} \tag{2.17}$$

where $W(T)$ is Debye-Waller factor, b is incoherent length of hydrogen, $n(\omega, T)$ is $1/[\exp{(\omega/T)} - 1]$, $G(\omega)$ is the phonon density of Ice IV of Figure 2.3, n is the density of hydrogen film, ω is the frequency of phonon, ω_{max} is the maximum frequency of phonon, E_0 is the kinetic energy of neutron in the hydrogen film, and A_{H} is the area density of hydrogen.

It was confirmed that the numerical calculation of formula (2.17) tended to be somewhat lower but consistent [24][25]. Figure 2.4 shows the calculation result of the temperature dependence of UCN loss probability using the phonon density from Figure 2.3, where the density of hydrogen and the incident energy of neutron are assumed to be 7.2×10^{23} (atoms/cm^3) and 100 neV, respectively. This calculation result is consistent with the result of the original paper [24].

11
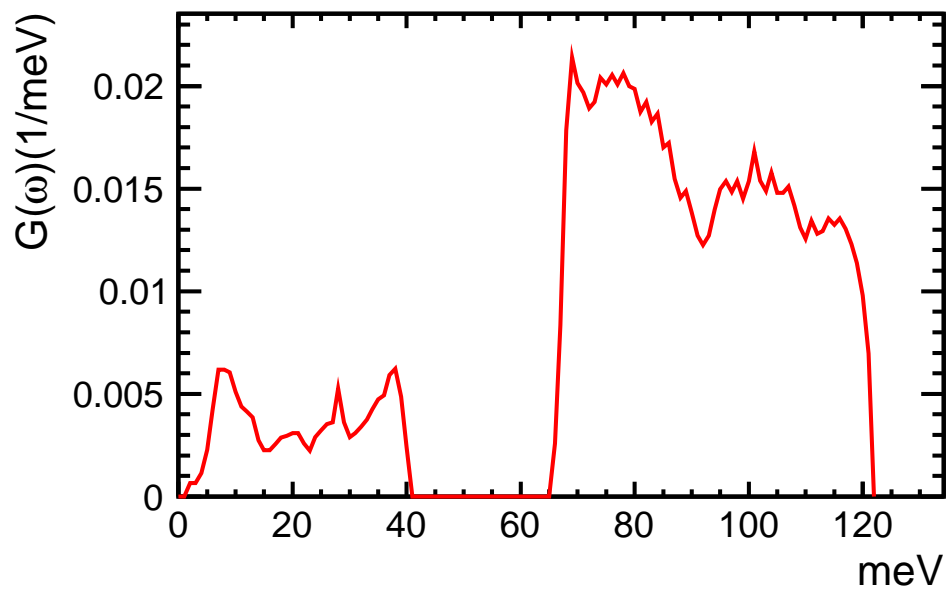
Figure.2.3   Phonon density of ice IV [24]. The total sum of the spectrum of phonon density of ice IV is normalized to 1. The vertical axis is the phonon density of ice IV and the horizontal axis is the energy of the phonon.

Graph

$\times 10^{-3}$
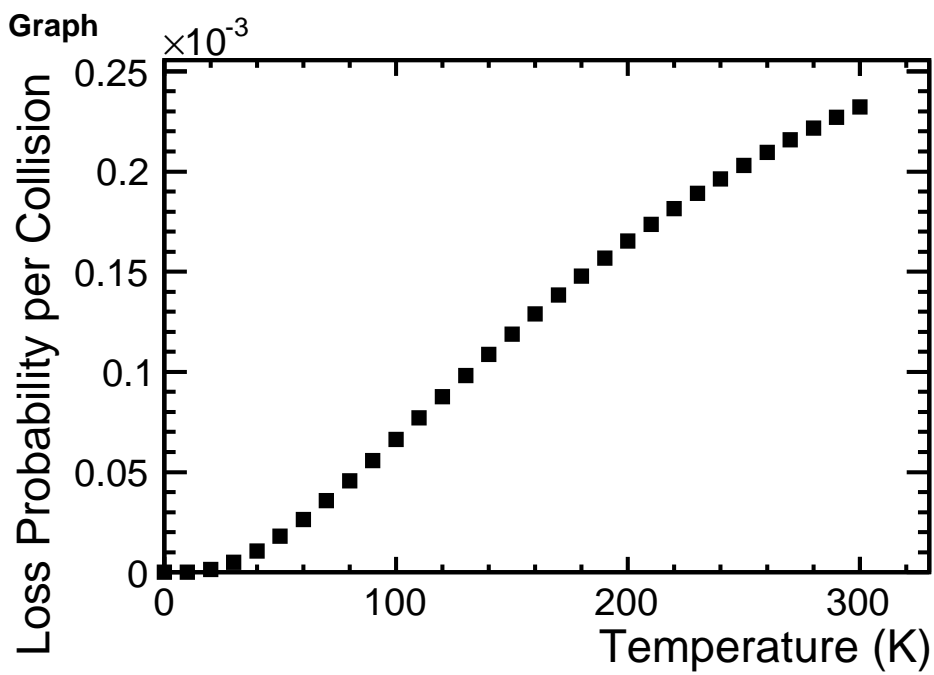
Figure.2.4 Temperature dependence of loss probability coefficient of formula (2.17). The vertical axis shows loss rate of formula (2.17) and the horizontal axis shows temperature. Temperature dependence of loss probability coefficient of formula (2.17) is calculated using phonon density in Figure 2.3.

2.3 Diffuse Scattering

In this study, the ratio of the pulsed beam intensity when using the rebunch method to that when not using the rebunch method is referred to as the rebunch efficiency. In the experiment of J-PARC P33, the rebunch efficiency is significant to assure the experimental capability. However, the rebunch efficiency decreases if the non-specular reflection occurs on the inner surface of the transport guide. On the other hand, if UCNs collectively rotate along the sidewall of the cylindrical measurement cell, the systematic errors due to the relativistic magnetic field and the distortion of the electric/magnetic field become enhanced. In this case, the systematic errors increase if the non-specular reflection does not occur on the inner surface of the storage container. Therefore, it is important for the neutron EDM experiment to control the degree of the non-specular reflection and incorporate these effects into the simulation study. Conventionally, Lambert's cosine law was used to model the non-specular reflection. The scattering intensity of non-specular reflection which Lambert's cosine law predicts is expressed as follows:

$$dI_{\mathrm{lambert}} = I_0 \cos\theta d\Omega \qquad (2.18)$$

where dI_{lambert} is the intensity of reflection beam incident on a differential solid angle $d\Omega$, I_0 is the intensity of incident beam, and θ is the polar angle.

However, in recent years, it is reported that this model does not match experimental result for a well-polished surface, while the micro-roughness model showed a good agreement with an actual measurement [26, 27]. For reference, Figure 2.5 shows the schematic diagram for the non-specular reflection predicted by Lambert's cosine law and that of the micro-roughness model. The micro-roughness model is one of the
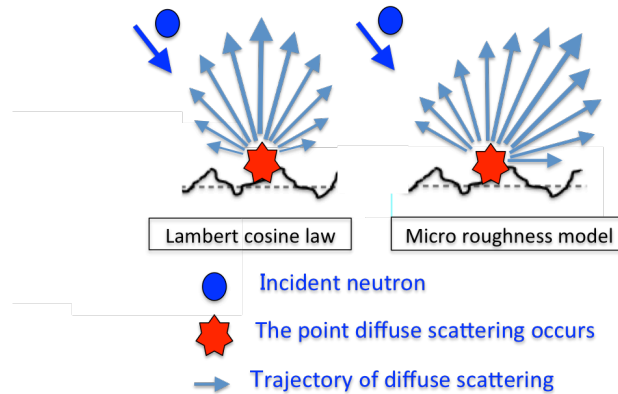
Figure.2.5   Difference between Lambert's cosine law and micro-roughness model

models of DWBA theoretical model [28]. In DWBA theoretical model, the contribution of non-specular reflection is calculated by using the distorted wave Born approximation (DWBA). The specular reflection is regarded as a plane wave reflected from a perfect surface, and the non-specular reflection is regarded

to be caused by the deviation between the perfect plane and the undulated plane. The difference in potential corresponding to the substance between the perfect plane and the undulated plane cause the perturbation Hamiltonian of the distorted wave Born approximation. In this section, the x-axis is defined as the direction that an incident beam travels, and the z-axis is defined as the surface normal of the perfect plane, and the direction orthogonal to x and z is defined as the y-axis. In the DWBA theorem, the non-specular reflection due to the sample roughness is derived by perturbation calculation. Hence, the modeling of the surface state is needed. Shinha shows that the non-specular reflection distribution of X-rays can be reproduced very well by using the following differential scattering cross section and autocorrelation function [28]:

$$\left(\frac{d\sigma}{d\Omega}\right)_{diff} = L_x L_y N_b^2 |T(\vec{k_1})|^2 |T(\vec{k_2})|^2 S(\vec{q_t}) \tag{2.19}$$

$$T(\vec{k_1}) = \frac{2k_{1z}}{k_{1z} + k_{1z}^t} \tag{2.20}$$

$$S(\vec{q_t}) = 2\pi \frac{exp[-[(q_z^t)^2 + (q_z^{t*})^2]b^2/2]}{|q_z^t|^2} \int_0^\infty dR R (e^{|q_z^t|^2 C(R)} - 1) J_0(q_r R) \tag{2.21}$$

$$C(R) = e^{-(R/w)^{2h}} \tag{2.22}$$

where $L_x L_y$ is the irradiation area of beams (x-ray or neutron etc.), k_1 is the wave number vector of the incident beam, $k_1{}^r$ is the wave number vector of the reflection beam, k_1^t is the wave number vector of the transient beam, $\vec{q^t} = \vec{k_2^t} - \vec{k_1^t}$ is the transfer wave number vector of the transmit beam, and $J_0(x)$ is the Bessel function of the first kind of order zero, R is the distance between two points on the surface, and b, w, h, and $C(R)$ are RMS surface roughness, correlation length, hurst-exponent, and auto-correlation function, respectively. Regarding roughness parameters, b corresponds to the average value of the difference from the height of the surface roughness, w represents the roughness in the lateral direction of the surface, h represents information on irregularities on the local surface, and $C(R)$ models the surface roughness that causes the non-specular reflection. Therefore, $C(R)$ strongly depends on the surface profile of the sample.

Although Shinha's model is consistent with actual measurement, it becomes a problem that a large amount of CPU power is required to calculate the numerical integration of S parameter included in the expression (2.21). If we take $h \to 1, w \to \sqrt{2}w$ in the expression (2.22), then the integral of S parameter can be replaced for the analytic solution. Therefore, it is possible to greatly reduce the calculation time. Such a parameter fixed DWBA theoretical model is called "micro-roughness model" and is widely used in UCN physics [29, 30]. In the micro-roughness model, the non-specular reflection probability density $P(\theta_f, \phi_f)$ is given as follows (note that the incident azimuthal angle ϕ_i is assumed to be zero) [26]:

$$P(\theta_f, \phi_f) = \frac{k_c^4}{8\pi} \frac{(bw)^2}{\cos\theta_i} |F(\theta_i)|^2 |F(\theta_f)|^2 \times \exp\left[-\frac{(wk)^2}{2}(\sin\theta_i{}^2 + \sin\theta_f{}^2 - 2\sin\theta_i \sin\theta_f \cos\Phi_f)\right] \tag{2.23}$$

$$F(\theta) = 2\cos\theta/(\cos\theta + (\cos\theta^2 - k_c{}^2/k^2)^{1/2}) \tag{2.24}$$

15

where k is the wave number vector of UCN, θ_i is the incident polar angle to the normal of a surface, θ_f is the scattering angle to the normal of a surface, ϕ_f is the scattering azimuthal angle, b is the RMS roughness of a surface, w is correlation length of a surface, and k_c is the critical wave number vector for total reflection. In addition, it is also noted that k_c is defined as $\sqrt{\frac{2m_n V_F}{\hbar^2}}$, where m_n is neutron mass and V_F is the Fermi potential. Using formula (2.23), the non-specular probability of the micro-roughness model can be calculated as $P(\theta, \phi)d\theta d\phi$.
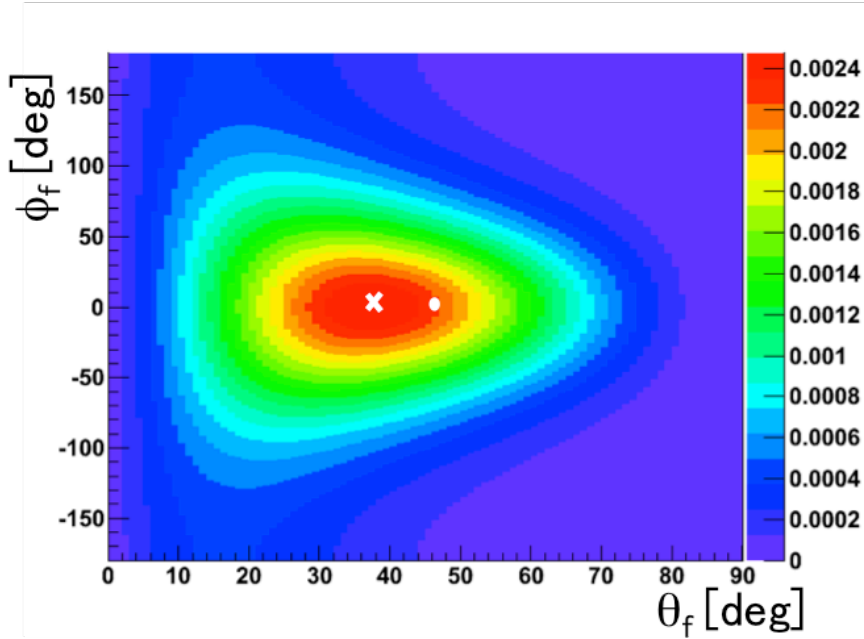
Figure.2.6   Non-specular reflection probability distribution of micro-roughness model. Distribution of non-specular reflection probability when neutron of 100 neV is incident with 45 degree. The horizontal axis corresponds to polar angle after scattering, and the vertical axis corresponds to the azimuthal angle. The white circle means an incident point. In addition, the white cross indicates the point having the maximum value. the image is cited from [31]

Figure 2.6 shows a typical non-specular reflection probability distribution of the micro-roughness model. As for the condition of Figure 2.6, $w = 33$ nm and $V = 200$ neV are used. It is noted that the total sum of non-specular reflection probability is normalized to unity. It is found that the distribution is localized depending on the incidence angle and is symmetric to ϕ.

Also, the $\theta - \phi$ distribution of the non-specular reflection where w are 5 nm, 50 nm and 100 nm, and $\lambda = 250$ nm are given in Figure 2.7. It is found that the distribution is narrowing as w becomes large. This corresponds to the fact that the surface becomes flat as w becomes large. Generally, the mean square radius of roughness, b, has a strong effect on non-specular reflection probability but does not affect distribution. For reference, a plot of roughness and the non-specular reflection probability are given in the left side of 2.8. Also, w is proportional to the non-specular reflection probability. For reference, a relation between the correlation length versus non-specular reflection probability is given in the right side of Figure 2.8. The vertical axis is the non-specular reflection probability, and the horizontal axis is
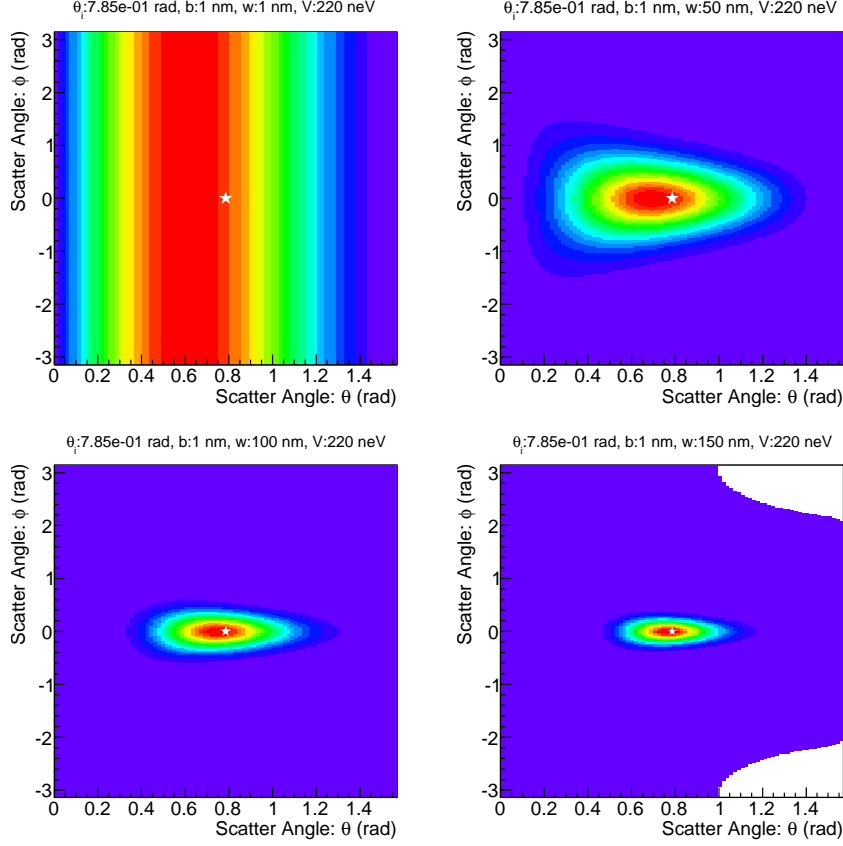
Figure.2.7 Correlation length dependence of non-specular reflection probability distribution. Non-specular reflection probability distribution is calculated assuming neutron having kinetic energy 100 neV incident on material surface with correlation length of 1 nm, 5 nm, 50 nm, 100 nm at 45 deg. The horizontal axis shows the polar angle after scattering, the vertical axis shows the azimuth angle after scattering, and a white star shows the incident point. Each square pads corresponds to a non-specular reflection distribution with correlation lengths of 1 nm, 5 nm, 100 nm and 50 nm from the upper left in a clockwise direction. Here, b and V_F are chosen to 2 nm and 200 neV.

the correlation length. It is noted that b and V are chosen to be 1 nm and 200 neV, respectively.

Since the perturbation calculation is used in the DWBA theorem, the micro-roughness model has the following application limit for surface roughness:

$$q_z b \ll 1 \tag{2.25}$$

where q_z is defined as $4\pi/\lambda \sin\theta = \frac{2\sqrt{2mE_{UCN}}}{\hbar}\sin\theta$.

The condition of $q_z b < 1$ for 10 m/s neutrons correspond to $b < 30$ nm. In fact, a more severe roughness is required as a condition when using the micro-roughness model because $q_z b \ll 1$ is the applicable limit. In this study, it is considered that the application limit condition of $q_z b \ll 1$ is satisfied if $b < 3$ nm.

17
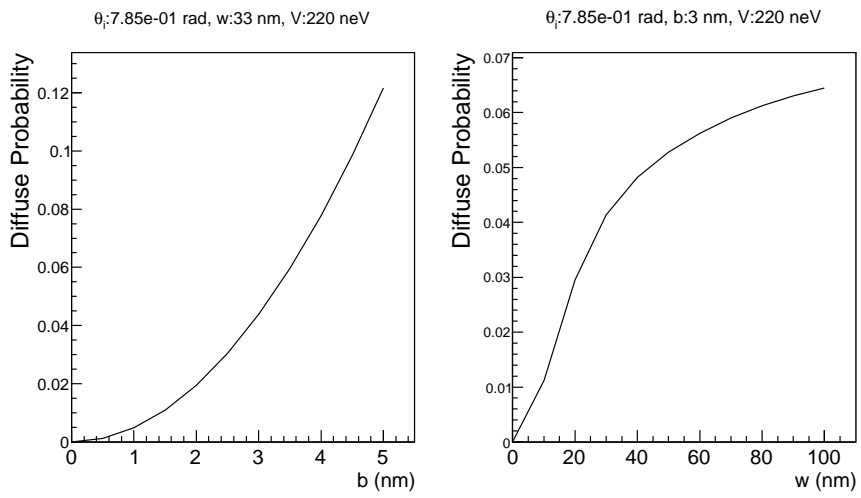
Figure.2.8 The dependence of non-specular reflection probability on root means square rough-
ness/correlation length. (Left) The root mean square roughness dependence of non-specular re-
flection probability when neutron having kinetic energy 100 neV incident on the material surface
at 45 degree. The horizontal axis represents the mean square roughness, and the vertical axis
represents the non-specular reflection probability. Correlation length and potential are chosen to
33 nm and 200 neV. (Right) Correlation length dependence of non-specular reflection probability
when neutron having kinetic energy 100 neV incident on the material surface at 45 degree. Here,
b and V_F are chosen to 2 nm and 200 neV.

2.4 UCN Source

This section explains the details of two UCN production method: the super-thermal method and the Doppler shift method.

2.4.1 super thermal UCN production

In general, fast neutrons produced by nuclear reactions can be cooled down to several meV with deceleration due to the elastic scattering with nucleons, but further cooling requires inelastic scattering of the quasiparticles such as phonons and magnons. In this thesis, the technique to generate ultracold neutrons in this way is called the super-thermal method. There are three candidate materials used for UCN source: liquid helium, solid deuterium, and solid oxygen. At the present time, liquid helium and solid deuterium are in practical use.

When the cold neutron flux Φ is irradiated to the substance having the cooling cross section σ for certain interval Δt, the density of generated UCN ρ and UCN production rate is expressed by the following equations [32][33].

$$\rho = P\tau(1 - \exp(-\Delta t/\tau)) \tag{2.26}$$
$$P = N\sigma\Phi \tag{2.27}$$

where N is the number of nuclei, P is the production rate of UCN source, and τ is the decay time determined by absorption and up-scattering in UCN source.

In this study, The UCN density produced when the UCN source is irradiated by DC beam for a long time denotes ρ_{DC}. On the other hand, the UCN density produced when a UCN source is irradiated by pulsed beam for Δt denotes ρ_{pulse}. In general, ρ_{DC} can be calculated by taking $t \to \infty$ in the expression (2.26), which results in $\rho_{\text{DC}} = P\tau = N\sigma\tau$. ρ_{pulse} can be calculated by taking $t \to \Delta t$ in the expression (2.26). It is noted that the flux for pulsed beam is changed as $\Phi \to \Phi/\Delta t$. Therefore, ρ_{DC} and ρ_{pulse} are represented as follows:

$$\rho_{\text{DC}} = N\sigma\Phi\tau \tag{2.28}$$
$$= P\tau$$

$$\rho_{\text{pulse}} = N\sigma\Phi/\Delta t\tau(1 - \exp(-\Delta t/\tau)) \tag{2.29}$$
$$\sim N\sigma\Phi$$
$$= P$$

From the above, it is understood that τ represents the DC beam characteristic and P represents the pulsed beam characteristic, respectively. As an example, the calculation below shows the UCN density produced in 5 K solid deuterium source. Hereafter, the cold neutron flux of a Maxwell distribution of 30 K is assumed. In the case of the DC beam irradiation, the following relation holds between the UCN density $\rho_{\text{DC,sD2}}$ and the cold neutron flux Φ (see Table 4 of document [34]).

$$\rho_{\text{DC,sD2}} = 1.5 \times 10^{-11} \Phi \tag{2.30}$$

On the other hand, the UCN density produced when a pulsed beam is irradiated can be calculated from the relation that $\rho_{\text{pulse}} = \rho_{\text{DC}} \frac{\rho_{\text{pulse}}}{\rho_{\text{DC}}} = \rho_{\text{DC}}/\tau$ and $\tau = 146$ ms for solid deuterium. As a result, the following relationship is satisfied between $\rho_{\text{pulse,sD2}}$ and Φ.

$$\rho_{\text{pulse,sD2}} = \left(1.5 \times 10^{-11}/146 \times 10^{-3}\right) \Phi \sim 10^{-8} \Phi \tag{2.31}$$

The characteristics of various ultracold neutron sources are given in Table 2.1 [20][23][34][35]. Generally, liquid helium has a low production rate but $P\tau$ is high, whereas solid deuterium is the opposite. In other words, liquid helium is suitable for DC proton beam experimental system because of its poor timing structure, but solid deuterium is suitable for the experiment using pulsed proton beam because of its good timing structure. For reference, The time evolution of $P\tau$ is shown in Figure 2.9, where it is assumed that the cold neutrons flux follow Maxwell distribution of 30 K and the amount of flux is $\Phi_0 = 2 \times 10^{12}$[n/cm^2/s], respectively.

Converter Material	Superfluid ^{4}He	Solid ortho-D$_2$	αO$_2$
Interaction	Phonon	Phonon	Phonon, Magnon
Ideal Temperature of Material	0.7 K	5 K	2 K
Ideal Neutron Flux Temperature	9 K	29 K	12 K
Production rate with 30 K neutrons	$9.3 \times 10^{-10}\Phi_0/cm^3/s$	$1.0 \times 10^{-8}\Phi_0/cm^3/s$	$2.4 \times 10^{-9}\Phi_0/cm^3/s$
Ideal storage time	886 s	146 ms	489 ms
UCN density with 30 K DC neutrons	$8.2 \times 10^{-7}\Phi_0/cm^3$	$1.5 \times 10^{-9}\Phi_0/cm^3$	$1.2 \times 10^{-9}\Phi_0/cm^3$

Table.2.1   Details of ultracold neutron source

Because τ value of liquid helium is very sensitive to temperature, temperature management is needed to maximize its performance. It gives the temperature dependence of helium τ in Figure 2.10. The temperature dependence of τ depends on the up-scattering cross section and absorption cross section. In general, the temperature dependence of the cross section of solid deuterium is not tight compared to liquid helium. Such an easy temperature control is an advantage of ultracold neutron source of solid deuterium.

Solid deuterium has two states: ortho and para. In the present work, a technique for aligning purity of 95% or more with ortho D$_2$ has been established. The absorption cross section of ortho solid deuterium is 520 microbarn against thermal neutron, and this contribution is smaller than the up-scattering cross section of Figure 2.1. The elastic scattering cross section and mean-free path of solid deuterium are 2.04 barn and 8.2 cm [36]. If elastic scattering occurs, the timing structure will be distorted somewhat when it is taken outside from the solid deuterium.

In general, the up-scattering cross section of solid deuterium depends greatly on how it is produced. It is believed that the crystalline state and residual stress of solid deuterium are influencing [37]. For example, when a solid deuterium is produced directly from deuterium gas, it becomes a solid with a very
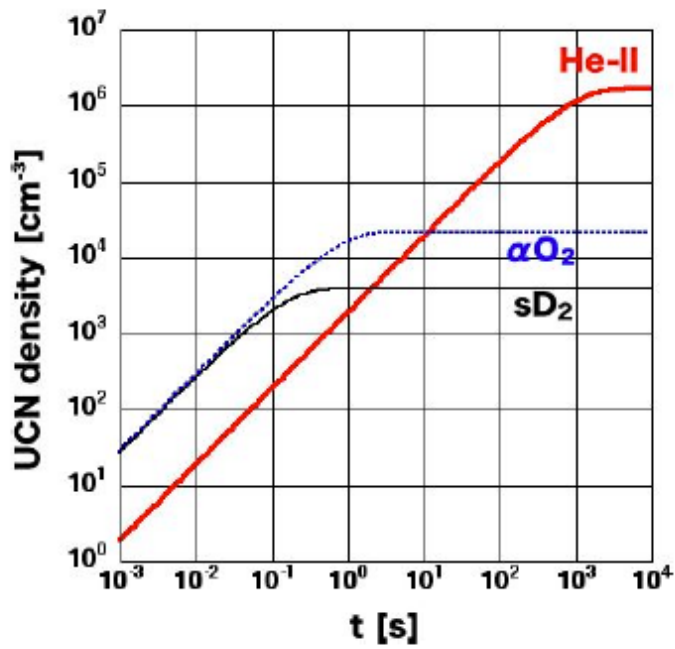
Figure.2.9   Time evolution of the UCN density accumulated in converters, the image is cited from [18]. For details see the text.

good crystalline state, and as a result, the residual stress decreases. In addition, because the proton beam radiation affects the crystallinity of solid deuterium, it degrades the UCN production performance. Thus, the UCN production method with pulsed beams can suppress the performance deterioration more effectively than with DC beams.
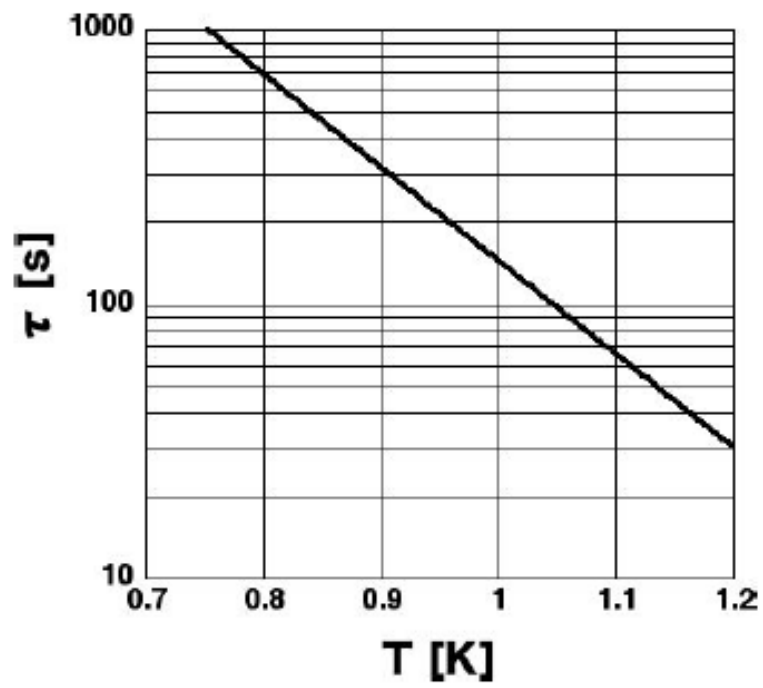
Figure.2.10 Temperature dependence of superfluid helium τ due to up-scattering, the image is cited from [18].

2.4.2 Doppler Shift

In general, particles are decelerated when reflected from a mirror moving in the same direction as follows [38]:

$$\vec{v}_r = \vec{v} + 2|(\vec{v} - \vec{v}_m){\cdot}\vec{n}|\vec{n} \tag{2.32}$$

where $\vec{v}_r$ is the velocity of the reflection neutron, $\vec{v}$ is the velocity of the incident neutron, $\vec{v}_m$ is the velocity of the mirror, and $\vec{n}$ is the normal vector of the reflection point.

A machine that decelerates neutrons by using the relation of formula (2.32) is referred to as Doppler Shifter. If $\vec{v}_m$ is chosen to have a $\vec{v}/2$, the reflected neutron becomes decelerated to nearly at rest. This is the principle to produce UCN with Doppler Shift method. By using multilayer mirror used for the reflector of Doppler Shifter, it is possible to decelerate neutron with an energy higher than the Fermi potential. In general, such a multilayer mirror is called a super mirror. The super mirror can be used for the Doppler Shifter to effectively produce ultracold neutrons. The super mirror of Doppler Shifter is referred to as a Doppler mirror hereafter.

Following the document [38], the three-dimensional velocity when the neutron reflected by a Doppler mirror are illustrated as in the Figure 2.11. The situation of Figure 2.11 is an analogy of the actual operation of the Doppler Shifter of J-PARC MLF BL05. Hereafter, the z-axis is defined as the beam direction, the rotation axis is defined as the x-axis, and the direction orthogonal to x and z is defined as the y-axis. In this thesis, the intersection point of the center of the mirror surface and the z-axis is referred to as a pseudo source point. In addition, it is assumed that the Doppler mirror rotates at the speed $v_m {\sim} v/2$ and the plane of the mirror is parallel to the x-axis. At this time, the velocity components v'_x, v'_y, v'_z of reflection neutrons can be written as follows:

$$\vec{V} = \begin{pmatrix} v'_x \\ v'_y \\ v'_z \end{pmatrix} \tag{2.33}$$

$$= \begin{pmatrix} 2v_m\delta_x \\ 2v_m(\delta_y + \theta(t)) \\ 2vm - v + 3v_m\theta(t)^2 \end{pmatrix} \tag{2.34}$$

where δ_x is the incident angle of the neutron in the x plane, δ_y is the incident angle of y plane, v and v_m are the magnitudes of $\vec{v}$ and $\vec{v}_m$, and $\theta(t)$ is the rotation angle of the mirror with respect to y axis at a certain time t. Also, when deriving the expression (2.34), we neglected terms which are higher than the third order in $|v_m - v/2|$, δ_x, δ_y and θ.

The UCN velocity can be calculated assuming an incident neutron velocity and formula (2.32). In this study, such a simulation is called the Doppler Shifter Simulation. Indeed, by substituting the typical neutron velocity and divergence to the expression (2.34), we can confirm that the UCN production by the Doppler Shifter. Specifically, using speed $v = 136$ m/s, $v_m = 68$ m/s, $\delta = \sqrt{\delta_x{}^2 + \delta_y{}^2} = 30$ mrad and $\theta = 0$, we can get the speed of reflected neutron as $v' = (v\delta_x, v\delta_y, 0) \rightarrow |v'| = v\delta < 7$ m/s. This result satisfies the definition of UCN.
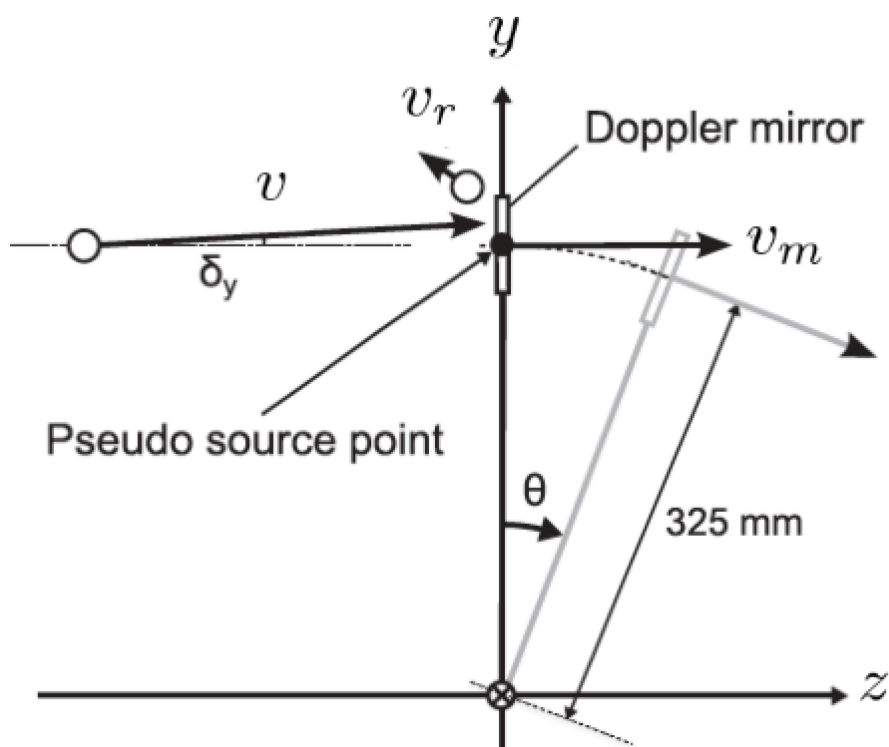
Figure.2.11 Schematic diagram of Doppler Shifter, taken from [38]

Chapter 3

Neutron EDM Experiment

3.1 The Principle of the Method to Determine Neutron EDM

The intrinsic non-zero neutron EDM (d_n) becomes parallel or antiparallel to the spin vector [39]. This fact assures that the neutron EDM has the same transformation rule as spin. The hamiltonian H of non-zero neutron EDM in an electric fields E is represented as $H = -d_n \cdot E$. In general, after a time reversal transformation, neutron spin change its plus/minus sign and the electric field E does not change sign. Therefore, the hamiltonian changes its sign as $H_{\text{before}} = -d_n \cdot E \rightarrow H_{\text{after}} = d_n \cdot E$, where H_{before} and H_{after} are hamiltonian before and after the time reversal transformation, respectively. If the physics does not change before and after the time reversal transformation, following relation holds: $H_{\text{before}} = H_{\text{after}} \Rightarrow d_n = 0$. From the contraposition, it is concluded that following logic becomes true: if an intrinsic non-zero neutron EDM is observed, time reversal symmetry is violated.

Neutrons precess in a magnetic field due to its magnetic moment μ_n. Similarly, if neutrons have EDM d_n, neutrons precess in an electric field. Assuming that neutrons have μ_n and d_n, a magnetic field is applied upward, and an electric field is applied parallel/anti-parallel to the magnetic field, and the neutron spin vector will precess with the following frequency ω:

$$\omega_{\uparrow\uparrow/\uparrow\downarrow} = \frac{2\mu_n B_{\uparrow\uparrow/\uparrow\downarrow} \pm 2d_n E}{\hbar} \tag{3.1}$$

where $\omega_{\uparrow\uparrow}$ represents the case where the magnetic field is upward and the electric field is upward, and $\omega_{\uparrow\downarrow}$ is the case where the magnetic field is upward and the electric field is downward.

In the formula (3.1), the contribution of the neutron EDM can be derived by taking the difference of the precession frequencies of the two cases. Using $\Delta\omega = \omega_{\uparrow\uparrow} - \omega_{\uparrow\downarrow}$, the neutron EDM can be written as follows:

$$d_n = \frac{\hbar\Delta\omega - 2\mu_n(B_{\uparrow\uparrow} - B_{\uparrow\downarrow})}{4E} \tag{3.2}$$

Normally, the contribution due to the term of $B_{\uparrow\uparrow} - B_{\uparrow\downarrow}$ can be regarded as zero. In this case, the amount of the neutron EDM can be derived using the precession frequency change as $d_n = \frac{\hbar\Delta\omega}{4E}$. For reference, a schematic illustration of the principle of neutron EDM measurement is given in Figure 3.1. If $B_{\uparrow\uparrow} - B_{\uparrow\downarrow}$ is non-zero in expression (3.2), this term becomes a systematic error.

$$\hbar\omega_+ = 2\mu_n B \boxed{+ 2d_n E} \qquad \hbar\omega_- = 2\mu_n B \boxed{- 2d_n E}$$

$$d_n = \frac{\hbar\Delta\omega}{4E}$$
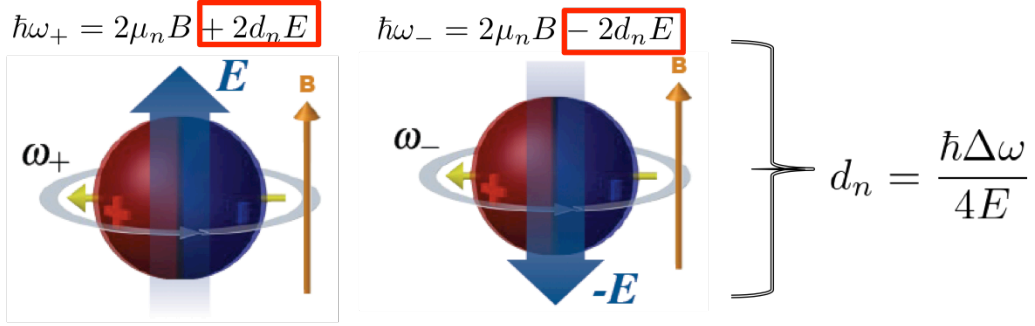
Figure.3.1   Illustration of the principle to measure the neutron electric dipole moment, the image is cited from [40]

In an actual neutron EDM experiment, a method called "the Ramsey separated-oscillatory-field magnetic resonance method" is used to detect the precession frequency change [41]. The schematic illustration of the sequence of the Ramsey separated-oscillatory-field magnetic resonance method is shown in Figure 3.2. At the beginning of the measurement cycle, polarized neutrons are filled in a storage container to which a static magnetic field B_0 and a static electric field E are applied. Next, the resonant oscillating field $B_{\rm rf}$ is applied in the direction orthogonal to B_0 in order to turn the spin of neutrons into parallel to the ground. Next, UCNs are made to precess for a long time. Finally, $B_{\rm rf}$ is applied again so that the spin turns in the opposite direction to that of the first neutron polarization. This is the procedure of Ramsey's method of separated oscillating fields.

After the Ramsey's method, UCNs are extracted from the storage container and then counted by a detector behind the spin filter. The oscillation in the detected counts corresponding to RF frequency as shown in Figure 3.3 [42] can be observed. Specifically, the count number measured after Ramsey's method follows as formula (3.3):

$$N_{\rm down/up}(\omega) = \overline{N_{\rm down/up}}[1 \pm \alpha \cos\left((\omega_{\rm rf} - \gamma_n B_0)(T + 4t_{\pi/2}/\pi)\right)] \tag{3.3}$$

$$\overline{N} = \frac{N_{\rm max} + N_{\rm min}}{2} \tag{3.4}$$

where $N_{\rm down/up}$ is the number of counted neutrons for each spin state, $\omega_{\rm rf}$ is the precession frequency by an oscillating magnetic field, T is the free precession time, $N_{\rm max}$ and $N_{\rm min}$ are the maximum and minimum values of the count number, and $\overline{N}$ is defined as the average of $N_{\rm max}$ and $N_{\rm min}$, α is the quantity called visibility and it is typically represented as $(N_{\rm max} - N_{\rm min})/(N_{\rm max} + N_{\rm min})$, and $t_{\pi/2}$ is the period of the $\pi/2$ spin-flip pulse.

Differentiating the formula (3.3) with respect to the frequency of the RF magnetic field, we obtain the following equation:

$$\left|\frac{dN(\omega)}{d\omega_{\rm rf}}\right| = \overline{N_{\rm down/up}}\alpha T \sin\left((\omega_{\rm rf} - \gamma_n B_0)(T + 4t_{\pi/2}/\pi)\right)$$

$$\sim \overline{N_{\rm down/up}}\alpha T \sin\left((\omega_{\rm rf} - \gamma_n B_0)T\right) \tag{3.5}$$
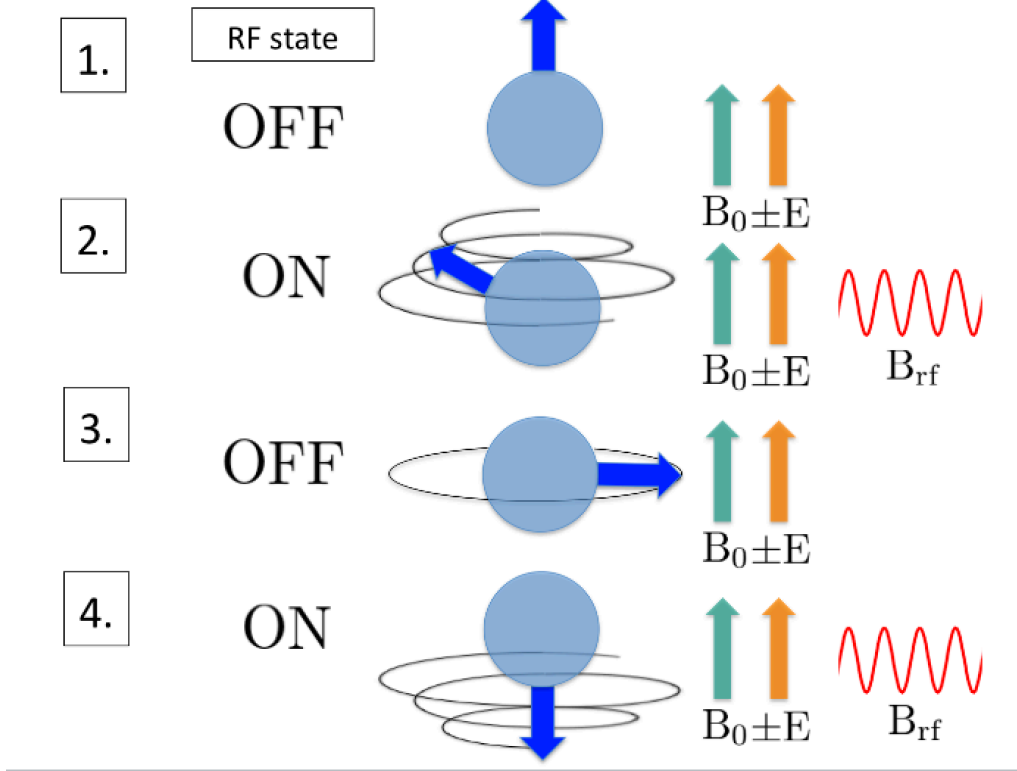
Figure.3.2   Schematic illustration of Ramsey method

The expression (3.5) becomes maximal when $(\omega_{\mathrm{rf}} - \gamma_n B_0)T = \pi/2$. Therefore, we can experimentally determine $\omega = (\omega_{\mathrm{rf}} - \gamma_n B_0)$ most efficiently by fitting two points near $\pi/2$ of the measurement data with the expression (3.3). If the neutron EDM is present, an additional shift contributed from the neutron EDM will occur in ωT. In this study, the total count number in the data with $(\omega_{\mathrm{rf}} - \gamma_n B_0)T = \pi/2$ is referred to as N hereafter. On the other hand, as mentioned in 3.2, neutrons for each spin state are counted in every measurement cycle. Therefore, N can be represented as $N = \overline{N_{\mathrm{up}}} + \overline{N_{\mathrm{down}}}$. In this way, the sensitivity of the measurement can be derived as follows:

$$\sigma_{\omega_{\mathrm{rf}}} = \left| \frac{d\omega_{\mathrm{rf}}}{dN} \right| dN = \frac{1}{(\alpha T \sqrt{N})} \tag{3.6}$$

In an actual neutron EDM measurement, the dataset with the electric field upward and downward are subtracted from one another to eliminate the contribution of the magnetic field (see formula (3.1) and (3.2)). Therefore, the statistics of the formula (3.6) must be regarded as one-half and the error propagation factor $\sqrt{2}$ must be multiplied. In such a way, the following formula can be obtained as the sensitivity of the neutron EDM experiment:
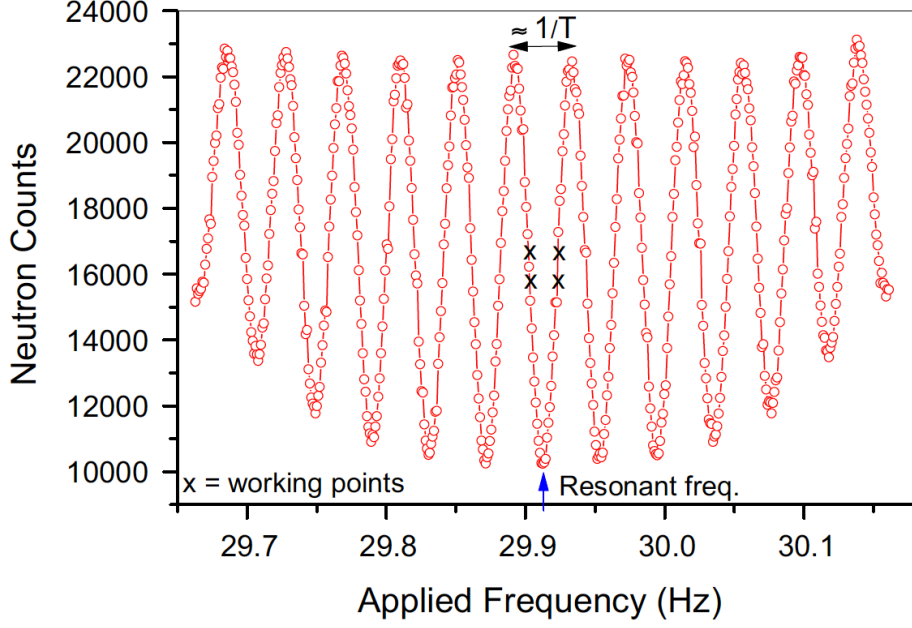
Figure.3.3 RF frequency dependence of count number in the neutron EDM measurement experiment, the image is cited from [42]. The vertical axis represents the number of detected UCNs, the horizontal axis represents the frequency of RF, and T in the figure represents free precession time of neutrons in Ramsey's method. The counted number after Ramsey's method vibrates according to the RF frequency. The count number changes most largely at the point $\frac{1}{4T}$.

$$
\begin{aligned}
\sigma_{d_n} = \frac{\hbar \sigma_{\omega_{\mathrm{rf}}}}{4E} &\sim \hbar \sqrt{2} \frac{1}{(\alpha T \sqrt{N/2})} \frac{1}{4E} \\
&= \frac{\hbar}{(2\alpha E T \sqrt{N})} \quad (3.7) \\
&= \frac{\hbar}{(2\alpha E T \sqrt{n N_{1\mathrm{meas}}})} \quad (3.8)
\end{aligned}
$$

where N represents the number of UCNs counted in the whole experiment, $N_{1\mathrm{meas}}$ represents the number of UCNs counted in one EDM measurement cycle, and n represents the number of repetition for the measurement cycle used in the whole experiment.

The sensitivity of the neutron EDM experiment is scaled by $1/\sqrt{N}$. In addition, the sensitivity of the experiment is improved the most when the denominator becomes maximum. Assuming the time evolution of UCN number N follows $N = N_0 \exp(-T/\tau)$, we obtain the following condition as the best statistical sensitivity:

$$
\begin{aligned}
\frac{d}{dT}\left(T\sqrt{\exp(-T/\tau)} \right) &= 0 \\
&\rightarrow T = 2\tau \quad (3.9)
\end{aligned}
$$

In this study, the condition of formula (3.9) is used to estimate the statistical precision of J-PARC P33.

3.2 ILL Experiment

This section explains the procedure of the neutron EDM measurement experiment of the ILL experiment. Figure 3.4 shows the setup of the ILL experiment [42]. In the ILL experiment, the following apparatuses are used: ultracold neutron source, transport guide, polarizer, storage cell, polarized Hg cell, door system, electrode, magnetic shield, and ^{3}He detector. Following the document [42], give an explanation of the main apparatuses below.
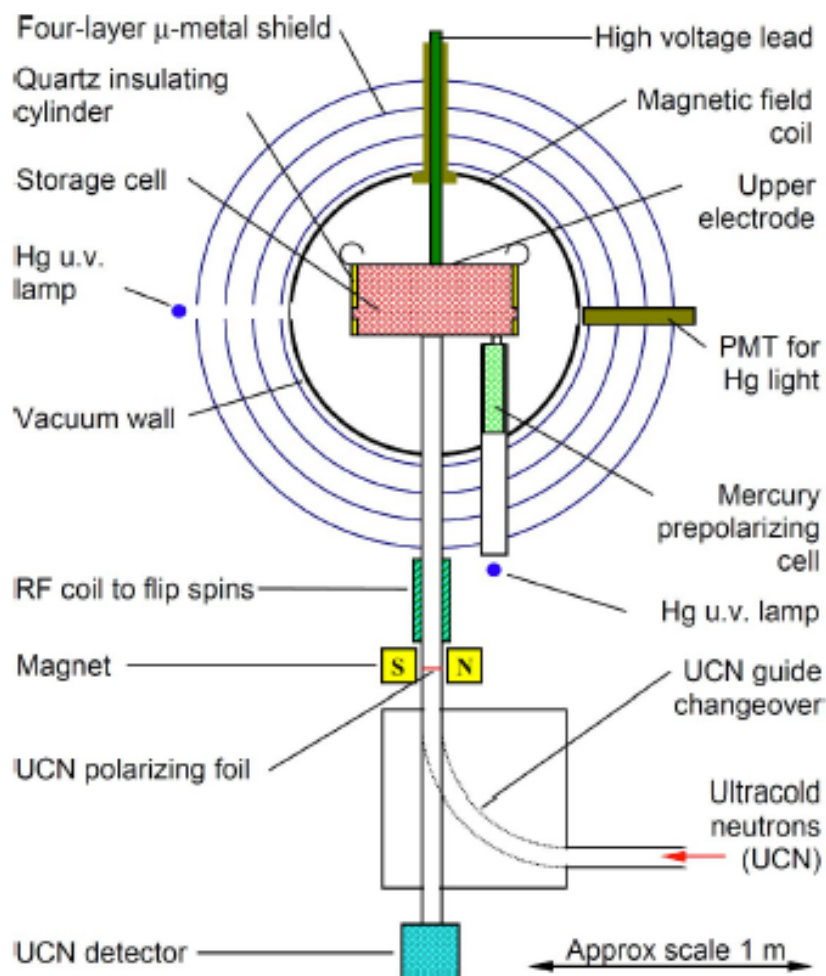
Figure.3.4   Schematic view of setup used for the ILL experiment. the image is cited from [42]

Ultracold neutron source

The schematic diagram of UCN source of ILL is shown in Figure 3.5 [20]. Nuclear fission neutrons emitted from the reactor of ILL are moderated with 20 K by heavy water and then transported

upward with a 12 m long guide pipe with a curve. Since high-speed neutrons cannot curve, only cold neutron less than 50 m/s reaches the tip of transport guide. Finally, UCN production is done by Doppler shifter.

Storage Container

The storage container used in the ILL experiment consists of quartz glass cylinder and discs coated with DLC film. DLC film was deposited on 30 mm aluminum substrate with 1 μm. The inner shape of the container was 47 cm in diameter and 12 cm in length (21 L). In general, the potential of quartz glass is 91 neV, and the potential of DLC is 210 neV. The reason why quartz is used on the side of the container is that current flows occurs unless it is an insulator. Two holes are drilled in the lower disk, and its opening and closing can be controlled with two doors, called UCN door and Hg door. There are small windows on both sides of the sidewall of the storage cell, where the laser can be incident from the outside on one side of the window and its intensity can be monitored with a photomultiplier tube outside the windows.
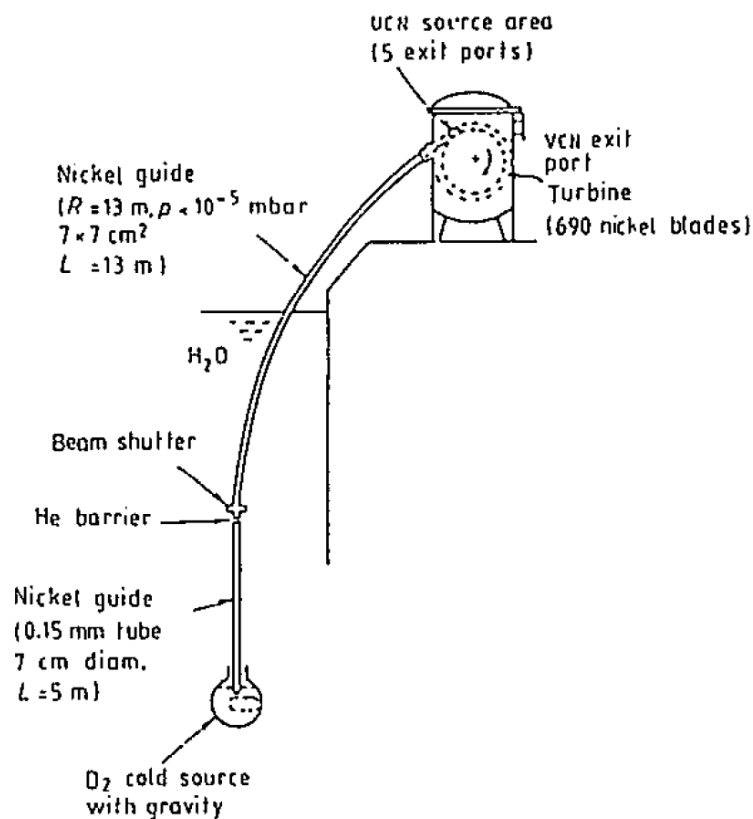
Figure.3.5 Schematic diagram of the ultracold neutron source of the ILL experiment, the image is cited from [20].

Polarized Hg chamber

When polarized ^{199}Hg is irradiated with right-handed circularly polarized light of a wavelength of
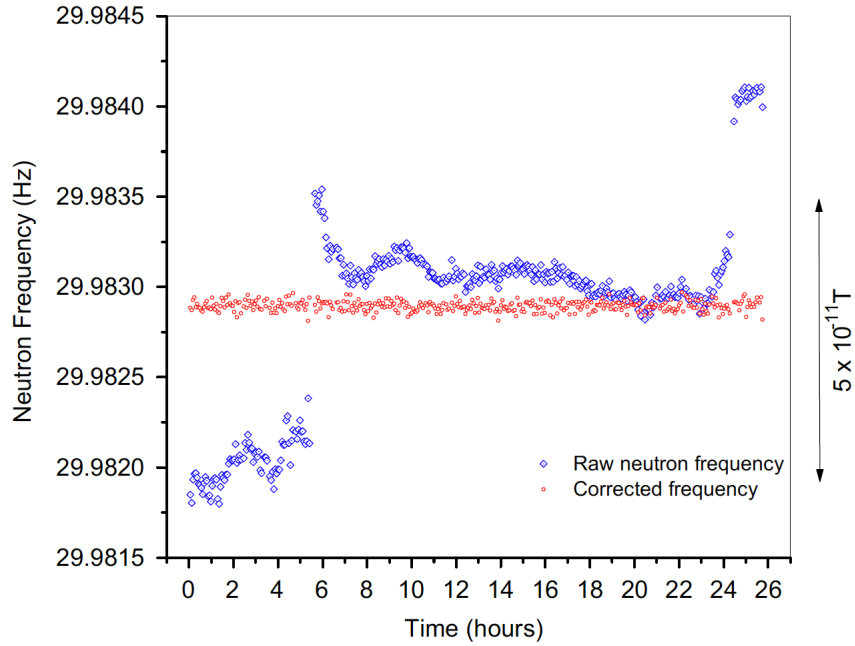
Figure.3.6 Example of the effect of Hg co-magnetometer, the image is cited from [42]. The vertical axis shows the fluctuation of the precession frequency, the horizontal axis shows the measurement time, the blue and red shows the data before and after correction by Hg co-magnetometer. Before the correction, $\sim 5 \times 10^{-11}$ T errors occurred due to the fluctuation of the magnetic field, but it is sufficiently suppressed after the correction.

254 nm, its intensity is attenuated according to the spin component of ^{199}Hg. Hence, it becomes possible to monitor the state of precession of the ^{199}Hg gas confined in the storage container to which a magnetic field is applied. In the ILL experiment, the fluctuation due to environmental magnetic field was corrected by monitoring the precession frequency of polarized ^{199}Hg cohabiting with UCNs in the chamber. Such a tool of correcting the magnetic field drift by Hg atoms is called Hg co-magnetometer. In the ILL experiment, ^{204}Hg lamp was used as the light source used for Hg co-magnetometer. The effect to compensate an environmental magnetic field fluctuation is shown in Figure 3.6. The blue and red points represent the drift of magnetic field in the neutron EDM measurement before and after correction of the environmental magnetic field. Before the correction, the magnetic field change amount to 10^{-25} e·cm, but it is suppressed to a much smaller magnetic field change after correction.

Door system

The storage container has two holes. One hole is 67 mm in diameter at the center and 4 cm deep, which serves to connect the storage container to the UCN detector. The other is a hole with a diameter of 10 mm, which serves to connect the storage container to the Hg chamber. The function of opening and closing of the door was implemented by moving the UCN door consisting of beryllium-copper coated by DLC, and its opening and closing was controlled by the compressed air. The gap of the door and hole was less than 100 μ m. All the device consist of nonmagnetic

materials. In the ILL experiment, a survey at a distance of 2 cm from the inner wall of the surface was carried out with a flux gate magnetometer with an accuracy of 1 nT, and it was confirmed that there was no residual magnetic field. In other words, in the ILL experiment, the possibility that a magnetic field of less than 1 nT existed cannot be excluded. This caused systematic errors, so that this issue must be discussed in detail later in the section of systematic errors.

Electrode

In the ILL experiments, a DLC/Aluminum disk was used as the electrode. The HV feedthrough was connected to the upper disk and the lower disk was grounded. In the ILL experiment, the magnitude of the voltage applying in the upper and lower disks was 7 kV/cm. In the ILL experiment, it was found that there was a dipole magnetic field synchronized with the direction of the electric field applying in the HV feedthrough. This will cause systematic errors, so that this issue must be touched in detail later in the section of the systematic error.

Polarizer

The Fermi potential of iron with saturation magnetization depends on the polarization of neutron and it becomes 90 neV or 300 neV. In the ILL experiment, the transport path was blocked with a Si/Fe filter that becomes magnetization saturation with 0.1 T permanent magnet. As a result, since the UCNs on one polarization cannot pass through the filter, it is operated as a polarizer.

Magnetic shield

The time change of the environmental magnetic field has a huge effect on the neutron EDM measurement. Therefore, a magnetic shield was constructed by disposing four layers of mu-metal around the measurement container. However, it was difficult to make the arrangement of the mu-metal perfectly symmetrical. Non-uniformity of the magnetic field caused systematic errors, so that this issue must be discussed in the section of the systematic error.

^{3}He gas proportional counter

In the ILL experiment, ^{3}He gas proportional counter was used as UCN detector. Helium 3 cause the following nuclear reaction with neutrons: ^{3}He + n $\rightarrow ^3$ H + p. The interaction cross section is very large as great as 5333 barn. Thus, ultracold neutrons are detected through the above-mentioned reaction.

In the ILL experiment, the neutron EDM measurement was performed by the following procedure.

1.Production of ultracold neutrons

The nuclear fission neutrons emitted from the reactor of ILL are cooled with heavy water, transported upward by a nickel guide pipe with a curve, and finally converted into ultracold neutrons by Doppler Shift method.

2.Transport of UCNs

UCNs are transported from turbine house to the storage container.

3.Polarizing UCNs

The degree of polarization of neutrons is increased by passing through the above-mentioned polarizer on the way of transport.

4.Start of storage sequence

UCNs are filled inside the storage container with the UCN door open for 20 s. Then the UCN door is closed, and the Hg door is opened instead and the container is filled with polarized Hg. Finally. the Hg door is closed again.

5.Applying RF1

RF is applied and the UCN spin is turned parallel to the ground.

6.Applying static electric field and magnetic field

The electrostatic field is made apply parallel/antiparallel to the static magnetic field for 140 s.

7.Applying RF2

RF is applied and the spin is turned in the direction perpendicular to the ground.

8.End of storage sequence

The central door is opened and the UCN from the container is evacuated.

9.Detecting polarized UCNs

UCNs are counted with the detector installed on the underside of the storage container. At this time, the number of UCNs is evaluated while applying RF to the coil by a certain time interval.

10.Repeat of process1

Repeat procedures 1 to 9 while using different RF adopted in procedures 5 and 7.

11.Repeat of process2

Repeat procedures $1 \sim 10$.

3.3   Our Proposed Experiment: Neutron EDM Experiment at J-PARC

This section explains the experimental procedure of J-PARCP 33. In the J-PARC P33 experiment, fast neutrons are produced by the nuclear spallation reaction between a lead target and J-PARC pulsed proton beam. Then, fast neutrons are cooled to few meV by the elastic scattering of nuclei, and further cooled to O(100 neV) by the inelastic scattering from a solid deuterium. At present, such a low energy neutrons are extracted from the ultracold neutron source as UCN beam and are transported with refocused in front of the storage container by the rebuhch method and taken in the storage container. This procedure repeats until UCN density becomes nearly maximum, and thereby statistical precision and heat load can be improved efficiently compare to other experiments.

For reference, schematic diagrams of J-PARC P33 experiment are given in Figure 3.7, and an enlarged figure around the storage container is given in Figure 3.8. In addition, a schematic diagram of UCN transportation with UCN rebunch method is given in Figure 3.9 and 3.10.

For J-PARC P33, the neutron EDM measurement is assumed to be performed at room temperature. Therefore, many main apparatuses are common with the ILL experiment. Specifically, the polarized Hg cell, the door system, the electrode and the magnetic shield are common. On the other hand, the ultracold neutron source, the transport guide, the polarizer, the storage container, and the detector are different from ILL. Also, the rebuncher is an apparatus that does not exist in ILL.

Only six main apparatuses different from the ILL experiment are explained in the following.

Ultracold neutron source
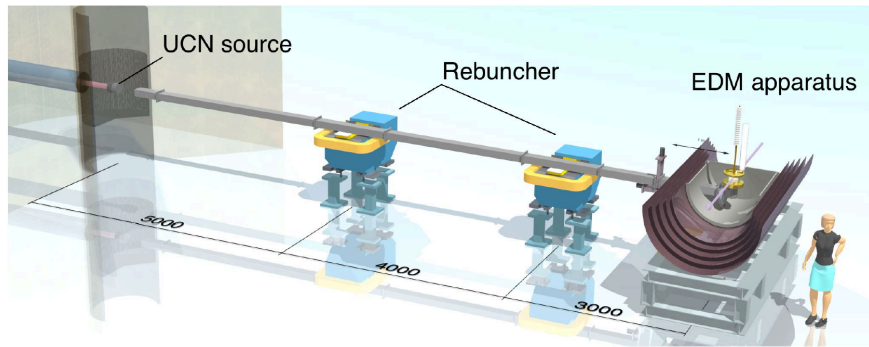
Figure.3.7 Outline of J-PARC EDM experiment. (1) A lead target is irradiated with J-PARC proton beam and fast neutrons is produced by nuclear spallation reaction. (2) Fast neutrons are cooled down to several meV (referred to as cold neutrons) by elastic scattering by liquid deuterium and heavy water. (3) Cold neutrons are further cooled to ultracold neutrons by inelastic scattering of solid deuterium phonon. (4) To extract the high intensity pulse UCN produced by transport guide. (5) The high-speed component of UCN is decelerated with rebunch method and refocus it in front of the storage container. (6) To open the shutter and take the UCN in the container, and then immediately close the shutter to minimize backflow. (7) Repeat 1∼6 until reaching almost maximum density. (8) Start measurement of precession. The image is cited from [18].
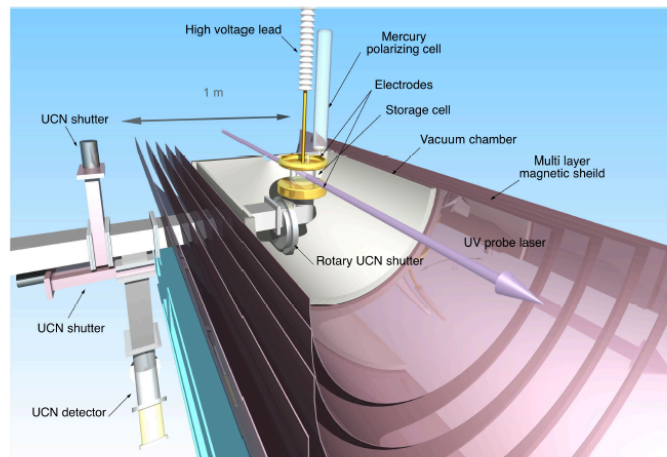
Figure.3.8 Apparatuses of J-PARC P33 experiment. Schematic diagram of apparatuses of J-PARC P33. The front UCN shutter is used for cutting out the rebunch pulse, and the rear shutter is used for preventing backflow during measurement. The image is cited from [18].

The ultracold neutron source consists of a lead target, heavy water of 300 K, liquid deuterium of 20 k and solid deuterium of 5 K. When J-PARC proton beam is incident on the lead target, fast neutrons are generated by nuclear spallation reaction. By cooling it from O(MeV) to several meV through collisions of deuterium molecules in heavy water and liquid deuterium, cold neutrons can be obtained. Then, ultracold neutrons are produced by further cooling from meV to O(100 neV)

sD2 UCN Source
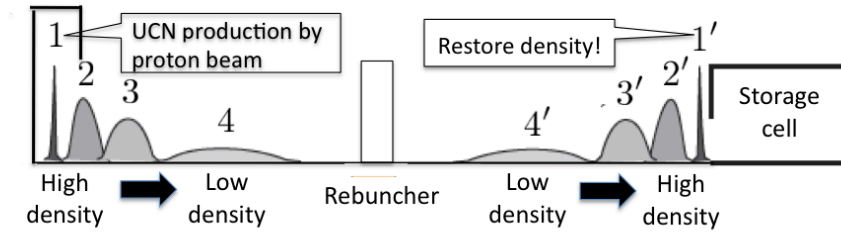
Figure.3.9   UCN supply method assumed in J-PARC P33. The flow from 1 to $1'$ represents the time evolution. At the time of 1, a large amount of UCN is generated instantaneously by J-PARC pulse proton beam which has the world's highest instantaneous intensity, but it becomes diffused according to the speed as time grows from 1 to 4. So, decelerate the high-speed component using the rebuncher, and refocus it as $4' \to 1'$ to restore the UCN density in front of the storage container. The image is cited from [43] and partially changed.
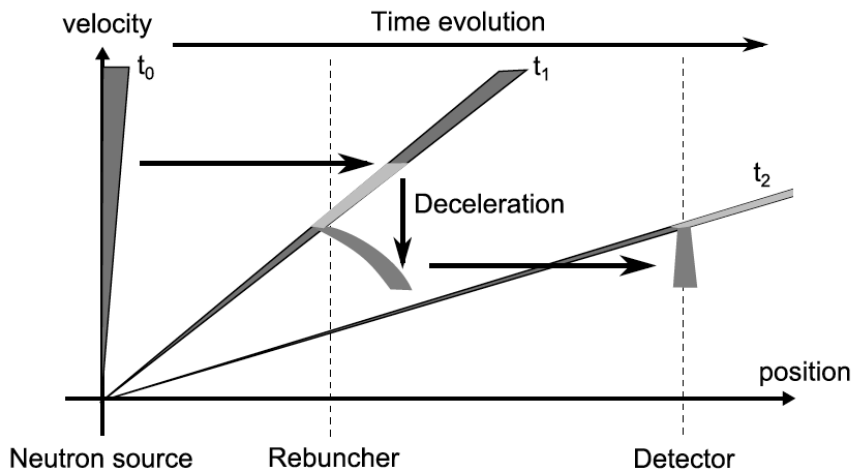
Figure.3.10   Illustration of the principle of the rebunch method, the image is cited from [44]. Pulse neutrons emitted from the neutron source at time t_0 undergo deceleration of different magnitude for each velocity at time t_1, and as a result, it is focused to the detector point at time t_2.

or less due to inelastic scattering of phonon in solid deuterium. The solid deuterium is surrounded by a nickel mirror to prevent leaking the ultracold neutron flux. Because the solid deuterium reacts immediately, the incident timing of the pulse proton beam is well conserved. Note that the reason why deuterium is used for cold neutron production is that the absorption is lower than that of hydrogen, and as a result, the intensity of cold neutrons can be increased more.

Transportation guide

High intensity pulse UCN is transported to the storage container. The inner surface of the transport guide is made of high reflectivity material, such as NiP or NiMo or DLC.

Rebuncher

Rebuncher is a neutron accelerator instrument combining gradient static magnetic field and RF magnetic field. Both magnetic fields are orthogonal one another. In this study, it is assumed that gradient magnetic field region is set at a point 5 m from the tip of the transport guide and RF magnetic field region is extended to its center to 20 cm. In addition, -3.2 T/m for magnetic field gradient, and 6 ~ 30 MHz for RF frequency are assumed, respectively. If RF is applied while changing RF frequency, the resonant spin reversal will occur only where the spin resonant condition is satisfied. When the spin reversal occurs in the stronger magnetic field region in the gradient magnetic field, the more the energy increases (decreases). Therefore, if the application timing of RF magnetic field is adjusted to decelerate UCNs having high-speed component, it is possible to refocus the pulse UCN in front of the storage container. In this study, spin reversal probability of 100% is assumed for simplicity.

Storage container

The storage container consists of a cylindrical container coated with a highly reflective material having high insulation properties and two disks coated with a non-magnetic material. It is assumed that the inner shape of the storage container and the door system of UCN and Hg are the same specifications as the ILL experiment, but it is undecided whether UCN intake port is set on the side or bottom of the container.

Polarizer

A magnetic field area of 5 T is applied between UCN source and the transport guide. This will automatically polarize all the UCNs going to the storage container.

Detector

In the ILL experiment, Helium-3 proportional counter was used. However, the dead time is too long to use for next generation neutron EDM experiments such as PSI or TRIUMF. Therefore, we are planning to use a more rapid detector. For example, a lithium glass scintillator or similar is a candidate.

The experimental result of J-PARC is directly affected by the performance of the main apparatuses. For example, the repetition frequency of the pulsed beam, the proton beam current, the initial time distribution when ultracold neutrons are produced, the UCN extraction efficiency from the solid deuterium ultracold neutron converter, the rebunch efficiency of the transport guide, and the ability to be stored, and so on. The effect of these performances is considered in chapter 4. In addition, the above performance is sensitive to the performance of the developed reflector. The current status of development of reflective materials is described in chapter 5.

The procedure of J-PARC P33 experiment is as follows:

1.Production of nuclear spallation neutrons

A lead target is irradiated with J-PARC LINAC pulsed proton beam to generate nuclear spallation neutrons.

2.Production of ultracold neutrons

Nuclear spallation neutrons are made cooled to ultracold neutrons by using elastic scattering in

the heavy water and liquid deuterium and the inelastic scattering in solid deuterium.

3.Conversion to fully polarized UCNs

A magnetic field of 5 T is applied near the outlet of UCN source and only the upward spin component is taken out.

4.Transportation of UCNs

Polarized neutrons are transported to the storage container. UCN with high-speed component is decelerated by rebuncher during transportation and refocused in the front of the storage container.

5.Start of UCN storage

The UCN door is opened to take in only the refocused UCN beam. This procedure is repeated until the number of UCNs in the storage container becomes almost maximum. After that, UCN door is closed, Hg door is opened instead and the container is filled with polarized Hg. Finally, the Hg door is closed again.

6.Applying of the second RF magnetic field

RF magnetic field is applied for a certain time to align the spins of UCN in a direction parallel to the ground.

7.Duration of UCNs freely precessing for a long time

The electrostatic field of 10 kV/cm is applied parallel/antiparallel to the static magnetic field for a long time.

8.Applying of the second RF magnetic field

RF is applied and spin is turned in a direction perpendicular to the ground.

9.End of UCN storage duration

UCNs are released from the storage container.

10.Duration of detection of polarized UCNs

The number of UCNs is counted with a detector. At this time, measurements are performed by alternately applying RF to the coil installed in front of the detector, and the number of both polarized UCNs can be evaluated.

11.Repetition

Repeat steps 1∼10 with different RF used in procedures 5 and 7.

3.4   Other Next Generation Experiments

Other next generation neutron EDM experiments are proceeding, all of which employ the super-thermal method for UCN production. These experiments are explained in the following.

PSI is already ready for next generation neutron EDM experiment and the measurement is started. In this experiment, using 1.2 MW Proton Cyclotron, the beam of 590 MeV and 2 mA are incident on Pb target for 6 sec to produce nuclear spallation neutrons and then cooled it with 30 liters of solid D_2 and D_2O moderator. PSI group is aiming to achieve 5×10^{-27} e · cm in the first stage and finally 5×10^{-28} e · cm EDM measurement. Details of the neutron EDM experiment at PSI can be found in [45, 46, 47, 48].

TRIUMF also plans a next generation neutron EDM experiment using liquid He-II as a spallation UCN source. The spallation source using He-II has already been demonstrated at RCNP, where Pb target is irradiated with 400 W (400 MeV, 1 μA) proton beam accelerated by Cyclotron (DC) for about 100 seconds to produce nuclear spallation neutrons and cooled it with 8 liters of 0.7 K by He-II and D_2O moderator. It was confirmed that 15 UCN/cm^3 (E < 90 neV) can be achieved. Even at TRIUMF, in the first stage 10^{-27} e $\cdot$ cm, in the second stage 5×10^{-28} e $\cdot$ cm or less. For details of the neutron EDM experiment of TRIUMF, please refer to the document [49].

ILL is planning a new neutron EDM experiment called CryoEDM that cold neutrons emitted from the nuclear reactor are cooled with He-II. In CryoEDM, cold neutrons are incident on a container filled with liquid Helium to produce UCNs, and it is transported to a cell filled also with liquid Helium. In this experiment, the distortion of the magnetic field is corrected using the only SQUID without using co-magnetometer. In the CryoEDM experiment, a strength of electric field can make twice higher because of insulation of liquid He, which results in improving the precision by two digits as compared to the conventional ILL experiment. However, in order to carry out this experiment, it is necessary to redevelop the experimental apparatuses as a whole. For details of CryoEDM, please refer to the document [50].

SNS is planning next generation neutron EDM experiment. In this experiment, as well as CryoEDM, a cold neutron is incident on a container filled with He-II to produce UCNs for experiments. On the other hand, unlike CryoEDM, a small amount of ^{3}He doped in liquid helium is used as co-magnetometer. Specifically, the precession of ^{3}He is monitored from the modulation of detection of the scintillation light due to the absorption of polarized ^{3}He. For the details of SNS experiment, please refer to the document [51, 52, 53].

In addition, WWR-M is planning a new neutron EDM experiment using a method that the 15 MW neutron flux emitted from the nuclear reactor is cooled with He-II. They are aiming at measuring neutron EDM with less than 5×10^{-28} e $\cdot$ cm. For the details of the experiment of WWR-M experiment, please refer to the documents [54, 55].

Chapter 4

Dependence Study of the Statistical Sensitivity on the Performance of the Reflection Material of UCN

This chapter describes the study to evaluate the dependence of the statistical sensitivity on the reflection performance of J-PARC P33 experiment. For the J-PARC P33 concept, there was a problem that the experimental capability had not been evaluated. Due to it, the experimental sensitivity expected at the present time could not be evaluated, and any optimization studies to improve the sensitivity could not be done. In general, although the statistical sensitivity of the J-PARC P33 experiment depends on a lot of factors, it was particularly difficult to understand how much the storage efficiency and transport efficiency affect the statistical sensitivity through the reflection loss and the non-specular reflection from the material surface. In this study, for solving this problem, the dependence of the statistical sensitivity on such reflection performances was evaluated by a full simulation that can deal with an experimental system and entire procedures based on J-PARC P33 concept. Using PHITS [56], Geant4UCN [57] and an original program that was developed by the author, all of J-PARC P33 procedures and the necessary interactions for UCN were incorporated into the simulation. The magnetic field structure of the prototype of the rebuncher was used to represent the rebunch method, and the neutron optical theory and the micro-roughness model were used to handle the above-mentioned reflection interactions. In such a way, the J-PARC P33 experiment was totally simulated from the upstream to the downstream in order to quantitatively investigate the dependence of the statistical sensitivity on the reflection performance. Details of this study are described below.

This chapter is organized as follows. First, the detail of the pulsed beam property of J-PARC LINAC, which is the basis of the J-PARC P33 experiment, is explained in 4.1. In 4.2, the UCN density produced in the solid deuterium ultracold neutron source is evaluated. This information is necessary to relate the intensity of UCN beams that must be assumed in the Monte Carlo simulation to that of UCN beams expected in the actual J-PARC P33 experiment. In 4.3, details of the rebuncher are explained, which is the key device for J-PARC P33 experiment. In 4.4, details of J-PARC P33 simulation are described. Specifically, in 4.4.1, the phase space density of UCNs is evaluated, which is used for the transport and storage simulation. In 4.4.2, it is described how essential points affecting the results of the simulation

were chosen. In 4.4.3, the transportation simulation is performed to evaluate the dependency of the rebunch efficiency, especially on non-specular reflection. In 4.4.4, the storage simulation is performed to evaluate the expected number of UCNs that can be stored with the rebunch storage method and the dependence of it on reflection performances. In 4.4.5, the statistical sensitivity of the J-PARC P33 and the dependence of it on reflection performances are evaluated. Finally, a short summary of this chapter is given in 4.5.

4.1 Proton Beam Property at J-PARC Neutron EDM Experiment

In this section, the property of J-PARC LINAC proton beam is described. The schematic illustration of the J-PARC LINAC proton beam is shown in Figure 4.1. In the future plan of J-PARC, the proton beam will be supplied at LINAC with 50 Hz, of which 25 Hz goes to RCS and the remaining 25 Hz is used in LINAC. The beam energy is 181 MeV so far, and it is going to be 400 MeV in the future. This study assumes a part of the beam of LINAC is used for the neutron EDM experiment. The J-PARC LINAC proton beams consist of 25 macropulses, which further consist of many micropulses (see Figure 4.1). The pulse width of a macropulse is 500 μ s, the pulse width of a micropulse is 560 ns, and the interval between two adjacent micropulses is 1065 ns (181 MeV) or 815 ns (400 MeV). Therefore, a macropulse consists of 500 micropulses that can be calculated from (500×10^{-6}) / (1065 ns). In addition, the pulse width of a macropulse t_{macro} can be changed continuously by the factor of 1/10 to 1, the pulse width of a micropulse t_{micro} can be changed continuously by the factor of 1/5 to 1, and the interval between two adjacent micropulses T_{micro} can be discretely changed to 1, 1/2, and 1/4.

If all of two pulse width factors and the interval factor of a micropulse are chosen to be 1, the average current of the macropulse of the J-PARC LINAC is $I_{\mathrm{avg}} = 375$ μA(181 MeV) or 625 μA(400 MeV). On the other hand, the instantaneous current of the J-PARC macropulse can be derived from $I_{\mathrm{avg}} \times \frac{1/(25\mathrm{Hz})}{500\ \mu\mathrm{s}}$, which result in 30 mA (181 MeV) or 50 mA (400 MeV). Because the average beam power of J-PARC LINAC is 67.9 kW (181 MeV) or 250 kW (400 MeV), the instantaneous beam power of J-PARC LINAC is 5.4 MW (181 MeV) or 20 MW (400 MeV).

In this study, the repetition rate and the peak power of the J-PARC LINAC beam are chosen to be 0.5 Hz and 20 MW, respectively. The characteristics of the beam condition used into this study are summarized in Table 4.1.
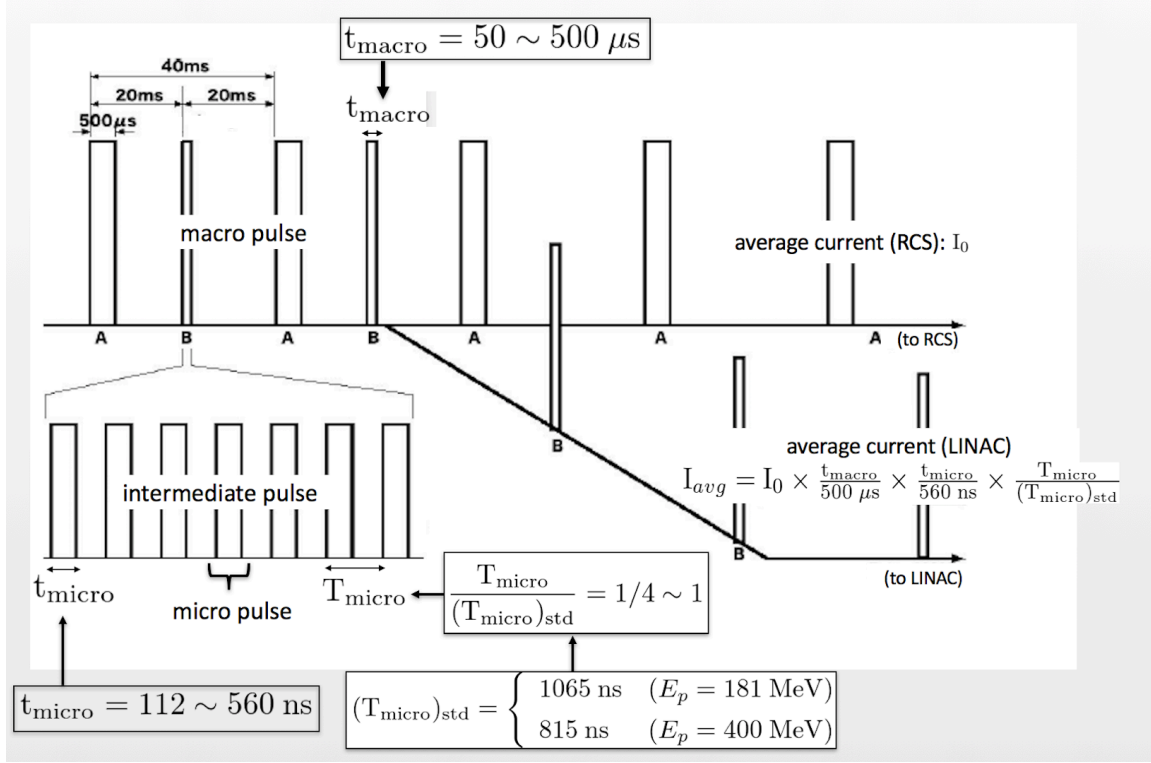
Figure.4.1 Schematic illustration of beam distribution of J-PARC LINAC. Although macro pulse of 50 Hz will be supplied to J-PARC LINAC, only half of macropulses can be used in the experiment which will be conducted in LINAC. In this study, it was assumed that only 0.5 Hz out of 25 Hz was used for the neutron EDM measurement. In addition, it was also assumed that t_{macro} was 500 μs, t_{micro} was 560 ns, and $\frac{T_{\mathrm{micro}}}{(T_{\mathrm{micro}})std} = 1$ where $(\mathrm{T}_{\mathrm{micro}})_{\mathrm{std}}$ is the standard value of the interval between two adjacent micropulses. The image is cited from [18, 19] and partially changed.

Proton Energy	400 MeV
Pulse width	0.5 ms
Repetition used in Experiment	0.5 Hz
Repetition Rate of J-PARC LINAC	25 Hz
Peak Proton Current	50 mA
Average Proton Current	0.625 mA
Peak Power	20 MW
Average Power	250 kW

Table.4.1 Details of the beam condition of J-PARC P33 used in this study

4.2 UCN Source at J-PARC Neutron EDM Experiment

In this section, the density of UCN produced in the solid deuterium converter is evaluated. In J-PARC P33, the ultracold neutron source is assumed to consist of cylindrical solid deuterium having a diameter of 10 cm and a length of 20 cm, liquid deuterium of 20 K, heavy water of 300 K, lead target and graphite. The geometry conditions and schematic diagram used in PHITS simulation are shown in the Table 4.2 and Figure 4.2.

Generally, the density of UCNs produced in the ultracold neutron source is proportional to the intensity of cold neutron flux passing through it. In J-PARC P33, cold neutron flux was simulated with the heavy ion transport calculation code PHITS. Regarding the accuracy of the PHITS calculation, there is an actual comparison between the actual measurement result of J-PARC MLF BL10 and the simulation result. It has been confirmed that both results agree with the accuracy of $10\% \sim 20\%$ [58]. In this comparison, a proton beam of 3 GeV and a mercury target were used for producing nuclear spallation neutrons, and cold neutrons were produced by decelerating it with liquid hydrogen, which corresponds to the case of J-PARC MLF. On the other hand, for J-PARC P33 concept, as shown in Table 4.1 and Table 4.2, the proton beam of 400 MeV and the lead target are used for producing nuclear spallation neutrons, and cold neutrons are produced by decelerating it with heavy water and liquid deuterium.

The cold neutron flux distribution passing through solid deuterium converter calculated by PHITS is given in Figure 4.3. The horizontal axis is the energy of incident neutron, the vertical axis is the neutron flux passing through the solid deuterium converter, the black line is calculation result, and the red line is the fitting result with Maxwell distribution. Note that the phonon interaction of the PHITS simulation creates the peak structure of the flux energy distribution of Figure 4.3.

In Figure 4.3, the cold neutron flux Φ can be calculated by integrating of 10 meV or less, resulting in $\Phi = 5.8 \times 10^{11} \mathrm{cm}^{-2}\mathrm{s}^{-1}$. On the other hand, the fitting result of Figure 4.3 showed that the most probable energy of cold neutron flux is approximately 2.6 meV. In other words, the cold neutron flux of Figure 4.3 can be approximated to be Maxwell distribution of 30 K. Because the expression (2.31) is possible to be used for Maxwell distribution of 30 K, UCN production can be estimated by substituting $\Phi = 5.8 \times 10^{11} \mathrm{cm}^{-2}\mathrm{s}^{-1}$ into the expression (2.31). In such a way, $\rho = 5,800 \ \mathrm{UCN/cm}^3$ was obtained as the density of UCN produced in solid deuterium converter. This is evaluation result for UCN production of J-PARC P33 experiment. It is noted that the maximum energy of UCNs produced in the solid deuterium is assumed to be 252 neV in the expression (2.31).

Proton Charge	25 μC
Target	Lead (Φ10 cm$\times$ 20 cm)
Shield	Lead (Φ30 cm$\times$ 30 cm $\times$ 15 cm)
Converter	Solid D_2 (Φ10 cm$\times$ 20 cm)
20 K Moderator	Liquid D_2 (Φ20 cm$\times$ 30 cm)
300 K Moderator	Heavy Water (Φ50 cm$\times$ 50 cm)
Reflector	Graphite (Φ 100 cm $\times$ 100 cm)
Distance from target to converter	22.5 cm
sD_2 density	0.196 g/cm3
sD_2 atom density	0.0590 atoms/barn/cm
sD_2 atom density	0.0295 molecule/barn/cm

Table.4.2   Simulation condition of PHITS
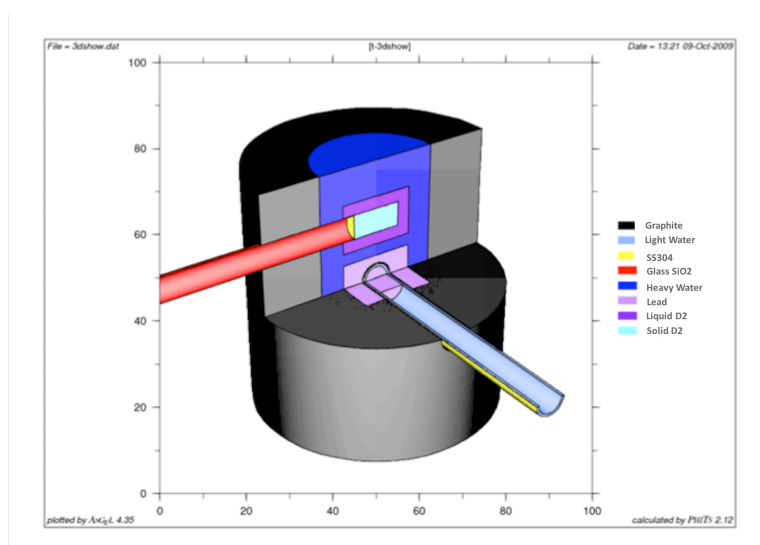
Figure.4.2   The arrangement of the ultracold neutron source used in PHITS simulation. Fast neutrons due to nuclear spallation reactions caused by pulse proton beams with the Lead Target (pink) were decelerated by the elastic scattering by Heavy Water (Blue) and Liquid Deuterium (Purple), and by the inelastic scattering by solid deuterium placed in the center (light blue). As a result, it is converted into ultracold neutrons. Ultracold neutrons are extracted from the transport guide (red) and transported to the EDM measurement apparatus.
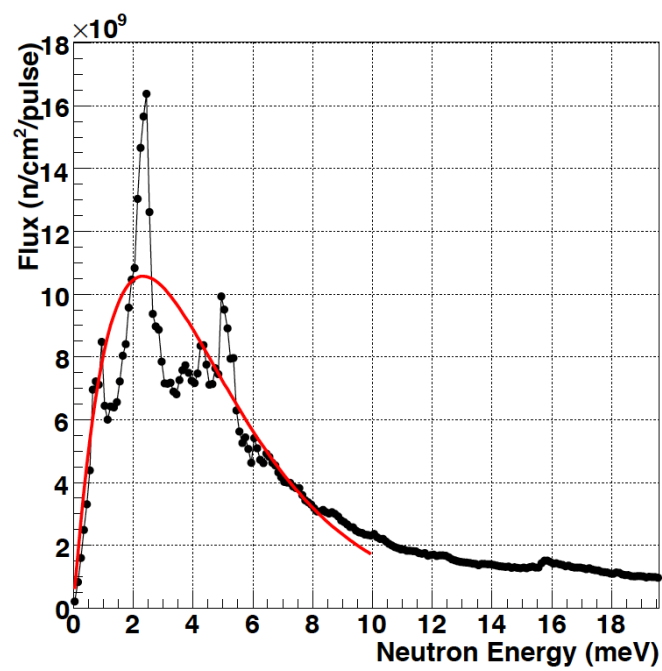
Figure.4.3   The energy spectrum of cold neutron flux passing through the solid deuterium converter, the image is cited from [18]. The horizontal axis is the energy of the incident neutron, the vertical axis is the neutron flux passing through the solid deuterium converter. The calculation was performed by PHITS. See the text for details.

4.3 Rebuncher

In this section, the design concept and the operation principle of the optical equipment rebuncher are explained. In addition, the demonstration experiment of the rebuncher conducted in ILL is explained.

The rebuncher is designed to make pulsed UCN beams refocused at a certain point by changing the amount of the velocity of UCNs as described in chapter 3.3. The rebuncher operation is based on the experimental technique to control the spin resonant reversal in a gradient static magnetic field. In general, if neutron is in a static magnetic field of B, the neutron spin reversal can be induced by applying the rotating magnetic field with the spin reversal resonant frequency ω orthogonal to B. The spin resonant reversal condition is given as follows:

$$\hbar\omega = 2\mu B \tag{4.1}$$

where μ is neutron magnetic moment.

If neutron spin is reversed in a static magnetic field with a certain gradient $B(z)$, the potential energy change of $2\mu B(z)$ occurs according to each position z. Therefore, a desired kinetic energy change can be realized by controlling the spin reversal point in the static gradient magnetic field. This is the operational principle of the rebuncher. For this reason, the rebuncher consists of an electromagnet to supply a static gradient magnetic field and a spin flipper to supply a rotating magnetic field. For reference, the schematic illustration of the magnetic field generator of the rebuncher prototype is given in Figure 4.4 [18]. In this system, by combining a normal conducting electromagnet and anisotropic intermediate magnetic poles, the linear gradient magnetic field of -3.2 T/m is realized. The measurement result of the linear gradient magnetic field of the rebuncher prototype is shown in Figure 4.5.
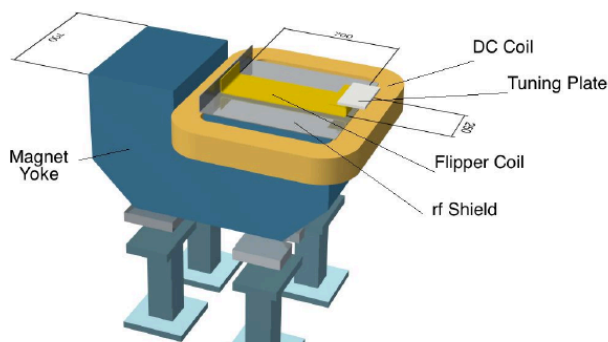
Figure.4.4   The cross-section view of the rebuncher prototype. The image is cited from [18].

If neutron travels in the static magnetic field of the gradient $\frac{dB}{dz}$ and the rotating magnetic field B_{rf} is
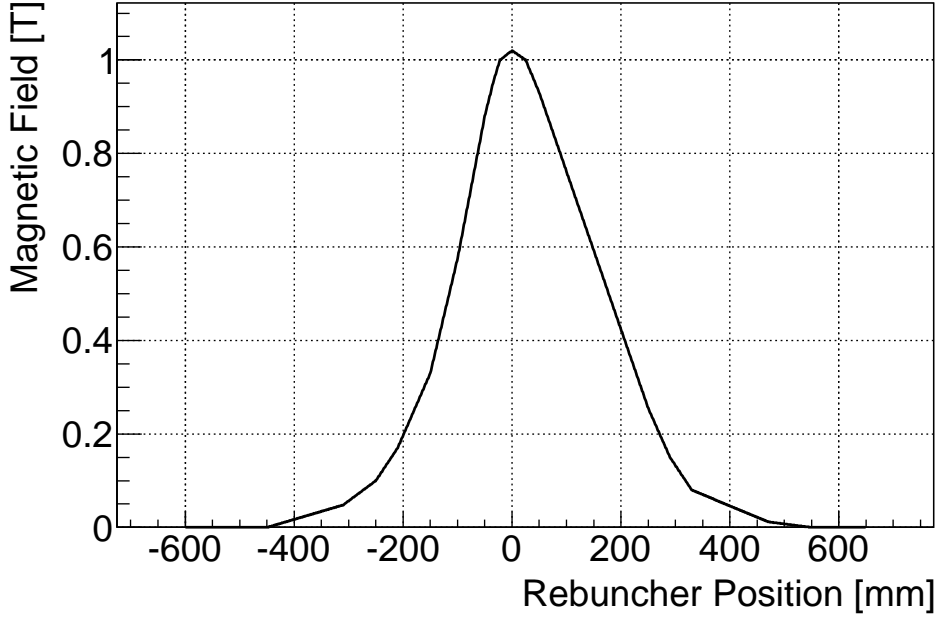
Figure.4.5 Linear gradient magnetic field used in rebuncher

applied to this region, the neutron spin is reversed in the following probability p [44]:

$$p = 1 - \frac{1}{1+k^2} \sin^2\left(\frac{\pi}{2}\sqrt{1+k^2}\right) \tag{4.2}$$

$$k = \frac{\omega_L}{\omega_B} = \frac{\gamma_n B_{\rm rf}^2}{v_n \frac{dB}{dz}} \tag{4.3}$$

where k is the adiabatic parameter, v_n is the component of the neutron velocity in the direction of travel, ω_L is the frequency of the applied rotating magnetic field, and ω_B is the resonant frequency. For reference, a plot of the spin reversal probability is given in the Figure 4.6.

Regarding the rebuncher prototype, the magnetic field gradient in the accelerating region is -3.2 T/m. In this case, we need $k > 1.4$ to achieve a spin reversal rate of 90% or more from the formula (4.2). Thus, it is estimated that a rotating magnetic field intensity of $B_{\rm rf} = 0.35$ mT is required. Actually, because the RF magnetic field is a combination of clockwise and counterclockwise rotating magnetic fields, the experiment requires twice the magnetic field intensity. Therefore, by using RF with a magnetic field intensity of more than 0.7 mT, experiments with spin reversal probability more than 90% can be easily achieved.

In 2012, the demonstration experiment of the rebuncher was performed at the ILL/PF 2 TES port (see document [59] for details). In this experiment, by a shutter coated with gadolinium oxide to make pulsed UCN beams from DC UCN beams supplied at ILL, the change of time of flight due to rebunch effect was checked. If the rebunch effect appears, time-of-flight should be changed when UCNs are detected at a certain point. A schematic diagram of the experimental setup and the time of flight spectrum obtained are shown in Figure 4.7 and 4.8, respectively [44]. It was actually confirmed that UCN of 5 m/s was
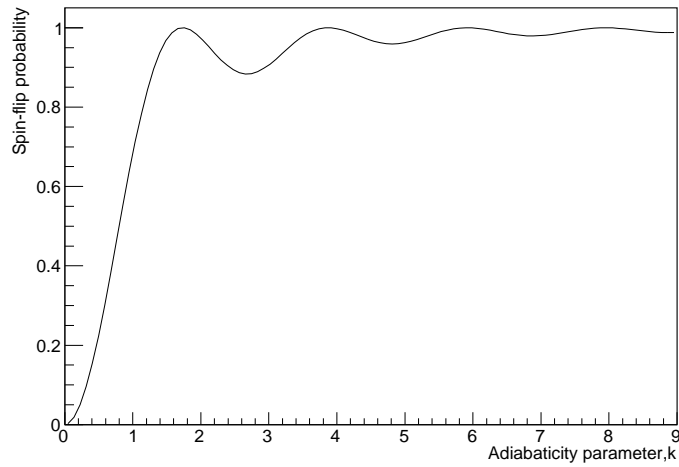
Figure.4.6   Relation of adiabatic parameter k and spin-flip probability

decelerated to 4 m/s by the rebuch method, and that the instantaneous intensity of the UCN beam increased by about 1.4 times. On the other hand, the spin reversal probability at the demonstration experiment was confirmed to be 0.5. It is thought to be due to the incomplete impedance matching of the RF resonator. Currently, an improved machine is being developed, and the test at J-PARC Material Life Science Research Facility Beam Line No.5 is being prepared.
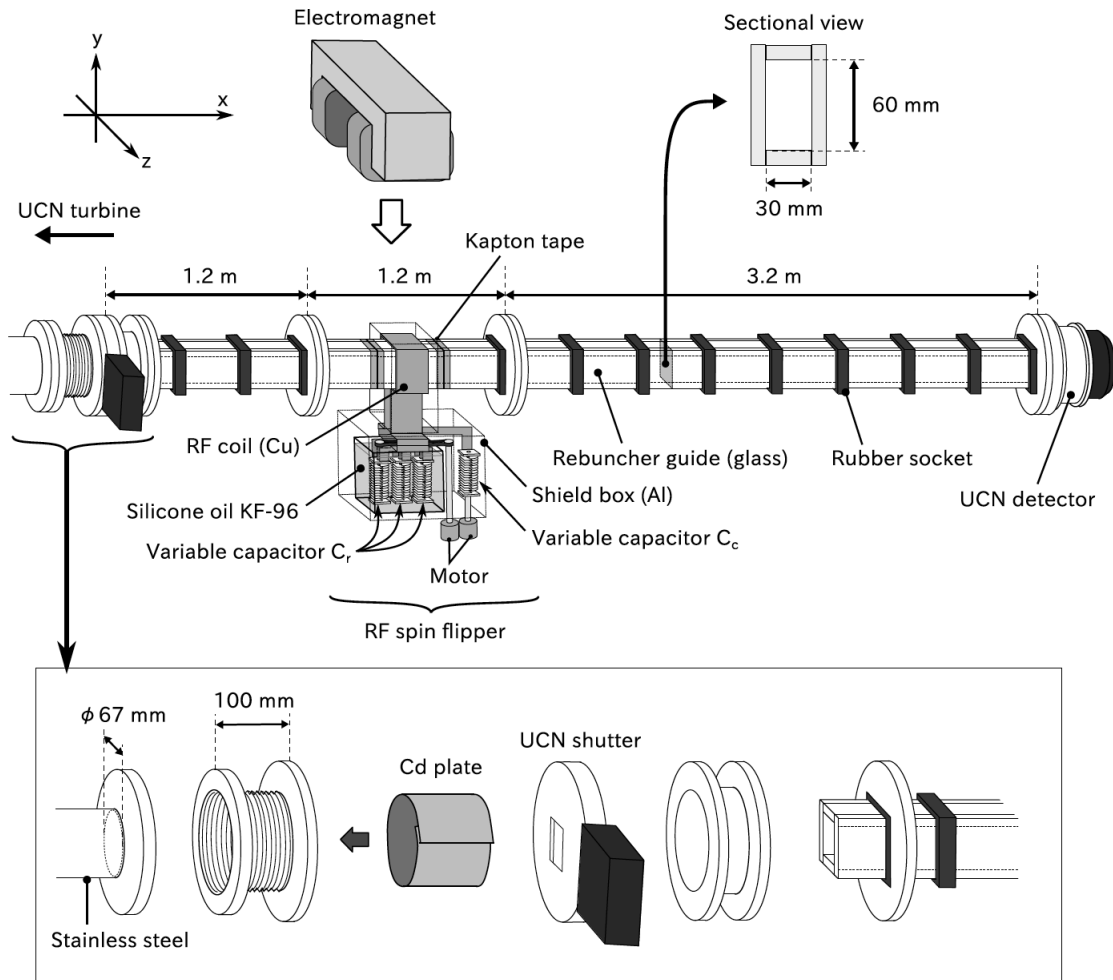
Figure.4.7   Schematic diagram of the setup used for the rebuncher demonstration experiment performed at ILL, the image is cited from [44]. (1) UCN beam supplied in ILL is transported to the front of the shutter through ϕ 67 mm stainless steel pipe. (2) UCN beam is collimated with a 100 mm long bellows whose inside wall is covered with cadmium plate. (3) The UCN beam is pulsed by cutting out with opening/closing the shutter and is supplied to the rebuncher guide consisting of a square pipe of 60 mm (H) $\times$ 30 mm (W) $\times$ 5.6 m. Here, the longitudinal-gradient magnet with anisotropic interpole and an RF coil are installed in the middle part, and a UCN detector is installed in the endpoint. (4) RF magnetic field of intensity 0.5 mT with a frequency of 17.5 MHz to 28.6 MHz was applied to the rebuncher for 80 ms from the chopped timing.
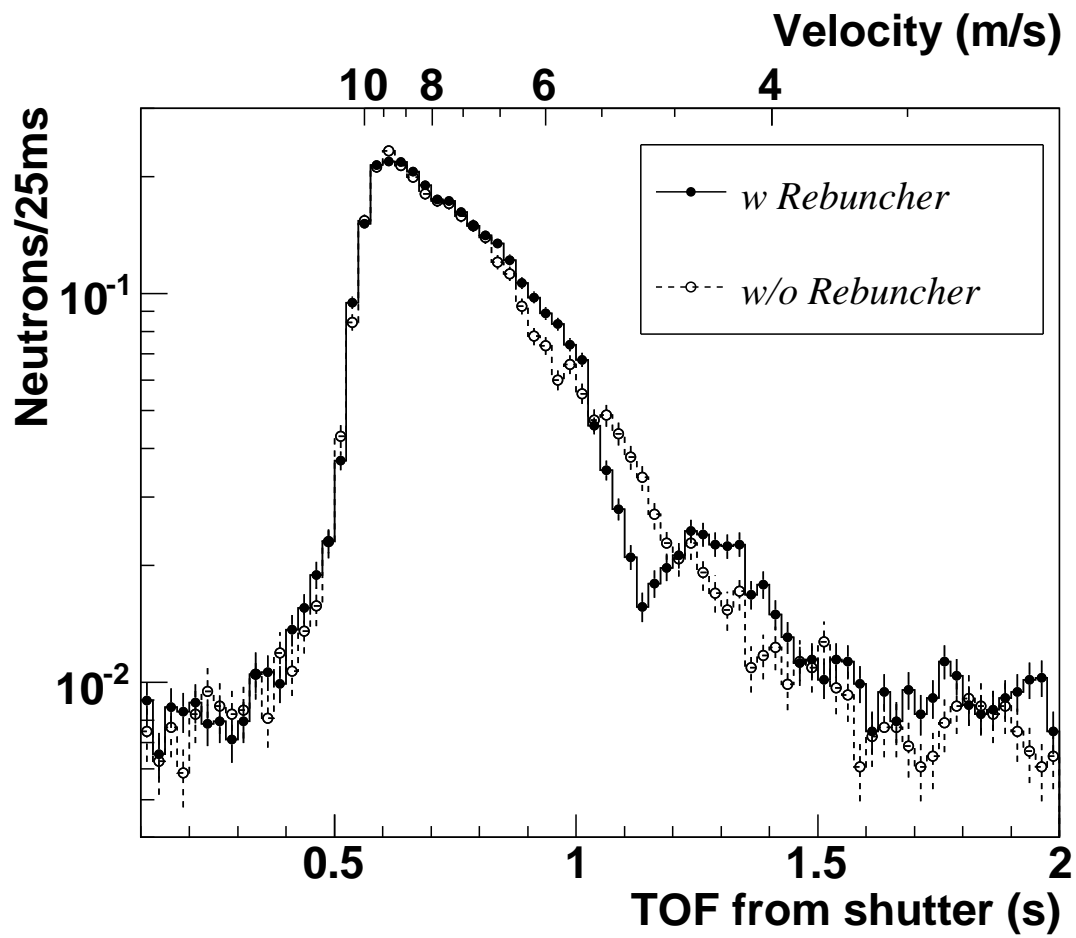
Figure.4.8 The refocused TOF confirmed at the rebuncher demonstration experiment at ILL, the image is cited from [44]. The horizontal axis is TOF, the vertical axis is the counting rate, the white point marker is the spectrum when the spin flipper is not used, and the black dot marker is the spectrum when used.

4.4　J-PARC P33 simulation

In this section, the phase space distribution, the rebunch efficiency, the number of UCNs that can be accumulated in the storage container by the rebunch storage method, the statistical sensitivity of J-PARC P33 experiment, and the dependence of these quantities on the performance of reflection materials were evaluated. The schematic representation of the simulation setup in this study is shown in Figure 4.9. Furthermore, details of the simulation setup assumed in this study is summarized in Table 4.3. In this study, it was assumed that the rebuncher equipment is installed at 5 m from the tip of the transport guide. Regarding the magnetic field generator, the static gradient magnetic field of -3.2 T/m and the RF magnetic field of the frequency changing from 6 MHz to 30 MHz were assumed. Furthermore, the spin reversal probability of 100% was assumed. In this simulation, Geant4UCN [57] and an original program developed by the author were used. The total experimental duration of EDM measurement was assumed to be 3 years, while the amount of the time used for the measurement was assumed to be 18 hours/day. In addition, the ratio of ortho-deuterium to para deuterium and elastic scattering cross section for solid deuterium converter, which have a large effect on the statistical precision of the J-PARC P33 experiment, were assumed as below. Regarding the ortho-para ratio, although it has been reported that other institutes such as PSI have achieved 98%, this study adopted 95% for conservative evaluation. With respect to the elastic scattering cross section of solid deuterium, only the incoherent cross section was taken into account. These general assumptions are summarized in Table 4.4.

sD_2 Converter	$\Phi100\times L200$ mm^2
Transport Guide	100×100 mm^2 $\times10$ m
Rebuncher Position	5 m (from the tip of the transport guide)
Storage Container	$\Phi470\times L120$ mm^2
Focus Guide (cross section)	35×35 mm^2 (at the exit)
Focus Guide (Length)	15 mm

Table.4.3　Details of the geometry

Total EDM Experimental Duration	Assuming 3 years
Measurement time	Assuming 18 hours/day
Simulation Framework	Using Geant4UCN and original program
Ortho-Para Ratio of sD_2	95:5
Elastic Scattering Cross Section of sD_2	Assuming only the incoherent cross section
Static Gradient Magnetic Field of Rebuncher	Using the magnetic field of Figure 4.5
RF Magnetic Field of Rebuncher	Using the magnetic field of Figure 4.10
Spin reversal probability	100 %

Table.4.4　General assumptions in this simulation
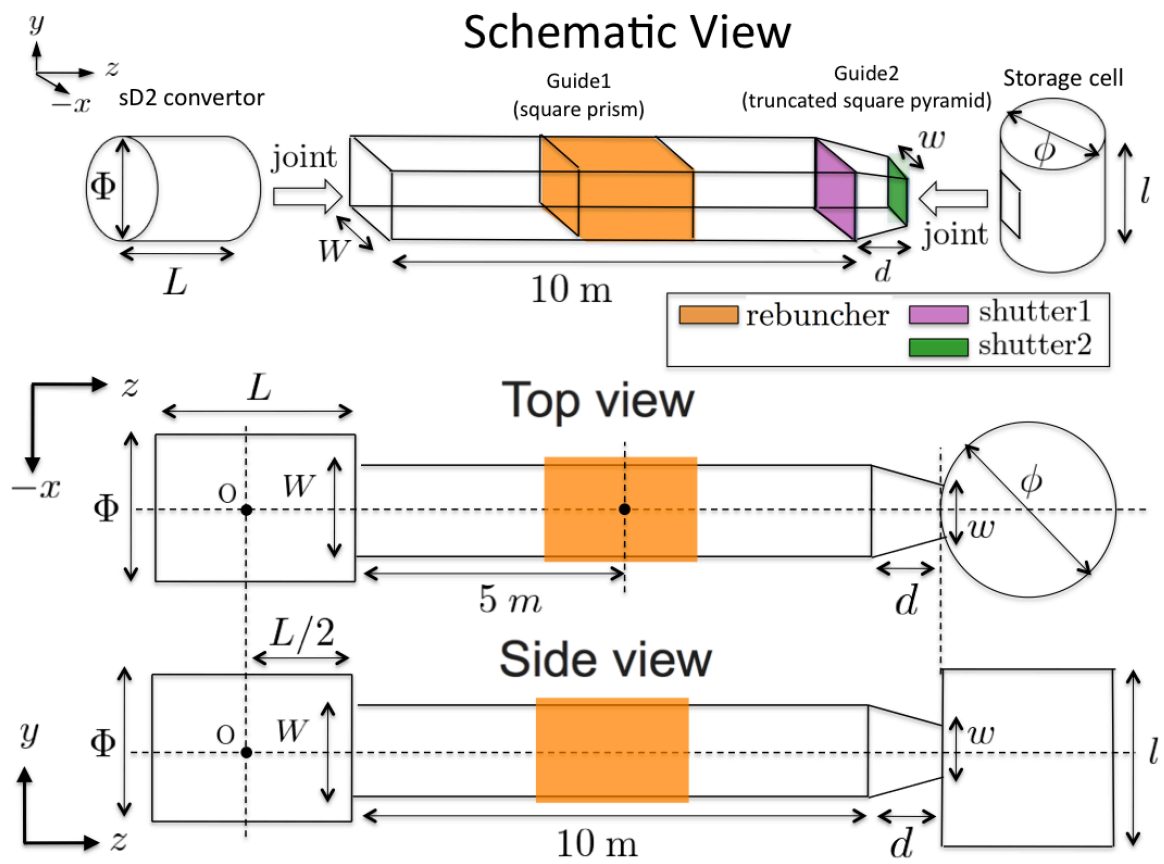
Figure.4.9   Schematic diagram of the setup assuming in the J-PARC P33 simulation
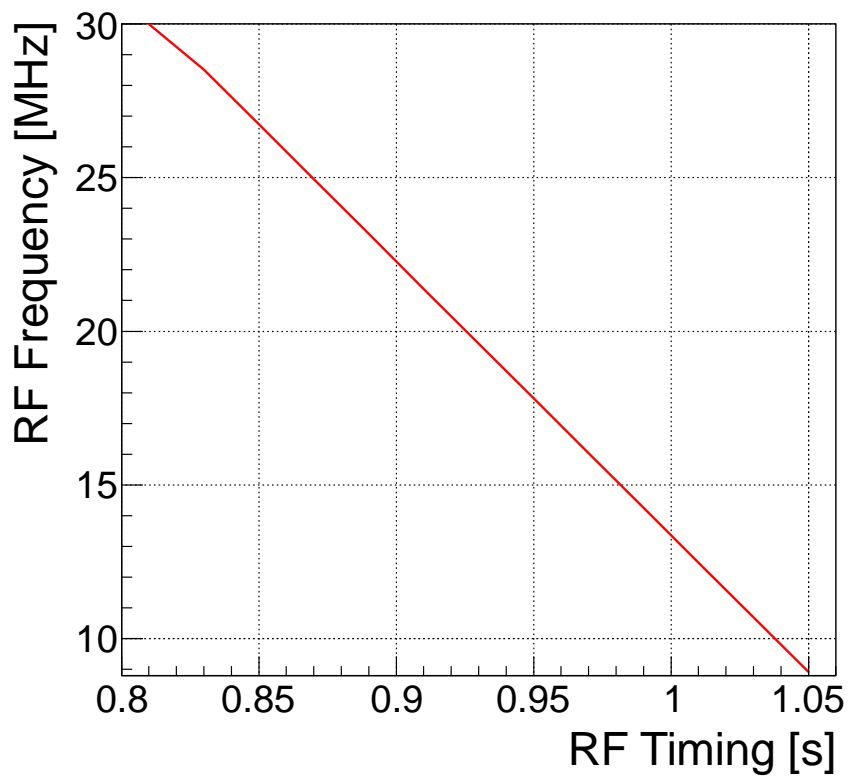
Figure.4.10   Relation between RF magnetic field frequency and application time. The vertical axis shows the RF frequency used in the simulation, the horizontal axis shows the RF magnetic field application time

4.4.1 Phase Space of J-PARCP33 setup

In this section, the phase space distribution of the J-PARC P33 experiment, necessary to simulate the transport and storage of UCNs, is evaluated. The conditions used in the simulation to evaluate the phase space distribution are described below.

1. A solid deuterium cylinder of $\Phi 100$ mm $\times$ L200 mm laid out horizontally, which is surrounded by nickel reflector.
2. UCNs are uniformly produced for space in solid deuterium and the direction of initial velocity is isotropic.
3. An initial energy E is assigned according to the probability density distribution of $\sqrt{E}$, which is known to be valid for low energy neutrons produced by the super-thermal method.
4. Considering the reaction cross section of neutron absorption and up-scattering of solid deuterium.
5. Considering the effect of acceleration due to the difference in the Fermi potential between the vacuum space and the solid deuterium.

In the simulation, the position and velocity distribution of UCNs reaching the boundary between the solid deuterium converter and the inlet of transport guide were recorded. The obtained energy distribution, absolute velocity distribution, longitudinal velocity distribution, and transverse velocity distribution are given in the Figure 4.11, 4.12, 4.13, and 4.14. The phase space distribution includes the position distribution, but it is not given here because it is obvious. In this study, the time at which the UCN is generated since the J-PARC proton beam is injected to Pb target is called T_0 hereafter. The T_0 distribution calculated by PHITS is given in Figure 4.15. It is understood that T_0 is suppressed to be less than 5 ms.
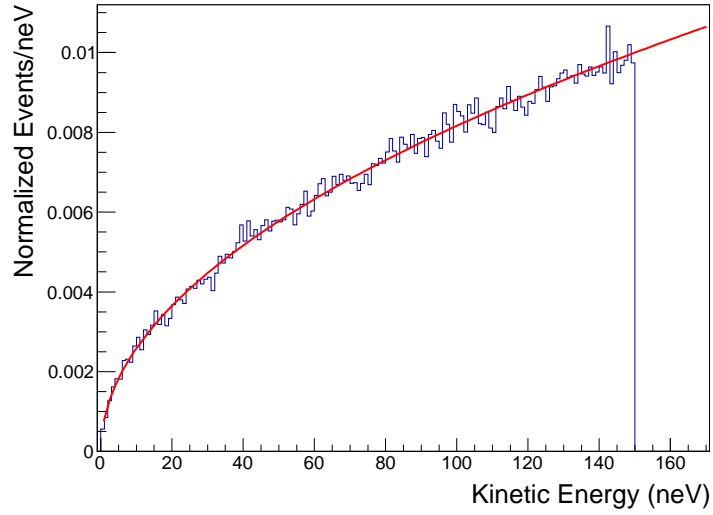
Figure.4.11   Energy distribution of UCN in solid deuterium.   The vertical axis is the number of Monte-Carlo events, and the horizontal axis is the kinetic energy of UCN generated in solid deuterium. The total sum of the number of events is normalized to 1.
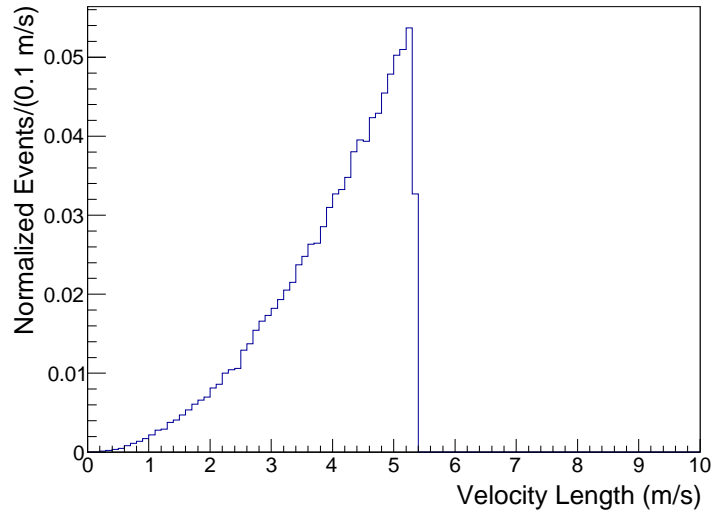
Figure.4.12   Absolute velocity distribution of UCN in solid deuterium. The vertical axis is the number of Monte-Carlo events, and the horizontal axis is the absolute velocity of UCN generated in solid deuterium. The total sum of the number of events is normalized to 1.
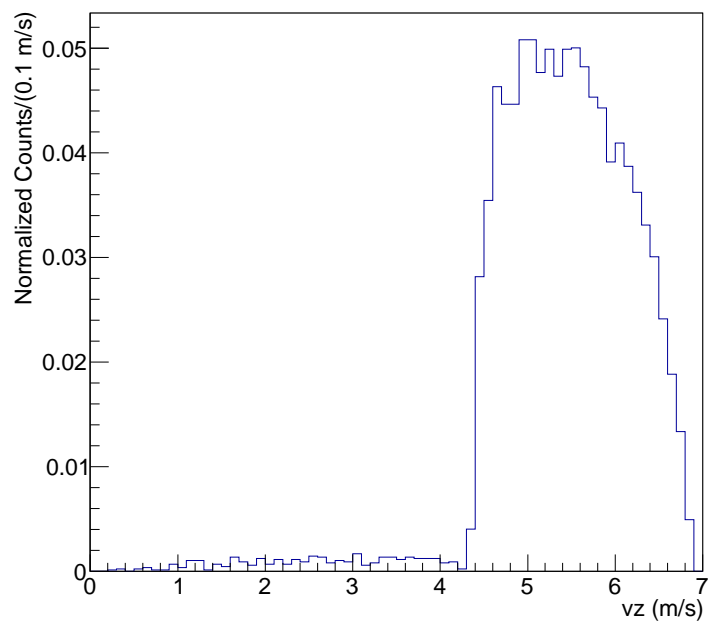
Figure.4.13 Longitudinal velocity distribution of UCN beam. The vertical axis is the number of Monte-Carlo events, and the horizontal axis is the longitudinal velocity length of UCN reaching the boundary between the transport guide and the solid deuterium converter. The total sum of the number of events is normalized to 1.
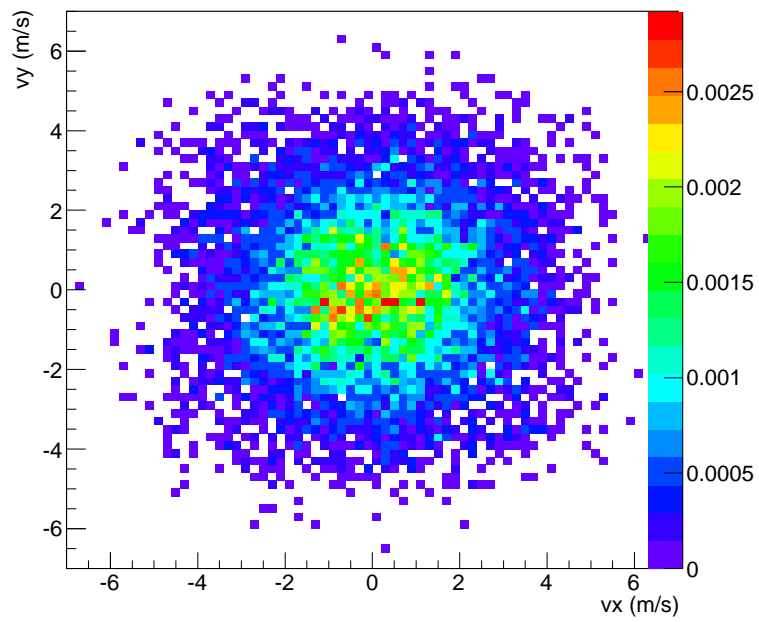
Figure.4.14   Transverse velocity distribution of UCN beam. The vertical and horizontal axis denote components of the transverse velocity of UCN reaching the boundary between the transport guide and the solid deuterium converter, and the color represents the number of Monte-Carlo events. The total sum of the number of events is normalized to 1.
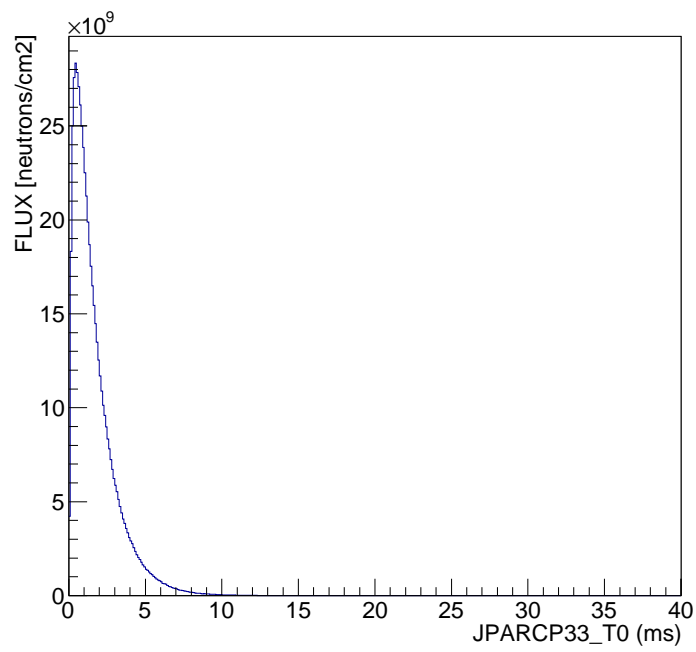
Figure.4.15 T_0 distribution when UCNs generate in the solid deuterium converter. The vertical axis is the neutron flux calculated by PHITS, the horizontal axis is the time at which the UCN is generated since the J-PARC proton beam is injected to Pb target, T_0.

4.4.2 Essential Point of Simulation

In this section, it is explained what kind of criteria is adopted for the simulation study. Simulation results are affected by the following factors:

1. Rebunch Efficiency
2. Storage Performance
3. Rebunch Storage Performance
4. Guide Size
5. Bottle Size
6. Electric field strength

The performance of the rebunch efficiency is determined by the non-specular reflection, the application timing of the RF magnetic field, the gradient magnetic field, and the spin reversal resonance probability. Regarding the non-specular reflection, the micro roughness model is used in this study. In this model, because the surface roughness is a significant principal parameter, these parameters are changed within realistic conditions. Regarding the RF magnetic field, it is adjusting within the realistic range expected to be feasible from the development of the rebuncher. Regarding the gradient magnetic field, the same value as the prototype of the actual rebuncher system is adopted in this study. Regarding the probability of spin reversal resonance, in order to evaluate the upper limit of the experimental ability, it is chosen as 1 which is the ideal condition.

The storage performance is determined by Fermi potential and UCN loss probability coefficient. Regarding Fermi potential, ILL and PSI values are assumed in this study. Regarding the loss probability coefficient (η), it is affected by temperature and the surface condition. η typically amounts to $\sim \mathrm{O}(10^{-4})$ at room temperature, but it also amounts to several 10^{-5} by cooling it. It is found that η has large variation depending on conditions (refer [85][86][82]). Therefore, in this study, η is changed in the range from several 10^{-5} to several 10^{-4} according to these references.

The rebunch storage performance is determined by the distance from UCN source to the shutter position, the beam repetition of J-PARC pulse proton beam, the shutter opening/closing timing, the rebunch efficiency, and the storage performance. In this study, the distance from UCN source to the shutter position is chosen to 10 m, based on the specification value of J-PARC P33 experiment. Then, it takes 1.4 s $\sim$ 2.4 s to detect UCNs from the time when UCN is produced by nuclear spallation. In this study, for simplicity, the beam repetition of J-PARC pulse proton beam is chosen to 0.5 Hz = 2 s to exclude the effect of pulse pile up. Therefore, in this study, it is estimated how much the following three factors contribute to the changes in the rebunch storage performance: the timing adjustment of opening/closing of shutter, the rebunch efficiency, and the storage performance.

Regarding the size of the transport guide, it is modeled by the specification of the J-PARC P33 experiment. Regarding the magnitude of the electric field, it is determined by the discharge limit. Regarding the bottle size, it is chosen to be the same size as ILL and PSI.

4.4.3 Rebunch Efficiency

In this study, the transportation simulation assuming J-PARC P33 experiment was performed and the effect of the rebunch method was evaluated by analyzing the time of flight at the shutter point. In addition, the experimental setup of Figure 4.9, the general assumptions of Table 4.4, and the initial position and initial velocity distribution described in chapter 4.4 are assumed, respectively. Therefore, the rebuncher is assumed to be at 5 m, and a gradient magnetic field of Figure 4.5 and an RF magnetic field of Figure 4.10 are assumed to be applied. The time of zero in this simulation is regarded as that of the proton beam injection. In this situation, UCNs are generated in the solid deuterium and transported to the measurement cell through the rebuncher. Both rebuncher magnetic fields make UCNs concentrating on shutter 1 point of Figure 4.9 at the time of 2.15 s to 2.2 s (see later Figure 4.16 for details).

In this study, the period that shutter opens after the J-PARC proton beam injection is referred to as "cut-out time". Thanks to the rebunch method, the UCN density in the measurement cell becomes improved most effectively by adjusting the cut-out time width to the time for which the pulsed UCN beams refocus on a shutter point. Hence, the cut-out time width used in this section is chosen to be 2.15 s to 2.2 s for which pulsed UCN beams refocus on shutter 1 point of Figure 4.9.

In general, the rebunch efficiency decreases when non-specular reflection occurs during transport of UCN. Therefore, this study evaluated the effect of non-specular reflection by using the micro-roughness model, confirmed to be well matched with the actual measurement. In this study, it was assumed that the non-specular reflection occurs only on transport guide according to micro-roughness model. The following benchmark points were considered for three free parameters of the micro-roughness model.

Surface roughness of guide

This simulation study considered the cases of $b = 0$ nm, 0.5 nm, 1 nm, 1.5 nm, 2 nm, 2.5 nm, 3 nm RMS. It is decided to estimate the effect of roughness more precisely within the practical range on the application limit of micro roughness model (see chapter 2.3).

Correlation length of guide

This simulation study considered the cases of $w = 22$ nm, 33 nm, 45 nm. It is estimated by the actual measurement of neutron mirrors such as NiC and DLC, which were evaluated to be 22 nm and 45 nm with AFM (DI-3100, Veeco Instruments Inc.) [31].

Surface potential of guide

This simulation study considered $V_F = 210$ neV. It corresponds to the mirror made by NiP plating method. The plating method can coat large area, and NiP is inexpensive and nonmagnetic. That is why NiP mirrors are chosen as a benchmark in this study.

Based on the above-shown assumptions, the transport simulation is performed as below. First, UCNs are generated uniformly in the solid deuterium converter according to the phase space distribution as described in chapter 4.4.1, and then UCNs are transported from UCN source to the shutter 1 of Figure 4.9. In this way, if UCN reaches shutter 1 point, the time of flight of UCN is recorded. The same procedure repeats 100,000 times, which generates the time-of-flight distribution of J-PARC P33

experiment. Finally, by analyzing obtained result, the number of Monte Carlo events recorded on 2.15 to 2.2 s and the dependence of it on the non-specular reflection are evaluated. The larger the number of Monte Carlo events is, the higher the rebunch efficiency becomes.

For reference, Time of Flight distribution obtained by the transport simulation is shown in Figure 4.16. The horizontal axis shows Time of Flight when UCNs reach the shutter 1 of Figure 4.9, the vertical axis shows the number of Monte Carlo Events, the line color denotes the roughness of the transport guide or whether the rebunch method is used or not. When assuming specular reflection, 6896 events were obtained as the Monte Carlo Events of UCNs which can reach at the shutter 1 position. On the other hand, the number of trials is 100,000 Events. Therefore, the extraction efficiency from UCN source was estimated as 6.896±0.08 % in this simulation condition.

The intensity of UCN flux varies depending on the rebuncher and shutter operation, which can be estimated from Figure 4.16. If using neither the rebunch nor the shutter operation, the intensity is calculated as 6896±80 Events/2 s = 3448±40 Events/s. Similarly, if using both the rebunch method and the shutter opening/closing operation with the cut-out time width 2.15 s to 2.2 s, the intensity is calculated as ∼ 2,020±40 MC Events/50 ms = 40,400±800 Events/s. The difference corresponds to 11.7 times. This fact indicates that the intensity of the UCN flux varies greatly according to the cut-out time width and the time focusing effect by the rebuncher.

The analysis results of dependence on the non-specular reflection is shown in Figure 4.17. Obviously, the intensity within the time window 2.15 s to 2.2 s becomes drastically attenuated as the surface roughness increase, which is reduced to be 1/5 as the surface roughness increases from $b = 0$ to 3 nm. Therefore, it is found that the non-specular reflection has a serious effect on the intensity of UCN beams. In Figure 4.17, the effect of correlation length, w, is very small. Hence, in this study, the parameter w is fixed to 33 nm for simplification hereafter.

This study chose the cut-out time width to be 2.15 s to 2.2 s at which pulsed UCN beams refocus on shutter 1 point so that the rebunch efficiency becomes maximal. However, in general, effectiveness of rebunch method changes depending on how the cut-time out width is synchronized with UCN beams because it has effect on the instantaneous intensity. For reference, the dependency study of the instantaneous intensity on the cut-out time in some extremely cases is given in the Appendix H.
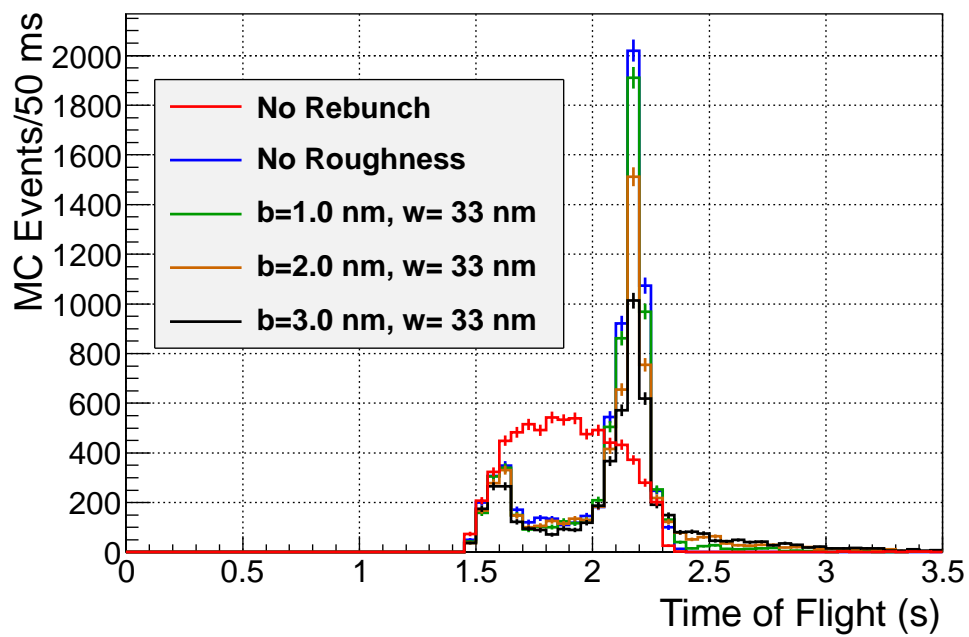
Figure.4.16　Example of TOF distribution change due to the non-specular reflection. TOF change at the shutter 1 point was evaluated in the case that UCN passes through a transport guide with different surface roughness. The horizontal axis is TOF, and the vertical axis is the number of UCNs which can reach shutter.
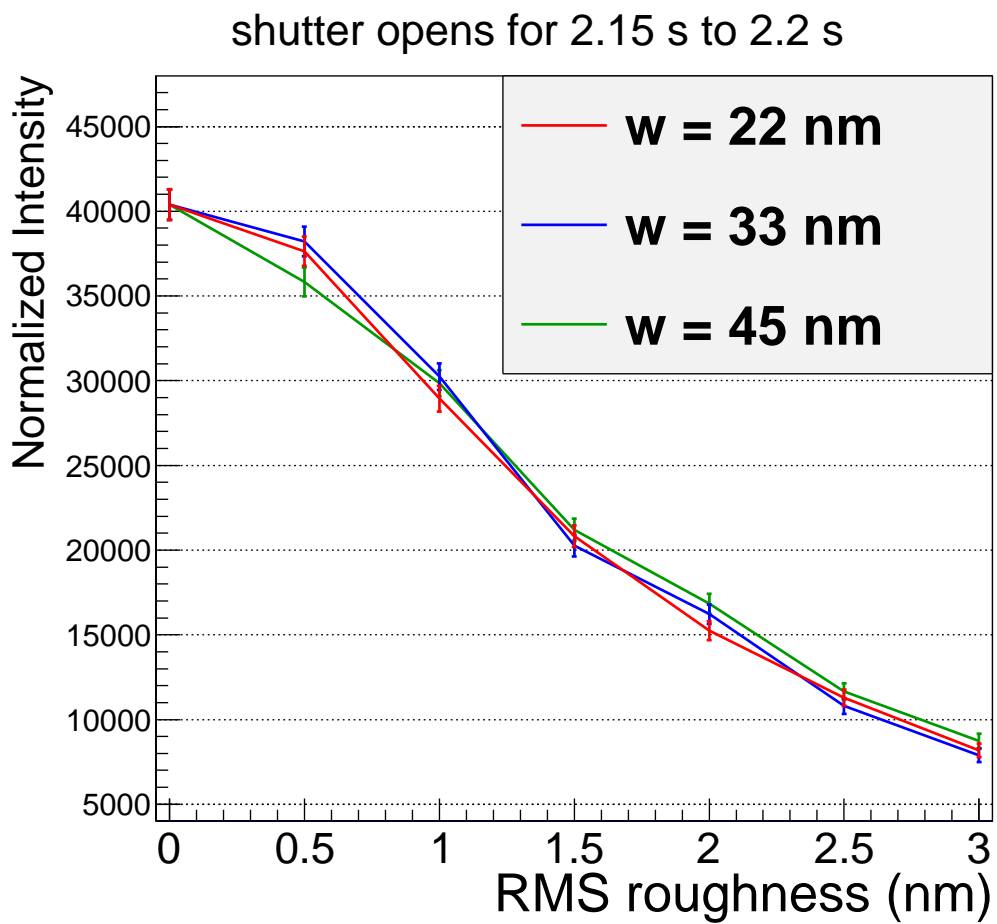
Figure.4.17 Dependence of the rebunch efficiency on the surface roughness. The vertical axis is the number of Monte Carlo events normalized to 1 s, the horizontal axis is the RMS value of the surface roughness of transport guide, and the line color denotes the correlation length.

4.4.4 Rebunch Storage

In this section, it is confirmed how much UCN number will increase when refocused UCN beams are accumulated in a storage container with the rebunch storage method. And also, it is confirmed how the number of the storable UCN depends on the reflection performance of the storage container and the non-specular reflection.

In this study, it was assumed that pulse UCNs are supplied from the ultracold neutron source every two-seconds cycle. Therefore, the time evolution of the number of UCNs in the storage container can be represented by accumulating that of one pulse. In addition, the time dependence of total storage number is expressed as $S(t)$, and the time dependence of storage number due to one pulse is expressed as $s(t)$ hereafter. In this way, $S(t)$ was derived by evaluating $s(t)$ and piling it up. This relation is represented clearly as follows:

$$S(t) = \sum_{i=0}^{i_{\max}} s(t + 2i) \tag{4.4}$$

where $i_{\max}$ indicates the upper limit of the number of pulses piled up. In this study, $i_{\max} = 50$ was used so that the storage time becomes long enough. In other words, it means that the accumulation up to 100 s was considered in this simulation.

The number of UCN achieved by the rebunch storage method changes depending on the accumulation period and the reflection performance of the storage container and non-specular reflection. In this study, the accumulation period was defined as the elapsed time until $S(t)$ becomes the maximum value of 90 % since the start of accumulation of UCNs. Furthermore, benchmark points of reflection performance were chosen to be the following 8 points shown in Table 4.5. As mentioned in section 4.4.2, Fermi potential assumed in this study is chosen to be that of ILL and PSI experiment. And also, η values are chosen to be from 8×10^{-5} to 5×10^{-4} because η value is typically changed from $\sim \mathrm{O}(10^{-4})$ to several 10^{-5} depending on conditions. In addition, in this study, micro-roughness model assuming parameters used in the previous section was adopted to represent the non-specular reflection on the transport guide surface.

potential ID	potential (bottom and top)	potential (side)	η
1	210	91	$(8 \times 10^{-5}, 1 \times 10^{-4}, 3 \times 10^{-4}, 5 \times 10^{-4})$
2	210	160	$(8 \times 10^{-5}, 1 \times 10^{-4}, 3 \times 10^{-4}, 5 \times 10^{-4})$

Table.4.5   Reflection performance of the storage container considered in this study

Simulation assumption and procedure are described below. First, the experimental setup of Table 4.3 and the general assumptions of Table 4.4 are assumed. Second, the cut-out time width of 2.15 s to 2.2 s is assumed. Third, regarding parameters having effects on the non-specular reflection of the inner surface of the transport guide, the RMS roughness of $b = 0 \sim 3$ nm, the correlation length of $w = 33$ nm, and V_F of 210 neV are assumed. Fourth, it is assumed that only specular reflection occurs at the inner surface of the storage container. Fifth, it is assumed that the inner wall of the storage container has

the reflection performance of Table 4.5. Sixth, it is assumed that pulsed UCN beams are generated by one proton beam injection and emitted from the ultracold neutron source in J-PARC P33 environment. Under such six assumptions, the transport simulation repeats 100,000 times to evaluate $s(t)$, and then $S(t)$ is derived by piling up $s(t)$ by every two-second cycle. Finally, the number of UCNs that can be stored with the rebunch storage method is evaluated as the maximum value of 90 % of $S(t)$.

An example of a function of $s(t)$ and $S(t)$ are given in Figure 4.18. The vertical axis is the number of UCNs in the storage container, the horizontal axis is the elapsed time since the start of accumulation of UCN, red is $s(t)$, and black is $S(t)$. The potential ID1 corresponds to a container having the same potential as the ILL experiment, and the potential ID2 corresponds to a container having the same potential as the deuterated polystyrene that PSI developed. In other words, in the former it is assumed that DLC coated on aluminum on the top and bottom and SiO_2 on the side are used, and in the latter it is assumed that DLC coated on aluminum on the top and deuterated polystyrene on the side are used.
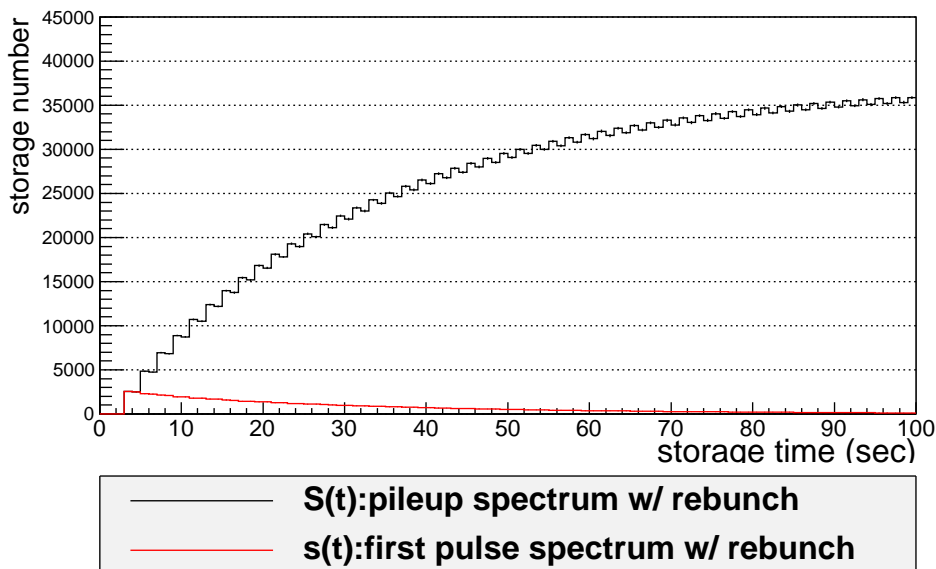
Figure.4.18   Examples of functions $s(t)$ and $S(t)$

For reference, the time evolution of the rebunch storage number for potential ID1 and 2 and a loss probability coefficient of 3×10^{-4} is given in Figure 4.19. The vertical axis corresponds to the number of stored UCNs, and the horizontal axis corresponds to the storage time. The maximum value of the stored UCN varies depending on the potential difference. In general, the UCN loss probability coefficient also has a similar effect.

The analysis result obtained from this study is given in Figure 4.20 and 4.21. The vertical axis is the number of the rebunch storage, and the horizontal axis is the surface roughness. The number of the rebunch storage strongly depends on the non-specular reflection, which decreases $1/2.5$ to $1/3$ as b increases from 0 nm to 3 nm RMS. Regarding the Fermi potential, the number of the rebunch storage in the case of using the potential lD1 becomes $1/1.7$ to $1/2.1$ compared to the case of using potential ID2.

Also, the number of UCNs that can be achieved with the rebunch storage method decreased about 1/1.5 as η varied from 8×10^{-5} to 5×10^{-4}. From the above, it is understood that the non-specular reflection has the most serious effect on the performance of the rebunch storage method.

Figure 4.20 shows that the best case achieves 35,000, while the worst case achieves 5,000. There was a difference of 7 times between two cases; it is thought that such a large difference was due to the change in the rebunch efficiency and the storage efficiency. Because the number of trials of simulation for the transportation of one-pulse UCN is 100,000 times, it is found that the number of UCNs that can be stored by the rebunch storage method amounts to 5% to 35% compared to the number of UCNs generated in the solid deuterium converter by one proton beam injection.
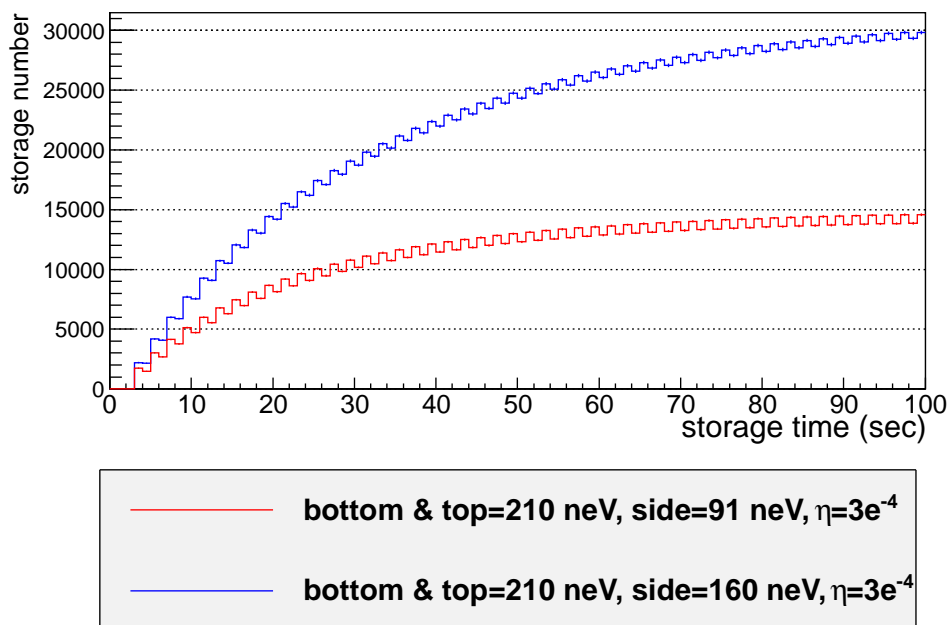
Figure.4.19 Example of the effect of the potential on the rebunch storage number. The vertical axis shows the rebunch storage number and the horizontal axis shows the storage time. See the text for details.
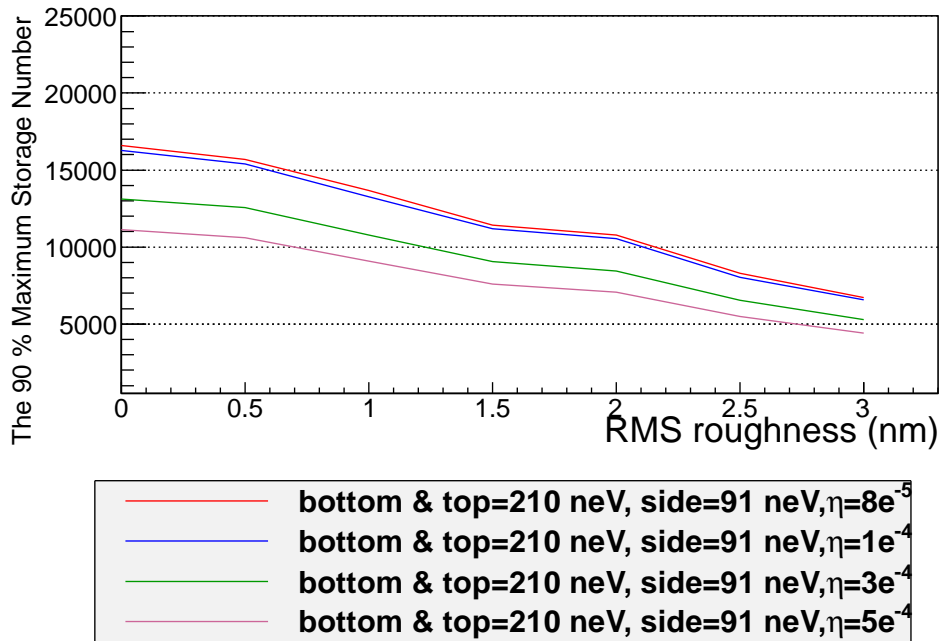
Figure.4.20 Dependence of the rebunch storage number on the non-specular reflection. The vertical axis shows the number of storage and the horizontal axis shows the surface roughness. See the text for details.
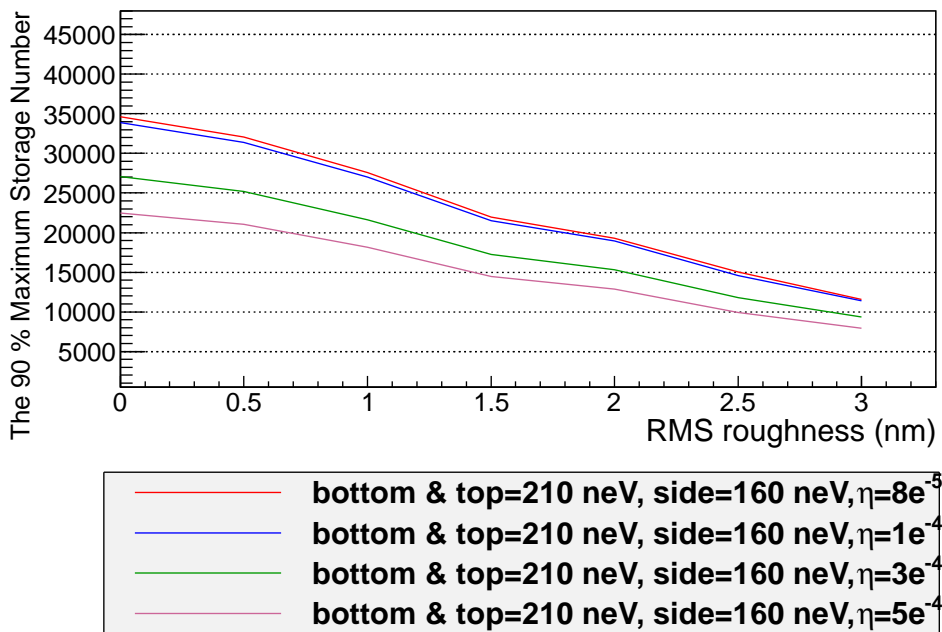
Figure.4.21 Dependence of the rebunch storage number on the non-specular reflection. The vertical axis shows the number of storages and the horizontal axis shows the surface roughness. See the text for details.

4.4.5 Statistical Sensitivity

In this section, the dependence of the statistical precision on the performance of the reflection material are evaluated. The evaluation flow is explained as below. In general, in order to evaluate the statistical sensitivity, following five variables must be determined: E, α, T, n, and $N_{1\mathrm{meas}}$ (refer formula (3.8) for details). Of these variables, the electric field strength (E) and the visibility (α) can be fixed using the reference values based on the ILL and PSI experiment. In this study, 10 kV/cm and 0.86 are used as E and α, respectively. The detection number of UCNs expected in one measurement ($N_{1\mathrm{meas}}$) and the time needed for one measurement (T) can be determined by the UCN storage simulation and the maximum statistical sensitivity condition of expression (3.9). This study uses the rebunch storage number evaluated in previous section as the number of UCNs stored in the container at the beginning of the storage duration. The repetition number of measurements (n) can be determined by dividing the total measurement duration (T_{tot}) by the time necessary for one measurement cycle ($T_{1\mathrm{meas}}$). T_{tot} is determined by the assumption of Table 4.4. $T_{1\mathrm{meas}}$ can be determined by the following formula: $T_{1\mathrm{meas}} = T_{\mathrm{acc}} + T + T_{\mathrm{rel}}$, where T_{acc} denotes the time needed for accumulation of UCN, and T_{rel} denotes the time needed for release of UCNs. T_{acc} can be determined by the rebunch storage simulation. On the other hand, in this study, T_{rel} is assumed to be 100 s, for which UCNs in the storage container of 21 Litter can be evacuated enough (refer Appendix.F.2 for the case of the storage container of 98 Litter). In such a way, all E, α, T, n, and $N_{1\mathrm{meas}}$ can be determined. Thereby, the statistical precision is derived and its dependence on the reflection performances is analyzed.

Simulation assumptions and procedure are described below. First, the electric field strength is chosen to be 10 kV/cm. Second, the total experimental duration and the measurement time per one day are assumed to be 3 years and 18 hours/day, respectively. Third, visibility α is assumed to be 0.86, which is the evaluation value of the document [63] assuming time invariance of α during storage. Fourth, it is assumed that UCNs are released from the measurement cell for 100 s after UCN storage period. Fifth, it is assumed that the rebunch storage number, evaluated in previous section, is used as the number of stored UCNs in the measurement cell at the beginning of UCN storage period. Sixth, it is assumed this study inherits all of the reflection performance used in the rebunch storage simulation adopted in previous section. Under such six assumptions, UCN storage simulation is performed 500 times to search the storage time and the storable number of UCNs satisfying the maximum sensitivity condition of expression (3.9). As a result, E, α, T, $N_{1\mathrm{meas}}$, and n are determined. Finally, by substituting these values for five variables of formula (3.8), the statistical sensitivity is evaluated.

For reference, an example of the time evolution of the number of UCNs obtained from the storage simulation is given in the Figure 4.22. The vertical axis corresponds to the number of stored UCNs, and the horizontal axis corresponds to the storage time. It represents the storage time dependence of the number of UCNs in the storage containers whose potential ID are 1 or 2 in Table 4.5 and UCN loss coefficient η is 3×10^{-4}.

The statistical precision obtained in this simulation is given in Figure 4.23 and 4.24. Each figure corresponds to the result assuming different potential ID 1 or 2, respectively. The horizontal axis represents

the surface roughness, the vertical axis represents the statistical precision that can be achieved when the experiment continued for 3 years, and color denotes η differences. The best statistical precision obtained by the simulation was $(7.2 \pm 0.2) \times 10^{-28}$ e·cm, whereas the worst statistical precision was $(5.9 \pm 0.2) \times 10^{-27}$ e·cm. There was a difference of 8 times between two cases; such a large difference was due to the change in the rebunch efficiency and the storage efficiency. The statistical precision was deteriorated by the non-specular reflection, and it was changed by about 1.6 times with b varied from 0 nm to 3 nm. In addition, the statistical precision changed by about 3 times as η varies from 8×10^{-5} to 5×10^{-4}, while it improved by $1.5 \sim 1.7$ times with the potential of sidewall increased 91 neV to 160 neV. In this way, the dependence of the statistical sensitivity on the performance of the reflective material of UCN of J-PARC P33 was numerically clarified. It is concluded that accurate evaluation of reflection performance is needed for reliable estimation of the statistical sensitivity of J-PARC P33. In particular, it is important to evaluate the UCN loss probability having the largest effect on the sensitivity. In other words, it is understood that development of highly functional reflective materials is extremely effective for improving the statistical sensitivity of J-PARC P33.
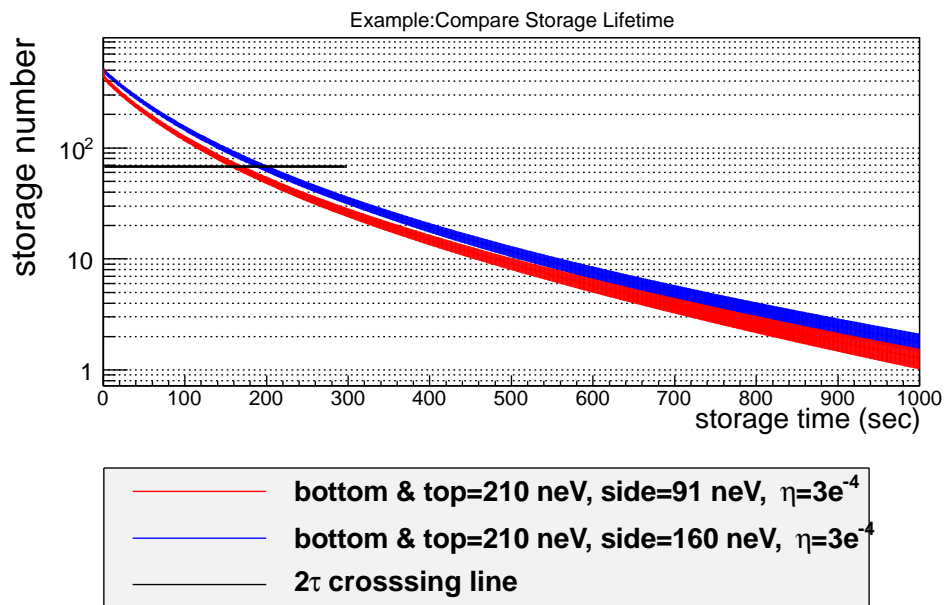
Figure.4.22   Example of time change of UCN storage number. The time evolution of stored UCNs is simulated. The vertical axis is the number of UCNs in the container, and the horizontal axis is the storage time. $\eta = 3 \times 10^{-4}$ and potential ID = 1 (red) or 2 (blue) were selected as the reflection performance of the container. The number of trials of Monte Carlo was chosen to be 500. The black line (2τ crossing point) corresponds to the number of UCNs satisfying the maximum sensitivity condition of expression (3.9).
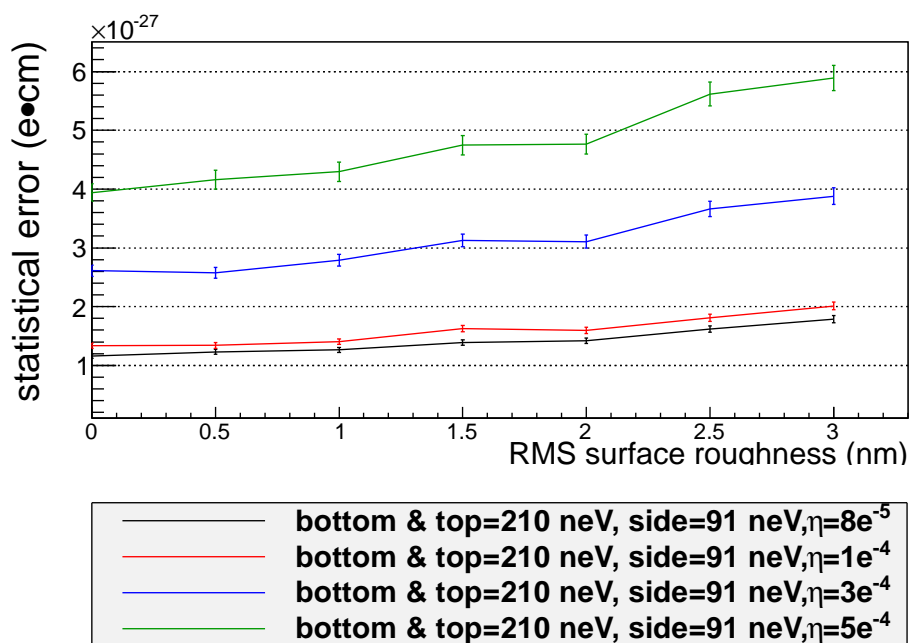
Figure.4.23   Dependence of the statistic precision on the non-specular reflection and UCN reflection loss. Simulation was used to estimate the statistical precision of the J-PARC neutron EDM experiment. The horizontal axis represents surface roughness, the vertical axis represents the statistical precision, and the line color represents potential and η. Note that the use of a container with Potential ID = 1 is assumed here.
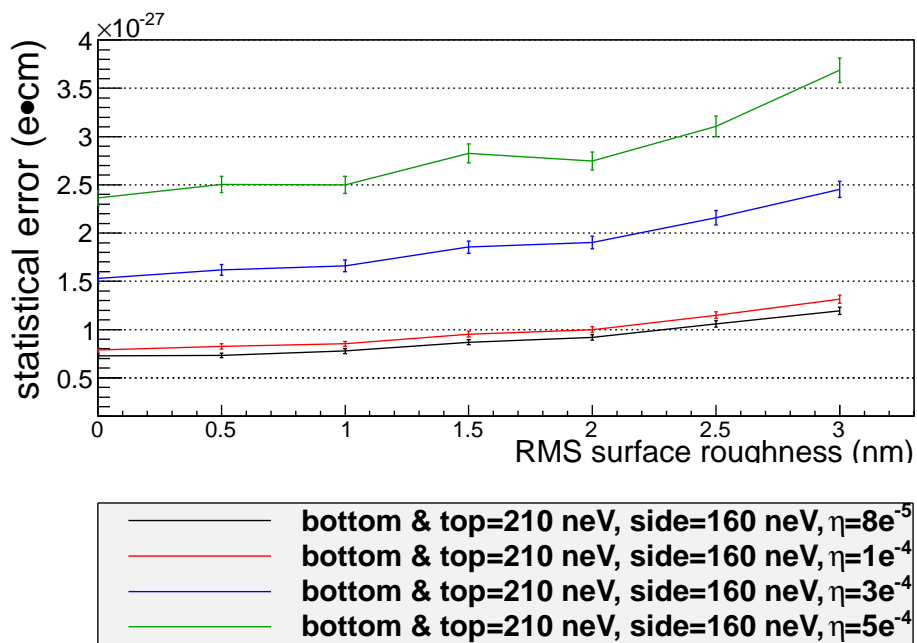
Figure.4.24 Dependence of the statistic precision on the non-specular reflection and UCN reflection loss. Simulation was used to estimate the statistical precision of the J-PARC neutron EDM experiment. The horizontal axis represents surface roughness, the vertical axis represents the statistical precision, and the line color represents potential and η. Note that the use of a container with Potential ID = 2 is assumed here.

4.5 Short Summary

1. Using PHITS simulation, the energy distribution of the neutron flux passing through the solid deuterium converter of J-PARC P33 ultracold neutron source was evaluated. As a result, an energy distribution in Figure 4.3 was obtained, which can approximate to Maxwell distribution with a peak at 30 K. By normalizing the flux distribution with the beam current of one pulse of J-PARC LINAC proton beam, 5.8×10^{11} cm^{-2}s^{-1} was obtained as the evaluation of total neutron flux sum.

2. Assuming Maxwell distribution with a peak at 30 K, the UCN density generated in the solid deuterium was estimated. As a result, 5,800 UCN/cm^3 was found to be produced in the solid deuterium when injecting one pulse of J-PARC LINAC proton beam to the ultracold neutron source.

3. Transportation of J-PARC P33 was simulated. As a result, the TOF distribution and its non-specular reflection dependence were evaluated as Figure 4.16 and Figure 4.17. It was confirmed that the rebunch method makes the intensity gained by 11.7 times if not taking account non-specular effect, and that the non-specular reflection makes the intensity attenuated by 1/5 times as b increased 0 nm to 3 nm RMS.

4. Rebunch storage simulation was performed. As a result, the time dependency of the number of the rebunch storage was evaluated as Figure 4.20 and 4.21. This result indicated that the number of UCNs decreased by 1/2 or less due to non-specular reflection, by 1/1.7 or less due to the Fermi potential difference, and by 1/1.5 due to loss probability coefficient difference.

5. The simulation to evaluate the statistical precision of J-PARC P33 neutron EDM experiment was performed. As a result, the statistical precision as Figure 4.23 and Figure 4.24 were obtained. 3 years is assumed for an experimental period and its duty is 3/4. This result indicated that statistical precision becomes deteriorated by about 1.6 times due to non-specular reflection difference, by about 1.5 times due to the Fermi potential difference, and by about 3 times due to the loss probability coefficient difference, respectively.

Chapter 5

Development of Neutron Mirror for Neutron EDM Experiment

In this chapter, the details of the development of the neutron reflective material are summarized. In the previous chapter, it became clear that the development of reflective materials is key to high precise neutron EDM measurement. The performance of the reflector can be indicated by the Fermi potential, the non-specular reflection probability, and the UCN loss probability coefficient as described in the previous chapter. In addition to those indexes, a nonmagnetic property is desirable because a low spin reversal probability is achieved. Furthermore, a high insulating property is desirable for a sidewall material of the storage container because it suppresses leakage current flowing in the sidewall. Therefore, NiMo (nonmagnetic, high Fermi potential) and Diamond Like Carbon (nonmagnetic, high insulation, low non-specular reflection probability) have been developed in this study.

The performance of the reflector was evaluated by surface analysis such as neutron reflectometry, Rutherford backscattering spectroscopy/elastic recoil detection analysis (RBS/ERDA), X-ray reflectometry, electron microscope, glow discharge optical emission spectrometry (GDOES), and so on. As for the UCN loss probability coefficient, two evaluation ways are possible: one is the method using RBS/ERDA and the other is the method using UCN storage experiment. In this chapter, only evaluation method using RBS/ERDA is taken. The method using UCN storage is described in the next chapter.

This chapter is organized as below. First, the reflective material about NiMo is described. Specifically, the feature as neutron mirrors and the manufacturing method are explained. In next section, similar explanations for Diamond Like Carbon are given. This section consists of three subsection dealing with manufacturing methods, plasma based ion implantation deposition method, ionized evaporation deposition method, and filtered arc ion plating deposition method. Next, the details of the surface analysis methods are described. Next, the performance of all the developed materials evaluated by the surface analysis is summarized. Finally, the short summary of this chapter is given.

5.1   Fabrication method of Nickel Molybdenum Alloy

Nickel is an excellent material with high Fermi potential of 252 neV. However, Nickel does not become an excellent neutron mirror because its polycrystalline structure causes poor surface roughness. Generally,

amorphous structure tends to have better surface roughness. Therefore, nickel alloys doped with an element such as C, Mo, V are used for neutron mirrors. In particular, the alloy doped with Mo at a weight ratio of 15% is a promising material that has been confirmed to achieve high transportation efficiency [64, 65].

Normally, the sputtering method is used for the preparation of the alloy film, but it cannot deal with the formation of large area substrate. In this study, vapor deposition method was tried to prepare NiMo alloy. In order to obtain an alloy film by vapor, it was necessary to use a special method in which Ni and Mo are separately evaporated and mixed on a substrate. Hereafter, such method is called binary vapor deposition. A schematic illustration of binary vapor deposition method is shown in Figure 5.1. In this study, with the technical cooperation of Kanagawa Institute of Industrial Science and Technology [66], development of NiMo mirrors became possible. The equipment used in this study is summarized in the Table 5.1.

In the film formation process, the chamber was evacuated to 10^{-5} Pa, and Ni and Mo were evaporated by electron beams, and it was exposed to the substrate. In this study, 10 kV and 320 mA were used as electric power and current of the electron beam. The substrate was rotated to prevent non-uniformity while binary vapor deposition proceeding. The film thickness was evaluated by measuring the step between silicon masking region and the other. In step measurement, laser microscope with the precision of ~ 1 nm was used.

The NiMo alloy preparation flow is illustrated as follows.

1. Ni and Mo are evaporated alone to confirm the deposition rate.
2. The time of irradiating an electron beam to each target is determined.
3. NiMo is deposited on 10 mm square silicon by using the film deposition condition of 2.
4. The composition ratio of the sample made at 3 is evaluated.
5. The work of 2 – 4 repeats to search for optimum film formation condition.

The composition ratio of NiMo was evaluated by X-ray Photoelectron Spectroscopy (XPS) and a crystal oscillator, and the result was feedback to adapt film formation condition. The depth profile measurement using XPS showed that there was no dependence of depth direction and there was little contamination of oxygen and nitrogen. Although the composition ratio of Mo measured by XPS systematically tended to be higher than that of a crystal oscillator, the results of XPS measurement and the result of the crystal oscillator measurement had a strong correlation. For example, in a certain case, Ni:Mo ratio was 86.8%:13.2% in the result of XPS, 88.6%:11.4% in the result of the crystal oscillator. Finally, by quartz oscillator evaluation, it was confirmed that NiMo film with the weight ratio of 13.6 % was achieved.

5.2 Fabrication method of Diamond-Like Carbon

Diamond has a potential of 304 neV, which exceeds Nickel, and it has high insulation and nonmagnetic property. However, its polycrystalline structure causes poor surface roughness (and also it is expensive). From this point of view, in recent years, Diamond-Like Carbon (DLC) is paid attention. DLC is referred to as a carbon film having the properties of graphite (planar structure) and diamond (three-dimensional
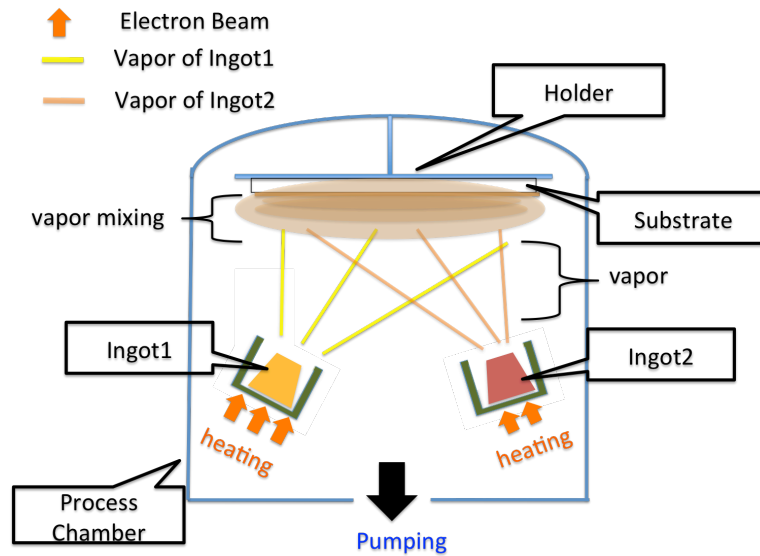
Figure.5.1 Schematic illustration of binary vapor deposition method. An alloy film of a desired composition ratio can be obtained by giving different amounts of heat to each ingot to evaporate them separately and mix them on the substrate. Please see the text for details.

Equipment	Purpose	Manufacturer
Ion plating apparatus (SIP-700)	Film formation	SHOWA SHINKU Co., Ltd.
VersaProbe2	XPS	ULVAC-PHI, Inc.
CRTM-9000	Crystal Oscillator	ULVAC, Inc.
JEBG-303UA	Electron Beam	JEOL Ltd.
ST-10F	Power Source	JEOL Ltd.
Dektak 3030ST	Stepmeter	Sloan Co., Ltd

Table.5.1 Details of apparatuses used for film formation of NiMo

structure). DLC generally has an amorphous structure, so that this surface is smooth and it is possible to be an excellent mirror for a transport guide. In addition, DLC has high insulation for diamond characteristics, which is desirable for a side material of the neutron EDM experiment to prevent electric current flow.

In general, a carbon film whose hydrogen ratio is about 20 to 30% is also included in the definition of DLC. For this reason, the characteristics of DLC can be represented as a triangle plot having vertexes. The triangle plot of the nature of DLC is given in Figure 5.2. The vertex of sp3 indicates the diamond structure ratio, the vertex of sp2 indicates the graphite structure ratio, and the vertex of H indicates the hydrogen content ratio [67]. It can be seen from Figure 5.2 that DLC can be classified into various types depending on the ratio of sp3, sp2, and H. ta-C DLC is categorized to the group having the highest sp3 ratio, which indicates the strongest diamond property. Thus, both of high Fermi potential and high insulation can be expected. Graphite is used as the source material in a ta-C DLC film formation process.
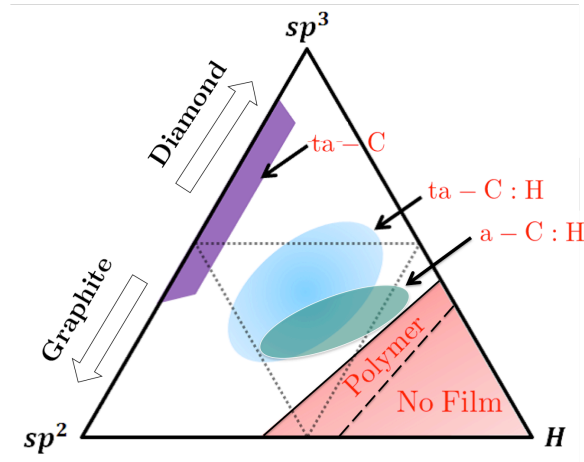
Figure.5.2 Classification diagram of DLC, the image is cited from [67]. A triangle diagram shows the classification of properties of DLC film. See the text for the details.

On the other hand, ta-C:H DLC is categorized to the group having both of a hydrogen content and a diamond-like property. In general, the source material of ta-C:H DLC is organic gas such as benzene. Although ta-C:H DLC has a diamond-like property, it is inferior to that of ta-C DLC. However, ta-C:H DLC has engineering merits such that large area coating and three-dimensional coating can be performed, which ta-C DLC does not have.

In this study, ta-C DLC and ta-C:H DLC have been examined. The reason why ta-C DLC was adopted is that it shows both of high Fermi potential and high insulation. On the other hand, the reason why ta-C:H DLC was adopted is as below. (1) By using deuterated substitution technique, it can achieve the Fermi potential of 200 neV or more. (2) Large-area three-dimensional coating is possible. In general, hydrogen deteriorates both of the Fermi potential and UCN loss probability per one bounce, whereas deuterium improves them. Therefore, ta-C:H DLC after deuterated substitution is possible to apply to the sidewall material of a neutron EDM measurement cell. In fact, the Fermi potential of the sidewall material of ILL experiment and PSI experiment are 91 neV (quartz glass) and 160 neV (deuterated polyethylene). This fact implies the possibility that ta-C:H DLC after deuterated substitution becomes an excellent sidewall material. Deuterated DLC has already been evaluated in documents [68][69], but they have not prepared mirrors from which hydrogen was completely eliminated. In this study, deuterated benzene of a deuteration rate of 99.5% was used as source gas.

In the following section, the details of DLC film formation will be described. Three types of DLC deposition method tried in this study are shown in Table 5.2.

5.2.1   Ionization Evaporation Method

A schematic diagram of the ionized evaporation method is shown in the Figure 5.3. In ionized evaporation method, a hydrocarbon gas is ionized by using thermal electrons emitted from a filament, and it sprayed on a substrate with a bias voltage. In this way, ionized gas is attracted to the substrate and DLC film

DLC formation method	Type	Corp	Apparatus
IEM	ta-C:H	NANOTEC Co.,Ltd. [70]	ICF-330
PBIID	ta-C:H	KURITA SEISAKUSHO Co.,Ltd. [71]	PBII-R1000
FAIPD	ta-C	ONWARD CERAMIC COATING Co., Ltd. [72]	AC-X

Table.5.2 Apparatus used for DLC film formation. Details of IEM DLC, PBIID DLC, and FAIPD DLC are described in chapter 5.2.1, 5.2.2, and 5.2.3, respectively.
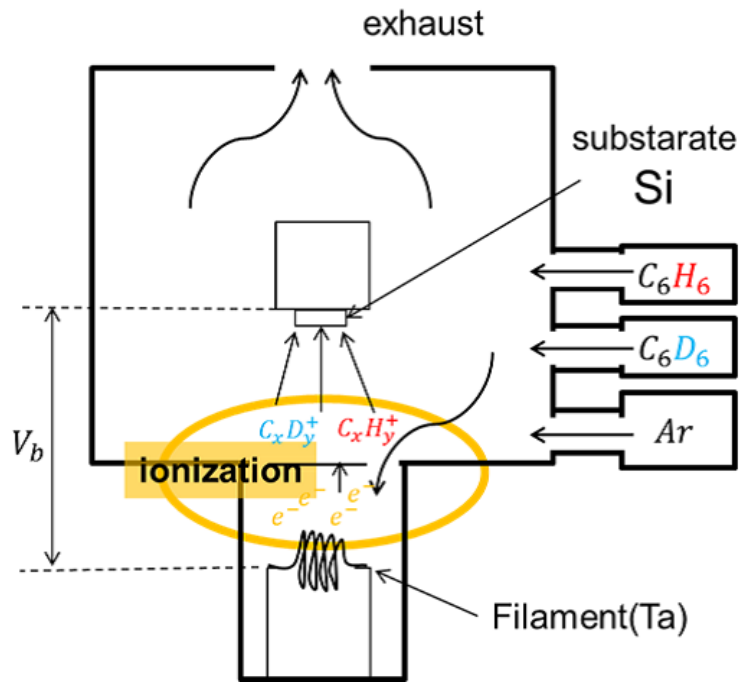
Figure.5.3 Schematic illustration of the ionized evaporation method, the image is cited from [67]. See the text for details.

deposition proceeds.

In this study, DLC produced by the ionized evaporation method is referred to as IEM DLC. The flow of film formation for ionized evaporation method is shown below:

1. The silicon substrate is fixed to the film-forming table.

2. The pressure is evacuated to 10^{-2} Pa with a turbo molecular pump.

3. The heater keeps operated for about 3 hours to realize the thermal equilibrium state.

4. Substrate is bombarded with argon gas to remove the oxide film on the substrate surface.

5. Deuterated benzene is made filled into the chamber.

6. Gas is made ionized with thermal electrons emitted from tungsten filament.

7. Bias voltage is applied to the film-forming table.

8. The silicon substrate is exposed to ionized gas, which is attracted by an electric field of the film-forming table.

9. DLC film growth proceeds.

In this study, ICF-330 (Nanotec corporation) was used for DLC film formation [70]. Inside ICF-330, an ionization vacuum gauge, a baratron vacuum gauge, and a thermometer are installed. The temperature can be controlled 300 to 500 degrees by a heater, the flow rate of the deposition gas can be controlled 0.1 to 9.9 sccm, and the bias voltage on a substrate can be adjusted to 0 to 3 kV.

Since it has been confirmed that there is a correlation between the gas flow rate and the pressure, it is possible to control the pressure by the gas flow. Therefore, in this study, pressure, bias voltage and temperature were adopted as the parameter to control DLC film state.

From the formula (2.2), the Fermi potential of a sample is determined by its composition ratio and density, which greatly changes depending on the film formation conditions of DLC. Namely, the reflection performance of DLC is determined by the film forming conditions. In this study, temperature, pressure and substrate voltage are adopted as conditions. As for temperature, "Low" is defined as 200 degrees, "Middle" is defined as 300 degrees, "High" is defined as 450 degrees. With regard to the flow rate, "Low Pressure" is defined as 0.6 sccm, "Middle Pressure" as 3.1 sccm, and "High Pressure" as 6.2 sccm. In this study, a lot of number sample were tested. Film formation conditions used are shown in Table 5.3.

5.2.2 Plasma Based Ion Implantation Deposition

Plasma Based Ion Implantation Deposition (PBIID) is the method of applying an RF and a pulsed negative high voltage to the substrate installed in the process chamber filled with a source gas. Schematic illustration of PBIID film formation process is given in Figure 5.4 and 5.5. DLC film is formed by plasma and afterglow generated around the substrate. For brevity, DLC fabricated by PBIID is referred to as PBIID DLC in this thesis hereafter.

Generally, in PBIID film formation, both RF plasma and afterglow contributes to DLC film formation. The afterglow mainly contributes film formation. Thanks to afterglow, film formation can be performed at a temperature as low as 300 degrees, which is far lower than plasma CVD using only RF plasma. As a result, the residual stress of the DLC film is relaxed. In addition, the substrate and DLC film are connected by ion implantation, resulting in enhancement of the adhesion of film. Furthermore, because the film is formed by afterglow around the substrate, uniform three-dimensional coating is possible.

The PBIID deposition procedure is described as follows:

(a) Gas Fill

Process gas is flowed into vacuum chamber.

(b) Plasma CVD

A high frequency voltage (RF) is applied to a substrate, and plasma is generated around the substrate. When RF is applied, electrons with high mobility are absorbed by the substrate, but the ions tend to remain, and as a result, the substrate is negatively biased on average.

(c) Plasma Left Behind

When stopping applying RF field, the plasma is left behind around the substrate.

(d) Ion Implantation

No	kV	sccm	Temp
12	3	3.1	middle
14	0.5	3.1	middle
17	1.5	3.1	middle
31	0.5	3.1	middle
32	0.5	3.1	middle
33	1.5	3.1	middle
34	3	3.1	middle
35	0.1	3.1	middle
36	0	3.1	middle
37	0.1	3.1	middle
38	0	3.1	middle
40	0.05	3.1	middle
41	0.05	3.1	middle
42	1	3.1	middle
43	1	3.1	middle
44	0.3	3.1	middle
45	0.3	3.1	middle
46	0.75	3.1	middle
47	0.75	3.1	middle
65	0.5	6.2	middle
66	1.5	6.2	middle
68	0.5	6.2	middle
71	0.5	3.1	low
72	0.5	3.1	low
73	0.5	3.1	middle
74	0.5	3.1	middle
76	1.5	3.4	middle
77	1.5	3.1	middle
78	1	3.1	middle

No	kV	sccm	Temp
79	0.5	3.1	middle
80	0.5	3.1	middle
81	0.5	3.1	middle
82	0.5	3.1	high
83	0.75	3.1	high
84	1	3.1	high
87	1.25	3.1	high
88	0.75	3.1	high
89	1.25	3.1	middle
90	1.25	3.1	middle
93	0.75	0.6	middle
94	0.75	3.1	middle
95	0.75	0.6	middle
96	1	0.6	middle
97	0.5	0.6	middle
98	0.25	0.6	middle
103	0.38	0.6	middle
104	1	0.6	middle
105	0.25	0.6	middle
106	0.5	0.6	middle
107	0.75	0.6	middle
111	0.5	0.6	middle
112	0.63	0.6	middle
114	0.5	3.1	middle
115	0.75	3.1	middle
117	0.75	3.1	middle
118	0.75	3.1	middle
119	0.75	3.1	middle
120	0 .75	3.1	middle

Table.5.3   Details of the film formation condition of IEM DLC

When a high pulse voltage of about -10 kV is applied, ions are drawn into the substrate. As a result, ion implantation between the DLC film and the substrate occurs.

(e) Afterglow

Ions is drawn by high voltage pulse to collide with the source gas and cause ionization. As a result, around the substrate, high-density radicals (= afterglow Plasma) is increased, and film formation proceeds further.

(d) Restart

Afterglow plasma is lost. Return to (a) and start film formation process again.

In this study, with the technical cooperation of KURITA SEISAKUSHO CO., LTD, development of PBIID DLC mirrors became possible. KURITA SEISAKUSHO CO., LTD is one of the leading companies to fabricate PBIID. In general, film formation parameters for PBIID DLC are the pressure in the chamber, the pulse voltage value, and the repetition frequency of the pulse voltage. In this study, the pulse voltage value and the repetition frequency are chosen as film formation conditions, and the pressure in the chamber is fixed at 4 Pa. Film formation conditions are shown in Table 5.4.

Name	Pulse Voltage	Pulse Width	Repetition
sample1	-10 kV	20 μs	1000 pps
sample2	-15 kV	5 μs	4000 pps
sample3	-5 kV	5 μs	4000 pps
sample4	-10 kV	10 μs	2000 pps
sample5	-10 kV	5 μs	4000 pps

Table.5.4   Film formation condition of PBIID DLC
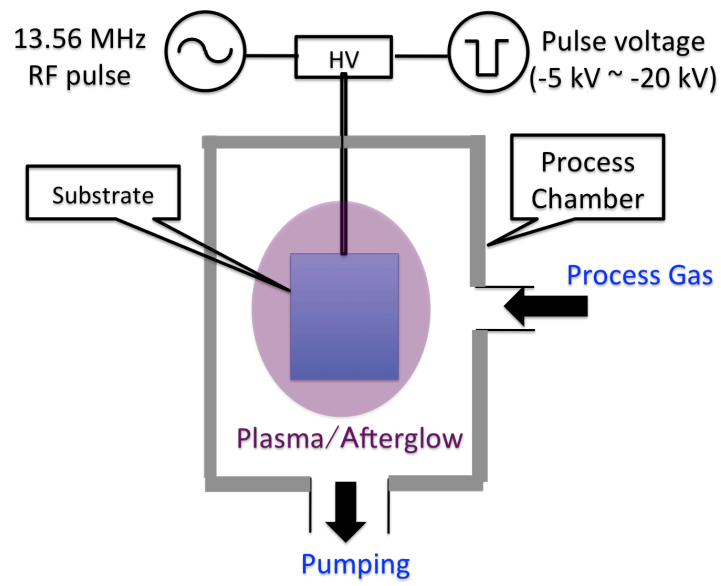
Figure.5.4   Schematic diagram of the PBIID method. See the text for details.
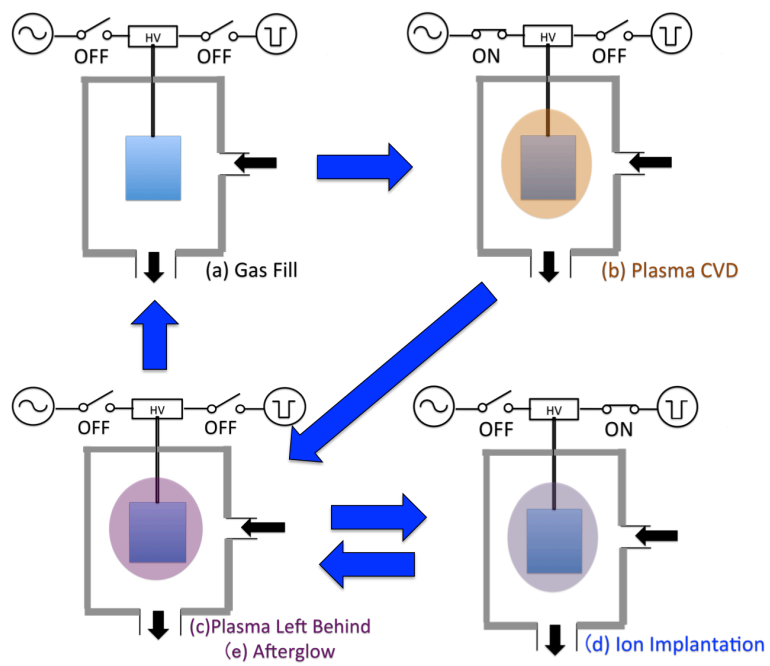
Figure.5.5   Illustration of the flow of DLC film formation by PBIID method. By turning on and off the RF and high voltage pulse power supply alternatively, the state transits along following arrow direction: (a) → (b) → (c) → (d) → (e) → (a) ... etc. Please refer to the text for details.

5.2.3 Filtered Arc Ion Plating Deposition

Arc discharge on graphite surface cause carbon ions vapor, and ta-C DLC film can be obtained by exposing the carbon ions flux to a negative biased substrate. Such film formation method is called arc ion plating deposition method (AIPD). AIPD has two advantages. First, it is possible to obtain the most diamond-like carbon film. Second, it is possible to obtain diamond-like carbon film having no hydrogen which deteriorates neutron reflection performance. On the other hand, AIPD has a disadvantage that neutral macroscopic particles, called droplets, mix in carbon ions vapor and it deteriorates the film surface state. Therefore, the method to filter droplets by using magnetic field was proposed to solve the disadvantage. Such method is called filtered arc ion plating deposition (FAIPD). Schematic diagram of FAIPD is given in Figure 5.6. By using FAIPD, we can achieve ta-C DLC film having polished surface, high carbon density, and a high insulator property.

For brevity, DLC fabricated by FAIPD is referred to as FAIPD DLC in this thesis hereafter. In this study, AC-X (Onward Ceramic Coating Corporation) was used for DLC film formation. The reason why AC-X was chosen as the apparatus used in deposition is that according to the catalog, it is able to fabricate the hardest film, which is equivalent to high carbon density. In this study, W26 mm×L50 mm×T1 mm synthetic quartz glass and Φ76 mm×T2 mm silicon were used as substrates.
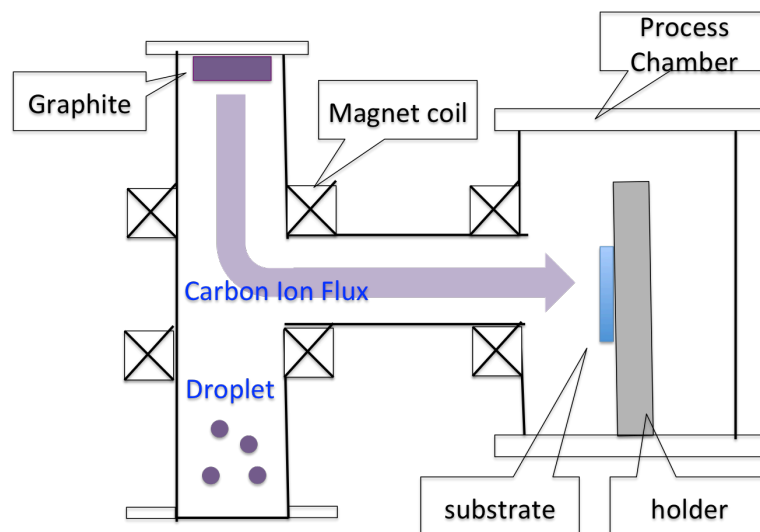
Figure.5.6 Illustration of DLC film formation by FAIPD method. When arc discharge occurs on the surface of graphite, carbon vapor ions are generated. DLC film formation proceeds by depositing ions vapor on the substrate to which a negative bias voltage is applied. Thereby, the highest dense DLC film can be obtained. FAIPD method improves surface roughness by removing neutral particles (called droplets) emitted together with carbon ions.
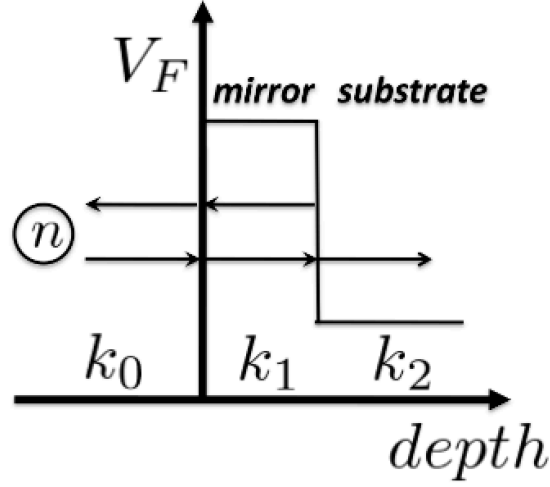
Figure.5.7   Fermi potential of the neutron mirror consisting of a substrate and a single layer. The vertical axis represents the potential, and the horizontal axis represents the depth direction. From the left: air: 0, neutron mirror material: 1, substrate: 2.

5.3   The Method of Surface Analysis

5.3.1   Neutron Reflectometry

This section introduces the principle of neutron reflectometry. By using neutron reflectometry, we can evaluate the reflectivity distribution of sample consisting of a substrate and a single layer. For brevity, a sample consisting a film of X and a substrate of Y is expressed as X/Y hereafter. The reflectivity of the sample as shown in Figure 5.7 can be derived by solving a one-dimensional Schrödinger equation as follows [73]:

$$R = \mathrm{DWT}(q_z, \sigma) \frac{(k_0 - k_1)(k_1 + k_2) + (k_0 + k_1)(k_1 - k_2)\exp{(ik_1 d)}}{(k_0 + k_1)(k_1 + k_2) + (k_0 - k_1)(k_1 - k_2)\exp{(ik_1 d)}} \tag{5.1}$$

$$\mathrm{DWT}(q_z, \sigma) = \exp{(-q_z^2 \sigma^2)} \tag{5.2}$$

where R is the reflectivity of sample, q_z is the transfer wave number during reflection, σ is the RMS surface roughness, and d is the thickness of the film material. k_i for $i = 0, 1, 2$ represent that the wave number of neutrons in each region, DWT is Debye-Waller factor which express the surface spreads due to thermal vibration. It is noted that the incident region is 0, the film region is 1, and the substrate region is 2, and $k_i = \sqrt{k_0^2 - \frac{2mV_i}{\hbar^2}}$ for $i = 1, 2$. In addition, it is also noted that Debye-Waller factor is obtained separately from the Schrödinger equation [74].

At specular reflection, the incident wave number and the reflected wave number are same, and q_z is represented as $2k_0$. Therefore, the expression (5.1) is a function of q_z, and its Fermi potential can be extracted directly by fitting the neutron reflectivity distribution with the expression (5.1).
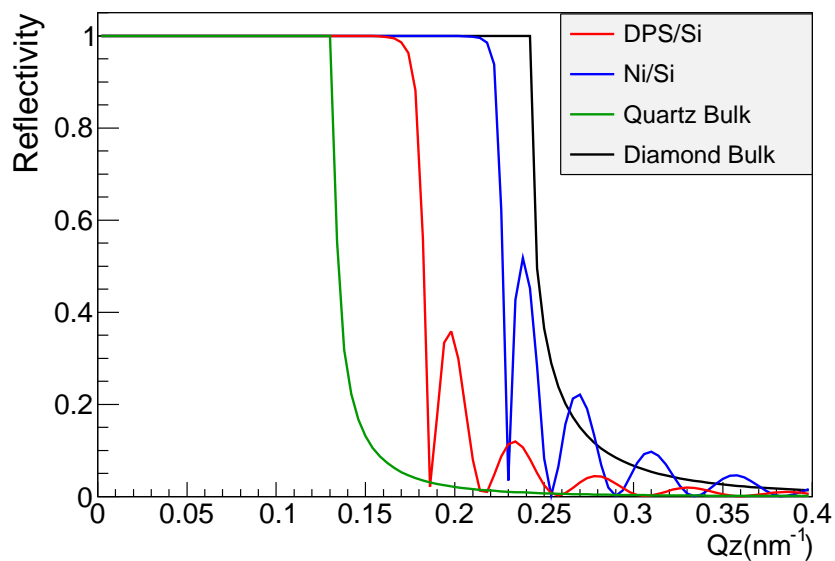
Figure.5.8 Example of reflectivity. Theoretical values of the neutron reflectivity distribution of deuterated polystyrene/Si (red line), Ni/Si (blue line), Quartz bulk (green line), Diamond bulk (black line). The vertical axis shows reflectivity, the horizontal axis shows the transfer wave number Q_z on specular reflection.

An example of reflectivity distribution is given in Figure 5.8. Figure 5.8 is the case that single layer film has 100 nm thickness, and surface roughness is zero. In general, the rougher the surface is, the faster the attenuation is in the wide-angle side. In addition, the thicker the film is, the lower the frequency is. Further, the higher the potential is, the larger the critical angle becomes.

For reference, the relationship between the critical angle and the potential are given in Figure 5.9. This relation of Figure 5.9 is used to evaluate the systematic error of the reflectivity measurement at J-PARC MLF BL16.
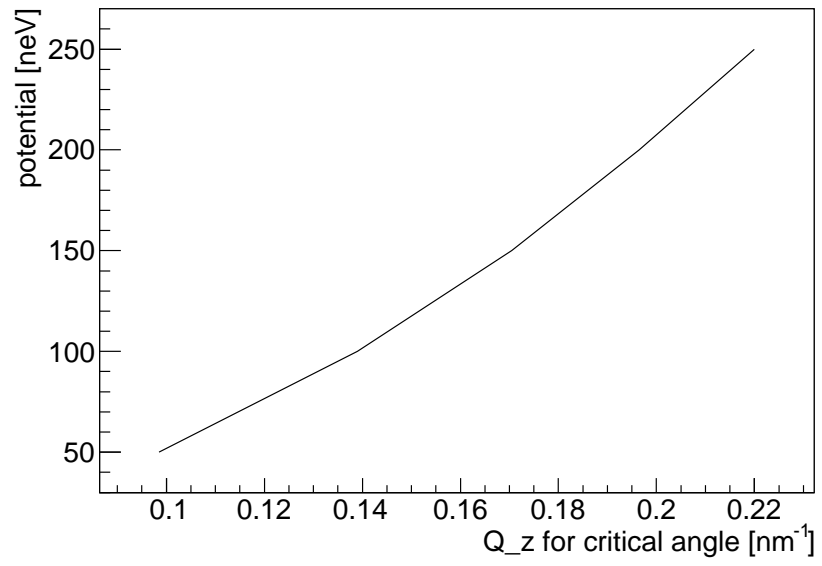
Figure.5.9   Relation of critical angle and the Fermi potential.
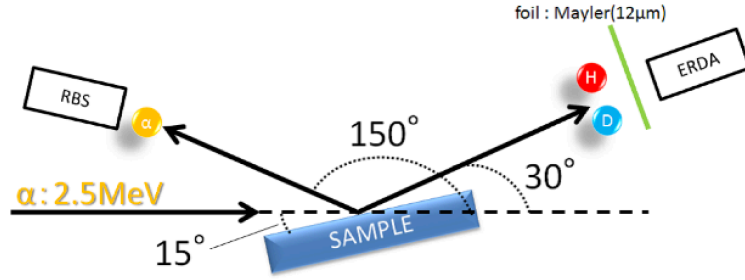
Figure.5.10 Outline of RBS/ERDA experiment, the image is cited from [67]. An accelerated alpha particles of 2.5 MeV hit a sample tilted by 15 degree with respect to the beam axis, and the occurrence events were observed by silicon detectors fixed at 150 degree and 30 degree.

5.3.2 Rutherford Backscattering Analysis and Elastic Recoil Detection Analysis

In this study, RBS (Rutherford Backscattering Spectroscopy) and ERDA (Elastic Recoil Detection Analysis) are used for sample composition analysis. In the RBS/ERDA analysis, when an accelerated ion beam is irradiated to the sample, ions scattered in the forward and backward directions are detected and the element composition ratio is derived. Divalent helium ions were used as incident ions in this study. A schematic diagram of measurement setup is shown in Figure 5.10.

For reference, the schematic illustration of the reaction used in RBS and ERDA analysis are shown in Figure 5.12 and Figure 5.13. In this section, the initial energy and the mass of the incident alpha particle are represented as E_0 and M_1, and the mass of target atom is represented as M_2.

Regarding RBS analysis, the energy and the cross section of the backscattering are calculated as the following formula (5.3) and (5.4) [67].

$$E_{\mathrm{RBS}} = \left(\frac{M_1 \cos\theta + \sqrt{(M_2^2 - M_1^2 \sin^2\theta)}}{M_1 + M_2} E_0 \right) \tag{5.3}$$

$$\sigma(E, \theta)_{\mathrm{RBS}} = \left(\frac{Z_1 Z_2 e^2}{2E} \right)^2 \sin^{-4}\theta \frac{\left(\cos\theta + \sqrt{1 - (\frac{M_1}{M_2})^2 \sin^2\theta} \right)^2}{\sqrt{1 - (\frac{M_1}{M_2})^2 \sin^2\theta}} \tag{5.4}$$

where σ_{RBS} is the elastic backscattering cross section and E_{RBS} is energy of the back scattered particle and θ is the angle between the beam axis and the back-scattered direction.

Regarding ERDA analysis, the energy and the differential cross section of the recoiled reaction are calculated as the following expression (5.5) and (5.6) [67].

$$E_{\text{ERDA}} = \frac{4M_1 M_2 \cos^2 \phi}{(M_1 + M_2)^2} E_0 \tag{5.5}$$

$$\sigma(E, \phi)_{\text{ERDA}} = \left(\frac{Z_1 Z_2 e^2 (M_1 + M_2)}{2M_2 E} \right) \cos^{-3} \phi \tag{5.6}$$

where σ_{ERDA} is the elastic recoil scattering cross section and E_{ERDA} is the energy of the recoiled scattered particle and ϕ is the angle between the beam axis and the recoil scattered direction.

In RBS/ERDA measurement, the following relational expression (5.7) holds regarding the detected counts.

$$Y_i = I_0 \frac{N_i \sigma_i}{A} \Omega_{\text{RBS/ERDA}} \tag{5.7}$$

where Y_i is the count of the element i obtained by RBS/ERDA, N_i is the number of nuclei, σ_i is the cross section of the element i, I_0 is the incident intensity, A is the irradiation area, and $\Omega_{\text{RBS/ERDA}}$ represents the solid angle cut by the detector.

By dividing Y_i of the element i for the RBS side by Y_j of ERDA side for the element j, following expression can be obtained:

$$\frac{Y_i}{Y_j} = \frac{N_i \sigma_i \Omega_i}{N_j \sigma_j \Omega_j} \tag{5.8}$$

In formula (5.8), by transforming $\frac{Y_i}{Y_j}$ to the composition ratio $\frac{N_j}{N_i}$ and setting $i \to \text{ERDA}, j \to \text{RBS}$, we obtain the following relational expression.

$$\frac{N_{\text{ERDA}}}{N_{\text{RBS}}} = \frac{Y_{\text{ERDA}}}{Y_{\text{RBS}}} \frac{\sigma_{\text{RBS}}}{\sigma_{\text{ERDA}}} \frac{\Omega_{\text{RBS}}}{\Omega_{\text{ERDA}}} \tag{5.9}$$

Therefore, the element composition ratio in the sample can be determined by using the counting ratio, the cross section ratio, and the solid angle ratio. In general, the counting ratio is obtained by the measurement, and the cross section ratio is picked up from the reference value or is determined by an actual measurement with a standard sample, and the solid angle ratio is obtained from the actual measurement with a standard sample. In this study, the solid angle ratio was evaluated by the fitting with analysis software SIMNRA [75].
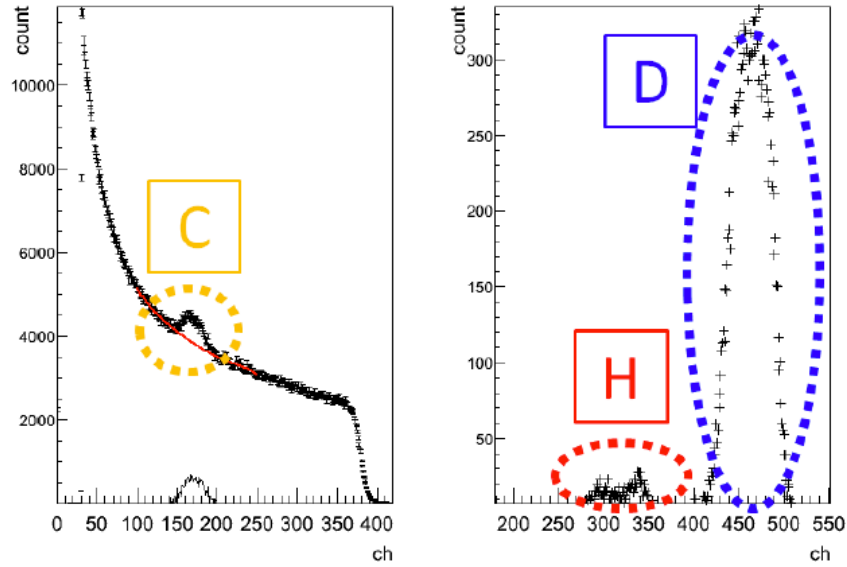
Figure.5.11 RBS/ERDA spectrum example, the image is cited from [67]. This is the case that deuterated DLC/Si with DLC film thickness of $\sim$ 100 nm is measured by RBS/ERDA. The left is RBS and the right is ERDA spectrum. The vertical axis is the count number, and the horizontal axis is the A/D converted value of the detector signal. In RBS, the carbon spectrum piles up on the silicon spectrum. In ERDA, separation of hydrogen and deuterium spectrum is realized.
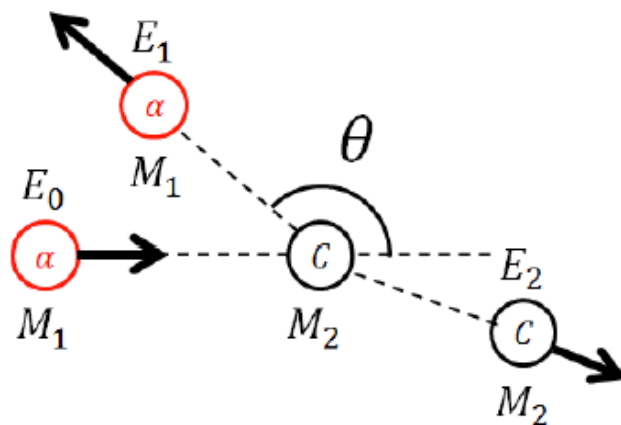
Figure.5.12 Schematic diagram of scattering of incident ions by target atoms, the image is cited from [67]
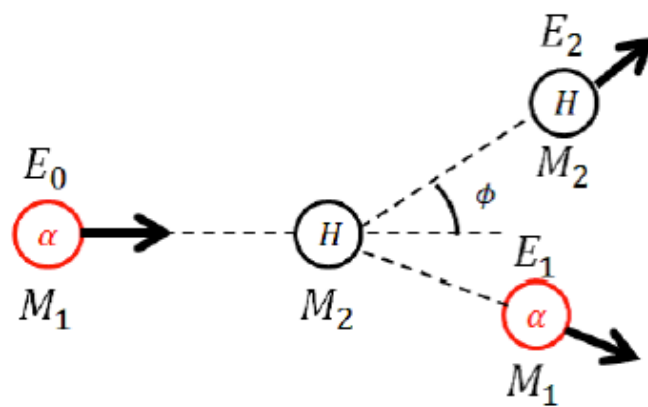
Figure.5.13　Schematic diagram of recoil of target atoms by incident ions, the image is cited from [67]

5.3.3 X-ray reflectometry

This section introduces the principle of X-ray reflectometry. In general, the refractive index of a material has an information of the electron density ρ_e, and X-ray reflectivity show an intrinsic pattern according to it. Therefore, we can extract the electron density from X-ray reflectivity distribution. Such surface analysis method is called X-ray reflectometry. The following relationship holds for electron density ρ_e and refractive index n:

$$n = 1 - \lambda^2 \rho_e r_e / 2\pi \tag{5.10}$$

where λ is the incident wavelength, ρ_e is the electron density, r_e is the electron classical radius.
For conciseness, the incident region is denoted as 0, the film region is denoted as 1, and the substrate region is denoted as 2, and the refractive index in each region is denoted as n_i hereafter. When X-rays strike different layers i, j as shown in Figure 5.14, the reflection amplitude r_{ij}^F at the interface between i and j is given by the following equation (5.11).
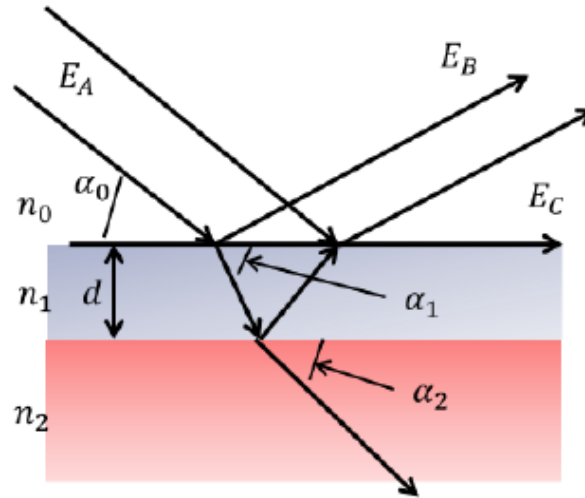
Figure.5.14 Schematic diagram of X-ray reflection at material interface, the image is cited from [67]. Reflection and refraction are illustrated when X-rays are incident on a sample on which a film of thickness d is formed on a substrate. Note that multiple reflections are not depicted here.

$$r_{ij}^F = \frac{n_i \sin \alpha_i - n_j \sin \alpha_j}{n_i \sin \alpha_i + n_j \sin \alpha_j} \tag{5.11}$$

Expression (5.11) represents only a single reflection. When taking into account the effect of multiple reflections, the generalized theoretical X-ray reflectivity R can be obtained as follows:

$$R = \exp\left(-q_z^2 \sigma^2\right) \frac{r_{01}^F + r_{12}^F \exp\left(i2k_1 d\right)}{1 + r_{01}^F r_{12}^F \exp\left(i2k_1 d\right)} \tag{5.12}$$

The formula (5.12) is a theoretical expression giving the X-ray reflectivity distribution that can be compared with the actual measurement.

As is clear from the expression (5.11), each term of the expression (5.12) depends on the incident angle. Therefore, by measuring the reflectivity of incident monochromatic X-rays while changing the incident angle θ, we can obtain an intrinsic distribution depending on the electron density of the sample. The value of the electron density ρ_e is analytically extracted by fitting the X-ray reflectivity distribution. This is the principle for X-ray reflectometry.

For reference, an example of X-ray reflectivity distribution is shown in Figure 5.15. In this figure, a
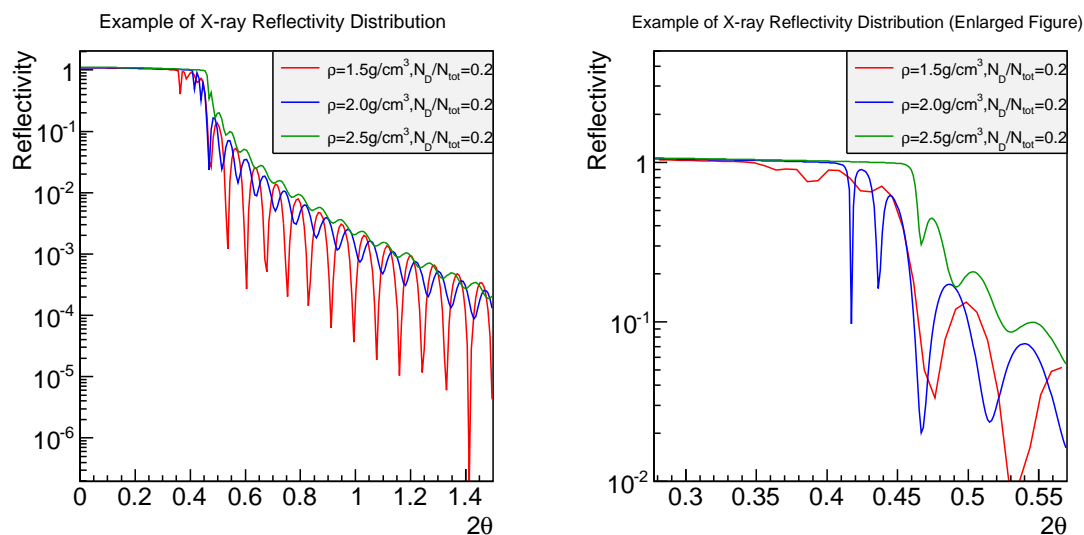
Figure.5.15 Example of X-ray reflectivity distribution. It is assumed that a sample consists a single layer of deuterated organic compound film and a silicon substrate. The film properties are: film thickness 100 nm, surface roughness 1 nm, deuterium ratio $N_D/N_{tot} = 0.2$, and density 1.5 g/cm^3 (red) or 2 g/cm^3 (blue) or 2.5 g/cm^3 (green).

sample is assumed to consist of a single layer of a deuterated organic compound and a silicon substrate (see Figure 5.15 for details). In Figure 5.15, the reflectivity becomes maximum up to a certain incident angle. This total reflection angle is called critical angle. Generally, the critical angle has an effect on film density, and film thickness has an effect on the oscillation period, and surface roughness has an influence on the attenuation on wide angle side. It is noted that an extra beat appears and node size does not become constant in the sample with the multilayer film.

5.4 Surface Analysis of Developed Material

This section reports on details of the results obtained from surface analyses of Neutron Reflectometry, RBS/ERDA, X-ray Reflectometry, GDOES, an electron microscope measurement, and surface roughness measurements.

5.4.1 Result of Neutron Reflectometry

In this study, neutron reflectivity was measured at J-PARC MLF BL16 Soft Interface Analyzer (SOFIA). Time-of-Flight method was used to calculate the reflectivity of incident neutrons (see Appendix.A for details). For reference, the actual Time-of-Flight distribution obtained in SOFIA is given in Figure 5.16. Schematic illustration and block diagram of the experimental setup of BL16 are given in Figure 5.17 and 5.18. The BL16 setup consists of three 5 mm thick B_4C slits, the stand for sample mounting, a two-dimensional detector, an A/D converter, and a PC network. The incident angle and irradiation area can be adjusted by controlling the relative position of the B_4C slit and the stand for sample mounting as shown in Figure 5.17 and 5.18. In this way, reflected beam or direct beam can be measured, and neutron reflectivity can be calculated by the ratio of reflection beam intensity (I_{ref} to direct beam intensity (I_0). R3292 (HAMAMATSU Co.Ltd) and ZnS/LiF scintillator (AST Co.Ltd) were used as the two-dimensional detector, and NeuNET, developed by KEK-KENS DAQ group, was used for A/D converter. NeuNET records wave height and Time-of-Flight (TOF) on receiving the signal transmitted from R3292&ZnS/LiF, and TOF gives us to information of neutron wavelength, λ.

The analysis procedure of BL16 measurement is as follows:

1. To measure the wavelength of direct beam intensity so that the sample is avoided from the beam injection.
2. To measure the wavelength of reflected beam intensity so that the sample is intersected to the incident beam.
3. The dependence of neutron reflectivity on wavelength is derived by dividing reflection beam intensity by direct beam intensity.
4. Assuming only the specular reflection, the wavelength is converted to the transfer wave number, $Q = \frac{4\pi}{\lambda} \sin(\theta)$, where λ is a wavelength of neutron and θ is a glancing angle of incident beam.
5. To fit the obtained neutron reflectivity, $|R(Q)|^2_{exp}$, with the formula (5.1).
6. To extract the Fermi potential from fitting result.

The fitting results of the neutron reflectivity are shown in from Figure 5.19 to Figure 5.24. Regarding IEM DLC sample, only the result of sample 97 in Table 5.5 is given because the number of IEM DLC samples is too many.

The analyzed result of the Fermi potential is listed in Table 5.5. In this study, measurement was conducted in two ways. one was with incident angle 0.5 degree and irradiation area 15×15 mm^2, another was with incident angle 0.3 degree and irradiation area 30×30 mm^2. Note that only 7 samples

for IEM DLC were summarized because the number of IEM DLC samples is too many. It is also noted that the IEM DLC sample 97, which achieved the best performance, was measured twice, as shown in Figure 5.24. The second measurement was performed two years after the initial measurement. In this measurement, three kinds of substrates, silicon, SUS304 and synthetic quartz were used, and it was guaranteed that the flatness was 20 μm or less even for the worst case.

In this measurement, a systematic error of Q exists due to the beam incident angle divergence. Such systematic error can be expressed as $|\frac{(\sin((\theta_i + d\theta_i) \times \frac{\pi}{180}) - \sin(\theta_i \times \frac{\pi}{180}))}{\sin(\theta_i \times \frac{\pi}{180})}|$, where $d\theta_i$ is deviation of incident angle. In this study, such error was evaluated from beam divergence measurement of direct beam. The result of direct beam divergence measurement is given to Figure 5.25. In the case of the incident angle of 0.5 degree & irradiation area 15×15 mm^2, the systematic error of Q was found to be 1.8%. On the other hand, in the case of the incident angle of 0.3 degree & the irradiation area of 30×30 mm^2, the systematic error of Q was turned out to be 2.8%. As a result, errors of the Fermi potential can be calculated by substituting errors of Q for the plot showed in Figure 5.9. Systematic errors of the Fermi potential are listed in Table 5.5.

The highest potential values obtained in neutron reflectivity measurement were 228 $\pm$ 13 neV for NiMo, 243 $\pm$ 8 neV for IEM DLC, 264 $\pm$ 14 neV for FAIPD DLC, and about 190 $\pm$ 11 neV for PBIID DLC, respectively. PSI succeed in fabricating NiMo of weight ratio 15 % and its Fermi potential was 210 $\pm$ 10 neV [64]. The result was consistent in that of our samples. The best Fermi potential of IEM DLC was comparable to that of nickel. The best Fermi potential of PBIID DLC was 193 neV, which was inferior to IEM DLC. But it is noted that PBIID DLC is possible to apply to the sidewall of a storage container. The value of 193 neV is quite high for the side wall materials. The best Fermi potential of FAIPD DLC was 264 neV, which is one of the highest values. This value is close to the result of laser ablation which PSI group fabricated.

According to Table 5.5, it was found that the Fermi potential of IEM DLC gets higher as the substrate voltage and the gas flow rate gets smaller, and does not depend on the temperature of the substrate. In addition, it was also found that PBIID DLC samples have almost same Fermi potential. The consideration on this phenomenon is given in chapter 5.4.5.
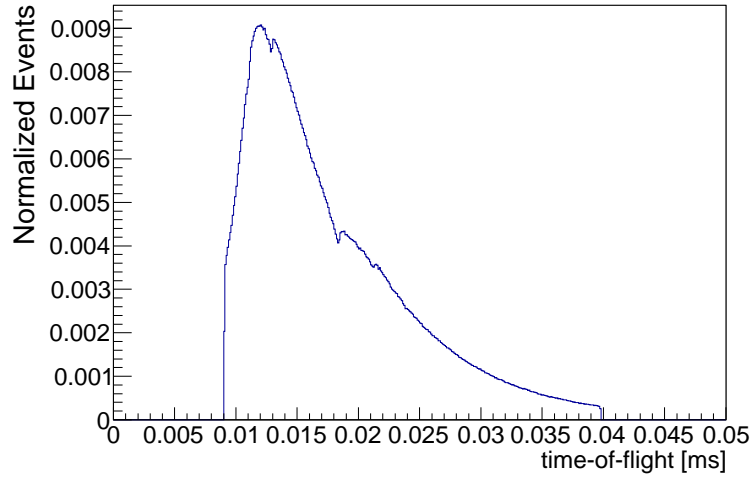
Figure.5.16   TOF distribution of beam supplied in J-PARC BL16 SOFIA. The horizontal axis is TOF (ms), and the vertical axis is count rate. Here, the TOF of direct beam measurement is given. Note that the total sum of the histogram is normalized to 1. The distance from the spallation point to the detector is ∼ 17.9 m
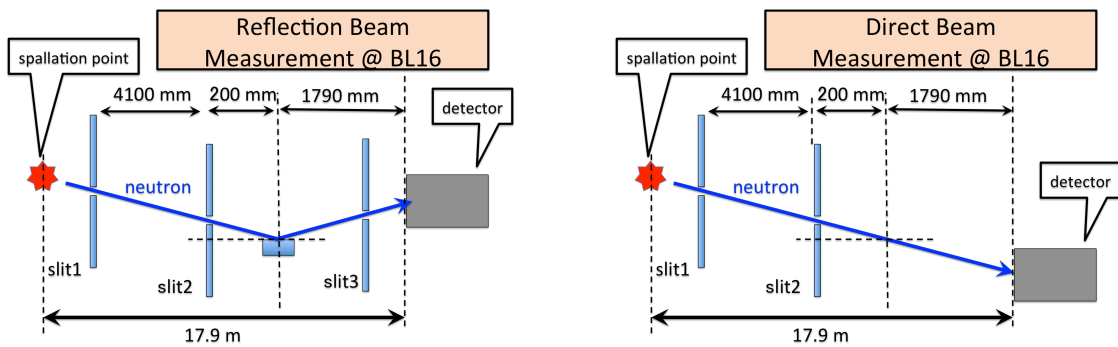
Figure.5.17   Schematic diagram of the setup in J-PARC BL16 SOFIA used for the reflection beam measurement (Left) and the direct beam measurement (right). Incident angle and beam irradiation area (called footprint) were determined by the arrangement of the slit1 and slit2. In the reflection beam measurement, only beam reflected at sample and passing through an angle of slit2 and slit3 was measured. On the other hand, In direct beam measurement, beam coming from slit2 was directly measured. Reflectivity of the sample was estimated from the count ratio obtained in two measurements.

94
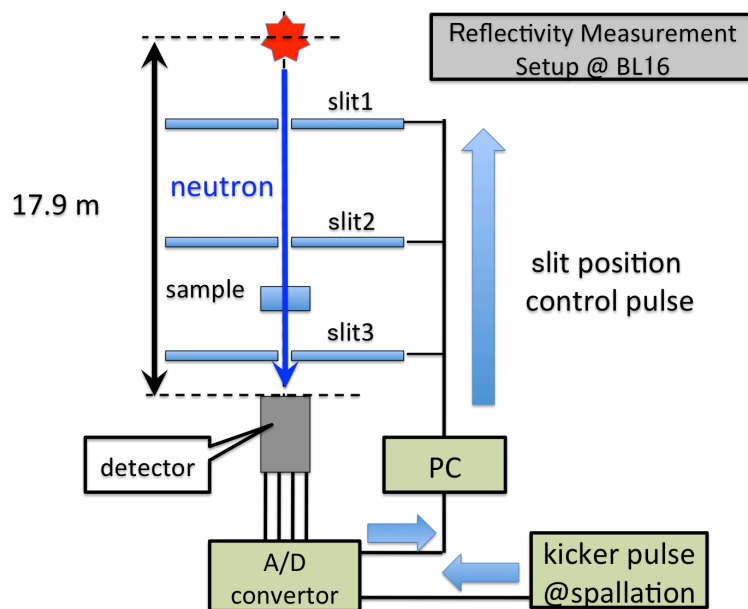
Figure.5.18 Block diagram of experimental setup in J-PARC BL16 SOFIA. PC can remotely control the relative positions of the slits 1 to 3, the sample and the detector. Detector signal is carried to NEUNET, it is A/D converted together with the kicker pulse signal, and it is saved in the PC.
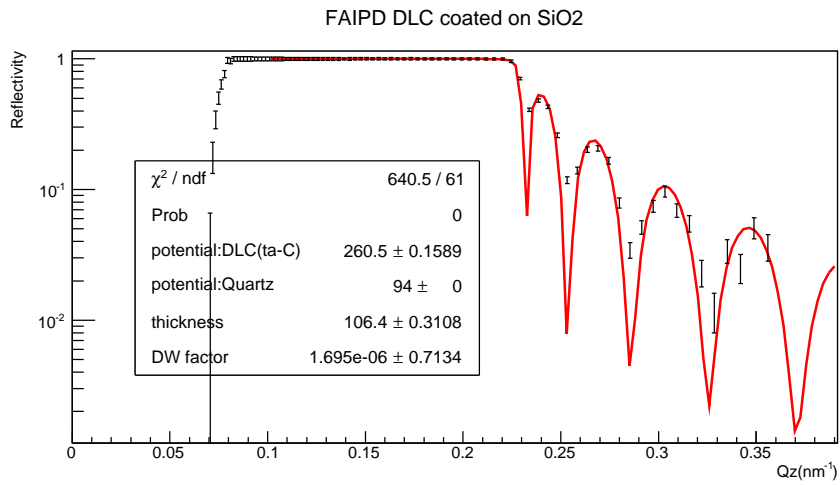
Figure.5.19   Reflectivity of FAIPD DLC/SiO$_2$. The incident angle is 0.3 degree. The vertical axis is the reflectivity of FAIPD DLC/SiO$_2$, and the horizontal axis is $Q_z = \frac{4\pi}{\lambda}$.
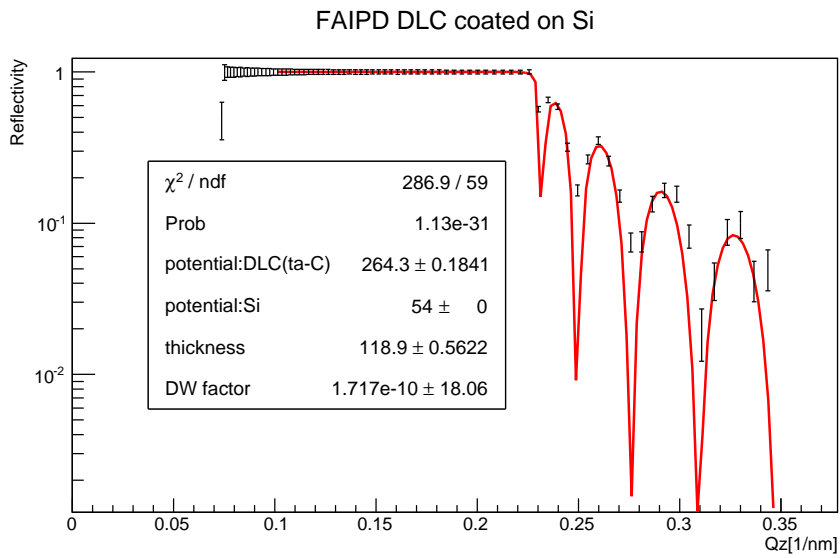
Figure.5.20   Reflectivity of FAIPD DLC/Si. The incident angle is 0.3 degree. The vertical axis is the reflectivity of FAIPD DLC/Si, and the horizontal axis is $Q_z = \frac{4\pi}{\lambda}$.
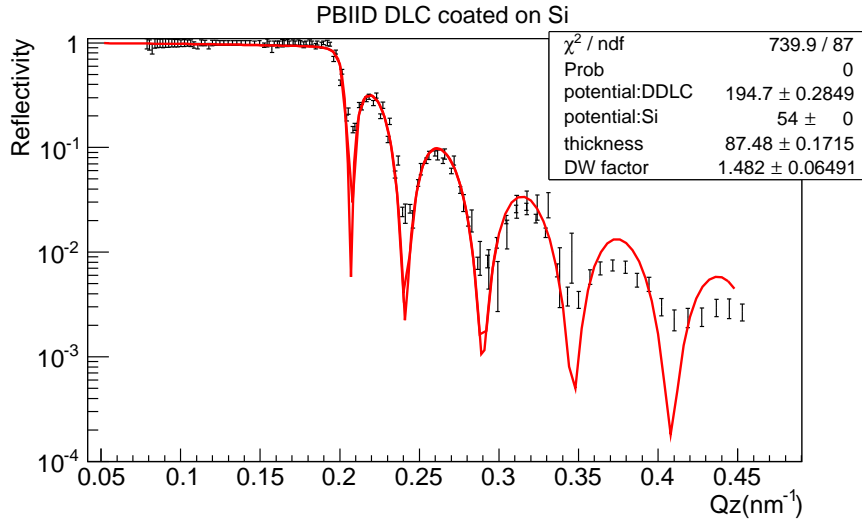
Figure.5.21 Reflectivity of PBIID DLC/Si. The incident angle is 0.3 degree. The vertical axis is the reflectivity of PBIID DLC/Si, and the horizontal axis is $Q_z = \frac{4\pi}{\lambda}$.
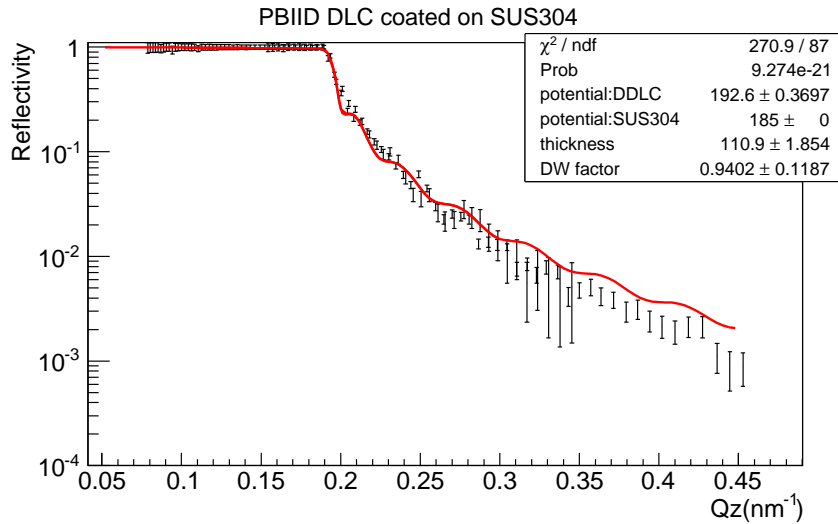
Figure.5.22 Reflectivity of PBIID DLC/SUS304. The incident angle is 0.3 degree. The vertical axis is the reflectance of PBIID DLC/SUS304, and the horizontal axis is $Q_z = \frac{4\pi}{\lambda}$.
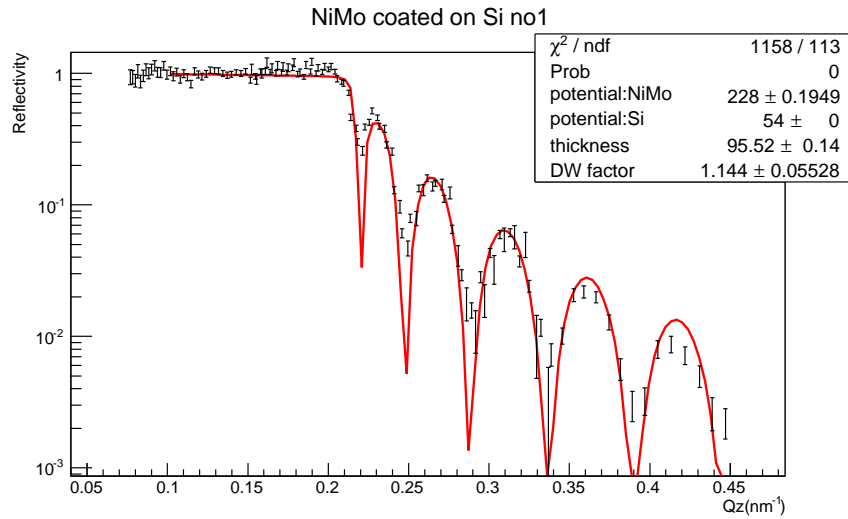
Figure.5.23 Reflectivity of NiMo/Si. The incident angle is 0.3 degree. The vertical axis is the reflectivity of NiMo/Si, and the horizontal axis is $Q_z = \frac{4\pi}{\lambda}$.
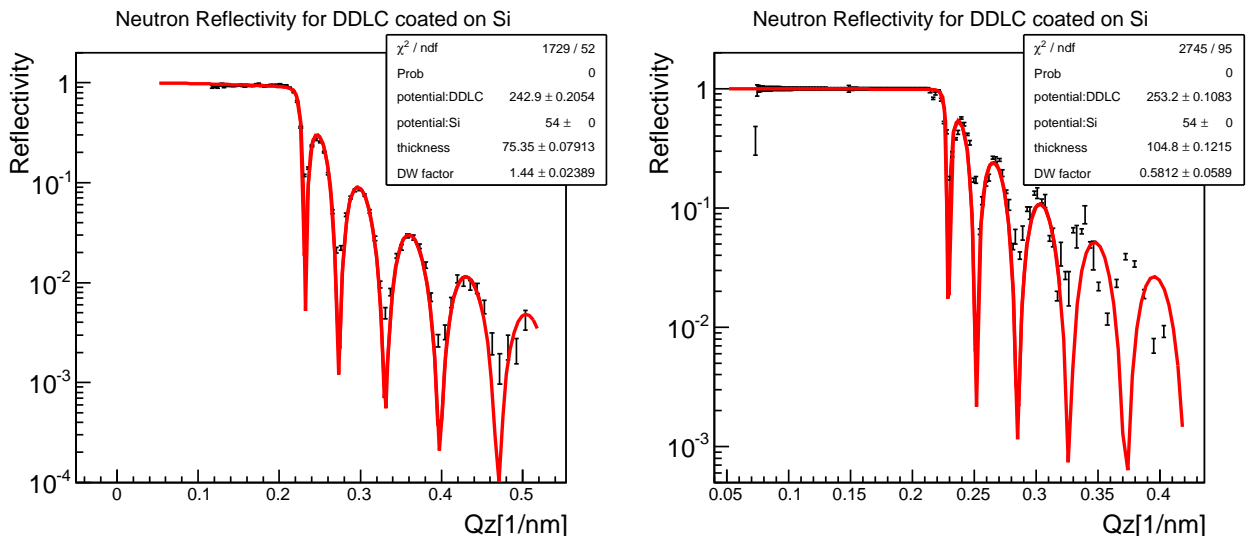
Figure.5.24 (Left) The first measurement result of IEM DLC/Si (incident angle 0.5 deg)(right) The second measurement result of ionized evaporation DLC/Si (incident angle 0.3 deg). The vertical axis is the reflectivity, and the horizontal axis is $Q_z = \frac{4\pi}{\lambda}$.

Method	Substrate	Potential	Condition	Others
IEM (sample12)	silicon	190 ± 7 neV	θ_i=0.5 deg	(3.0 kV ,3.1 sccm, middle)
IEM (sample17)	silicon	210 ± 8 neV	θ_i=0.5 deg	(1.5 kV ,3.1 sccm, middle)
IEM (sample31)	silicon	226 ± 8 neV	θ_i=0.5 deg	(0.5 kV ,3.1 sccm, middle)
IEM (sample65)	silicon	227 ± 9 neV	θ_i=0.5 deg	(0.5 kV ,6.2 sccm, middle)
IEM (sample97)	silicon	243 ± 8 neV	θ_i=0.5 deg	(0.5 kV ,0.6 sccm, middle)
IEM (sample72)	silicon	228 ± 9 neV	θ_i=0.5 deg	(0.5 kV ,3.1 sccm, low)
IEM (sample82)	silicon	219 ± 8 neV	θ_i=0.5 deg	(0.5 kV ,3.1 sccm, high)
IEM (sample97)	silicon	253 ± 13 neV	θ_i=0.3 deg	remeasure two years later
NiMo	silicon	228 ± 13 neV	θ_i=0.3 deg	average of three samples
FAIPD	synthetic quartz	260 ± 14 neV	θ_i=0.3 deg	–
FAIPD	silicon	264 ± 14 neV	θ_i=0.3 deg	–
PBIID (sample1)	silicon	193 ± 11 neV	θ_i=0.3 deg	–
PBIID (sample2)	silicon	192 ± 11 neV	θ_i=0.3 deg	–
PBIID (sample3)	silicon	195 ± 11 neV	θ_i=0.3 deg	–
PBIID (sample4)	silicon	190 ± 11 neV	θ_i=0.3 deg	–
PBIID (sample5)	silicon	190 ± 11 neV	θ_i=0.3 deg	–
PBIID (sample1)	SUS304	193 ± 11 neV	θ_i=0.3 deg	–
PBIID (sample2)	SUS304	192 ± 11 neV	θ_i=0.3 deg	–
PBIID (sample3)	SUS304	193 ± 11 neV	θ_i=0.3 deg	–
PBIID (sample4)	SUS304	194 ± 11 neV	θ_i=0.3 deg	–
PBIID (sample5)	SUS304	194 ± 11 neV	θ_i=0.3 deg	–

Table.5.5   Measurement result of the Fermi potential
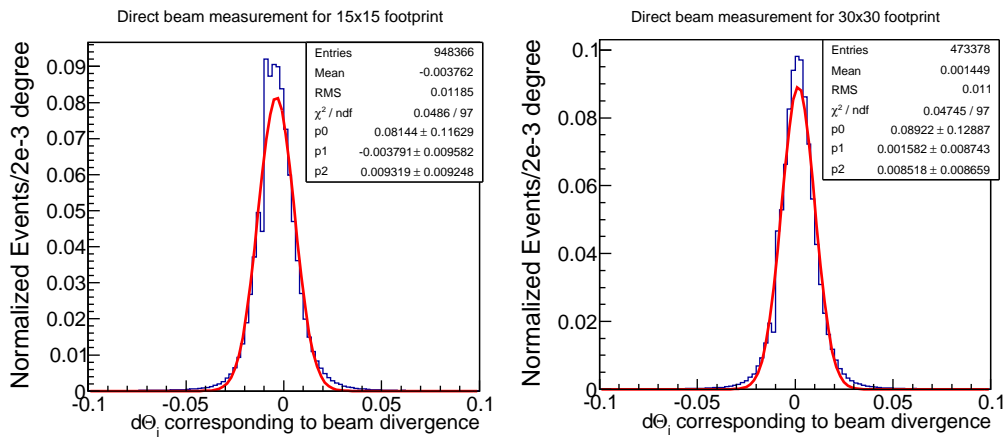
Figure.5.25 Fluctuation of incident angle due to beam divergence of J-PARC BL16. The horizontal axis represents the fluctuation of the incident angle of the direct beam, and the vertical axis represents the count. Since the distance between slit2 and detector is 2170 mm, we can convert the amount of the beam spread into the fluctuation of the incident angle. Note that total sum of the histogram is normalized to 1. The result fitted with Gaussian function is the red line, and p_2 in the figure means standard deviation. From this, we can extract the standard deviation of the fluctuation of the incident angle, $d\theta_i$.

5.4.2 The Result of RBS/ERDA

In this section, the result of RBS/ERDA measurement is described. In this study, IEM DLC and PBIID DLC that coat on silicon or SUS304 substrate were used for samples. RBS/ERDA measurement was performed at accelerator facility of Applied Accelerator Division, University of Tsukuba [76] in order to determine the composition ratio of DLC films. A schematic illustration of the experiment has been shown in Figure 5.10). In this measurement, Alpha particle was accelerated to 2.5 MeV by Tandetron accelerator system and was irradiated to the sample of $\sim 10 \times 10$ mm^2. A sample was installed in the chamber of 10^{-4} Pa and was tilted at 15 degree relative to the beam axis at the center. In this way, the number of particles scattered around was counted with two detectors. Regarding two detectors, one was silicon detector BU_014_050_100 of ORTEC ULTRA SERIES, and the other was the silicon detector PD 50_12_100 AM of CANBERRA PIPS. The former was installed in 150 degree for RBS measurement, while the other was installed in 30 degree for ERDA measurement. In addition, the Mylar film was installed before PD 50_12_100 AM to collimate the recoil particles except for hydrogen and deuterium. For data conversion, Wilkinson type ADC of 2201A of Labo Co. Ltd. was used. In this measurement, the counting rate of this measurement was $\sim 1,000$ counts per second and dead time was less than ~ 2 %.

In this study, the number of nuclei of hydrogen, deuterium, carbon and all elements are denoted as N_H, N_D, N_D, and N_tot. An outline of the analysis is given below:

1. Extract the quantities Y_H, Y_D and Y_C from measured data in the same manner as described in Figure 5.11

2. Substituting Y_H, Y_D and Y_C into the expression (5.9), the ratio of an element to carbon is calculated as $N_\mathrm{H}/N_\mathrm{C}$, $N_\mathrm{D}/N_\mathrm{C}$, $N_\mathrm{tot}/N_\mathrm{C} = N_\mathrm{C}/N_\mathrm{C} + N_\mathrm{H}/N_\mathrm{C} + N_\mathrm{D}/N_\mathrm{C}$

3. From the above, the composition ratio is easily derived as $N_\mathrm{H}/N_\mathrm{tot}, N_\mathrm{D}/N_\mathrm{tot}, N_\mathrm{C}/N_\mathrm{tot}$

In this analysis, the value in document [77] was used as the cross section of hydrogen and the value in document [78] was used as the cross section of deuterium. In addition, the solid angle ratio of RBS to ERDA was chosen to 2.7 (for IEM DLC measurement) or 6.1 (for PBIID DLC measurement), which correspond to the calibration data in such a way as described in chapter 5.3.2.

The composition ratio obtained by this analysis is shown in the Table 5.6. It was found that Hydrogen amount ratio of DLC/SUS304 was less than that of DLC/Si in the Table 5.6. For reference, the actual ERDA spectrum of sample 1 of PBIID DLC/Si and PBIID DLC/SUS304 are shown in Figure 5.26. In Figure 5.26, it was confirmed that there was the bump of hydrogen in the spectrum of DLC/Si, while it did not exist in the spectrum of DLC/SUS304. The reason why such difference appears is considered as follows:

1. In general, surface oxide causes hydrogen occlusion. In this study, a longer sputtering period is adopted in the case of DLC/SUS304 than in the case of DLC/Si. Thus, a surface oxidation of SUS304 was effectively removed than silicon, resulting in a reduction of hydrogen.

2. A large amount of hydrogen was contained in the silicon substrate. Indeed, the GDOES analysis shows hydrogen content in the silicon substrate (see chapter 5.4.5 for details).

UCN loss probability coefficient can be estimated by using an area density of hydrogen, A_H, as shown in formula (2.17). Generally, the area density of the number of atoms can be extracted from energy loss rate in the matter, dEdx. RBS/ERDA spectrum also has information of A_H because it consists of dEdx spectrum. So, in this study, the UCN loss probability coefficient of PBIID DLC/SUS304 (sample1) was evaluated from ERDA spectrum in the following procedure:

1. To regard PBIID DLC/SUS304 as containing no hydrogen because dEdx of hydrogen is too small.
2. To extract the area density of the total number of atoms, A_{tot}, from ERDA spectrum by using a function implemented in analysis software SIMNRA.
3. To multiply A_{tot} with actual hydrogen composition ratio 1.4 % and derive the area density of the number of hydrogen atoms as $A_H = 1.4\,\% \times A_{tot}$.
4. To calculate the UCN loss probability coefficient by assigning A_H with formula (2.17).

In this way, A_H and the UCN loss probability coefficient can be evaluated as 2.7×10^{16} atoms/cm2 and 1.5×10^{-4}, respectively.
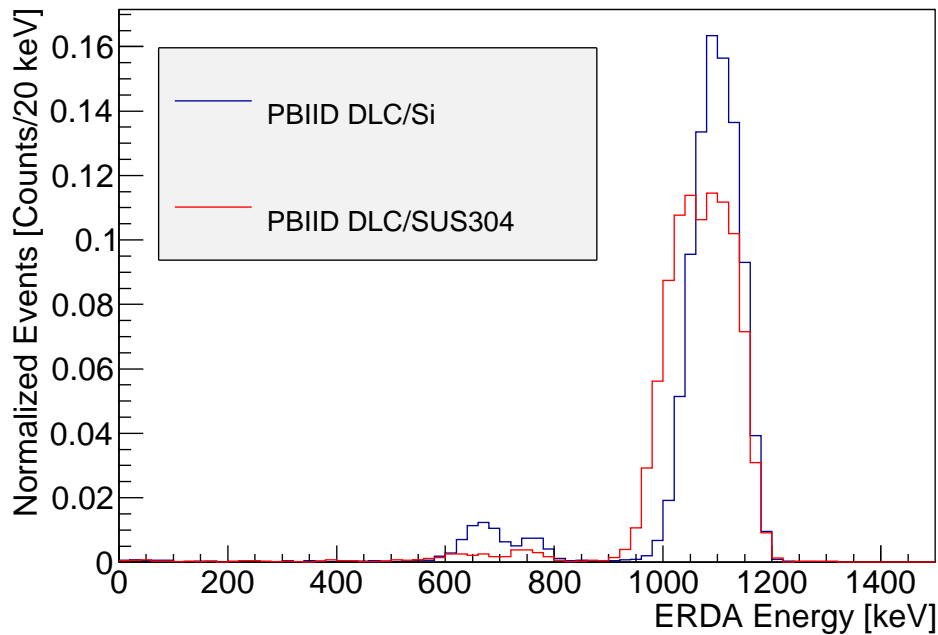
Figure.5.26   Comparison of ERDA spectra of DLC/Si and DLC/SUS304. The vertical axis is count and the horizontal axis is energy. Total sum is normalized to 1. The energy on the horizontal axis is derived by energy calibration of the value of A/D conversion.

No	method	substrate	$N_{\mathrm{H}}/N_{\mathrm{tot}}$	$N_{\mathrm{D}}/N_{\mathrm{tot}}$	$N_{\mathrm{C}}/N_{\mathrm{tot}}$
12	IEM	silicon (W10 mm×L10 mm× T2 mm)	0.035 ± 0.002	0.31 ± 0.02	0.66 ± 0.02
17	IEM	silicon (W10 mm×L10 mm×T2 mm)	0.024 ± 0.002	0.29 ± 0.01	0.69 ± 0.01
31	IEM	silicon (W10 mm×L10 mm×T2 mm)	0.027 ± 0.002	0.33 ± 0.01	0.65 ± 0.01
65	IEM	silicon (W10 mm×L10 mm×T2 mm)	0.015 ± 0.001	0.35 ± 0.01	0.64 ± 0.01
72	IEM	silicon (W10 mm×L10 mm×T2 mm)	0.024 ± 0.002	0.39 ± 0.02	0.59 ± 0.02
82	IEM	silicon (W10 mm×L10 mm×T2 mm)	–	–	–
97	IEM	silicon (W10 mm×L10 mm×T2 mm)	0.038 ± 0.005	0.31 ± 0.02	0.65 ± 0.02
1	PBIID	silicon (W10 mm×L10 mm×T2 mm)	0.037 ± 0.002	0.23 ± 0.01	0.73 ± 0.01
2	PBIID	silicon (W10 mm×L10 mm×T2 mm)	0.028 ± 0.001	0.22 ± 0.01	0.75 ± 0.01
3	PBIID	silicon (W10 mm×L10 mm×T2 mm)	0.037 ± 0.003	0.29 ± 0.02	0.68 ± 0.01
4	PBIID	silicon (W10 mm×L10 mm×T2 mm)	0.033 ± 0.002	0.22 ± 0.01	0.74 ± 0.01
5	PBIID	silicon (W10 mm×L10 mm×T2 mm)	0.026 ± 0.001	0.25 ± 0.01	0.72 ± 0.01
1	PBIID	silicon (W10 mm×L10 mm×T0.7 mm)	0.035 ± 0.002	0.22 ± 0.01	0.75 ± 0.01
2	PBIID	silicon (W10 mm×L10 mm×T0.7 mm)	0.031 ± 0.002	0.23 ± 0.01	0.74 ± 0.01
3	PBIID	silicon (W10 mm×L10 mm×T0.7 mm)	0.034 ± 0.003	0.26 ± 0.02	0.70 ± 0.01
4	PBIID	silicon (W10 mm×L10 mm×T0.7 mm)	0.034 ± 0.002	0.22 ± 0.01	0.74 ± 0.01
1	PBIID	SUS304 (W10 mm×L10 mm×T1 mm)	0.014 ± 0.001	0.23 ± 0.02	0.75 ± 0.02
2	PBIID	SUS304 (W10 mm×L10 mm×T1 mm)	0.013 ± 0.001	0.21 ± 0.02	0.77 ± 0.02
3	PBIID	SUS304 (W10 mm×L10 mm×T1 mm)	0.016 ± 0.003	0.23 ± 0.04	0.75 ± 0.03
4	PBIID	SUS304 (W10 mm×L10 mm×T1 mm)	0.012 ± 0.001	0.21 ± 0.02	0.77 ± 0.01
5	PBIID	SUS304 (W10 mm×L10 mm×T1 mm)	0.015 ± 0.002	0.18 ± 0.02	0.80 ± 0.01

Table.5.6   The composition ratio of DLC evaluated by RBS/ERDA

No	method	substrate	ρ_e
12	IEM	silicon(W10 mm×L10 mm×T2 mm)	$(5.73 \pm 0.02) \times 10^{23}$
17	IEM	silicon(W10 mm×L10 mm×T2 mm)	$(6.05 \pm 0.02) \times 10^{23}$
31	IEM	silicon(W10 mm×L10 mm×T2 mm)	$(6.25 \pm 0.03) \times 10^{23}$
65	IEM	silicon(W10 mm×L10 mm×T2 mm)	$(6.13 \pm 0.02) \times 10^{23}$
72	IEM	silicon(W10 mm×L10 mm×T2 mm)	$(6.11 \pm 0.02) \times 10^{23}$
82	IEM	silicon(W10 mm×L10 mm×T2 mm)	–
97	IEM	silicon(W10 mm×L10 mm×T2 mm)	$(6.48 \pm 0.03) \times 10^{23}$

Table.5.7   Example data of total electron density determined by X-ray reflectometry

5.4.3   The Result of X-ray Reflectometry

In this section, the result of X-ray Reflectometry is described. X-ray Reflectometry enables us to get the information about electron density from X-ray reflectivity distribution. In this study, IEM DLC and PBIID DLC were used for samples. In this study, smart Lab (Rigaku Co. Ltd.) [79] was used for X-ray reflectometry, which is a machine that can automatically conduct all functions necessary for X-ray reflectometry such as X-ray emission, adjustment of angle, inclination of sample, and so on. In this measurement, Cu K_α radiation was chosen as an incident X-ray beam. The beam intensity was measured with a photomultiplier, and the beam divergence was reduced with Ge(220) single crystal and a slit. X-ray was irradiated to sample of Φ 76 mm while changing an incident angle to obtain X-ray reflectivity spectrum.

The reflectivity distribution of IEM DLC is given in Figure 5.27. The horizontal axis is the incident angle of the X-ray, and the vertical axis is the X-ray reflectivity. In each panel, the measurement data for other bias voltage conditions from 0.1 kV to 3 kV used in the IEM DLC film formation is plotted. On the other hand, the X-ray reflectivity distribution of PBIID DLC is shown in Figure 5.28. In each panel, the measurement data for other film formation conditions listed in Table 5.4 is plotted.

For IEM DLC, the critical angle and the period of vibration were clearly shown, and the X-ray reflectivity distribution can be easily fitted by the theoretical expression (5.12). On the other hand, for PBIID DLC, not only short-period vibrations but also long-period vibrations were mixed. The spectrum was quite different from the distribution as shown in Figure 5.15 predicted from the theoretical formula (5.12). Therefore, it was not possible to fit the X-ray reflectivity distribution of PBIID DLC successfully. Such a strange behavior that PBIID DLC show is discussed in chapter 5.4.5.

In this measurement, carbon was considered to be especially dominant for X-ray reflection. In this analysis, DLC was therefore regarded as composed of only carbon, and the total electron density was extracted by fitting with the theoretical expression (5.12). The obtained electron density is summarized in Table 5.7.
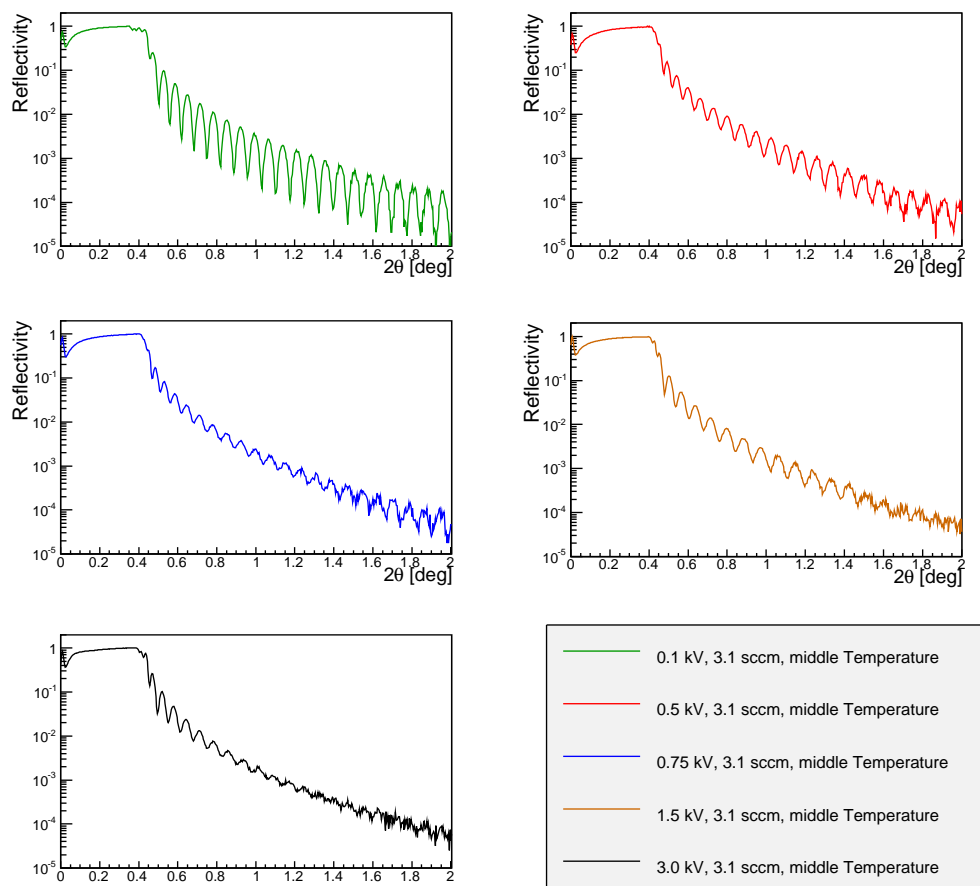
Figure.5.27   Example of X-ray reflectivity distribution of IEM DLC
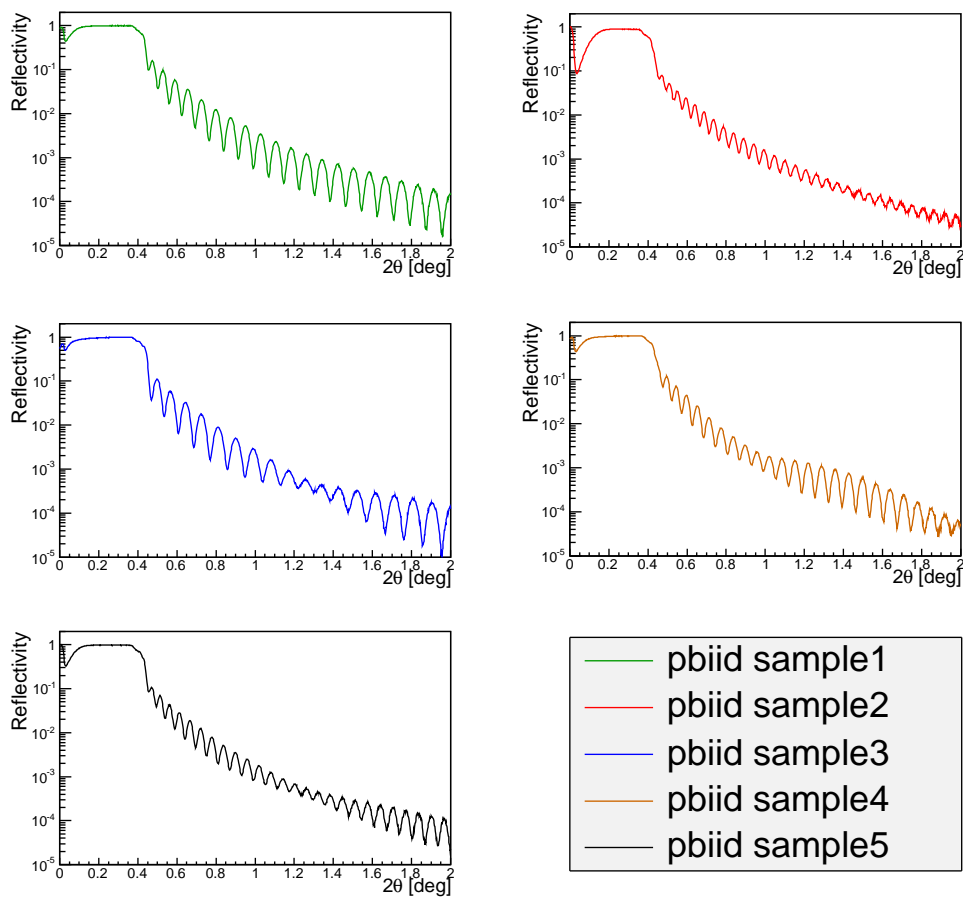
Figure.5.28   X-ray reflectivity distribution of PBIID DLC

5.4.4 Reflectivity consistency

In this section, the analysis result of the Fermi potential calculated by the result of X-ray reflectometry and RBS/ERDA is described, and the result obtained in this way is compared to that of neutron reflectometry. For deuterated DLC, the Fermi potential is expressed as follows:

$$V_F = b_C N_C + b_D N_D + b_H N_H \tag{5.13}$$

where b is coherent length and N is the density of atomic nucleus.

In addition, the density of atomic nucleus for each element can be derived using following equation:

$$Z_i N_i = \frac{Z_i N_i}{\sum_{k=0}^{k_{max}} Z_k N_k} \rho_e \tag{5.14}$$

where i is the identifier of each element, and N_i is the nuclear density of the element i, Z_i is the atomic number, and k_{max} is the number of elements, and ρ_e is the electron density.

The Fermi potential of formula (5.13) can be calculated by ρ_e obtained from X-ray reflectometry and N_H/N_C and N_D/N_C obtained from the RBS/ERDA. The comparison result of the Fermi potential obtained from two different ways was given in Figure 5.29. The vertical axis is the Fermi potential obtained from the neutron Reflectometry, the horizontal axis is the potential calculated with the expression (5.13) and (5.14). Although the error is fairly large, it can be seen that both results are consistent in the range of about 8%. The error is thought to be caused from the uncertainty of the cross section used in RBS/ERDA measurement.

5.4.5 Consideration of Unnaturalness of PBIID DLC

Regarding IEM DLC, it is confirmed that the film formation condition has a strong effect on DLC film density and composition ratio, resulting in variation of the Fermi potential (see Table 5.5 and Table 5.6). However, regarding PBIID DLC, all of PBIID DLC show the same potential irrespective of their film formation condition. Such an unnaturalness is thought to be due to the film formation process of PBIID. In PBIID, a mixing layer occurs between DLC film and a substrate due to the ion implantation process illustrated in Figure 5.5, which gives PBIID sample a property looks like DLC/SiC/Si rather than DLC/Si. Actually, X-ray reflectivity spectra of Figure 5.28 shows the anticipated behavior for a multilayered sample such that short-period and long-period oscillations mix. In addition, it is confirmed that the following two measurements indicate a mixing layer.

GODES

GODES measurement was performed with an instrument manufactured by Horiba corporation in order to investigate the depth profile. GDOES is one of the methods to determine the composition ratio in the depth direction. It is possible to evaluate the composition ratio by sputtering sample while monitoring the light intensity emitted from the scattered particles. It is noted that hydrogen and deuterium cannot be distinguished because of the same emission spectra. The actual obtained
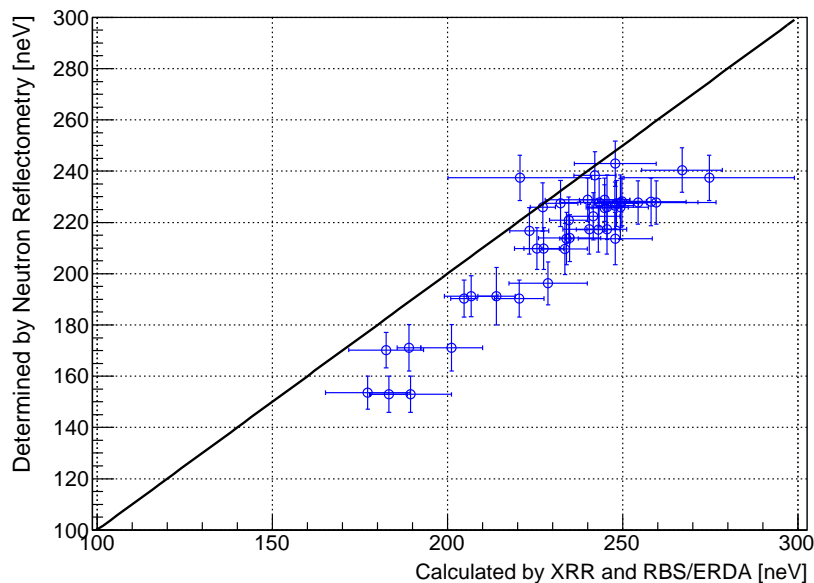
Figure.5.29 Comparison result of the Fermi potential determined by two methods. The vertical axis shows the value of the Fermi potential obtained from the neutron reflectivity measurement, and the horizontal axis shows the value of the potential calculated by the measured value of the RBS/ERDA and XRR. Both of them agreed with relative accuracy of about 8%.

spectrum is shown in Figure 5.30. Signal intensity of H and C continue even after sputtering reaches the silicon substrate. This fact indicates that a non-negligible amount of deuterium is mixed in the silicon substrate.

Transmission Electron Microscope

Transmission electron microscope measurement was conducted with JEM-4010 (JEOL Ltd.). The specimen was cut out from the original sample and the vicinity of the surface was polished well. In this way, the intensity distribution of transmitted electrons was investigated when scanning the side with an electron beam. The element composition and the nuclear density are reflected in the contrast of the obtained image. The result is shown in Figure 5.31. It is noted that, in this measurement, tungsten was deposited on the top layer to avoid radiation effect from gallium beams used on cutting out the specimen. In Figure 5.31, it is confirmed that there is a mixing layer between the silicon substrate and the DLC film layer. Further, it seems that DLC layer is divided into two layers. This indicates that film formation growth may be different in the process.

5.4.6   The Result of Measurement of Surface Roughness

In this section, the result of the surface roughness measurement is described. Because the surface roughness has a crucial effect on non-specular reflection probability, it was evaluated in this study. In the measurement, two different apparatuses were used. One is an atomic force microscope L-trace IIA
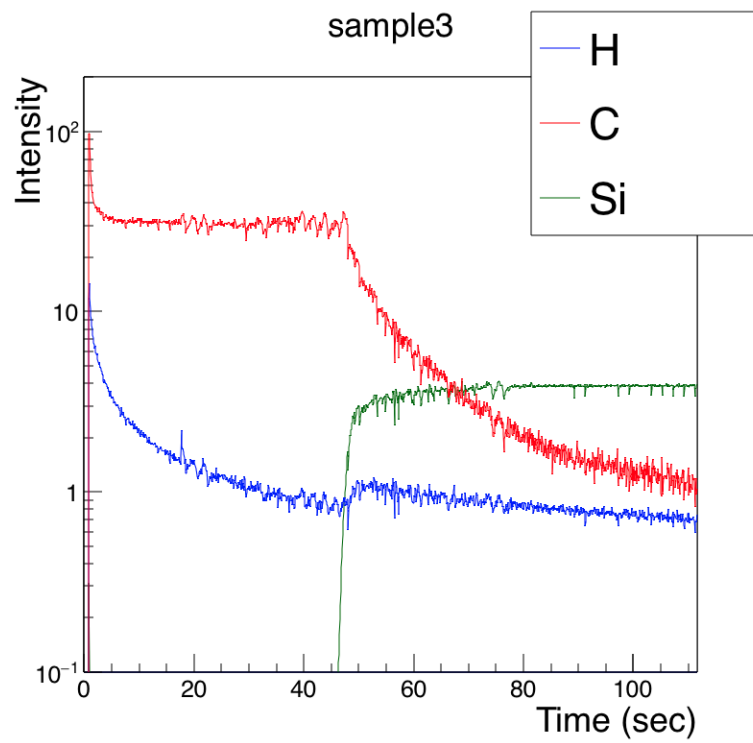
Figure.5.30   Example of rf-GDOES spectrum of PBIID DLC/Si
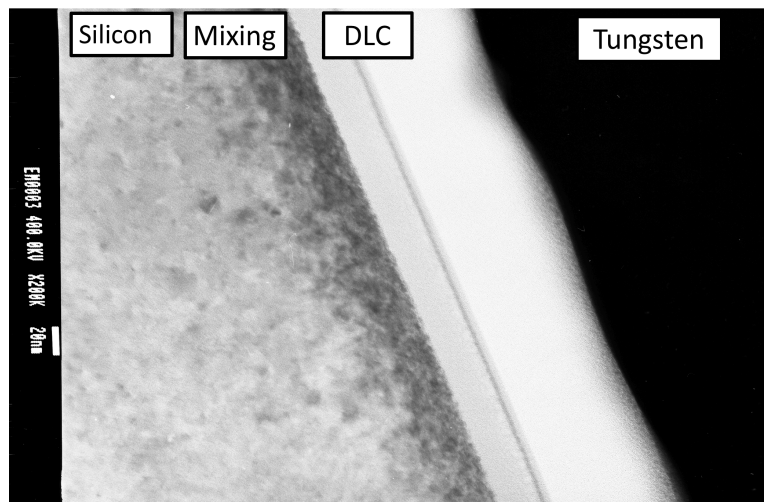
Figure.5.31   Example of lateral scanning of PBIID DLC/Si by transmission electron microscope

(Hitachi High-Technologies Corporation), and the other is a surface topography measurement instrument P-7 Stylus Profiler, serial number 7300163,(KLA Tencor Corporation). L-trace IIA and P-7 Stylus Profiler use techniques based on Scanning probe microscope (SPM). In general, SPM refers a technique to obtain surface profiles by scanning a specimen with a physical probe.

L-trace IIA uses Dynamic Force Mode (DFM) technique to determine the surface shape profile. In general, the probe feels the force depending on the distance from the sample surface to it due to inter-molecular force and air attenuation. Thereby, if the probe is vibrated while approaching to the sample surface, the vibration amplitude changes according to the distance. Therefore, the sample surface profile can be determined by scanning with the probe so that the vibration amplitude is maintained constant. According to the catalog, the vertical resolution of L-trace IIA is 0.05 nm. In this study, SI-DF 40P with width of 30 nm was used for the probe.

In P-7 Stylus Profiler system, surface roughness is determined by LVDC sensor. LVDC sensor can transform linear displacement into differential capacitive change. Therefore, the probe movement up and down according to surface roughness can be estimated by capacitance change of LVDC sensor. According to the catalog, the vertical resolution of P-7 Stylus Profiler is 0.4 nm for 1 σ. In this study, a diamond chip with a curvature of about 2 μm was used as the probe.

The results of surface roughness measurement of IEM DLC, FAIPD DLC, and PBIID DLC are given in Table 5.8. In this study, Φ 76 mm and 2 mm thick silicon (Furuuchi Chemistry Corporation) was used for the silicon substrate, of which surface roughness was evaluated to be 0.3 nm RMS by AFM (DI-3100, Veeco Instruments Inc.) [31]. In addition, 25.4 mm $\times$ 76.2 mm and 1 mm thick synthetic quartz (VIOSIL-SQ (W grade), Shin-Etsu Chemical Co., Ltd) was used for the quartz substrate. The surface roughness of synthetic quartz was measured by L-trace IIA, which was found to be 0.3 nm RMS. Furthermore, 50 mm $\times$ 80 mm and 5 mm thick SUS304 substrate made by Sanko Seiki Manufacturing Corporation was used. The surface roughness of SUS304 was measured by P-7 Stylus Profiler, which was found to be 1.8 nm RMS. Regarding samples, the surface roughness of DLC has been actually measured. As a result, it was confirmed that $\sim$ 3 angstrom for IEM DLC, $\sim$ 4.9 angstrom RMS for FAIPD DLC and 1 $\sim$ 2 nm RMS for PBIID DLC. The surface roughness of PBIID DLC was not good compared to the other. This is probably because PBIID DLC was inherited from the surface roughness of the SUS304 substrate.

5.5 Short Summary

1. NiMo of molybdenum weight ratio of 15% was fabricated with binary vapor deposition method. As a result, a film with the weight ratio of 13.6% can be obtained so far, which was evaluated by the crystal oscillator. By the neutron reflectivity measurement of J-PARC MLF BL16, 228 neV $\pm$ 13 neV was obtained as the Fermi potential (see Table 5.5 and Figure 5.23). The potential value was consistent with that fabricated by the conventional sputter method by PSI.

2. DLC was fabricated with ionization evaporation deposition method. More than hundred types of

method	substrate	instrument	condition	roughness [nm]
No Film	silicon	—	—	0.30 ± 0.01 RMS [31]
IEM (sample97)	silicon	L-TraceIIA	measure 10μm×10μm	0.30 ± 0.01 RMS
FAIPD	quartz	L-TraceIIA	measure 10μm×10μm	0.36 ± 0.01 RMS
FAIPD	quartz	L-TraceIIA	measure 10μm×10μm	0.62 ± 0.01 RMS
No Film	quartz	L-TraceIIA	measure 10μm×10μm	0.32 ± 0.01 RMS
No Film	quartz	L-TraceIIA	measure 10μm×10μm	0.28 ± 0.01 RMS
PBIID (sample1)	silicon	P-7 Stylus Profiler	Force: 2mg, scan: 0.2 mm	1.1 ± 0.4 RMS
PBIID (sample2)	silicon	P-7 Stylus Profiler	Force: 2mg, scan: 0.2 mm	1.2 ± 0.4 RMS
PBIID (sample3)	silicon	P-7 Stylus Profiler	Force: 2mg, scan: 0.2 mm	1.8 ± 0.4 RMS
PBIID (sample4)	silicon	P-7 Stylus Profiler	Force: 2mg, scan: 0.2 mm	1.9 ± 0.4 RMS
PBIID (sample5)	silicon	P-7 Stylus Profiler	Force: 2mg, scan: 0.2 mm	1.0 ± 0.4 RMS
PBIID (sample1)	SUS304	P-7 Stylus Profiler	Force: 2mg, scan: 0.2 mm	1.8 ± 0.4 RMS
PBIID (sample2)	SUS304	P-7 Stylus Profiler	Force: 2mg, scan: 0.2 mm	1.5 ± 0.4 RMS
PBIID (sample3)	SUS304	P-7 Stylus Profiler	Force: 2mg, scan: 0.2 mm	1.4 ± 0.4 RMS
PBIID (sample4)	SUS304	P-7 Stylus Profiler	Force: 2mg, scan: 0.2 mm	1.4 ± 0.4 RMS
PBIID (sample5)	SUS304	P-7 Stylus Profiler	Force: 2mg, scan: 0.2 mm	2.5 ± 0.4 RMS
No Film	SUS304	P-7 Stylus Profiler	Force: 2mg, scan: 0.2 mm	1.7 ± 0.4 RMS
No Film	SUS304	P-7 Stylus Profiler	Force: 2mg, scan: 0.2 mm	2.2 ± 0.4 RMS
No Film	SUS304	P-7 Stylus Profiler	Force: 2mg, scan: 0.2 mm	1.5 ± 0.4 RMS
No Film	SUS304	P-7 Stylus Profiler	Force: 2mg, scan: 0.2 mm	1.8 ± 0.4 RMS

Table.5.8　Measurement result of surface roughness.

DLC mirrors such as listed in Table 5.3 have been tested so far. Neutron reflectivity measurement of J-PARC MLF BL16 revealed that the sample having highest Fermi potential was 243 ± 8 neV, which is as high as the Fermi potential of nickel (Table 5.5 and Figure 5.24). On the other hand, by combining the results of X-ray reflectivity and RBS/ERDA measurements, the Fermi potential was evaluated to be systematically higher by ∼ 8% as shown in Figure 5.29. In addition, the surface roughness measured by AFM was evaluated to be 0.30 ± 0.01 nm RMS as listed in Table 5.8.

3. DLC was fabricated with Plasma Based Ion Implantation Deposition (PBIID) method. PBIID is known as a film formation method suitable for three-dimensional coating on the inner surface and for large area coating. Five samples listed in Table 5.4 have been tested so far. Neutron reflectivity measurement at J-PARC MLF BL16 showed that the potentials of PBIID DLC were aligned to ∼ 193 ± 11 neV irrespective of film formation conditions (Table 5.5 and Figure 5.21). Surface roughness was evaluated to be 1 ∼ 2 nm RMS using a high precision step meter as listed in Table 5.8. Surface roughness was not so good. That is probably because it inherited the roughness of SUS304 substrate of 1 ∼ 2 nm RMS.

4. DLC was fabricated with FAIPD method. In this study, the AC-X apparatus of Onward Co. Ltd was used for fabrication of FAIPD DLC. Neutron reflectivity measurement at J-PARC MLF BL16 indicated that the potential of 264 ± 14 neV was achieved (Table 5.5 and Figure 5.19) and Figure 5.20. In addition, the average value of the surface roughness measured by AFM was evaluated to be 0.49 ± 1 nm RMS as listed in Table 5.8.

Chapter 6

UCN Storage Experiment at J-PARC MLF

In this chapter, the result of UCN storage experiment enables us to directly determine UCN loss probability coefficient are described. UCN loss probability is one of the important parameters having a strong effect on the statistical precision of the neutron EDM measurement. For example, assuming gravity and non-specular reflection are negligible, the number of UCNs with the speed $\vec{v} = (v, 0, 0)$ confined in the box of one side length L will change in time according to the following expression (6.1).

$$N(t) = \exp\left(-\frac{t}{\frac{L}{v}\mu(v)}\right) = \exp\left(-\frac{t}{\tau}\right) \tag{6.1}$$

where $\mu(v)$ denotes the UCN loss probability depending on velocity.

Because the best statistical precision becomes inversely proportional to 2τ(the expressions (6.1) and (3.7) and 3.9), UCN loss probability μ has a serious effect on the neutron EDM measurement. Therefore, it is so much important to directly measure UCN loss probability by UCN storage experiment.

Generally, the UCN loss probability can be indicated by the loss probability coefficient, η (see the expression (2.6) and the expression (2.7)). In this study, η of NiMo or PBIID DLC were determined by measuring how the number of UCNs change when stored in the SUS316 storage bottle covered partially with NiMo or DLC. This experiment was performed at J-PARC MLF BL05 May and June 2016. In J-PARC MLF BL05, ultracold neutron can be used by using Doppler Shifter.

This chapter is organized as follows. In the first section, the experimental environment of J-PARC MLF BL05 is described. Next, the velocity distribution of UCNs emitted from Doppler Shifter in J-PARC MLF BL05 is explained. Next, the UCN storage experiment performed in J-PARC MLF BL05 are summarized. Finally, the results of UCN storage experiment and details of the analysis are described.

6.1 Material and Life Science Facility at J-PARC

Japan Proton Accelerator Research Complex (J-PARC) is an experimental facility located in Tokai, Ibaraki, Japan. It consists of three different accelerators LINAC, Rapid Cycling Synchrotron (RCS), and Main Ring (MR). The world's highest intensity pulsed proton beam of kW class is supplied to the beam line for experiments. In J-PARC, The protons emitted from the ion source are first accelerated to 181 MeV with LINAC of $\sim$330 m. Although the beam of LINAC has not been used for experiments

yet at the present time, it will be used in the future for the test of Accelerator Driven Reactor System (ADSR) and J-PARC P33 experiment. Beams that are not used in LINAC are sent to RCS with a diameter of 350 m and accelerated to 3 GeV, and then sent to the Material Life Science Laboratory (MLF) or sent to MR with a diameter of 1.6 km to be accelerated to 30 GeV.

The proton beams of RCS produce a nuclear spallation reaction in the liquid mercury target at the center of the Materials and Life Science Experimental Facility (MLF) and produce fast neutrons. The current beam supply period in RCS is almost 25 Hz. The H_2 moderator (20 K, 1.5 Pa) is arranged around the mercury target, and the fast neutrons are cooled to the room temperature while colliding with H_2, and then is emitted from the moderator surface. These are delivered to 23 beam lines for users of MLF.

In an experiment at MLF, users always receive two signals from facility, kicker pulse (kp) and timing pulse (tp). Both kp and tp are synchronized with the timing of proton beam incidence. By using the information on the timing of the proton beam incidence, the neutron velocity can be determined by the time-of-flight (TOF) method (see Appendix.A for details). Because only the signal of kp is interrupted when the proton beam delivery stops, users can know whether the entire MLF beam delivery system is down or when the beam is directed to MR.

6.2   The Experimental Apparatus at BL05

In this section, the experimental environment of J-PARC MLF BL05 is described. In BL05, neutron beam coming from the mercury target is divided into three branches: low divergence beam branch, a non-polarized beam branch, and a polarized beam branch. Neither branch has the ability to supply UCNs. Thus, UCNs are produced by decelerating neutrons emitted from a non-polarized beam branch by using Doppler Shifter. Apparatuses related to UCN storage experiment are transportation, m3.5 monochromatic mirror, focus guide, Doppler Shifter, UCN Storage System. All the equipments except UCN Storage System are arranged on the line of the unpolarized beam branch, while UCN Storage System is arranged perpendicular to unpolarized beam branch. For understanding the relative position of experimental setup, a cross-section diagram of the unpolarized beam branch of J-PARC MLF BL05 is given in Figure 6.1, and the schematic diagram of the UCN Storage System is given in Figure 6.2.

The five main apparatuses mentioned above are described below.
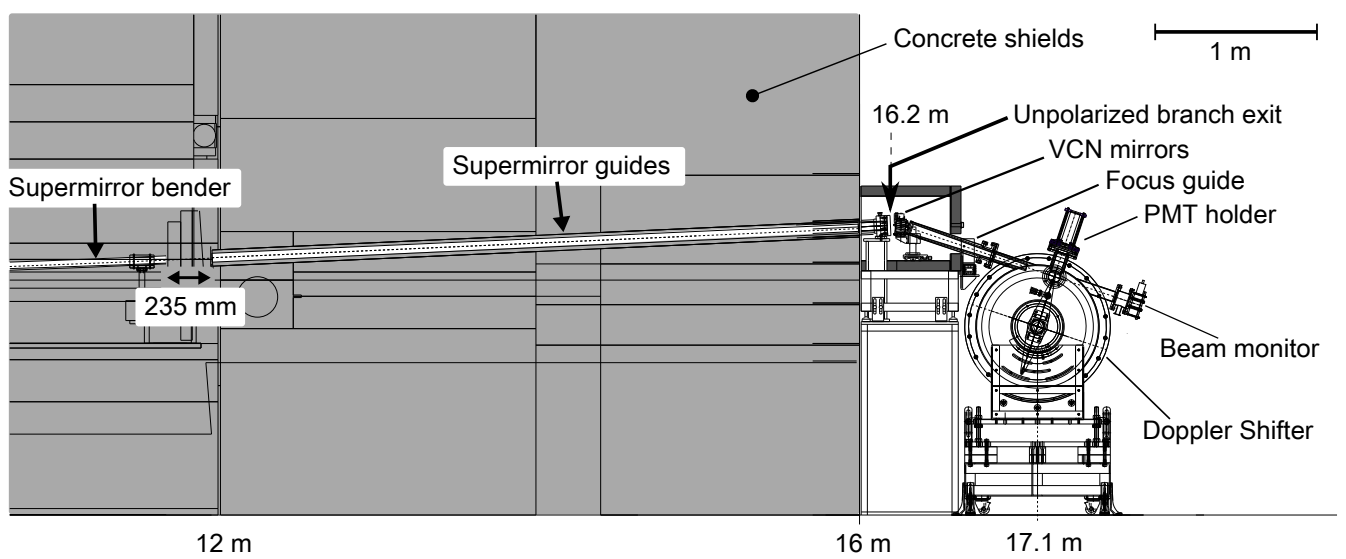
Figure.6.1   Cross-sectional view of the non-polarized beam branch in J-PARC MLF BL05. the image is cited from [38]. The neutron flux emitted from the moderator surface is transported to 7.8 m by the initial guide which is not shown in the figure, and then it is passed to the bender guide and is divided into three different super mirror guides at 12 m point. One of three branches in the center is called a non-polarized beam branch. Neutrons that have reached the exit of the unpolarized beam branch intersect the m3.5 monochromatic mirror. At this time, only the component of ~ 136 m/s is kicked out obliquely downward, it enters the focus guide tube, and only such neutrons finally reach the Doppler Shifter and is converted into ultracold neutron.
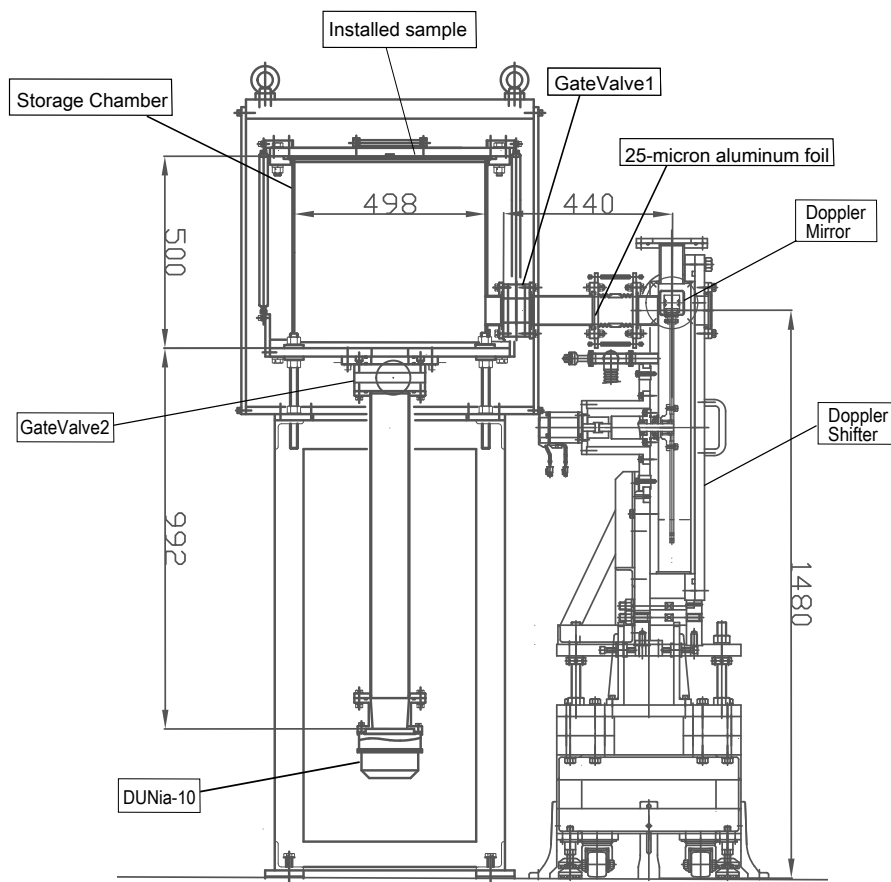
Figure.6.2   Overall view of UCN storage system in J-PARC MLF BL05

6.2.1 Transportation

Three guides are used to transport neutrons from the mercury target to the point of 16.2 m. Each guide is called as the initial guide, the bending guide, and the super mirror guides.

First, fast neutrons emitted from the moderator surface are transported to the point 7.8 m through the m2 initial guide. The neutron of J-PARC MLF BL05 is divided into three branches at the exit of the m2 initial guide. Guides having different characteristics are installed in the three branches. In low divergence branch, the beam having less transverse velocity is supplied. In non-polarized branch, the large output divergent beam is supplied. In polarized branch, the polarized beam is supplied. B_4C sintered bodies are installed near the entrance ports of the three branches in order to adjust neutron flux supplied from each branch. Neutrons incident on the unpolarized branch are transported to 12 m point along m3 bending guide with a slope of 2.6 degree upward, and fast neutrons are lost due to the curve. After this section, neutrons enter the entrance of the m3 mirror guide and transport to the exit of the unpolarized branch at 16.2 m point. The velocity distribution of neutrons emitted from the moderator surface follows the Maxwell distribution. Referring to the document [38], and the total flux of the unpolarized beam line is $\Phi = 2 \times 10^9$ [n/cm^2/s].

6.2.2 VCN transportation

Immediately behind the exit of the unpolarized beam branch, wideband multilayer monochromatic mirrors of m = 3.5 are installed as shown in Figure 6.3. Wideband multilayer monochromatic mirrors consist of 65 mm square 0.5 mm thick m3.5 mirrors stacked in 6 layers every 11 mm, fabricated at Kyoto University Research Reactor Institute (KURRI). The wideband multilayer monochromatic mirrors can kick neutrons only with $\sim$ 136 m/s into the direction almost parallel to the center axis of focus guide (tilted 18.6 degree to the ground). The setup related to wide-band monochromatic mirrors is shown in Figure 6.3. The kicked neutrons will be transported to Doppler Shifter along focus guide.

6.2.3 Focus guide section

Neutrons bounced by the wideband monochromatic mirrors go to Doppler Shifter through a focus guide. The inner surface of the focus guide is made of glass coated with Nickel. The focus guide consists of two of 515 mm and 230 mm guide, which are a square of 60 mm at the entrance and a rectangle of 40 mm × 26 mm at the exit. See Figure 6.3 for the detail.

6.2.4 Doppler Shifter

The whole figure of Doppler Shifter is shown in Figure 6.4, and an enlarged figure of the connection part with the focus guide is shown in Figure 6.5. In Doppler Shifter, a neutron of about 136 m/s is injected every 40 ms from the focus guide. The chamber of Doppler Shifter is evacuated to several Pa, and an
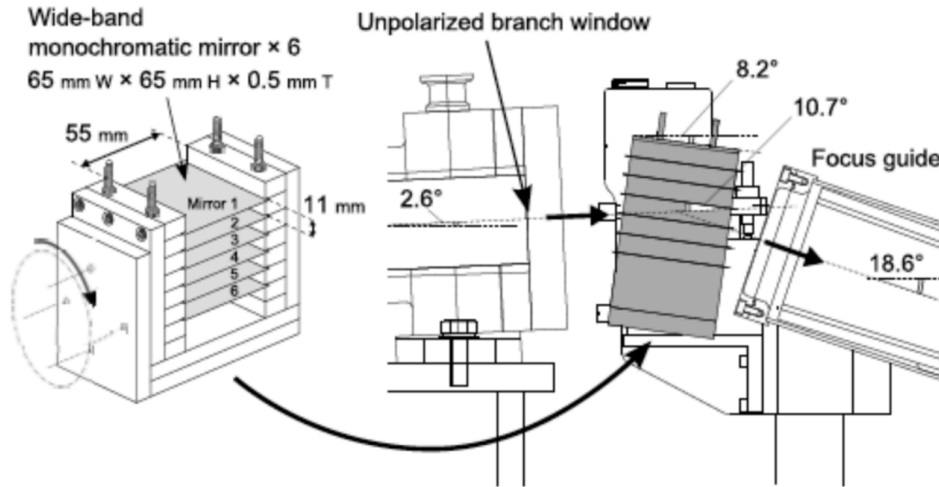
Figure.6.3 Schematic illustration of the arrangement of the wideband monochromatic mirrors. m3.5 mirrors are placed tilting 8.2 degree to the ground. Neutrons reflected by m3.5 mirrors are kicked and incident horizontally on the focus guide. See the text for details.

arm with a radius of 325 mm with a mirror (Doppler Mirror) attached at the tip rotating with 68 m/s. Doppler Mirror and incident beam intersect with a beam once in every 120 ms, which produces UCN at 8.33 Hz. As well as wide-band monochromatic mirrors, Doppler Mirror is also fabricated in KURRI, which consists of four NiC/Ti mirrors stacked on 0.3 mm thick silicon. The reflectivity of each mirror is given in Figure 6.6. The index of Figure 6.6 represents the order when counting the mirrors from the bottom. Regarding neutrons incident at 136 m/s against the Doppler Mirror rotated with 68 m/s, the $Q = 4\pi/\lambda$ and the reflectivity amount to 2.16/nm and 22.9 $\pm$ 0.4 %. Therefore, UCNs are produced according to formula 2.32 at the pseudo source point as described in chapter 2.4.2.

UCNs produced by Doppler Shifter can be taken from three ports above and beside the pseudo source point. In addition, the cold neutron beam which is not converted to UCN is monitored with MNH10/4.2F to correct the fluctuation of the neutron beam of J-PARC MLF (described in chapter 6.2.6). The Doppler shifter control device makes Doppler Mirror synchronized with the proton beam incident timing and produces the timing pulse when the mirror and the neutron beam are intersected. Although there is a slight rotation instability, this effect amounts to about 0.01 m/s in terms of speed conversion, which is negligible level in this experiment.

6.2.5 UCN Storage System

The whole figure of the UCN Storage System is given in Figure 6.2. UCNs emitted from the pseudo source point are transported through NiC/SiO$_2$ square guide and SUS316 cylinder pipe and are stored in SUS316 container of Φ498 mm $\times$ L500 mm. The interior of the chamber is polished to a surface roughness of 10 nm Ra or less by composite electrolytic polishing treatment. There are two ports on the
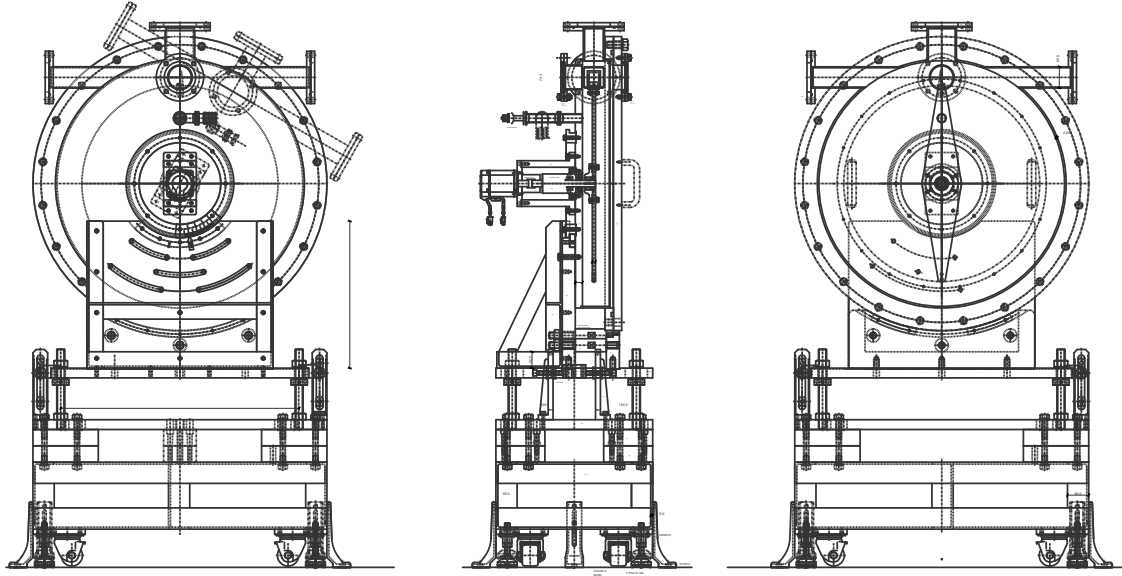
Figure.6.4 Overall figure of Doppler Shifter, the image is cited from [38]. The angle of the arm of Doppler Shifter can be variable and viewport is 100 mm away from Doppler Mirror center. In this experiment, The arm angle was fixed to 18.6 deg and the left viewport was used for UCN extraction.

sidewall and the bottom plate, of which diameters are $\Phi73$ mm and $\Phi100$ mm. Two gate valves (VAT inc.) are installed to control open/close two ports. The gate valves are made of SUS304 and its surface are coated with NiP after the electrolytic polishing treatment. The proportional counter (DUNia-10) is installed under ~ 900 mm to count UCNs. In this experiment, NiMo and PBIID DLC films deposited on a SUS304 substrate were used as test materials. The test material can be installed by replacing the SUS316 disk on the top of the storage container. The surface roughness of the SUS304 substrate was evaluated to be 1 nm Ra or less by measuring small test piece with a step meter (P-7 Stylus Profiler, KLA Tencor Corp).

For reference, the whole configuration of UCN storage system is given in Figure 6.7. The right is the Doppler Shifter and the left is the storage container. UCNs produced by the Doppler Shifter are transported from right to left. For further reference, the image taken when opening the upper lid is shown in Figure 6.8. In addition, the photograph of the inside of the specularly polished chamber is shown in Figure 6.9. In Figure 6.8, the inner surface of the test material faces inside Figure 6.9. In the storage experiment, different test materials are set by replacing as shown in these photographs. A gap between the container and the test material is several 100 μm, and the effect on the experiment is negligibly small. For reference, the photograph of PBIID DLC sample is shown in Figure 6.10. In storage experiment, the DLC coated green side is made facing the inside of Figure 6.9.
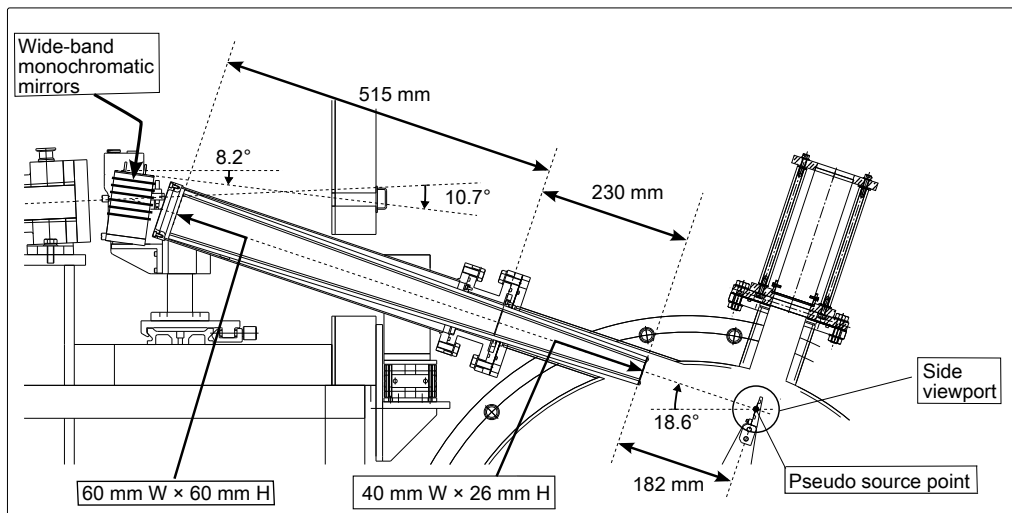
Figure.6.5 Enlarged figure around the inlet of focus guide. Neutrons kicked out by monochromatic mirrors go to Doppler Shifter through the focus guide. Ni/SiO$_2$ is affixed inside the focus guide tube, and its beam axis is inclined at 18.6 degree with respect to the ground. the image is cited from [38]

.
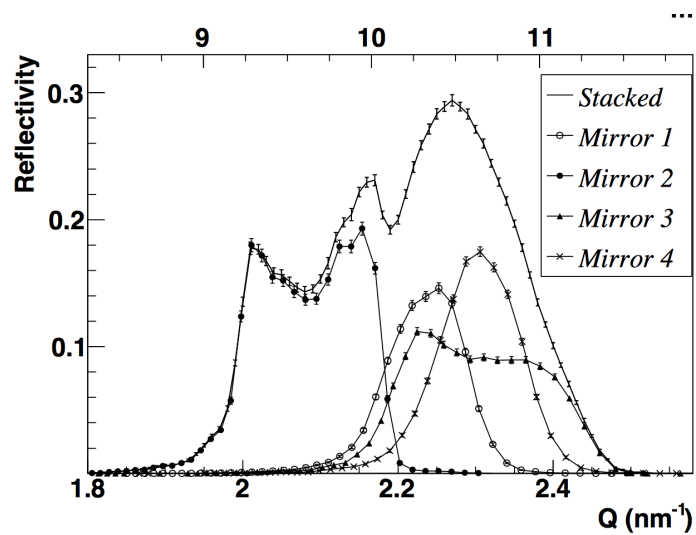
Figure.6.6 Reflectivity of Doppler Mirrors. The vertical axis is the reflectivity of Doppler Mirror, and the horizontal axis is $Q = \frac{4\pi}{\lambda}$. the image is cited from [38]. This Doppler Mirror is m10 super mirror having world's highest reflectivity and can reflect 136 m/s neutrons coming from the upstream of the unpolaized beam branch at J-PARC MLF BL05.
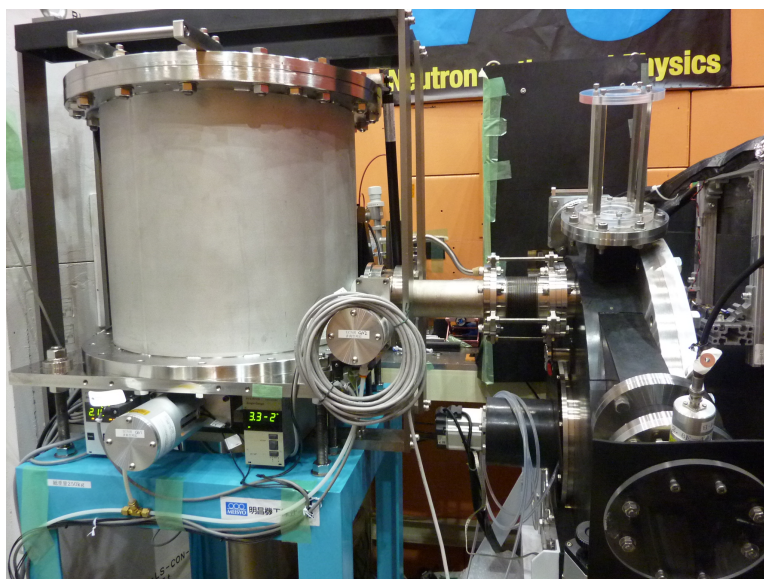
Figure.6.7　Overall picture of UCN Storage System. The storage container is on the left, the Doppler Shifter is on the right, the transport guide is in between.

Figure.6.8　Photograph of the storage container with top cover opened. The upper lid of the storage container was opened and the picture was taken from above. The white disc on the top of the cylindrical container is the test material.

Figure.6.9 Photograph of the inside of the storage container. The upper lid of the storage container was opened, the test material was removed, and the picture was taken from above. The inner surface is subjected to the composite electrolytic polishing treatment and the inner surface is lustered like a mirror.
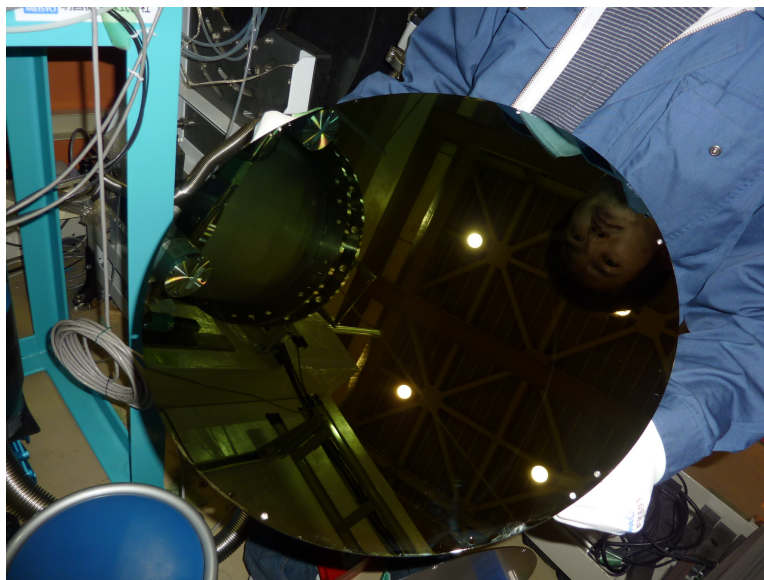
Figure.6.10 Example of the test material used in the actual storage experiment. The PBIID DLC/SUS304 actually used for the experiment was photographed. The green luster is due to DLC. Before the storage experiment, this shiny side was placed against the inner surface of Figure 6.9, the upper lid of the storage container of Figure 6.8 was closed, and the vacuum was drawn.

6.2.6　Detectors and DAQ system used in measurements

This section describes the detector and DAQ system used in the storage experiment.

DUNia-10

As a detector for the storage experiment, a ^{3}He gas proportional counter DUNia-10 (FLNP,JINR) was used. The real front view of this detector is given in the left of Figure 6.11 and the schematic diagram of the chamber cross section in the right of Figure 6.11. The dimension of the schematic diagram has an error of about 1 mm. The entrance window of DUNia-10 with a diameter of 90 mm is covered with a pure 100 μm thick aluminum sheet, which is supported by 2 mm thick aluminum bar placed at intervals of 10 mm. The mixed gas of 1858 Pa ^{3}He and 1.1 atms Ar 99% and CH4 1% was filled in the chamber. A tungsten wire of $\sim \Phi$ 100 μm is tensioned across the chamber, which was being applied with an electric potential in measurements. Neutrons entering in chamber interact ^{3}He gas elements with ^{3}He + n$\rightarrow$p +^{3} H and the avalanche multiplication occurring around the wire causes the signal. In this study, +1 kV potential was applied, resulting in the amplification factor of the wire of DUNia-10 $\sim$100 times. The electronic circuit of DUNia-10 used in this study is shown in Figure 6.12. An electronic circuit is installed in the back of DUNia-10, and the signal passes through this circuit before outputting. The secondary low-pass filter provided in the circuit does not only reduce noise but also amplify the signal.
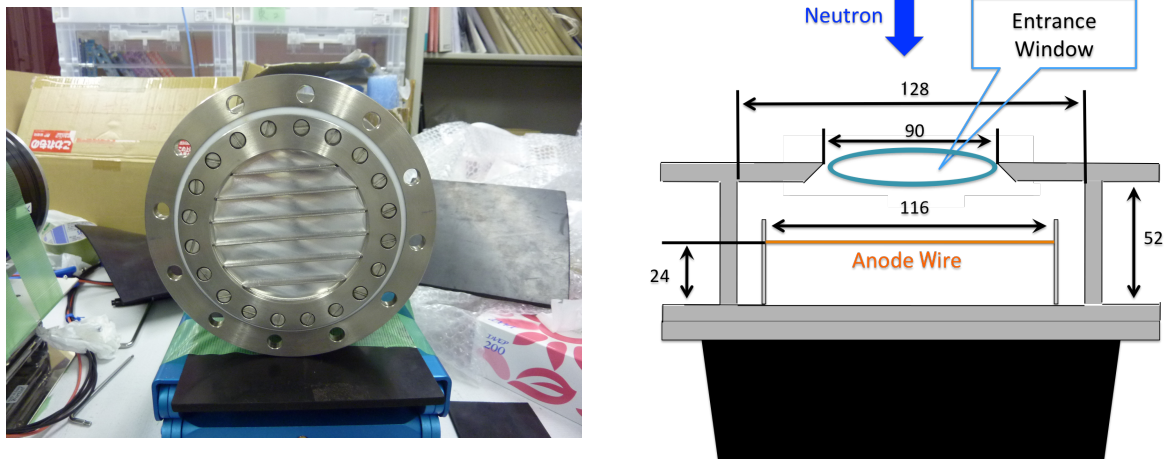

Figure.6.11　(Left) Front view of the actual product of DUNia-10 (right) Schematic diagram of the cross section of the chamber of DUNia-10. The 90 mm entrance window on the front of the chamber is covered with an aluminum sheet of 100 μm thick. Also, the Aluminum sheet is supported by 2 mm thick Aluminum bars from the outside.
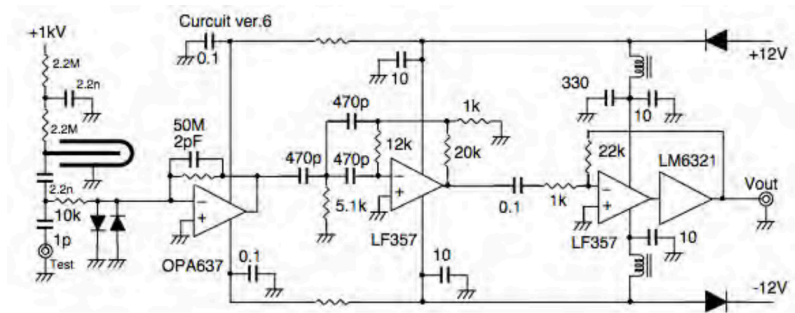
Figure.6.12   Electric circuit of DUNia-10

MNH10/4.2F

In this study, the neutron beam that is not converted to UCNs by the Doppler Shifter was monitored using MNH10/4.2F (CANBERRA) in order to correct the fluctuation of the intensity of UCN beam emitted from the Doppler Shifter (see Figure 6.13) [80]. The setup used for the measurement is shown in Figure 6.1. The current of J-PARC MLF proton beam fluctuates by about 3%, while it is suppressed to 1.4% or less. Thus, accurate storage experiment can be carried out. MNH10/4.2F is a proportional counter in which a mixed gas of argon and CH_4 of 1.3 Pa and a small amount of ^{3}He is filled. In this measurement, a voltage of $+1$ kV was applied to the wire of MNH10/4.2F. In addition, the output of MNH10/4.2F was amplified using CANBERRA 2006E and ORTEC 572. Please see the Appendix.B for the detail of suppression of beam fluctuation by using MNH10/4.2F.
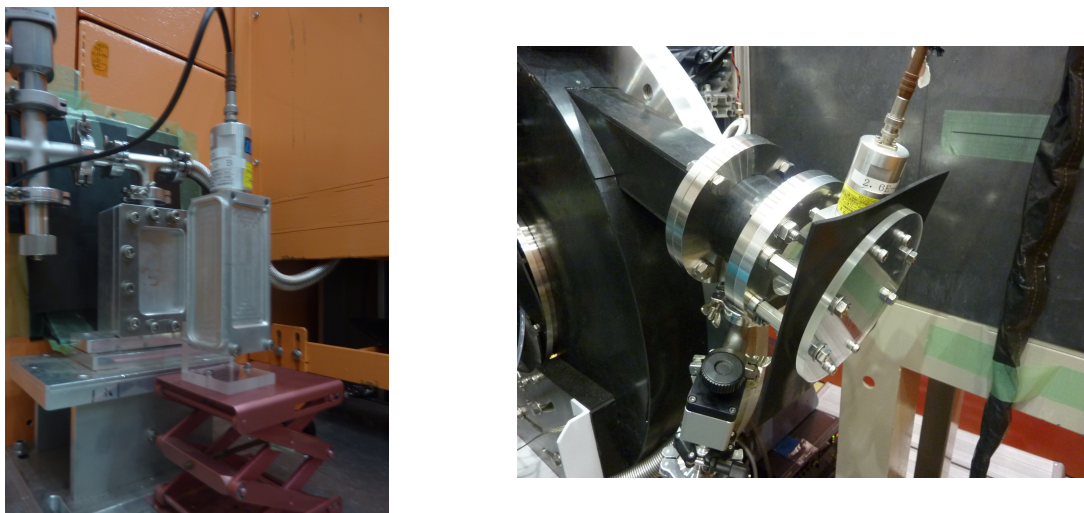
Figure.6.13   MNH10/4.2F. (right) A photograph that MNH10/4.2F installed at the neutron flux outlet of Doppler Shifter.

R3292-02(ZnS/LiF)

In this study, the two-dimensional sensitive detector consisting of R3292-02 (HAMAMATSU) and ZnS/LiF scintillator were used to evaluate divergence of neutron flux emitted from the focus guide described in chapter 6.3. ZnS/LiF scintillator containing natural lithium was used for the focus guide measurement. A schematic view of two-dimensional detector used in our study is shown in Figure 6.14. When neutrons are incident on ZnS/LiF adhered to the front of R3292-02, a lot of scintillation photon are yielded through the nuclear reaction of ^{6}Li + n $\rightarrow$ ^{3}H + α, and the photocathode convert them into photoelectrons. As a result, a photocurrent is generated by the electric field amplification through the mesh diode of R3292-02. In this study, a voltage of $+1$ kV was applied to the mesh diode. The photocurrent flows into the resistance dividing circuit of x and y, and signal wave heights are read from both end point of lines of x and y. If the four of signal wave heights are defined as X1, X2, Y1 and Y2, then the position X and Y can be calculated by X=X1/(X1 + X2) and Y=Y1/(Y1 + Y2). For R3292,

the position resolution has been evaluated to be 1 mm. In this study, the signal wave height was further amplified with a spectroscopic amplifier 4066-4A (CLEAR-PULSE Co., Ltd.) with shaping time 1 μs.

Although the composition ratio and density of this scintillator cannot be disclosed because of confidential corporate information, the mean-free path of 136 m/s in the ZnS/LiF scintillator is sufficiently longer than the scintillator thickness 100 μm. This fact guarantees that the wavelength dependence of the detection efficiency is proportional to be $1/v$ even if very cold neutrons are detected as described in chapter 6.3.
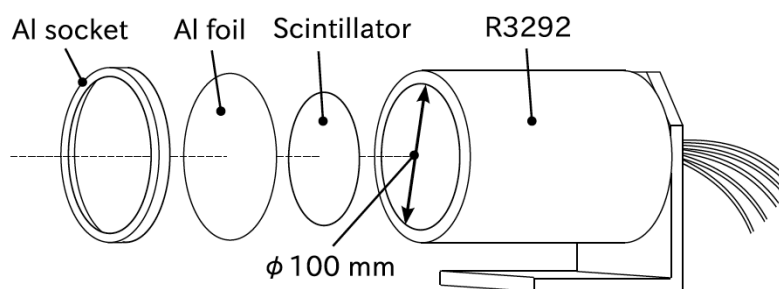
Figure.6.14   Two-dimensional detector used for our experiment, the image is cited from [44]. Detector consists of R3292-02 and ZnS/LiF scintillator. Actually, ZnS/LiF is affixed on the front of R3292-02.

DAQ System

In this study, 16 ch Peak Hold ADC A3400 VME Module (NIKIGLASS Co., Ltd.) was used as an Analog to Digital converter. When inputting a voltage wave with a peak value of 0 to 10 kV to the A3400, it will be automatically peak-held and A/D converted to 0 to 8192 digital value. Data conversion is performed when the voltage intersects to the ground level, and the time at the point is also recorded with accuracy 1 μ s. The data list is converted into a text file and stored in the PC. The data conversion time is 400 ns for each channel. Moreover, it does not hold the peak below the discriminator level that users can set through online. In this study, the peak value was less than 2000 ch. And the counting rate was 3000 counts per second at most. Using the rectangular wave emitted from a function generator, it was confirmed that there was not drop count to 100 kHz and the linearity of A/D conversion was kept up to 4000 ch.

Detector Calibration

Generally, by comparing with another detector whose feature is well known, it is possible to evaluate the detection efficiency. In this study, the detection efficiency was evaluated by comparing a proportional counter filled with 1 MPa ^{3}He gas, RS-P4-0812-223. The layout of RS-P4-0812-223 is given in the right of Figure 6.15. The signal of RS-P4-0812-223 is amplified by CANBERA Model 2006 Proportional Counter Preamplifier and ORTEC 572. Measurements were conducted at the low divergence beam branch at J-PARC MLF BL05. In this measurement, thermal/cold neutron beam was irradiated to the center of a

detector. At this time, the beam was narrowed down to ϕ 1 mm due to cadmium collimator. A schematic diagram of the measurement setup and the block diagram of RS-P4-0812-223 is shown in Figure 6.16 and 6.17.
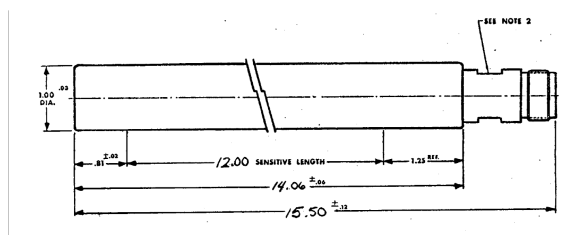
Figure.6.15 RS-P4-0812-223. (Left) Overall image of RS-P4-0812-223 (right) Drawing of RS-P4-0812-223. The chamber of RS-P4-0812-223 is made of SUS304. There is no leakage gas because the joint part is welded.

The detection efficiency ratio r (λ) of a test detector (DUNia10 or R3292) to RS-P4-0812-223 is given in the following equation:

$$r(\lambda) = \frac{(1 - \exp{(-p_1\lambda)})}{(1 - \exp{(-p_2\lambda)})} \tag{6.2}$$

where p_1 is the reaction coefficient of ^{3}He gas of DUNia-10 or ^{6}Li of ZnS/LiF scintillator, p_2 is the reaction coefficient of RS-P4-0812-223.

Actually, the effects of absorption of materials such as aluminum and SUS304, and attenuation from the wave height cut and the counting loss were included in the obtained result. Thus, in order to compare measured data with expression (6.2), it was necessary to correct these effects. In this study, the count obtained after absorption and attenuation effects are corrected is referred to as "the corrected count" hereafter.

The evaluation of the detection efficiency of DUNia10 is described as below. A schematic diagram of the measurement setup and the block diagram of DUNia-10 are shown in Figure 6.18 and 6.19. Figure 6.20 shows the result of fitting with expression 6.2 the corrected count ratio between DUNia-10 and RS-P4-0812-223. From the comparison between Figure 6.20 and expression (6.2), we got $\varepsilon(\lambda) = 1 - \exp{(-0.0708\lambda)}$ as the detection efficiency of DUNia-10. It is noted that the unit of λ is nanometers. The value of p_1 predicted from the gas pressure of ^{3}He at 1858 Pa is 0.071, which was consistent with the fitting result within the error range. It was confirmed that the detection efficiency of DUNia-10 was position dependent and time dependent. However, the effect of time dependence can be compensated by the measurement procedure of the storage experiment (described later). The position dependence was evaluated in the low divergence beam branch by the position scanning of DUNia-10 surface. Please refer to Appendix.C for details of position dependency evaluation.

127

The evaluation of the detection efficiency of R3292 & ZnS/LiF scintillator is described a below. The schematic illustration of the setup used for the measurement and its block diagram are shown in Figure 6.21 and Figure 6.22. The corrected count rate ratio of R3292 (ZnS/LiF) to RS-P4-0812-223 when the beam is irradiated to the center position of R3292 (ZnS/LiF) is given in Figure 6.23. By fitting the wavelength region 0.5 to 1.04 nm with the expression (6.2), $\varepsilon(\lambda) = 1 - \exp(-0.104\lambda)$ can be obtained. The detection efficiency of R3292 (ZnS/LiF) has the position dependency. In this study, in order to correct the effect, surface scan using the low divergence beam have been performed. The two-dimension map for relative detection counts obtained from the measurement is given in Figure 6.24.
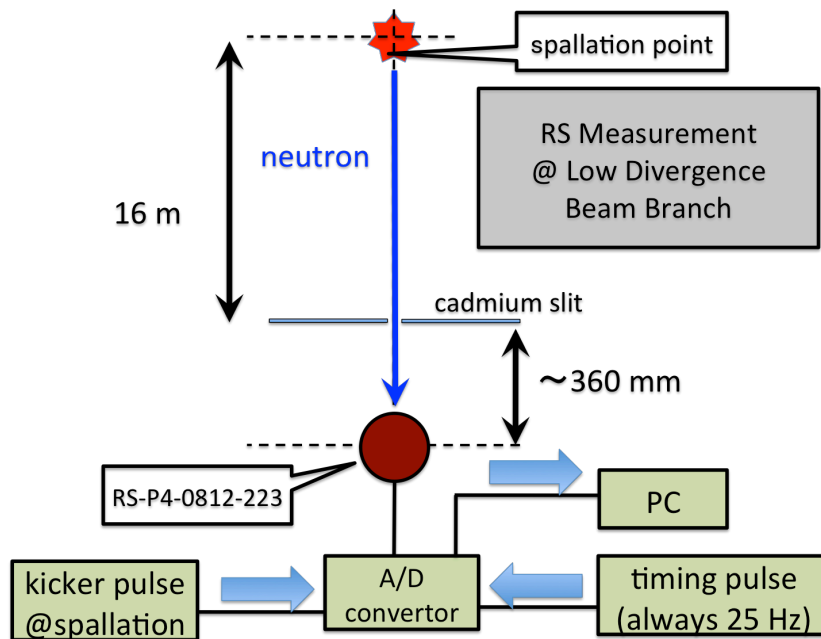
Figure.6.16 Setup used for the measurement of RS-P4-0812-223. RS-P4-0812-223 was set in a distance of ~ 100 mm from the exit of the low divergence beam branch. Cadmium slit of $\phi 2$ mm was affixed in the exit to narrow the beam. It is aligned so that the center of the neutron beam hits the detector center with an accuracy of 1 mm.
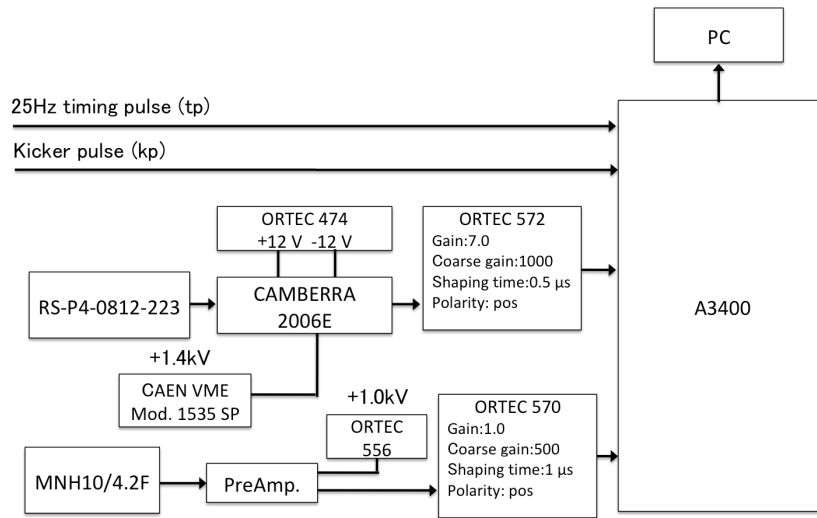
Figure.6.17 The block diagram of the setup of the measurement using RS-P4-0812-223 in low divergence beam branch.
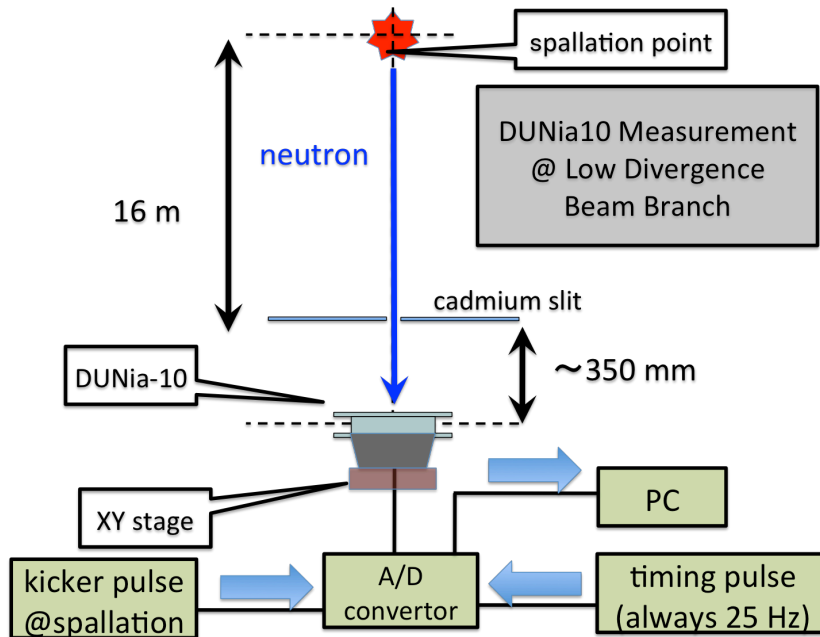
Figure.6.18 Setup used for the measurement of DUNia-10 detection efficiency. DUNia-10 was set at a distance of ~ 100 mm from the exit of the low divergence beam branch. Cadmium slit of $\phi 2$ mm was affixed to the exit to narrow the beam. It is aligned so that the center of the neutron beam hits the detector center with an accuracy of 1 mm.
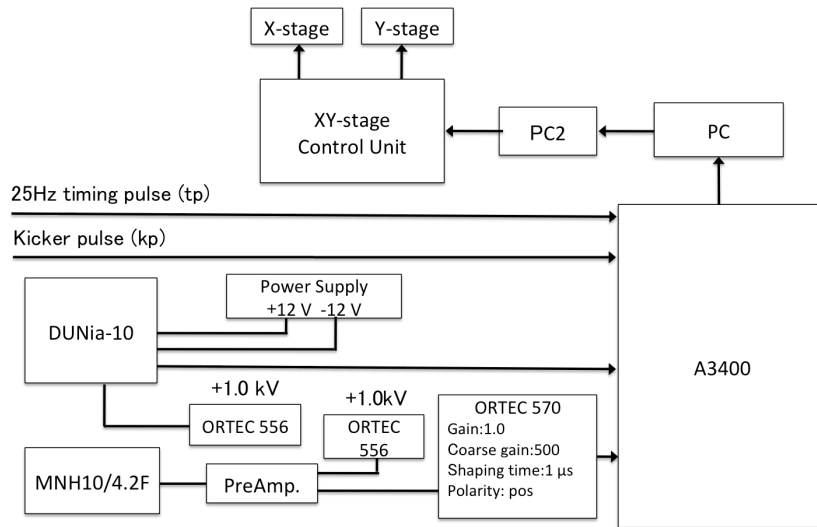
Figure.6.19   The block diagram of the setup of the measurement using Dunia-10 in low divergence beam branch.
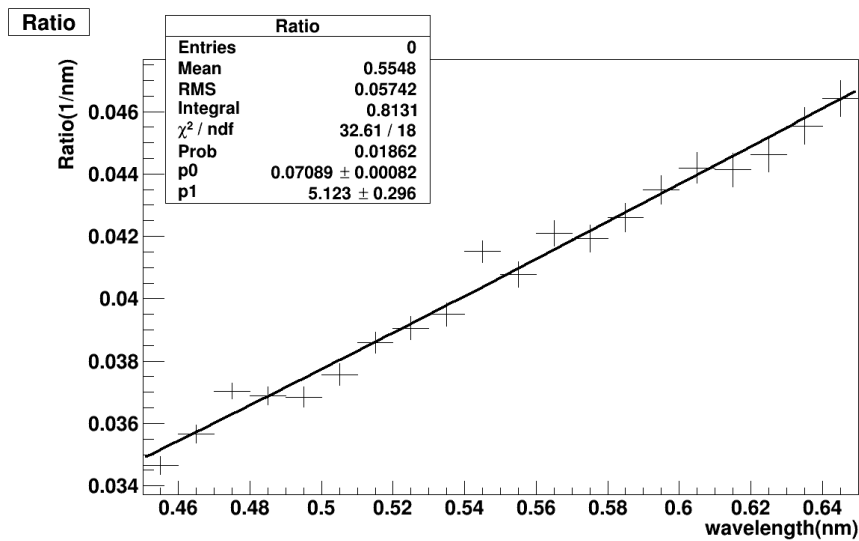
Figure.6.20   Wavelength dependence of count rate ratio of DUNia-10 and RS-P4-0812-223. Wavelength dependence of count rate ratio of DUNia-10 and RS-P4-0812-223. The red line is a fit by the expression (6.2). The vertical axis represents the count rate ratio, and the horizontal axis represents the wavelength (nm).
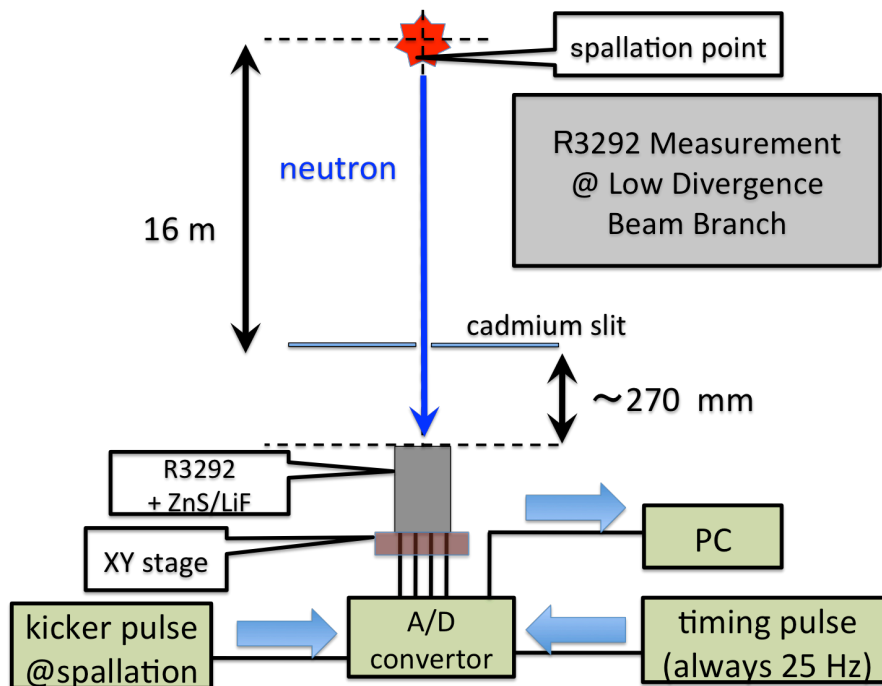
Figure.6.21   The setup used for the R3292 detection efficiency. Attaching cadmium slit to the exit of low divergence beam branch at J-PARC MLF BL05, the beam was irradiated to the detector installed at a distance of 270 mm from the exit point. In this situation, surface scanning was performed so that the detector was moved to the direction orthogonal to beam axis.
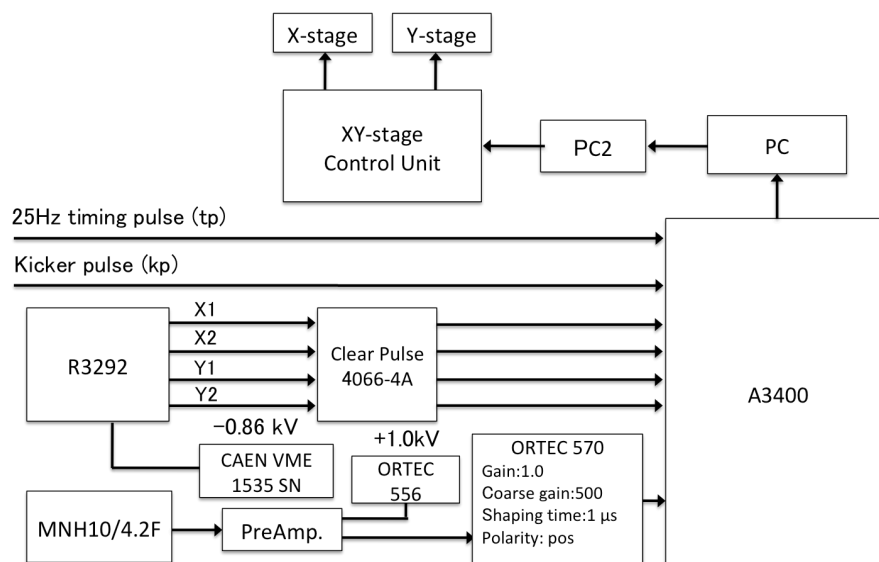
Figure.6.22   The block diagram of the setup of the measurement using two-dimensional detector in low divergence beam branch.
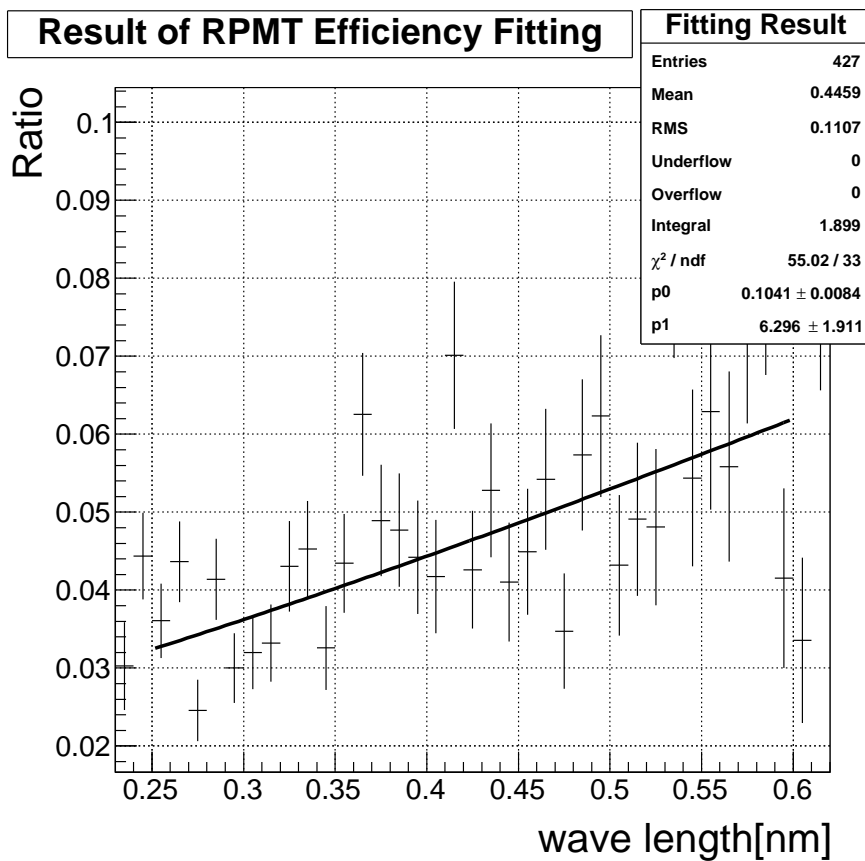
Figure.6.23 Wavelength dependence of the ratio of two-dimensional detector to RS-P4-0812-223. The red line is the fit result by the expression (6.2). The vertical axis represents the count rate ratio, and the horizontal axis represents the wavelength (nm).
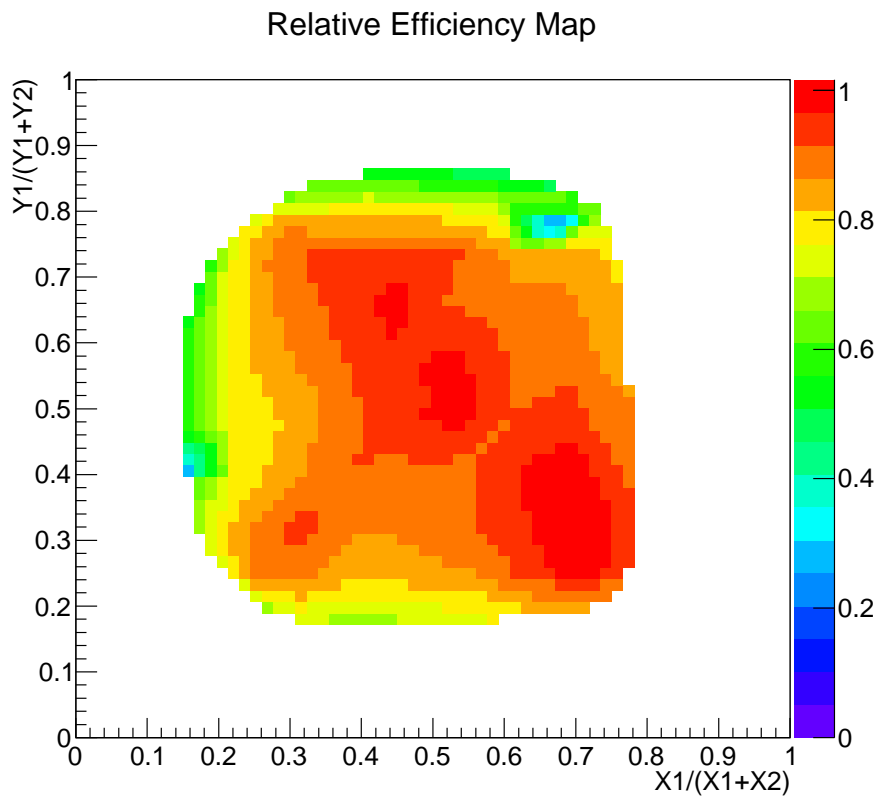
Figure.6.24　Relative detection efficiency of two-dimensional detector. Two-dimensional distribution of the intensity ratio obtained when scanning R3292-02 (ZnS/LiF) with a low divergence beam. The vertical axis is the relative position of Y, and the horizontal axis is the relative position of X.

6.3 Determination of UCN velocity emitted from Doppler Shifter

In this section, it is described how to determine the velocity of UCN beams emitted from the side port of the Doppler Shifter. As mentioned in chapter 2.4.2, the velocity distribution of UCN beams generated by the Doppler Shift method can be calculated by a simulation assuming the velocity distribution of neutrons incident to the Doppler Shifter. For J-PARC MLF BL05, such incident neutrons correspond to the very cold neutrons (VCNs) emitted from the focus guide (see chapter 6.2.3). The velocity of VCNs can be calculated from the beam divergence and TOF. For this reason, the author actually measured the beam divergence and TOF of VCNs emitted from the focus guide in June 2017.

The experimental setup used in this study is shown in Figure 6.25. In addition, the schematic illustration of this experimental setup is given in Figure 6.26, and the block diagram of the experimental setup is given in Figure 6.27. This setup consists of the focus guide, X-Y stage, two-dimensional detector, and helium flow tube. In this setup, a cadmium slit with 36 pinholes of ϕ 1 mm was pasted to the tip of focus guide (see the right of Figure 6.28), and a cadmium collimator of ϕ 4 mm (see the left of Figure 6.28) was affixed to the front end of the helium tube. In addition, the two-dimensional detector was mounted on the X-Y stage so that the center of the two-dimensional detector could be adjusted to one of 36 pinholes one by one. The distance between the slit and the collimator was about 2 mm. When the center of the two-dimensional detector is aligned with the center of one of pinholes of Cadmium slit, it is guaranteed that only the neutron flux emitted from the pinhole can reach the two-dimensional detector. The purpose of the helium flow guide was to suppress air scattering between the focus guide and the two-dimensional detector. In this way, using this experimental setup, VCN flux emitted from one of pinholes was measured one by one while aligning the center of the two-dimensional detector to the pinhole. The VCN beam divergence could be obtained from the beam spread on the two-dimensional detector surface, and the TOF could be obtained from the time at which UCNs are detected since the proton beams are injected at J-PARC MLF. Finally, VCN velocity can be calculated with the beam divergence, the TOF, the distance from the cadmium slit to the detector (482 mm), and the distance from the J-PARC mercury target to the detector (17.6 m).

As mentioned in the above, the UCN velocity can be calculated by the Doppler Shifter simulation assuming the VCN velocity distribution. The velocity of UCN beams obtained in this way is shown in Figure 6.29.
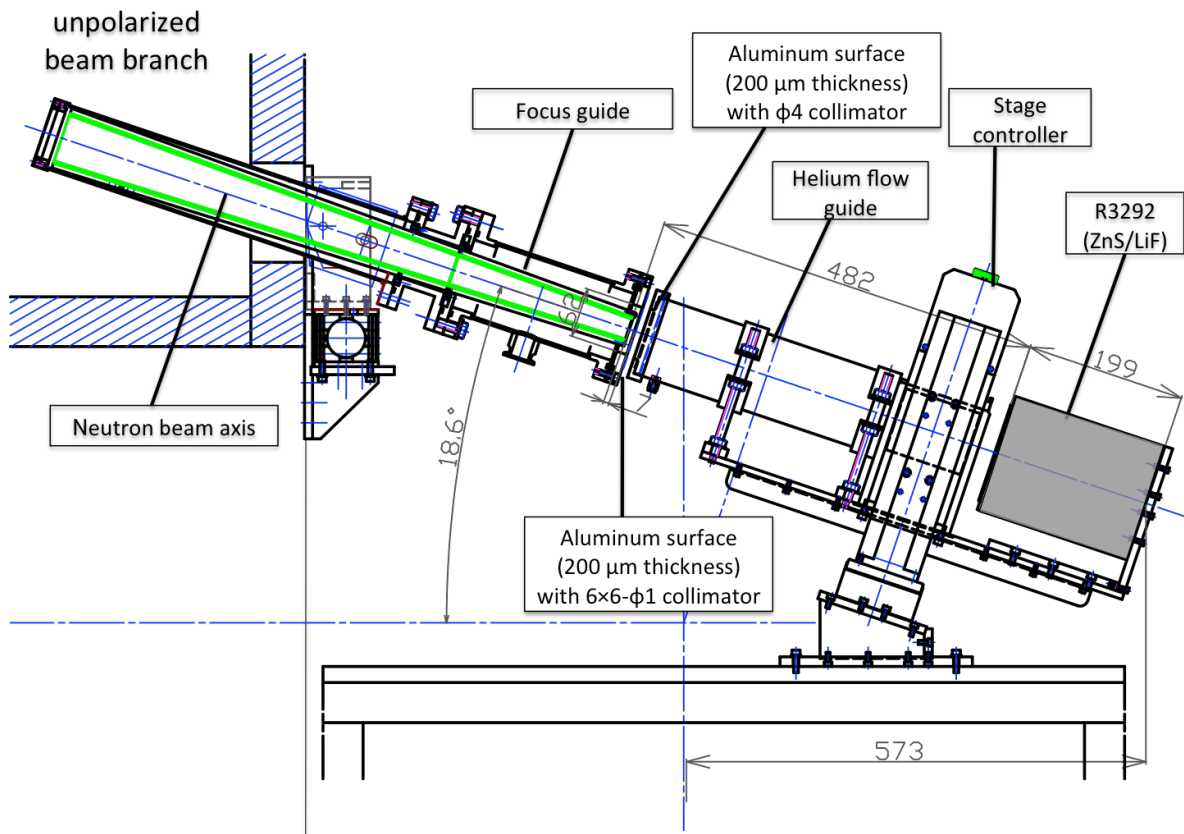
Figure.6.25   Experimental setup used for neutron flux measurement of the focus guide. A cadmium slit with 36 pinholes of ϕ 1 mm was pasted to the aluminum cover of the focus guide (see the right of Figure 6.28). A cadmium collimator of ϕ 4 mm in the left of Figure 6.28 was affixed to the front end of the helium flow tube. The both end of the helium flow guide is covered with an aluminum sheet of 200 μm thickness, the surface of the two-dimensional detector is covered with a foil of 100 μm thickness, and the tip of the focus guide is covered with an aluminum cap of thickness 200 μm. The distance between the slit and the collimator was about 2 mm. When the center of the two-dimensional detector was aligned with the center of the pinhole of Cadmium slit, only the neutron flux emitted from the pinhole reaches the two-dimensional detector surface.
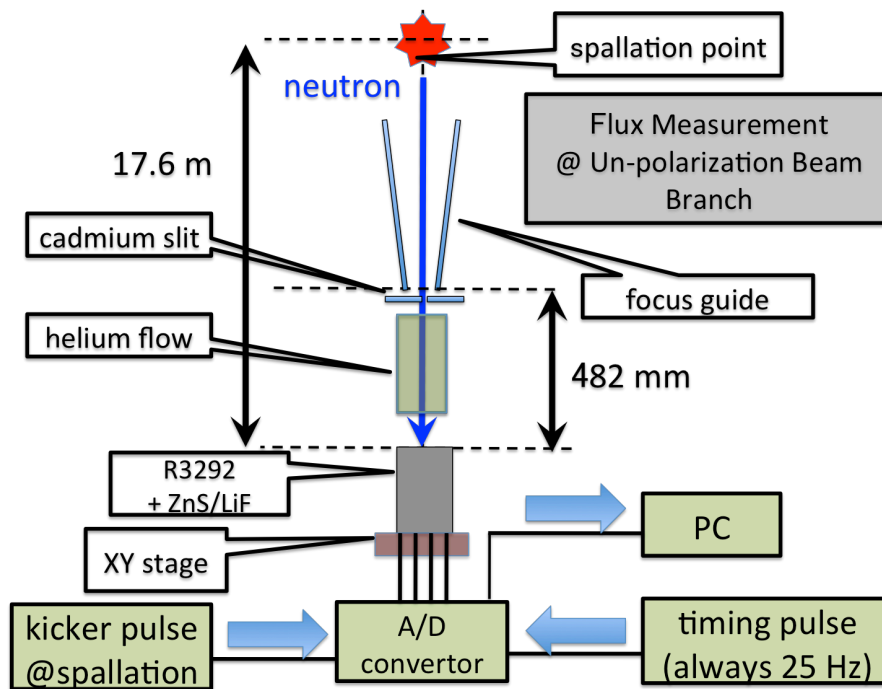
Figure.6.26 The schematic diagram of the setup used for measuring neutron flux of the focus guide. The distance from the moderator to the detector surface was ∼ 17.6 m, and the distance from the tip of focus guide to the detector was 482 mm. The signals of two-dimensional detector, timing pulse, and kicker pulse were Analog to Digital converted and recorded on the PC.
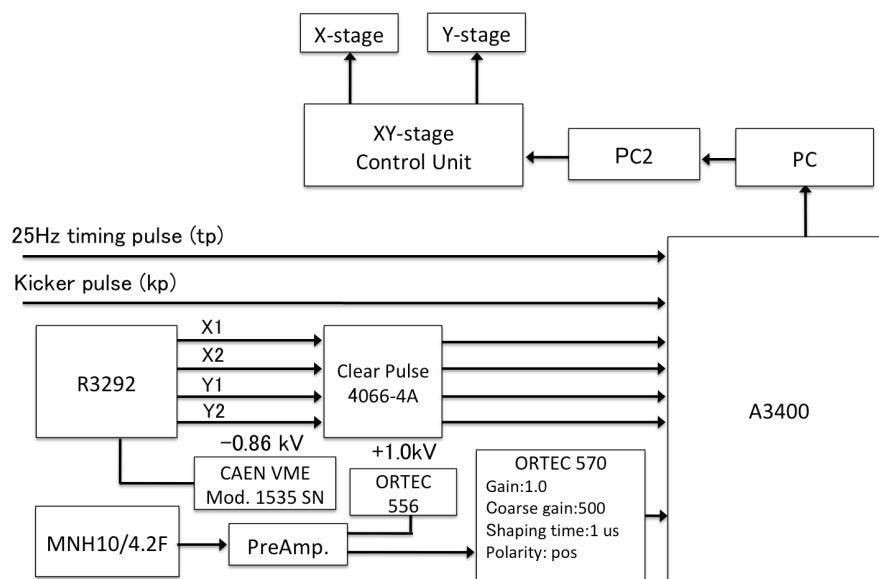
Figure.6.27 The block diagram of the setup used for measuring neutron flux of the focus guide
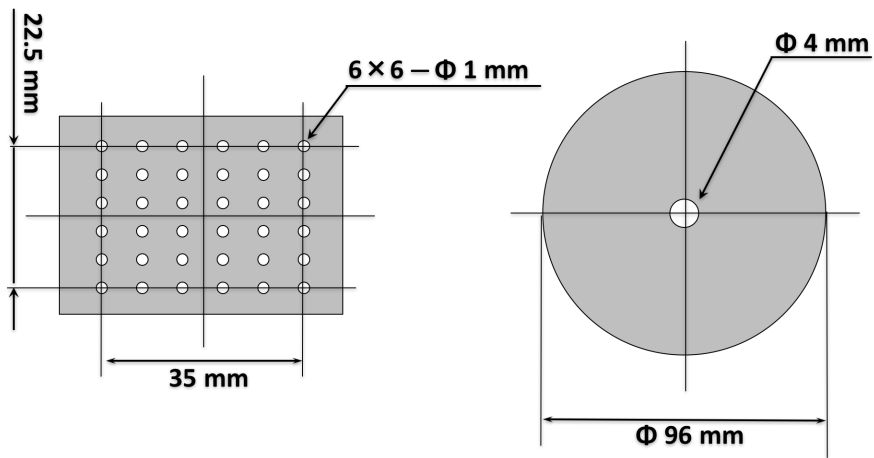
Figure.6.28   Cadmium slit and cadmium collimator used in experiment
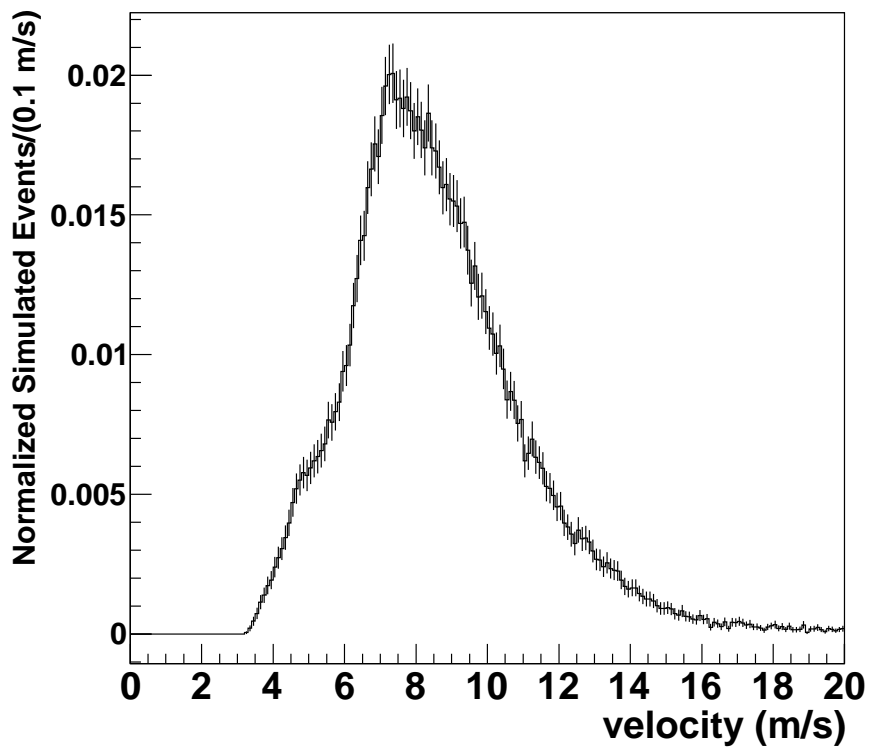
Figure.6.29   Velocity distribution of UCN emitted from Doppler Shifter side port. The horizontal axis shows UCN velocity calculated by Doppler Shifter simulation, and the vertical axis shows the number of Monte Carlo Events. Total sum is normalized to 1.

6.4 UCN Storage Experiment

In this section, details of UCN storage experiment are described. This section is divided into three parts. In the first part, the background of this experiment is introduced. In the second part, the obtained result is explained. In the final part, the details of the analysis to determine UCN loss probability coefficient are described.

6.4.1 Introduction of UCN Storage Experiment

UCN storage experiment was performed twice in May 2016 and June 2016. In the first storage experiment, SUS316 and DLC/SUS304 were used as a test material, and in the second storage experiment, NiMo/SUS304 and SUS316 were used. A block diagram of setup in which storage experiments were performed is shown in Figure 6.30, and a schematic diagram is shown in Figure 6.31. Features of this setup are as follows:

1. The UCN produced by Doppler Shifter was picked up by NiC transport guide installed in the viewport.
2. An aluminum foil, 25 μm, was attached to the tip of the NiC transport guide.
3. UCNs importation and storage and release were controlled by the opening/closing gate valves in Figure 6.31.

In the storage experiment, the measurement procedure consists of the following four parts: (1) monitoring of UCN (2) accumulation of UCN (3) storage of UCN (4) release and detection of UCN. Each state transition was controlled by managing two valves opening/closing. For reference, the sequence of the storage experiment is given in Figure 6.32. The details of the sequence are described as follows (Please also refer Figure 6.32):

UCN monitoring: (gate valve1 open, gate valve2 open):
> In this period, it is possible to count the number of raw UCNs coming from the Doppler Shifter and going to the detector. Its procedure is set for the purpose of correcting the fluctuation of the UCN beam. It is noted that its procedure is not used in the current analysis.

Accumulation of UCN (gate valve1 open, gate valve2 close):
> In this period, UCN coming from Doppler Shifter is accumulated in the storage container. In this way, the number of UCNs is increased to be nearly maximum.

Storage of UCN (gate valve1 close, gate valve2 close):
> In this period, UCN is kept stored for a certain time. In this way, the inner surfaces of the storage container and the test material are reacted with UCN.

Releasing UCN: (gate valve1 close, gate valve2 open):
> During this period UCN in the container is released. The released UCN is counted by DUNia-10 installed under the container.
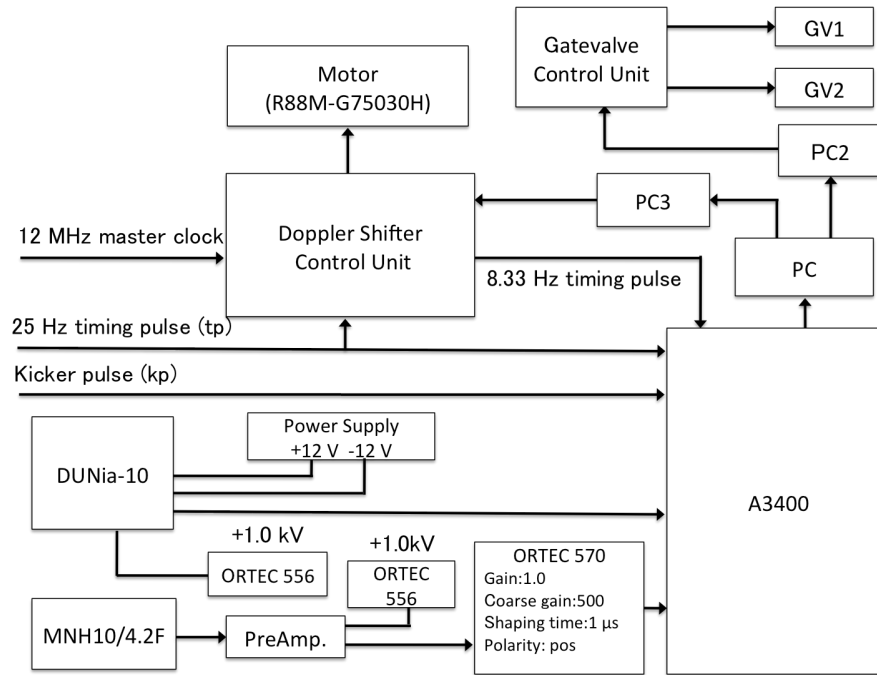
Figure.6.30　The block diagram of the setup of the storage experiment.

In this experiment, storage time was repeatedly changed for each run like 0 s → 100 s → 200 s → 300 s → 400 s → 0 s → … .

In this experiment, substances in upstream emit gamma radiation and it is picked up by detectors. In general, the energy that the gamma radiation deposits on the detector is smaller than that neutrons do. And also, the gamma radiation instantaneously increases at the timing of J-PARC pulsed proton beam injection. In this study, the following two cuts were applied for improving the signal to noise ratio.

Gamma cut

The wave height value recorded on A3400 should be 400 or more.

T_0 cut

The events recorded on A3400 after 0.4 ms from J-PARC pulsed beam injection are used.

6.4.2　Result of UCN Storage Experiment

The result of UCN storage experiment is described below. Regarding the first storage experiment, data acquisition and analysis were conducted as follows:

Setup

PBIID DLC/SUS304 or SUS316 is installed at the top of the container.

Data acquisition

Repeat following procedure: (1). To accumulate UCNs for 50 s (2). To choose the storage period from one of 0 to 400 s cyclically (3). To store UCNs for the storage period. (3). To release UCNs
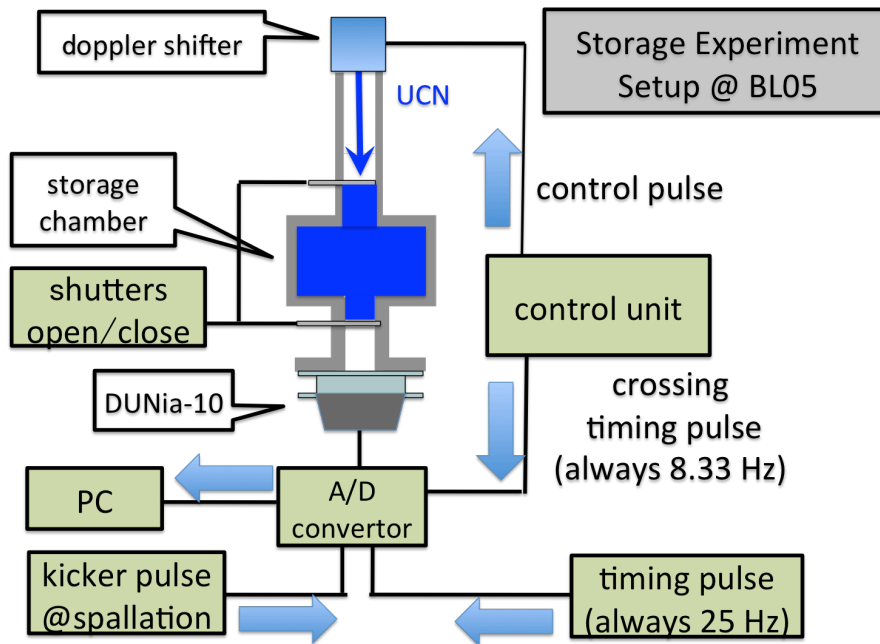
Figure.6.31 Schematic diagram of the setup of our storage experiment. When opening both gate valves, UCN coming from Doppler Shifter pass through the storage container and go to DUNia-10. When only the valve on the Doppler Shifter side is opened, UCN is accumulated inside the storage container. When both valves are closed, UCN is stored inside the storage container. When only the shutter on the DUNia-10 side is opened, UCN inside the container is released and counted by DUNia-10.

for 100 s.

Data process

The foreground was determined by DUNia-10 counts in the duration of release. On the other hand, the background was determined from the average counts of data acquired in the conditions shown in Table 6.2. Finally, signals were determined by subtracting the background from the foreground.

Signal Data

Statistics of the signal count are shown in Table 6.3.

In the second storage experiment, data acquisition and analysis were carried out as follows:

Setup

NiMo/SUS304 or SUS316 is installed at the top of the storage container.

Data acquisition

Repeat following procedure: (1). To accumulate UCNs for 50 s (2). To choose the storage period from one of 0 to 400 s cyclically (3). To store UCNs for the storage period (4). To release UCNs for 150 s or more.

Data process

The foreground was determined by DUNia-10 counts obtained from the UCN release period from
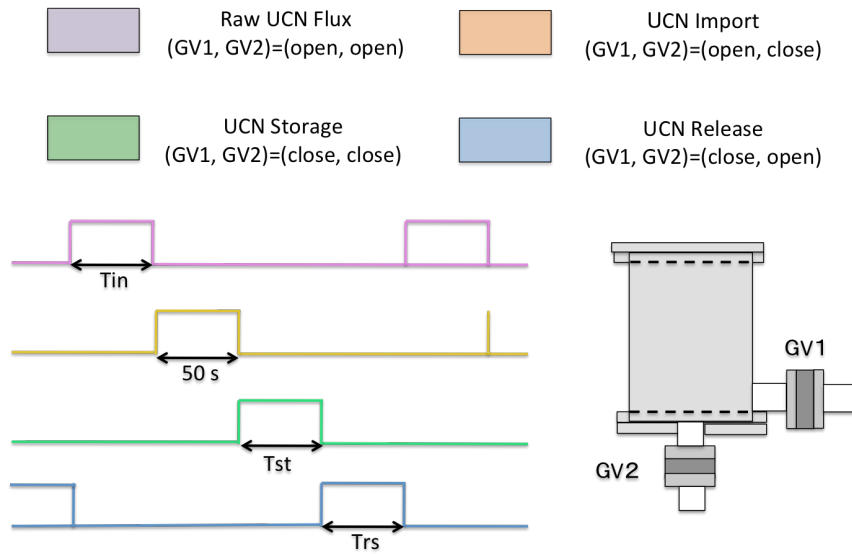
Figure.6.32   Sequence of the UCN storage experiment)

0 s to 100 s. On the other hand, the background was determined from DUNia-10 counts obtained from the UCN release period from 100 s to 150 s or more. Finally, the signal was determined by subtracting the background from the foreground.

Signal Data

Statistics of the signal count are shown in Table 6.4.

In the above data process, events were adopted when beam loss is suppressed to be 1 % or less during the accumulation period in J-PARC MLF. In this study, such events to satisfy the above condition is called "kp-ok events".

The obtained results are shown in Figure 6.33 and Figure 6.34. The horizontal axis is storage time, and the vertical axis is the average signal counts of DUNia-10 for one measurement cycle, and the black line is the result when SUS316 is used (both cases), and the red line is the result when DLC or NiMo is used.

Obviously, there is a significant difference in the count rate of Figure 6.33 and Figure 6.34. This is thought to be due to a detection efficiency deterioration between the first storage experiment in 2016 May and the second storage experiment in 2016 June (see Appendix.C for details). Although Appendix.C show such deterioration amounts to 10% for a month, it is noted that this difference does not affect the result of our storage experiment. That is because data taking was performed from 0 to 400 s cyclically for each runs and time change of detection efficiency was averaged over. As an example, assuming such efficiency deterioration changes in time linearly, the deviation corresponding for the period of 2000 s can be evaluated as $10\% \times \frac{2000s}{1\text{month}} = 0.05\%$. It is therefore too much less than a statistical precision for each data points.

141

Data id	Exp id	Sample	How to evaluate Background
1	1st storage	SUS316	Evaluated from the average of Table 6.2
2	1st storage	DLC/SUS304	Evaluated from the average of Table 6.2
3	2nd storage	NiMo/SUS304	Extracted from 150 s released time distribution
4	2nd storage	SUS316	Extracted from 200 s released time distribution

Table.6.1   Details of storage experiment condition

data id	counts per 100 s	situation
1605150907	3.0 ± 0.6	Extracted from 200 s released time distribution
1605151018	2.4 ± 0.4	Same the above
1605160804	2.3 ± 0.4	Same the above
1605151325	2.7 ± 0.4	Extracted from the data measured with mirror avoided from beam
1605180536	3.3 ± 0.4	Extracted from the data measured with GV1 and GV2 closed
combine data	2.7 ± 0.2	Average the above

Table.6.2   Details of the background measurement of the first storage experiment

Name	time	Number of Signal Events	Number of kp-ok Events
sus316 1st	0	2530 ± 51	49
sus316 1st	100	1281 ± 37	48
sus316 1st	200	688 ± 29	47
sus316 1st	300	366 ± 22	43
sus316 1st	400	249 ± 20	45
dlc 1st	0	1987 ± 45	39
dlc 1st	100	1129 ± 35	41
dlc 1st	200	593 ± 26	37
dlc 1st	300	379 ± 22	36
dlc 1st	400	198 ± 17	33

Table.6.3   Details of signal count for 1st storage experiment

Name	time	Number of Signal Events	Number of kp-ok Events
sus316 2nd	0	1459 ± 42	34
sus316 2nd	100	873 ± 33	36
sus316 2nd	200	459 ± 26	35
sus316 2nd	300	276 ± 23	35
sus316 2nd	400	164 ± 20	33
nimo 2nd	0	3809 ± 64	87
nimo 2nd	100	1975 ± 48	82
nimo 2nd	200	1184 ± 40	84
nimo 2nd	300	670 ± 33	84
nimo 2nd	400	492 ± 30	87

Table.6.4   Details of signal count for 2nd storage experiment

Figure.6.33   Dependence of the counting rate on storage time in the first storage experiment. The horizontal axis is the storage time, and the vertical axis is the averaged counts per run. Black is the result of SUS316, red is the result of DLC/SUS304.
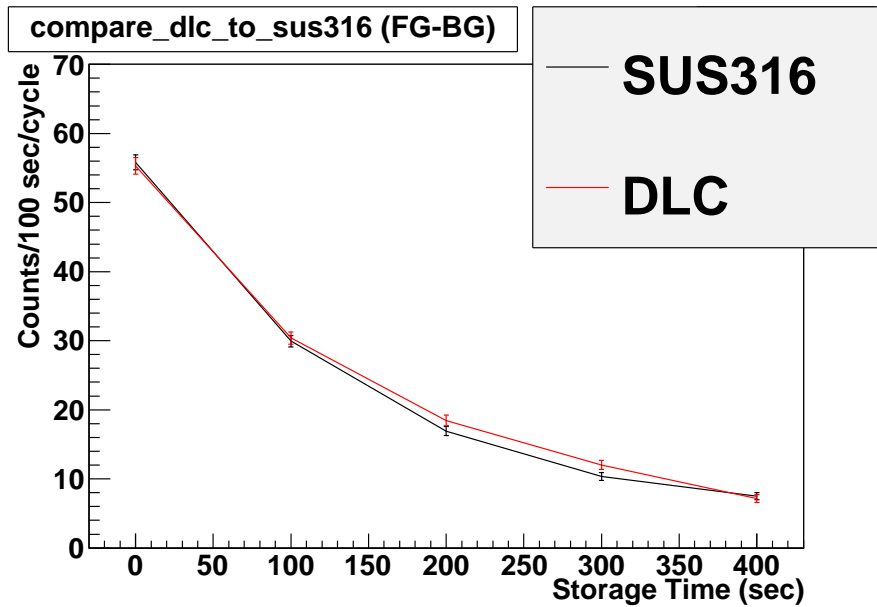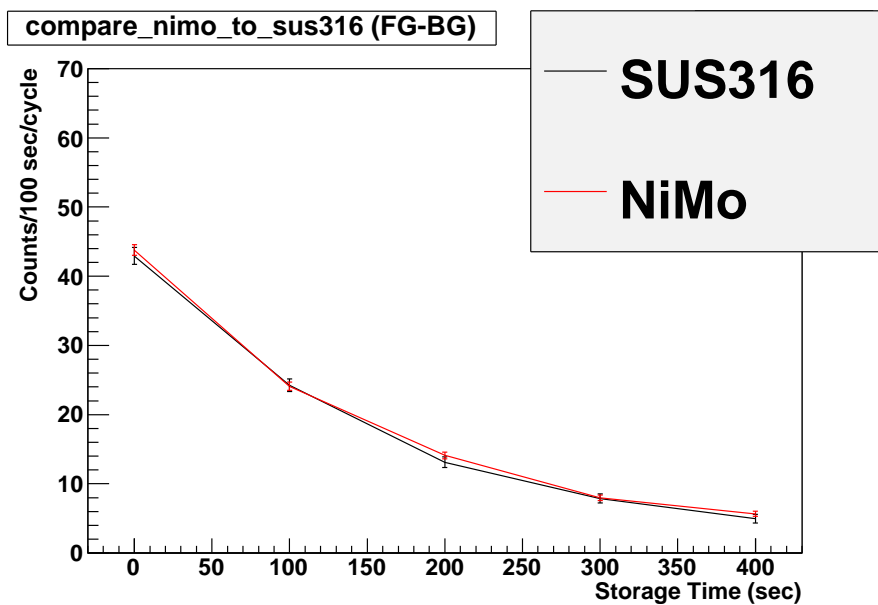
Figure.6.34 Dependence of the counting rate on storage time in the second storage experiment. The horizontal axis is the storage time, and the vertical axis is the averaged count per run. Black is the result of SUS316 and red is the result of NiMo/SUS304.

144

6.4.3 Analysis of UCN Storage Experiment

The analysis result of UCN storage experiment is described below. In this study, the chi-squared analysis was used to determine the loss probability coefficient from the time change of UCNs of Figure 6.33 and 6.34.

The definition of the chi-square value χ^2 adopted in this study is shown as follows:

$$\chi^2 = \sum_{i=0}^{4} \frac{(N_{\mathrm{exp,i}} - N_{\mathrm{tmp,i}})^2}{\delta_{\mathrm{tot,i}}} \tag{6.3}$$

$$\delta_{\mathrm{tot,i}} = \sqrt{(\delta_{\mathrm{exp,i}})^2 + (\delta_{\mathrm{syst,i}})^2} \tag{6.4}$$

$$\delta_{\mathrm{exp,i}} = \sqrt{N_{\mathrm{exp,i}}} \tag{6.5}$$

$$\delta_{\mathrm{syst,i}} = 0.014 \times N_{\mathrm{tmp,0}} \tag{6.6}$$

where $N_{\mathrm{exp,i}}$ is the number of UCNs actually measured after the storage time of i×100 s, $N_{\mathrm{tmp,i}}$ is the count number after storage time of i×100 s created by Monte Carlo simulation (template samples), and $\delta_{\mathrm{syst,i}}$ is the systematic error of an uncertainty of initial storage number due to the J-PARC beam fluctuation (see Appendix.B for details), respectively. In this study, the reduced chi-squared value of the expression (6.3) was used for analysis.

The conditions to prepare the template sample used in the chi-square analysis are given as follows:

Preparation of Template Samples

Template samples, necessary to be compared with experimental data, were generated by the storage simulation assuming the velocity distribution of Figure 6.29, the storage container configuration of Figure 6.2 and the theory of neutron optics. In this study, the velocity region from 3 m/s to 7 m/s was used for comparison. In addition, the number of Monte Carlo Events was chosen to be 100,000.

Non-specular Reflection

In this study, Lambert's cosine law was used to represent the non-specular reflection occurring in the storage container, and 5 % was assumed for its non-specular reflection probability. This value is chosen to be consistent with the evaluation value of 5.7 ± 2.1 % described in the document [81] for evaluation of the non-specular reflection probability of SUS316 subjected to composite electrolytic polishing.

Reflection on Gate Valve Surface

Only gate valves of Figure 6.2 were subjected to NiP coating and (merely) electrolytic polishing (see chapter 6.2.5 for details). In this analysis, the UCN loss probability coefficient, the Fermi potential and the non-specular reflection probability of the gate valves were chosen to be 0, 210 neV, and 0%, respectively. These assumptions are thought to be appropriate for following reasons:

1. The ratio of collision to gate valves is only 1 %.
2. Non-specular reflection probability is typically 10 % or less for an electrolytic polishing surface.
3. UCN loss probability coefficient is typically $O(10^{-4})$ for a well-polished surface.

145

For reference to the experimental ability, the comparison plot of η dependency of the template sample prepared by the above procedure is shown in Figure 6.35. This plot shows the η dependency of the number of UCNs confined in the storage container whose NiMo is used for test material. Please refer the figure caption for detailed simulation conditions. In fact, it can be found that a significant difference occurs according to the η difference. The η dependence of the chi-squared value for SUS316 is shown in Figure 6.36. According to Figure 6.36, the loss probability coefficient η of SUS316 can be evaluated to be $(2.4^{+0.31}_{-0.21}) \times 10^{-4}$ (the first storage experiment) and $(2.2^{+0.32}_{-0.24}) \times 10^{-4}$ (the second storage experiment). In this study, 2.3×10^{-4} was adopted as the evaluation value of the UCN loss probability coefficient of SUS316, which is the average value for the first storage experiment and the second storage experiment.

The η dependency of the chi-squared value for NiMo/PBIID DLC is shown in Figure 6.37. In Figure 6.37, the chi-square value becomes minimized for $\eta < 1 \times 10^{-4}$, while it drastically increases in the other region. This means that although it is impossible to identify the loss probability coefficient of the test material, it can be guaranteed that the reflection performance is superior to a certain level. In this study, a point of 1 σ away from the reduced chi-square value of $\eta < 1 \times 10^{-4}$ is adopted as the upper limit of the UCN loss probability coefficient for NiMo and PBIID DLC.

From the above, it is concluded that the upper limit values of the loss probability coefficient of NiMo and PBIID DLC were evaluated to be 3.6×10^{-4} and 3.4×10^{-4}, respectively, which are the point corresponding to 1 σ in Figure 6.37.

6.5 Short Summary

The results obtained in the storage experiment are summarized below.

1. The author succeeded in constructing a system that can store UCNs for the first time in the history of J-PARC. In this system, it is possible to control accumulation, storage and release of UCNs by management of opening/closing of two types of gate valve like Figure 6.31. The storage container is a cylindrical configuration of SUS316 with Φ498 mm $\times$ L500 mm, and its inner surface is subjected to the method of composite electrolytic polishing like Figure 6.9. The upper surface of the storage container can be replaced for a test material as shown in Figure 6.8 and Figure 6.10. By storing UCNs in the container and observing the time change for the number of UCNs, UCN loss probability coefficient for test material can be evaluated.

2. In unpolarized beam branch of J-PARC MLF BL05, the storage experiment using SUS316, NiMo/SUS304 and DLC/SUS304 were performed. As a result, the loss probability coefficient of SUS316 was evaluated to be $(2.4^{+0.31}_{-0.21}) \times 10^{-4}$ (the first storage experiment) and $(2.2^{+0.32}_{-0.24}) \times 10^{-4}$ (the second storage experiment). In addition, the upper limit value of the loss probability coefficient of NiMo and PBIID DLC were evaluated to be 3.6×10^{-4} and 3.4×10^{-4}, respectively, which are the point corresponding to 1 σ in Figure 6.37.
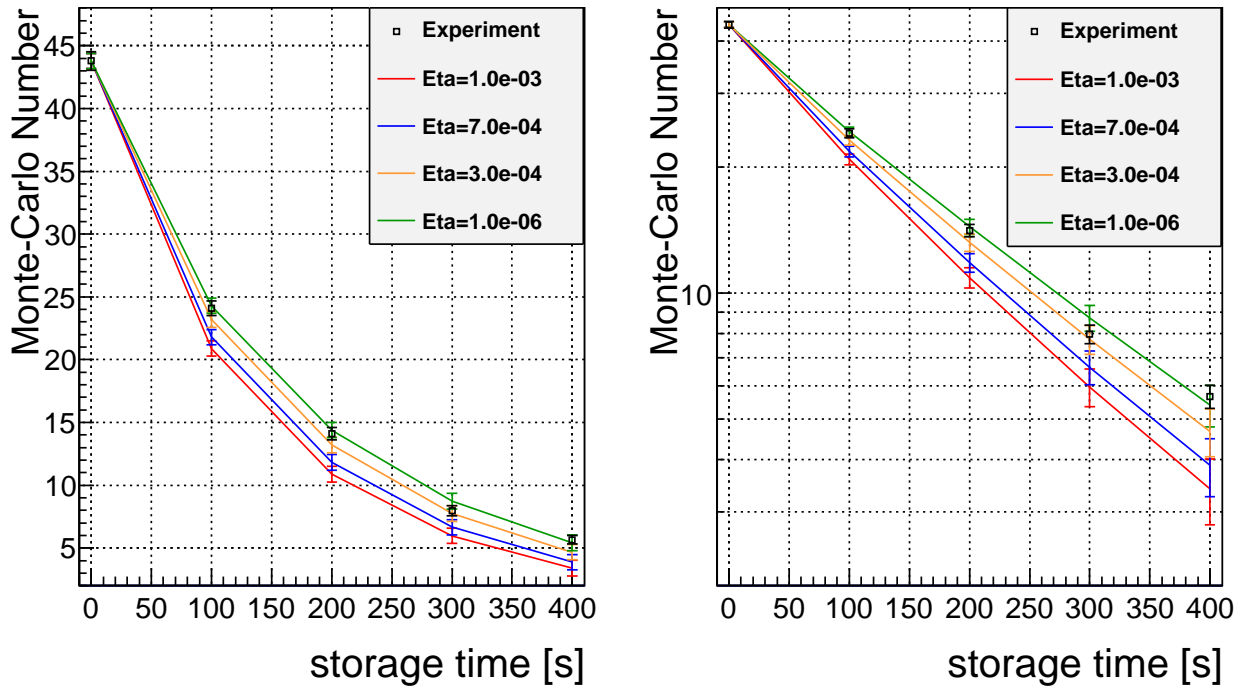
Figure.6.35 The comparison plot of template samples having different η. (Left) Linear scale (Right) Log Scale. The vertical axis is Monte-Carlo number, the horizontal axis is storage time, color lines are results of the template samples prepared assuming different η values. For reference, the obtained result of UCN storage experiment is also plotted in the Figure (square point). Each error bar of the square point corresponds to the statistic error of (6.5), while each error bar in the color line corresponds to the systematic error of (6.6). In this plot, it is assumed that NiMo is used for test material and the UCN loss probability coefficient of SUS316 is 2.3×10^{-4}. The plot of $\eta = 1 \times 10^{-6}$ corresponds to the case that the UCN loss is determined only by the SUS316 contribution. The value of each template sample at the time of zero is scaled to that of the actual measurement data.
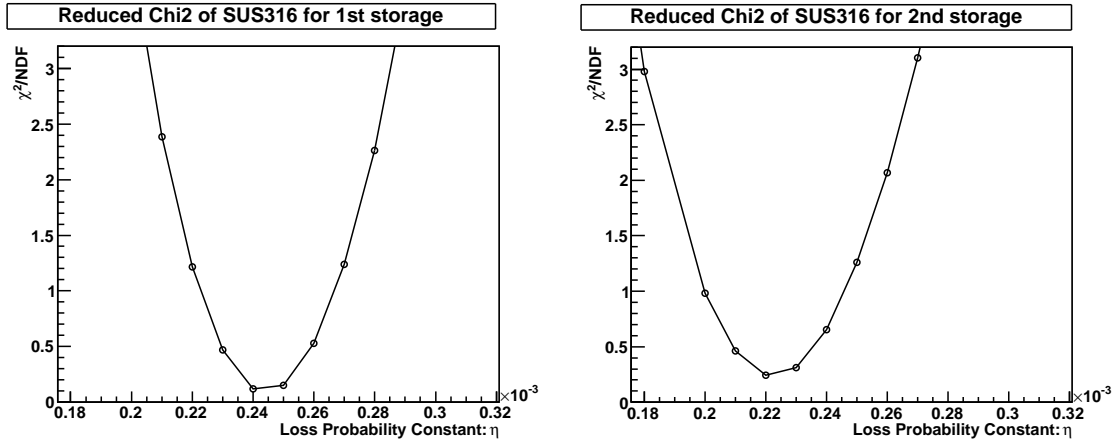
Figure.6.36 The dependency of the χ^2 of SUS316 on the loss probability coefficient. (Left) The case for first storage experiment (right) The case for second storage experiment. The vertical axis is reduced chi-square, and the horizontal axis is loss probability coefficient.
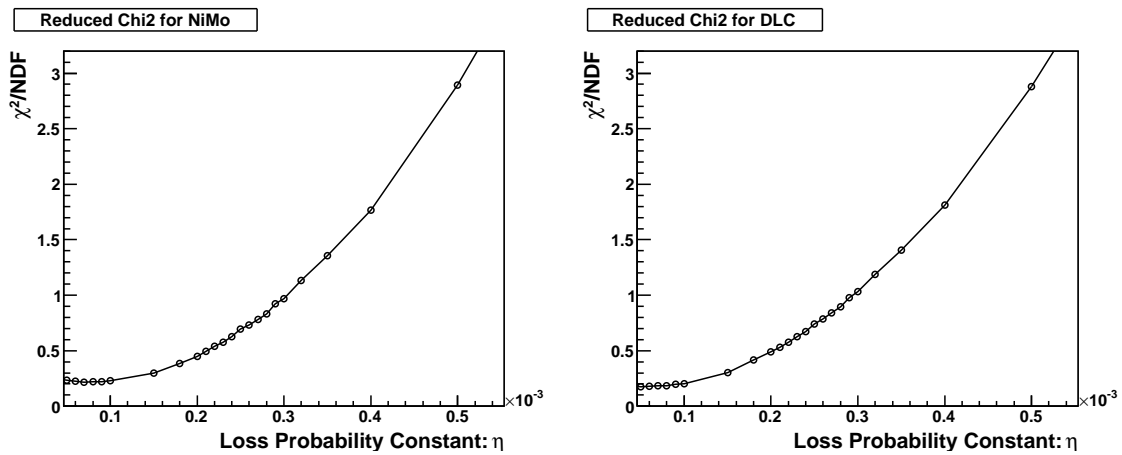
Figure.6.37 The dependency of the χ^2 of NiMo/PBIID DLC on the loss probability coefficient. (Left) The case for NiMo (right) The case for PBIID DLC. The vertical axis is reduced chi-square, and the horizontal axis is the loss probability coefficient η.

Chapter 7

Evaluation of the Experimental Sensitivity

In this chapter, the experimental precision of J-PARC P33 experiment was evaluated assuming the reflective materials described in chapter 5 and 6 are used. In this study, the statistical precision was evaluated by simulation, and the systematic error was derived through comparison with the preceding study. The details of the final evaluation of statistical precision and systematic error are described below.

7.1 Evaluation of Statistical Sensitivity

In this study, the statistical precision was evaluated using the procedure described in chapter 4 under the following simulation conditions:

UCN Production

Referring to the J-PARC Proposal 33, it was assumed that the pulsed proton beams with 400 MeV, 50 mA described in Figure 4.1 and Table 4.1 are supplied to a Pb target every 0.5 Hz for generating nuclear spallation neutrons. It was also assumed that spallation neutrons are cooled and converted into UCNs using the ultracold neutron source of Table 4.2 and Figure 4.2. Ultracold neutron source was assumed to consist of heavy water, liquid deuterium, and solid deuterium (sD_2). Furthermore, the density of UCN produced in sD_2 was assumed to be 5,800 UCN/cm^3 as evaluated in chapter 4.2.

Upscattering Cross Setion of sD_2 Converter

Although it is reported that other institutes such as PSI have achieved 98% for the ratio of ortho-D_2 to para-D_2, this study adopted 95% for conservative evaluation, and the up-scattering cross section was calculated with the relation in Figure 2.1.

Elastic Scattering of sD_2 Converter

In this study, referring to document [36], the elastic cross section and the mean-free path of 2.04 barn and 8.2 cm were assumed.

Experimental Setup

It was assumed that the experimental setup of Figure 4.9 consists of a solid deuterium converter of 100 mm diameter and 200 mm length, a transport guide of about 10 m long with 100×100 mm^2 cross section, a storage container of 470 mm diameter and 120 mm length, a focus guide, a

rebuncher and shutters.

Simulation Framework

This study used PHITS for the evaluation of the UCN yield, Geant4-UCN and an original simulation tool developed by the author for evaluation of UCN transportation and refocusing UCN and UCN storage simulations and systematic error. For the original simulation, the author implemented new functions in the Geant4 simulation framework. As a result, the refocusing of UCN, the opening and closing of shutters, the interaction during UCN reflection predicted by the theory of neutron optics, the non-specular reflection of UCN predicted by the micro-roughness model, and spin precession due to relativistic magnetic field are realized in our simulation study.

Storage Performance

The storage performance was determined by two factors: (1) the energy that incident neutron can be totally reflected from a material surface (2) the UCN loss probability less than 0.01 % per collision. The total reflection energy is the Fermi potential of the expression (2.2). On the other hand, the UCN loss probability is indicated by η of the expression (2.6). In this study, it was assumed to use reflective materials whose potential and η were measured by actual measurement for a reliable evaluation. NiMo (see chapter 5.1) and PBIID DLC (see chapter 5.2.2) can be used as such material. In this study, NiMo was assumed to be used for the electrode, and PBIID DLC was assumed to be used for the side surface of the storage container.

The measurement result for the Fermi potential and η are listed as follows:

Fermi potential(V_F)

Regarding V_F, 228 neV (NiMo) and 193 neV (PBIID DLC) were evaluated by the neutron reflectivity measurement described in chapter 5.4.1. The fermi potential for PBIID DLC was evaluated by X-ray reflectometry and RBS/ERDA. It was confirmed to be 8% higher than the neutron reflectivity measurement.

UCN loss probability (η)

η was evaluated by the UCN storage experiment described in chapter 6. It was confirmed that these upper limits of NiMo and PBIID DLC were evaluated be 3.6×10^{-4} and 3.4×10^{-4}, respectively, which are the point corresponding to 1 σ in Figure 6.37. On the other hand, η of PBIID DLC was evaluated by RBS/ERDA described in chapter 5.4.2. It was evaluated to be 1.5×10^{-4}.

In this study, for conservative estimation, 228 neV/3.6×10^{-4} (NiMo) and 193 neV/3.4×10^{-4} (PBIID DLC) were adopted as the result of V_F and η.

Transport Performance

Transport efficiency was determined by two factors, the Fermi potential, and non-specular reflection. In this study, ionized vapor deposition DLC (see chapter 5.2.1) and FAIPD DLC (see chapter 5.2.3) were assumed to be used on the inner surface of the transport guide. The potential of the two materials has been evaluated by the neutron reflectivity measurement described in chapter 5.4.1 and it was evaluated as 264 neV (IEM DLC) and 243 neV (FAIPD DLC). Regarding

non-specular reflection, it was handled using the micro-roughness model described in chapter 2.3. Regarding the parameters necessary to calculate the micro-roughness model, the root-mean-square roughness were evaluated to be 0.30 nm (IEM DLC) and 0.49 nm (FAIPD DLC) by a atomic force microscope, and the correlation length was chosen to be 33 nm (the averaged value of measured data of IEM DLC and NiC).

Implementation of Rebuncher

The rebuncher was assumed to be an apparatus shown in Figure 4.4 where the gradient static magnetic field of Figure 4.5 and the RF magnetic field of Figure 4.10 are applied. In the simulation, it is assumed that the rebuncher is installed at 5 m of the experimental setup with a spin reversal probability of 100 %. As a result, it was confirmed that UCNs refocus on the shutter 1 point of Figure 4.9 from 2.15 s to 2.2 s, as described in chapter 4.4.3.

Shutter Opening/Closing Time

It assumed that shutter 1 of Figure 4.9 is open from nuclear spallation between 2.15 s and 2.20 s.

The Condition of Best Statistical Sensitivity

For the evaluation of the statistical precision, the best statistical precision condition of the formula (3.9) was imposed, which is a reasonable assumption.

Experimental Period

Experiment period and the time assigned for the EDM measurement were assumed to be 3 years and 18 hours/day, respectively.

Measurement Time of UCN

It assumed that the UCN measurement time is 100 s.

Determination Strategy for Statistical Sensitivity

Under the following conditions, five variables of the expression (3.7) were determined to obtain the statistical precision of the neutron EDM measurement:

Electric Field Strength (E)

E is determined to be 10 kV/cm taking into account the discharge limit and past experimental results.

Visibility (α)

α is the amount determined by the spin polarization rate, the performance of the system counting polarized spins, and the effect of spin polarization relaxation time during storage. However, the J-PARC P33 experiment is not at the stage where the UCN spin can be measured. Therefore, in this study, the evaluation value 0.86 of the document [63] assuming time invariance of α during storage was adopted.

Storage Time (T)

The value of T was determined from the time which satisfies the condition of best statistical precision (expression (3.9)) by storage simulation.

Number of Measurement Repetition (n)

The value of n was derived from the experimental period, the UCN measurement time, and the T value.

Detected Counts (N)

The value of N was determined by evaluating the initial storage UCN number using the rebunch storage simulation described in chapter 4.4.4.

Rebunch Storage Number

In this study, the storage number was evaluated by the rebunch storage method for 100 s, and 90% of it was adopted.

As mentioned in "Transport Performance", the result of listed in Table 5.8 was used for the surface roughness of the transport guide assumed in this simulation study. Actually, in the measurement described in chapter 5, surface roughness was evaluated at several microscopic points but were not be compared with different samples. In addition, the sample size used in Table 5.8 was thought to be so small compared to the area of the transport guide of J-PARC P33. Thus, there is an uncertainty of surfaces roughness due to sample qualities or macroscopic positions. However, it is noted that substrates listed in Table 5.8 are typical semiconductor materials such as silicon and synthetic quartz. For those materials, surface flatness and zero defects are required. Hence, large area uniform polishing method is generally established for those materials. Furthermore, it is generally considered that film formation process used in this study is uniform on the substrate surface because films are created with continuous gas-like materials such as plasma and vapors. In the following, it is discussed how much a macroscopic surface roughness affects the evaluation result. According to the catalog of Shinetsu Corporation that delivers the synthesize quartz substrates used in this study, it is assured that the surface roughness is better than 0.3 nm Ra even if the size of the synthetic quartz is Φ 300 mm. On the other hand, Furuuchi Chemistry Corporation that delivers the silicon substrate used in this study ensured that the surface roughness of the silicon substrate is better than 0.6 nm Ra even if the size of silicon wafer is Φ 300 mm. Table 5.8 showed that the surface roughness of the neutron mirror was mainly determined by the surface roughness of the substrate. And also, for a gaussian distribution of unevenness of a surface, the RMS roughness R_{RMS} and the Ra roughness R_a satisfies following relation: $R_a = 1.25 R_{\mathrm{RMS}}$. So, assuming the surface roughness of a neutron mirror is 0.6 Ra $\times 1.25 = 0.75$ nm RMS in Figure 4.23 and 4.24, it is concluded that the deterioration of the statistical precision is suppressed to 10% or less. Hence, the surface roughness of each neutron mirror developed in chapter 5 is expected to be smooth enough for applying to an actual neutron EDM experiment.

Under the above assumption, the Time-of-Flight (TOF) distribution at the time when UCNs reach the shutter 1 position of Figure 4.9 was evaluated by the same procedure as described in chapter 4.4.3. The result is shown in Figure 7.1. The vertical axis is the number of UCNs transported, the horizontal axis is TOF, and the bin width is 50 ms. The blue line is the TOF distribution assumed to use IEM DLC, and the red line is the TOF distribution assumed to use FAIPD DLC. From the result, it is found that non-specular reflection is not critical for both cases and the large peak occurs from 2.15 s to 2.20 s.

Under the above assumption, the number of UCNs achieved by the rebunch storage method was evaluated by the same procedure as chapter 4.4.4. The result is shown in Figure 7.2. In this study, the storage simulation for one pulse was performed 100,000 times, and then the rebunch storage spectrum was created by piling them up. From Figure 7.2, 27,739 $\pm$ 146 (for IEM DLC) and 25,627 $\pm$ 141 (for FAIPD DLC) were obtained as the Monte Carlo Events. By using the formula (D.1) in Appendix.D,
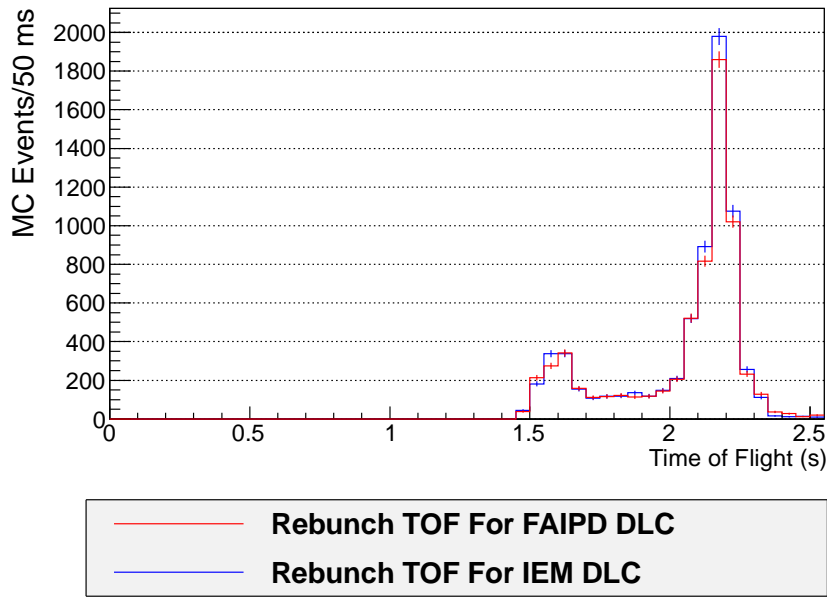
Figure.7.1 Time of Flight when refocused UCNs reach the shutter 1 position of Figure 4.9. (Left) The case for IEM DLC. (Right) The case for FAIPD DLC. The vertical axis is the number of transported UCNs, the horizontal axis is time when UCNs reach at shutter 1 position. The blue line is the TOF distribution assumed to use IEM DLC, and the red line is the TOF distribution assumed to use FAIPD DLC. It is noted that the number of Monte Carlo simulation is chosen to be 100,000.

the expected number of J-PARC P33 experiment was calculated. As a result, $N = 78,533 \pm 415$ (for IEM DLC) and $72,554 \pm 401$ (for FAIPD DLC) were obtained as the expectation value of the rebunch storage number.

Under the above assumptions, the time evolution of the number of stored UCNs was estimated by the same procedure as chapter 4.4.5. The result is shown in Figure 7.3. The spectrum is created by the storage simulation for 500 trials. The vertical axis is the number of stored UCNs, the horizontal axis is the storage time, the red line is the time evolution of the number of stored UCNs, and the black line is the number corresponding to 2τ. Finally, the 2τ value was evaluated to be 197^{+10}_{-10} s (for IEM DLC) and 198^{+10}_{-10} s (for FAIPD).

From the above, substituting five statistical variables, $E = 10$ kV/cm, $\alpha = 0.86$, $T = 2\tau = 197^{+10}_{-10}$ s (for IEM DLC) and 198^{+10}_{-10} s (for FAIPD), $N = 78,533 \pm 415$ (for IEM DLC) and $72,554 \pm 401$ (for FAIPD DLC), $n = 197,100 \pm 9,954$ experiments (IEM DLC) and $196,554 \pm 9,977$ experiments (FAIPD), into formula (3.7), $(\pm 1.6 \pm 0.2) \times 10^{-27}$ e · cm can be obtained as the statistical precision of an averaged value of IEM DLC and FAIPD DLC. This is the evaluation value for the statistical precision of the J-PARC P33 derived under the above conditions.
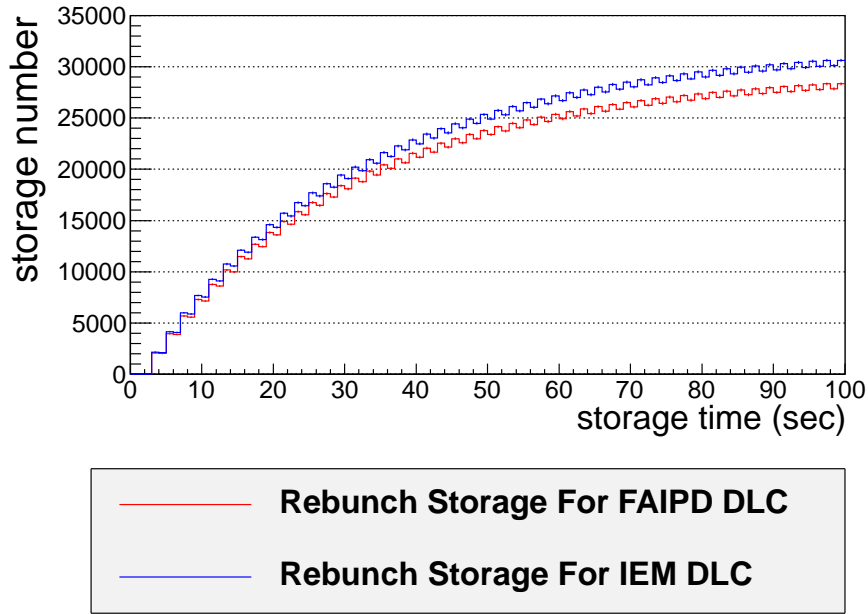
Figure.7.2   Time evolution of the rebunch storage number. (Left) The rebunch storage number when passing through the transport guide coated with IEM DLC. (Right) The rebunch storage number when passing through the transport guide coated with FAIPD DLC. The vertical axis is the rebunch storage number, the horizontal axis is the elapsed time during the rebunch storage. The red line is the spectrum considering only one pulse UCN, the blue line is the spectrum made with one pulse spectrum piled up. It is noted that one pulse spectrum is made with the number of Monte Carlo simulation 100,000.
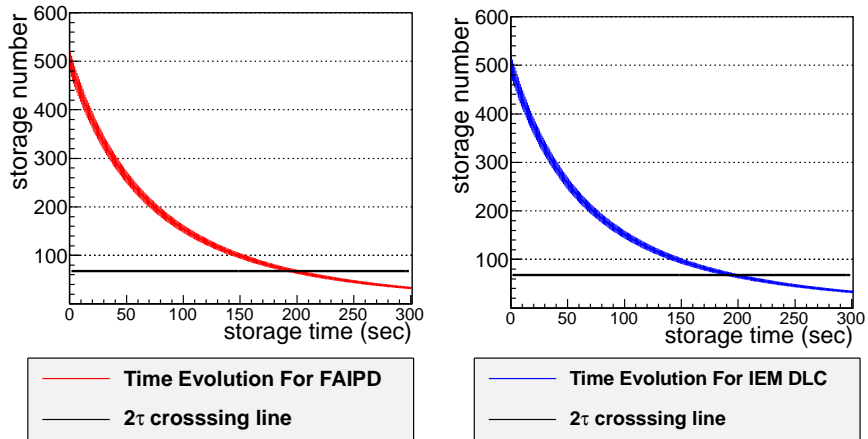
Figure.7.3   Time evolution of the number of UCNs confined in the storage container. (Left) Time evolution of UCNs supplied from the transport guide with IEM DLC. (Right) Time evolution of UCNs supplied from the transport guide with FAIPD DLC. The vertical axis is storage number, the horizontal axis is the elapsed time used in storage. Red and blue lines are time evolution of UCNs to be stored, the black line is the value corresponding two τ. It is noted that the number of Monte Carlo simulation is chosen to be 500.

154

7.2 Evaluation of Systematic Uncertainty

The systematic error depends strongly on the experimental procedure. In this study, the systematic error of the neutron EDM experiment was evaluated under the following assumption:

- The neutron EDM is measured from the time change of the polarization state when a magnetic field is applied to the polarized UCN filled in a storage container in one direction and an electric field is applied parallel/antiparallel to the magnetic field (see formula (3.1) in chapter 3.1).
- The neutron EDM is measured in the two cases of the magnetic field upward/downward, and a crossing point analysis is performed to eliminate the systematic error (GPE) due to the non-uniformity of the magnetic field inside the storage container (see Figure G.2 in Appendix.G).
- As described in chapter 3.2, the magnetic field fluctuation can be corrected by monitoring the intensity of the probe light emitted from ^{204}Hg passing through ^{199}Hg gas filled in the storage container (see Figure 3.6).

Generally, the systematic error arises from the subtraction of the two spin precession frequencies corresponding to when applying the electric field and magnetic field parallel/antiparallel. In this chapter, the systematic errors due to such procedure is called direct systematic error.

In this study, direct systematic error was evaluated as follows:

GPE

 In this study, the contribution of GPE was assumed to be eliminated by using the crossing point analysis described in Appendix.G.

v×E (Translation)

 When UCNs are collectively translated and the electrostatic field is curved in the storage container, a relativistic magnetic field occurs which is oriented parallel/antiparallel to the static magnetic field. The ILL experiment estimated it to be 1×10^{-29} e · cm (see document [2]). This thesis adopted it as evaluation of the systematic error of v×E (Translation). (see Appendix.I.4 for details).

v×E (Rotation)

 In this study, a simulation similar to the document [82] was used to evaluate the systematic error which is caused by the coupling of the electric field distortion inside the container and the relativistic magnetic field due to the collective rotational motion of UCNs (see chapter I.5). As a result, it was confirmed that even when the non-specular reflection probability caused by collision is 1%, the systematic error is suppressed to be 1×10^{-28} e · cm or less. In fact, the inner surface of the sidewall of the storage container is difficult to be polished to achieve a diffuse probability less than 1 %. Therefore, its systematic error is evaluated to be 1×10^{-28} e · cm or less (see Appendix.I.5 for details).

Leakage Current

 Regarding the systematic error induced by the magnetic field due to the application of electric field

(called Leakage Current), the evaluation using an actual experimental apparatus is important. However, because our group does not yet have an experimental facility for an evaluation, this systematic error was evaluated by scaling the evaluation value of the ILL experiment to the electric field strength of this experiment. As a result, 2×10^{-28} e $\cdot$ cm was obtained as the evaluation value (see Appendix.I.9 for details).

Electric force

With respect to the systematic error caused by the container being squeezed by the electric force (called electric force), it was evaluated to be 3×10^{-35} e $\cdot$ cm. This result corresponds to the measurement result of the distortion of the container at the time of the electric field application described in [83] (see Appendix.I.10 for details).

AC HV Ripple

With respect to the systematic error caused by the magnetic field generated when switching the direction of applied the electric field (called AC HV Ripple), the evaluation using an actual experimental apparatus is important. However, because our group does not yet have an experimental facility for evaluation, its systematic error was evaluated by scaling this evaluation value of the ILL experiment to the electric field strength of this experiment. As a result, 2×10^{-29} e $\cdot$ cm was obtained as the evaluation value (see Appendix.I.11 for details).

Uncompensated B drift

Regarding the systematic error caused by the magnetic field emitted from the mu-metal magnetized in the direction of application of the electric field (called uncompensated field drift), the evaluation using an actual experimental apparatus is important. However, because our group does not yet have an experimental facility for an evaluation, in this study, the source of this error is regarded as the same of ILL experiment. In the ILL experiment, the magnitude of the systematic error was evaluated as 3.4×10^{-27} e $\cdot$ cm [2] (see Appendix.I.3 for details).

For evaluation of this systematic error, it is also important to take into account the effect that is inversely proportional to the distance from mu-metal surface. ILL experiment used the mu-metal of the diameter of 1.5 m. On the other hand, this study assumes the use of mu-metal of diameter 3 m, and the systematic error 1.7×10^{-27} e $\cdot$ cm is adopted as evaluation of uncompensated B drift.

Hg EDM

Regarding the systematic error caused by EDM of ^{199}Hg, an EDM value $(2 \pm 6) \times 10^{-29}$ e $\cdot$ cm was adopted in this study, which is the theoretical value of the Hg EDM described in the document [2] (see Appendix.I.8 for details).

Direct Light shift

Regarding the systematic error caused by the change of the intensity of the probe light of ^{204}Hg depending on the direction of the applied electric field (Direct Light Shft), it is important to evaluate it using the actual apparatus. However, because our group does not yet have an experimental facility for evaluation, its systematic error was evaluated in the same manner as the ILL experiment described in the document [2]. As a result, 2×10^{-28} e·cm was adopted as the systematic error of Direct Light Shift in this study (see Appendix.I.7 for details).

In this study, it was assumed that GPE, which is a particularly large source, is removed by using the crossing point analysis. However, in that case, it becomes necessary to evaluate as new systematic sources due to the shift of the crossing point (Figure G.2 in Appendix.G) depending on the direction of the applied magnetic field. In this chapter, this kind of systematic error is called indirect systematic error.

In this study, the indirect systematic error was evaluated as follows:

Dipole Effect

The dipole magnetic field emitted from the magnetized part near the experiment apparatus change the crossing point and produces an indirect systematic error. In the ILL experiment, two sources of the dipole magnetic field were confirmed. In the literature [41], one is called "Door Cavity Dipole" and the other is called "Other dipole fields". For the evaluation of such dipole effect, it is necessary to perform comprehensive evaluation including the effect of the dipole magnetic field itself and the correction by using a high accuracy magnetometer. However, because the experimental setup is not available, it was not possible to study how systematic sources exist in apparatus. Therefore, in this study, it was assumed that the systematic error source is the same as the one actually confirmed in the ILL experiment.

Regarding Door Cavity Dipole, the effect can be suppressed to $(0.71 \pm 0.07) \times 10^{-26}$ e · cm by the analysis in the ILL experiment [2]. Therefore, this value was adopted as the evaluation value of the Door Cavity Dipole in this study. It is noted that 0.71×10^{-26} e·cm is not the term regarded as an error, but a correction term. Only the term of 0.07×10^{-26} e·cm should be regarded as an error for the Door Cavity Dipole. In this thesis, this evaluation value is adopted as one of Door Cavity dipole effect. Regarding Other dipole fields, the ILL experiment evaluated to be 6×10^{-28} e·cm [41][2]. The systematic effect of Other dipole fields was caused by the accuracy of the fluxgate magnetometer. Therefore, it is possible to improve the error by newly conducting a magnetic field survey using a high precision magnetometer. For example, PSI has successfully developed a Cs magnetometer that can measure at 10 pT accuracy with a distance of 4 cm from the wall at the present time. If residual magnetic fields are measured at a distance of 2 cm from the wall, its accuracy corresponds to 80 pT and Other dipole effect can be reduced to be 1/12 from the evaluation value of the error of ILL. Our group does not yet have a highly precise magnetometer. Hence, assuming that the Cs magnetometer is used, it is concluded that the effect of Other dipole fields is reduced to be 5×10^{-28} e·cm. In this thesis, this evaluation value is adopted as Other dipole fields effect.

From the above, in this study, 0.07×10^{-26} e·cm and 5×10^{-28} e·cm were adopted as the evaluation value of Other dipole effect.

Quadrupole Difference

If there is incompleteness in the symmetry of the mu-metal, the magnetic field distribution in the lateral direction inside the container changes slightly depending on the direction of the applied magnetic field. This appears to change the precession cycle of UCN according to the direction of the magnetic field, resulting in a change of the crossing point. This systematic error is called

Quadrupole Difference. This was evaluated with the spin precession change due to the rotation of the earth. For the evaluation of the Quadrupole Difference, it is important to check the distribution of the transverse magnetic field distortion components present in the actual experimental apparatus, but there is no setup yet for this experiment. Therefore, in this study, for the Quadrupole Difference, the same value as in the ILL experiment described in the document [2], $1.4 \pm 0.1 \times 10^{-27}$ e · cm was adopted (see Appendix.I.2 for details).

Indirect Light shift

The probe light emitted from ^{204}Hg causes an effective magnetic field as in formula (I.2), which affects the spin state of ^{199}Hg. Because the spin state of ^{199}Hg is used for correcting the magnetic field drift, the crossing point shifts through the Hg co-magnetometer. Such a systematic error is called the Indirect Light Shift. For the evaluation of the Indirect Light Shift, it is important to check the correspondence relation between the effective magnetic field and the probe light intensity using an actual setup, but there is no setup yet for this experiment. Therefore, in this study, for the Indirect Light shift, the same value of the ILL experiment described in the document [2], 0.8×10^{-27} e · cm was adopted (see Appendix.I.6 for details).

If these systematic errors are considered to be independent and propagated as a sum of squares, 2.5×10^{-27} e · cm is obtained as the total systematic error. This is an outline of the evaluation of the systematic error in this study.

7.3 Final Evaluation

By combining the statistical error derived from the above condition with the systematic error, the precision of the neutron EDM experiment is calculated to be $(\pm 1.6 \pm 0.2(\text{stat}) \pm 2.5(\text{syst})) \times 10^{-27}$ (e·cm) (see Table 7.1 for details). This is the final evaluation value of the experimental precision of the J-PARC P33 experiment.

Error Source	Error Value (e·cm)
Statistical Precision	1.6×10^{-27}
Door Cavity Dipole	7×10^{-28}
Other Dipole Fields	5×10^{-28}
Quadrupole	1.4×10^{-27}
Uncompensated B drift	1.7×10^{-27}
v×E (Translation)	1×10^{-29}
v×E (Rotation)	1×10^{-28}
Light shift (indirect)	8×10^{-28}
Light shift (direct)	2×10^{-28}
Hg EDM	6×10^{-29}
Leakage current	2×10^{-28}
Electric force	3×10^{-35}
HV AC ripple	2×10^{-29}
Total Sum of Systematic Errors	2.5×10^{-27}
Experimental precision	$(\pm 1.6(\text{stat}) \pm 2.5(\text{syst})) \times 10^{-27}$

Table.7.1   Summary of Experimental Precision

Chapter 8

Summary and Future Prospect

8.1 Sumarry

This thesis deals with the first basic study of the proposed experiment for searching the neutron electric dipole moment using ultracold neutrons produced by the J-PARC pulsed proton beams of the world's highest instantaneous luminosity.

The neutron electric dipole moment (EDM) is one of the most sensitive physical quantity to BSM. Currently, the best upper limit of the neutron EDM, obtained by the ILL experiment, is 3×10^{-26} e·cm (90% CL). Many BSM models such as SUSY predict 1 to 2 orders of magnitude larger EDM that can be detected by improving the current experimental techniques. The neutron EDM can be most precisely measured by confining UCNs in a storage container to which an electric field is applied and detecting the spin change when polarized UCNs interact with the electric field. Because the current neutron EDM measurement is mainly limited by the statistical error, a more intense UCN source is key to improving the experimental sensitivity. In recent years, a new production method that cools fast neutrons to ultracold neutrons by inelastic scattering of phonons in materials such as solid deuterium or He-II has been developed and put into practice, which is expected to achieve UCN production much higher than the ILL experiment. Therefore, new neutron EDM experiments adopting the super-thermal method are being planned all over the world. In particular, there is significant progress at PSI in Switzerland and TRIUMF in Canada, and they have announced that it has prospected to improve one or more order of magnitude from the ILL experiment. Both groups produce fast neutrons using an accelerator and cool it using the converter material such as liquid helium or solid deuterium.

At J-PARC, a new experimental concept is proposed for searching the neutron electric dipole moment (J-PARC P33 experiment). This proposal consists of the following three basic ideas:

1. To generate fast neutrons by using the J-PARC LINAC pulsed proton beams of the world's highest instantaneous luminosity.
2. To produce pulsed UCNs by using the super-thermal method and the solid deuterium converter.
3. To transport UCN effectively by using the newly proposed rebuncher system.

Actually, the phase space density of UCNs in the solid deuterium converter produced by J-PARC LINAC pulsed proton beams is estimated to be ~ 4.1 UCN(cm)$^{-3}$(m/s)$^{-3}$, while the phase space density

of UCNs for the ILL experiment is estimated to be ~ 0.084 UCN$(\text{cm})^{-3}(\text{m/s})^{-3}$ at its transport guide exit. When the generated UCNs are utilized efficiently by using transport with keeping the density, the statistical sensitivity of J-PARC P33 experiment should be expected to be drastically improved similarly to PSI and TRIUMF. However, despite the high experimental potential of the J-PARC P33 experiment, a reliable evaluation was yet to be performed so far.

In this thesis, fundamental properties of UCN and conceptual design of the J-PARC P33 experiment are discussed. The result of such a basic study which the author mainly performed are listed as follows:

(α): Development of a dedicated simulation for the J-PARC P33 experiment

For J-PARC P33 concept, there was a problem that the experimental capability had not been evaluated. Thereby, the experimental sensitivity expected at the present time could not be evaluated, and any optimization studies to improve the sensitivity could not be done. In this experiment, the sensitivity greatly depends on a lot of factors such as the experimental setup, the experimental procedure, the magnetic field structure of the rebuncher, the performance of the ultracold neutron source, the storage and transport efficiency of UCNs. Therefore, the author developed the full simulation that can deal with not only an experimental system and its entire procedures based on J-PARC P33 concept but also the storage and transport efficiency that depend on the performance of the reflective material. Specifically, PHITS and Geant4UCN, together with an original program that is developed by the author, were used. With these tools, J-PARC P33 experiment can be totally simulated from the upstream to the downstream, by which the statistical sensitivity of the J-PARC P33 experiment can be numerically evaluated.

(β): Evaluation of the effects of reflection performances

Regarding evaluation of the experimental sensitivity of J-PARC P33, it was particularly difficult to understand the effects of the non-specular reflection and reflection loss which depend on the performance of the reflective material used in the neutron EDM experiment; the non-specular reflection has the effect of deteriorating the rebunch efficiency and the reflection loss at the reflection has the effect of decreasing the number of UCNs that can be stored and transported. Regarding the non-specular reflection, in recent years, it turned out that Lambert's cosine law, which was believed to be able to handle non-specular reflection well, did not match actual measurement, and its effect could not be accurately evaluated. In this study, micro-roughness model, a theoretical model confirmed to be in good agreement with the actual measurement, was used for properly evaluating the effect of non-specular reflection. Regarding the reflection loss, neutron optical theory was used to represent it. The total reflection energy, V_F, and the UCN loss probability coefficient, η, were used for controlling the degree of the reflection loss, while RMS roughness b was used for controlling the behavior of the non-specular reflection. These reflection interactions were incorporated into the above-described simulation. Finally, by performing the simulation while changing values of V_F, η, and b within a realistic condition, the dependence of the statistical sensitivity on the performance of the reflective material of UCN of J-PARC P33 could be numerically clarified.

(γ): Development and Evaluation of highly efficient neutron mirrors

The precision of the neutron EDM experiment was seriously affected by the performance of the

reflective material used in the experiment. Therefore, high efficient neutron mirrors, Nickel Molybdenum alloy (NiMo) and Diamond-Like Carbon (DLC), were developed. NiMo was prepared by the binary vapor deposition, and DLC was fabricated by methods of Filtered Arc Ion Plating Deposition (FAIPD) and Ionized Evaporation Method (IEM) and Plasma Based Implantation Deposition (PBIID). These reflection performances were evaluated by surface analyses such as neutron reflectometry, Rutherford backscattering spectroscopy/elastic recoil detection analysis (RBS/ERDA), X-ray reflectometry, electron microscope, glow discharge optical emission spectrometry (GDOES), and so on.

(δ): Performing UCN storage experiment at J-PARC

UCN storage experiment was performed to directly measure η value at J-PARC Materials and Life Science Experimental Facility (MLF). In particular, the author has succeeded in performing the storage experiment at first in J-PARC history, and thereby established the solid basis for the further development.

(σ): Evaluating experimental sensitivity and feasibility

The sensitivity was evaluated by full simulation with the above-evaluated reflection performances along with the systematic error evaluated in a similar manner as the ILL experiment. Compared with the sensitivity of the ILL experiment, the feasibility evaluation at J-PARC P33 has been performed.

As for topics of (α) and (β). the simulation study assuming the J-PARC P33 was performed experiment as follows:

(1) the J-PARC pulsed beams of 20 MW/pulse (400 MeV, 50 mA) of 0.5 Hz (2) the rebunch method (3) the UCN production in solid deuterium (sD$_2$) of 5,800 UCN/cm^3 (4) the UCN loss at reflection (5) the experiment setup based on the J-PARC P33 (6) the ortho-para ratio of sD$_2$ of 95:5 (7) the elastic cross section of sD$_2$ of 2.04 barn (8) the gradient magnetic field of the rebuncher of -3.2 T/m (9) the total experiment period of 3 years (10) the time assigned to EDM measurement of 18 hours/day.

In this study, the Fermi potential of the transport guide was chosen to be 210 neV, that of the container side was chosen to be 91 neV or 160 neV, and that of the top-bottom side was chosen to be 210 neV, respectively. The UCN loss probability coefficient of the storage container was chosen to vary from $8 \times 10^{-5} \sim 5 \times 10^{-4}$, and that of the transport guide was chosen to be 0. The RMS roughness of the transport guide was chosen to vary from 0 to 3 nm, and that of the other parts was chosen to be 0.

From this simulation study, it was found that the statistical precision was evaluated as $(7.2 \pm 0.2) \times 10^{-28}$ e·cm (best case) to $(5.9 \pm 0.2) \times 10^{-27}$ e·cm (worst case). There was a difference of 8 times between two cases; such a large difference was due to the change in the rebunch efficiency and the storage efficiency. The statistical precision was deteriorated by the non-specular reflection, and it was changed by about 1.6 times with b varied from 0 nm to 3 nm. In addition, the statistical precision changed by about 3 times as η varies from 8×10^{-5} to 5×10^{-4}, while it improved by $1.5 \sim 1.7$ times with the potential of sidewall increased 91 neV to 160 neV. In this way, the dependence of the statistical sensitivity on the performance of the reflective material of UCN of J-PARC P33 was numerically clarified, which showed that development of highly functional reflective materials is extremely effective for improving the

statistical sensitivity of J-PARC P33.

As for topics of (γ) and (δ), Nickel Molybdenum Alloy (weight ratio Ni:Mo = 85:15) and Diamond-Like Carbon (DLC) have been developed. NiMo and DLC were fabricated using a quite unique film formation techniques such as binary vapor deposition method, Ionized Evaporation Method (IEM), Plasma Based Ion Implantation Deposition (PBIID) and Filtered Arc Ion Plating Deposition method (FAIPD). These reflection performance have been evaluated using various surface analysis methods as follows:

Total reflection energy

The total reflection energy, the Fermi potential V_F, was evaluated by neutron reflectivity measurement in J-PARC Material Life science Facility Beam Line16. As a result, 228 ± 13 neV for NiMo and 190 ± 7 neV $\sim 243 \pm 8$ neV for IEM DLC and about 193 ± 11 neV for PBIID DLC and 264 ± 14 neV for FAIPD were obtained. In the case of IEM DLC, the same value as nickel was achieved, which is a highly functional reflective material. In the case of PBIID DLC, the quite high Fermi potential was achieved as candidates possible to use as the sidewall material of the storage container. In the case of FAIPD DLC, it was confirmed that the value was achieved, which is comparable to highest total reflection energy as mirrors developed for neutron EDM measurement. In the case of IEM DLC, X-ray reflectivity and RBS/ERDA were also used for evaluation, and as a result, it was found that its evaluated value amount to $\sim 8\%$ higher than the case of neutron reflectivity measurement.

The UCN loss probability coefficient

The UCN loss probability coefficient, η, was evaluated by UCN storage experiment performed at J-PARC, which is the first case in J-PARC history. It was confirmed that these upper limits of NiMo and PBIID DLC were evaluated be 3.6×10^{-4} and 3.4×10^{-4}, respectively, which are the point corresponding to 1 σ in Figure 6.37. In general, it is also possible to evaluate η from the surface hydrogen amount. Therefore, for PBIID DLC, the indirect measurement has been performed. As a result, it was confirmed that its evaluation value corresponded to 1.5×10^{-4}.

RMS surface roughness

Atomic force microscope and a profilometer were used for evaluation. As a result, 0.30 ± 0.01 nm for IEM DLC and 1.7 ± 0.4 nm for PBIID DLC and 0.49 ± 0.01 nm for FAIPD DLC were obtained.

Finally, as for topics of (σ), assuming the reflection performance obtained as above and the experimental setup used in the full simulation study, the statistical precision of J-PARC P33 experiment was estimated. In this study, for conservative evaluation, the results of neutron reflectivity measurement and UCN storage experiment were adopted as reflection performance. Assuming that IEM DLC or FAIPD DLC is used for the transport guide and NiMo and PBIID DLC are used for the storage container, the statistical precision of an averaged value of both cases was estimated to be $(1.6 \pm 0.2) \times 10^{-27}$ e·cm. Therefore, by combining it with the systematic error 2.5×10^{-27} e·cm, it is concluded that the experimental precision is $(\pm 1.6 \pm 0.2(\text{stat}) \pm 2.5(\text{syst})) \times 10^{-27}$ e·cm. This is the first comprehensive evaluation of the experimental capability based on J-PARC P33 concept including the reflection performance, which provides a reliable basis for future experiment design.

8.2 Future Prospect

The result of this simulation showed that the sensitivity of the J-PARC P33 experiment exceeds the ILL experiment which is the current world's highest precision. However, it turned out that neutron EDM measurement of O(10^{-28} e·cm), which PSI and TRIUMF are aiming for, has not been reached. In the following, it is discussed what is necessary to perform the neutron EDM verification of the world's most precision. For improving statistical precision, following two experimental techniques are thought to be effective. First, by increasing the diameter of the solid deuterium converter and the cross-section of transport guide, the total UCN flux can be increased more according to the area, which enables us to perform the neutron EDM experiment using multiple measurement cells. Second, with the current rebuncher system, by adjusting applying the RF magnetic field and controlling the velocity distribution of the multiple UCN pulses, 3~4 pulses can be focused at the same time, and the UCN density can be increased more. For the systematic error, total systematic uncertainty can be improved effectively by suppressing GPE with the measurement cell size smaller. In such a way, by increasing the number of UCNs that can be used in the experiment and making the measurement cell size smaller simultaneously, both the statistical error and systematic errors are expected to be improved effectively. Thereby, it is considered that the experiment based on the J-PARC P33 concept not only easily achieves 10^{-27} e·cm, but also can verify several 10^{-28} e·cm by making full use of experimental techniques. From the above, it is concluded that this study has succeeded in providing a solid basis for future experiment design aiming for the neutron EDM verification with world's highest precision.

Acknowledgement

Appendix.A

Time-of-Flight Method

In following, explain the time-of-flight(TOF) method to measure the wavelength spectrum of low-speed neutrons. Since low-speed neutron has no charge, its detection is performed by measuring secondary particles derived from nuclear reaction with helium 3 or lithium 6 having a large neutron capture cross section. Neutron absorption reactions of helium 3 and lithium 6 are given by

$$\text{n} +^3 \text{He} \to^3 \text{H} + \text{p} + 0.76\text{MeV} \tag{A.1}$$

$$\text{n} +^6 \text{Li} \to^3 \text{H} + \alpha + 4.79\text{MeV} \tag{A.2}$$

Express t_0 as the time when the neutron is emitted from the neutron source, L as the distance between the pulsed neutron source and the detector, and t as the time when the detector measures the secondary particle. In general, using L, t, and t_0, the velocity (wavelength) component of the neutron can be obtained as follows.

$$v = \frac{L}{t - t_0} \tag{A.3}$$

$$\lambda = \frac{h}{mv} \tag{A.4}$$

where h is Plank's constant, and m is the mass of neutron. $\Delta t = t - t_0$ is called the time of flight (TOF) of neutron. The method of determining the velocity (wavelength) of neutron by using the equation of (A.4) is called the TOF method.

Generally, the reaction cross section of slow neutron with velocity v has the following rate dependence.

$$\sigma(v)v = \sigma(v_0)v_0 \tag{A.5}$$

where v_0 represents the thermal neutron velocity 2200 m/s.

In general, the probability P causing nuclear reaction with atoms when slow neutrons penetrate until x cm in the material can be written as follows.

$$P(x, \lambda) = 1 - \exp(-\rho\sigma(v_0)\frac{v_0}{v}x) = \exp(-\rho\sigma(v_0)\frac{v_0}{\frac{h}{m\lambda}}x) = 1 - \exp(-p_{\text{eff}}\lambda) \tag{A.6}$$

where ρ is the density of atoms per cubic cm constituting the material.

The parameter p_{eff} of the equation (A.6) is an important parameter indicating the detector performance, from which it is possible to evaluate the velocity dependence of the detection efficiency. Although p_{eff} can be extracted by fitting the measured velocity distribution with the equation (A.6), actual measurement data includes effects such as attenuation on the detector surface, attenuation due to cut efficiency to the wave height distribution, counting loss, and so on. Therefore, by fitting with the equation (A.6) the distribution corrected for these effects, it is possible to evaluate the detection efficiency using p_{eff}.

The gamma ray background, which is a problem in J-PARC MLF, is synchronized with the time at which proton beam spallation reaction occurs. Therefore, SN ratio can be effectively improved by using TOF method.

Appendix.B

Beam Fluctuation Suppression Using MNH10/4.2F

In this section, the method to correct beam fluctuation using MNH10/4.2F is described. March 2015, both UCN flux and neutron flux not converted to UCN was measured for 40,000 seconds continuously at J-PARC MLF BL05 unpolarization beam branch. In this measurement, DUNia-10 had been fixed at the viewport of Doppler Shifter and MNH10/4.2F had been fixed at beam emission port. The count ratio of DUNia-10 to MNH10/4.2F is shown in Figure B.1. The standard deviation of Figure B.1 was 1.4%, which was smaller than J-PARC proton beam current fluctuation 3%. The fact indicated that the count of MNH10/4.2F was correlated 1.4 % with the intensity of UCN beam. Thus, it can be understood that the UCN beam fluctuation can be suppressed to 1.4% by comparing the count of MNH10/4.2F.
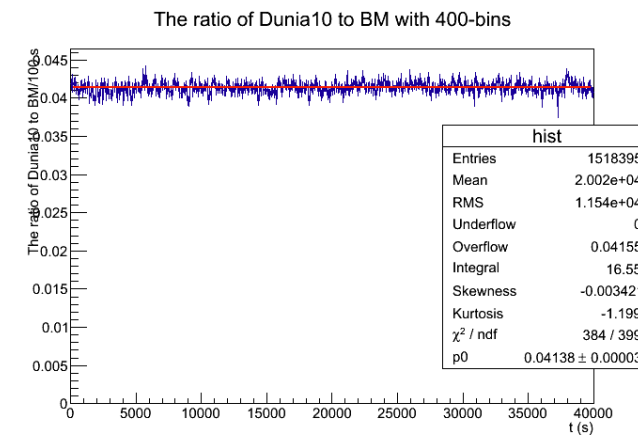

Figure.B.1 J-PARC MLF beam stability. The horizontal axis is DAQ time, the vertical axis is the ratio of UCN to cold neutron count. The red line is the fitting result by the zeroth order equation. Bin width was 100 s.

Appendix.C

Dependence of Detection Efficiency of DuNia-10 on Position and Time

In this section, the time dependence of the count rate of DUNia-10 is described. Such dependency was evaluated with a cold neutron beam irradiated at the center of DUNia-10 at a low divergence beam branch of J-PARC MLF BL05. These measurements were performed 4 times, before and after the first storage experiment and before and after the second storage experiment (see Table C.1)). In this section, each of measurements is classified as Event 1, 2, 3, 4.

ID	Situation
1	before the first storage experiment
2	after the first storage experiment
3	before the second storage experiment
4	after the second storage experiment

Table.C.1   Classification of low divergence beam measurement

The count rate and wave height distribution obtained from the measurement at low divergence beam branch are given in Figure C.1 and Figure C.2. It is found that the count rate decreases with time by about 10 %, and the pulse height distribution becomes closer to the low channel side.

It has confirmed that there is a position dependency in the counting rate of DUNia-10. The result of investigating the position dependence of the pulse height distribution by the on-plane scan using the low divergence beam is summarized in the Figure C.4. It can be seen that the wave height distribution greatly varies depending on the position.

The counting rate of the storage experiment has already been summarized into the Figure 6.33 and Figure 6.34. Between the beginning of the first storage experiment and at the end of the second storage experiment, the count rate has varied by 15%. It is larger than the time change obtained by measurement of the low divergence beam. Therefore, an explanation is required.

The reasons for this discrepancy can be considered as the following two points.

1. In the low divergence measurement, only the center of DUNia-10 was used to count the number

of UCNs, while in the storage experiment UCNs were detected using the whole surface. Thereby, the difference of the counting rate due to position dependency appeared strongly.

2. If the wave height distribution becomes closer to low channel, the cut efficiency of the wave height deteriorated with time growth. In this way, the counting rate further is thought to be decreased.
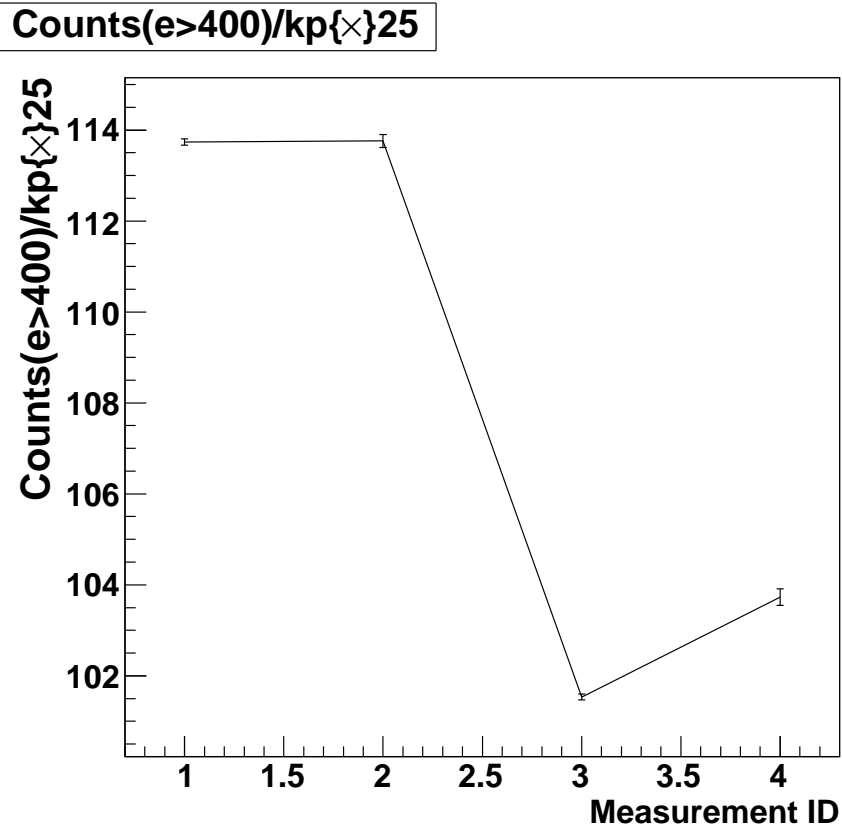
Figure.C.1 Time change of count rate of DUNia-10 found by low divergence beam measurement. The horizontal axis is measurement id and the vertical axis is count rate. It turns out that the count rate becomes lower as the time spend.
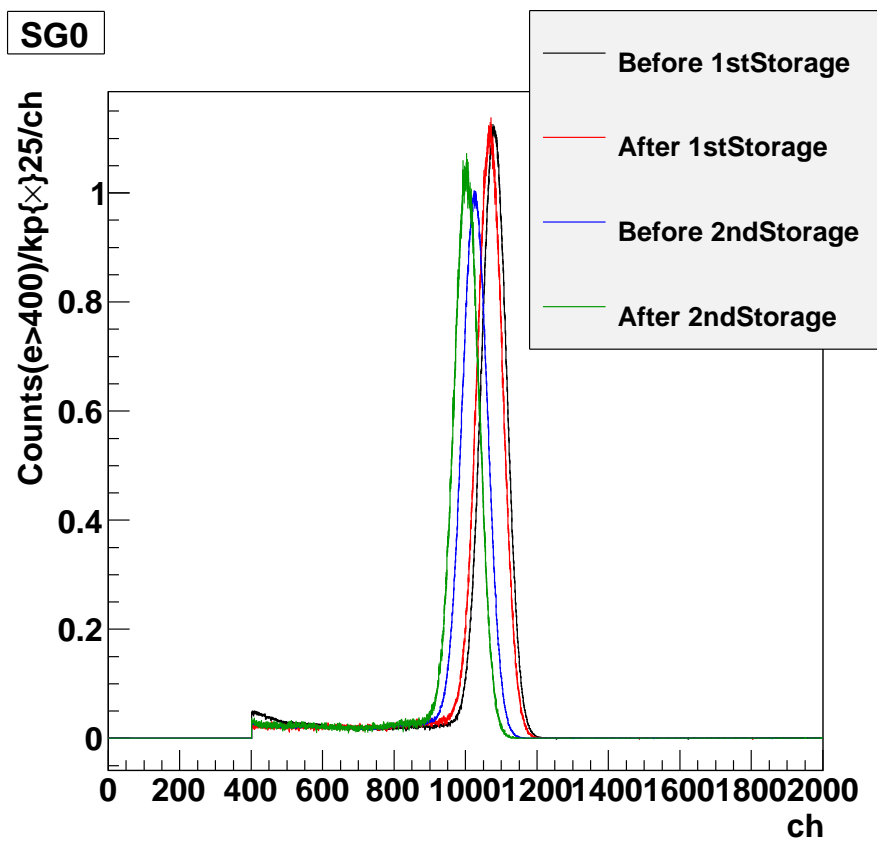
Figure.C.2   Time change of pulse height of DUNia-10 found by low divergence beam measurement. The horizontal axis is the pulse height value A/D converted, and the vertical axis is the count rate. We use neutrons of several meV to 25 meV for the measurement. It turns out that the distribution is shifting to the low channel side as time grow
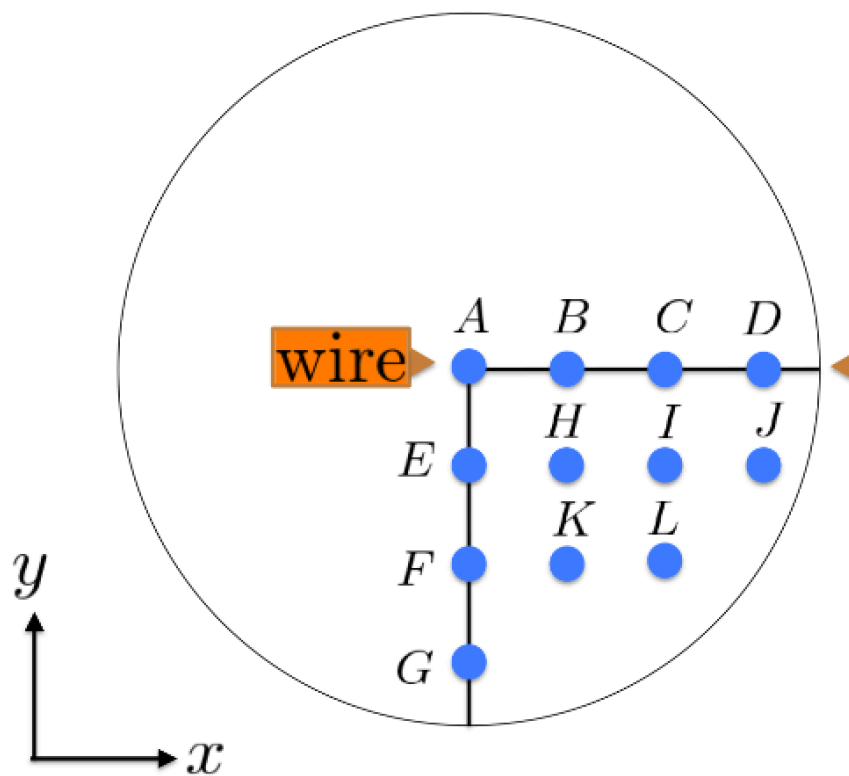
Figure.C.3 Surface position of DUNia-10 scanned in a low divergence beam branch. Since the electric field structure of DUNia-10 must be circularly symmetric, a low divergent beam was irradiated only to the lower right quadrant by 12.5 mm.
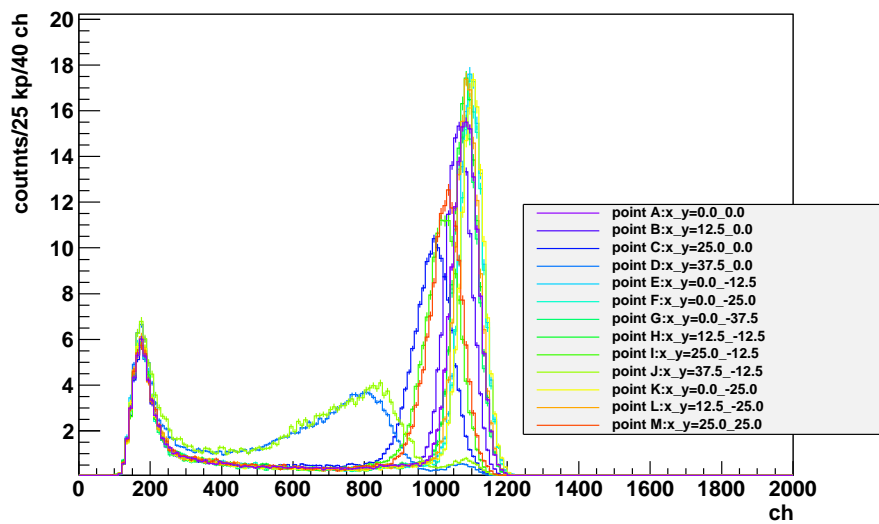
Figure.C.4   Pulse height distribution obtained by surface beam scan of DUNia-10. Pulse height distribution obtained by scanning of Figure C.3. The horizontal axis represents the A/D converted value of the wave height, and the vertical axis represents the count. The correspondence of each position is explained in the legend of the figure.

Appendix.D

Evaluation of UCN Density by Rebunch Storage Method

In general, UCN density can be calculated by using the following expression (D.1).

$$\rho_{\mathrm{chamber}} \mathrm{V}_{\mathrm{chamber}} = \frac{\rho_{\mathrm{sD2}} \times \mathrm{V}_{\mathrm{sD2}}}{\mathrm{N}_{\mathrm{Try}}} \times \mathrm{N}_{\mathrm{Survive}} \times \epsilon_{\phi} \qquad (\mathrm{D.1})$$

where ρ_{sD2} is the UCN density in solid deuterium converter, ρ_{chamber} is the UCN density in the container, $\mathrm{N}_{\mathrm{Try}}$ is the total trial number of transportation Monte Carlo simulation, N_{Survive} is the number of Monte Carlo events of UCN reaching in the container, $\mathrm{V}_{\mathrm{sD2}}$ is the volume of solid deuterium, and $\mathrm{V}_{\mathrm{chamber}}$ is the volume of the storage container. Finally, ϵ_{ϕ} represents the ratio of the phase space volume of UCNs produced in solid deuterium converter to the phase space volume of UCNs that can be extracted outside.

It is noted that, in this study, ρ_{sD2} is evaluated to be 5,800 UCN/cm^3 and ϵ_{ϕ} correspond to (150 neV)$^{3/2}$/(252 neV)$^{3/2}$. For reference, the UCN density in the storage container calculated by the expression (D.1) is summarized in Table D.1. It is noted that the effect of non-specular reflection is not taken account in Table D.1.

potential ID	$\eta = 8 \times 10^{-5}$	$\eta = 1 \times 10^{-4}$	$\eta = 3 \times 10^{-4}$	$\eta = 5 \times 10^{-4}$
1	16.8 UCN/cm3	16.5 UCN/cm3	13.3 UCN/cm3	11.3 UCN/cm3
2	35.2 UCN/cm3	34.5 UCN/cm3	27.5 UCN/cm3	22.8 UCN/cm3

Table.D.1   The UCN density in the storage container, calculated by the rebunch storage simulation.

Appendix.E

Evaluation of Time Dependence of Rebunch Storage Number

In the case of potential ID 0 of loss probability 3×10^{-4}, the time change of the number of UCNs in the container using the rebunch storage method and that of not using rebunch storage method are given in Figure E.1.
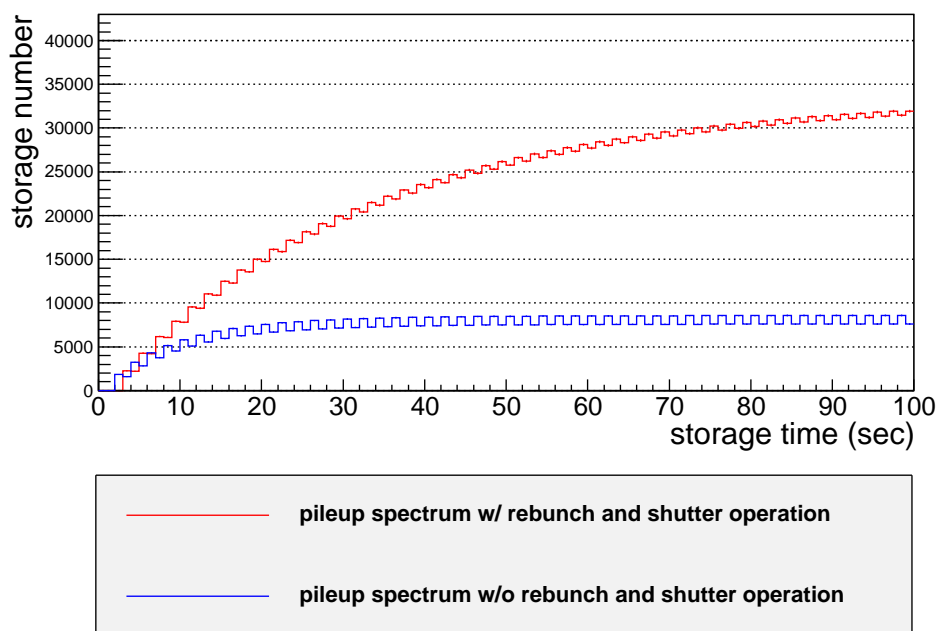
Figure.E.1   Effect of rebunch on the number of storage

Thanks to rebunch storage, the density increase about 4 times.

Appendix.F

Details of Storage Experiment not to be Described in the Text

In this section, what was too detailed to explain in the text is described.

F.1 Wave height distribution

An example of the wave height distribution obtained during the storage experiment is shown in Figure F.1.

Figure.F.1 Example of wave amplitude distribution at the storage experiment.

F.2 Released Time Distribution

 A typical released time distribution of the storage experiment is shown in Figure F.2. Horizontal axis is released time and vertical axis is counting rate. This result indicates the time evolution of the number of UCNs in the storage container of 98 Litter. It can be found that 100 s is enough long for evacuating UCNs

stored in the storage container. In this analysis, the integration value of the released time distribution 0 to 100 s was used as the UCN detection number, i.e. foreground. Because the count rate converges to a fixed value at 100 s or more, the background as the 2nd storage experiment was evaluated by using the integration value of 100 to 200 s. For the first storage experiment, it is note that the average of the run described in Table 6.2 was taken as the background.
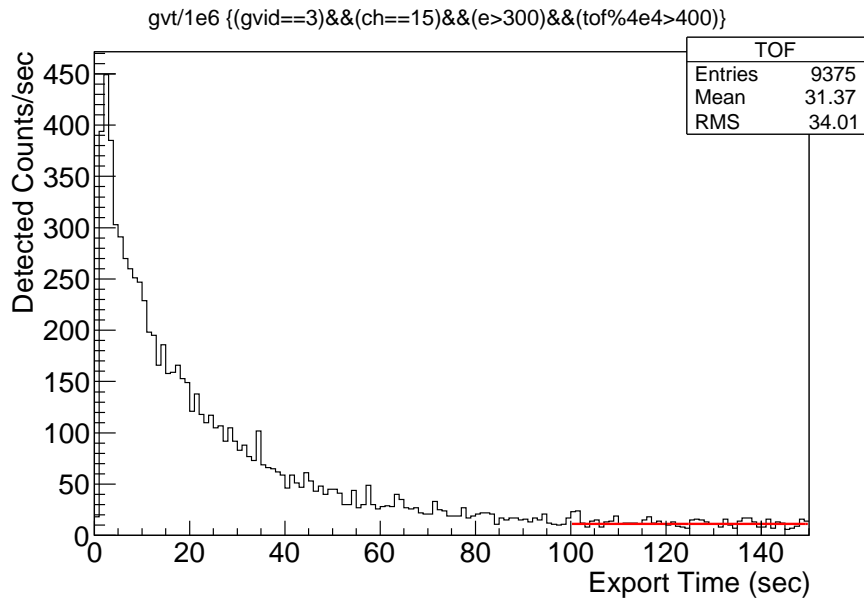
Figure.F.2 Example of released time distribution of the second storage experiment. The vertical axis shows detected counts, and the horizontal axis shows the released time. Because the count more than 100 s converges to constant, the time range can be regarded as the background.
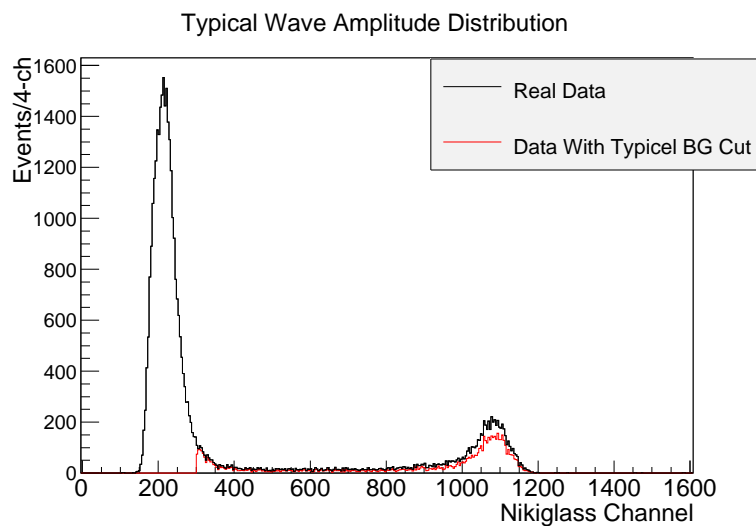
F.3 Import Time Distribution

In order to check import time dependency, the following sequence was adopted as follows:

1.import Accumulate UCNs in storage container with either of time between 10 s to 45 s.
2.storage Storage UCNs for 25 s.
3.release Release UCNs for 100 s and detect the number of UCNs.
4.cycle again Repeat procedure of 1 to 3 two times.

The dependency of the detected counts on the import time is shown in Figure F.3. In this study, the distribution of Figure F.3 is referred to as "Import Time Distribution" hereafter. Note that the statistical error was large because measurement cycles was performed only two times, and also the background has not been subtracted. The detected counts of Figure F.3 indicates that the storage number has reached maximum at 35 s. On the other hand, the import time in the storage experiment was 50 s (see chapter 6 for details). Therefore, it is considered that UCN was accumulated to the maximum during the storage experiment.

Figure.F.3   Dependence of the UCN detection number on the import time

Appendix.G

Geometric phase effect and crossing point analysis

This section describes the mechanism of systematic error called geometric phase effect (GPE). In the experimental environment, there is a magnetic field gradient $\frac{dB}{dz} = \sim 10$ nT/m and the associated curvature of the magnetic field. Generally, a transverse magnetic field proportional to $\frac{dB}{dz}$ is generated in the radial d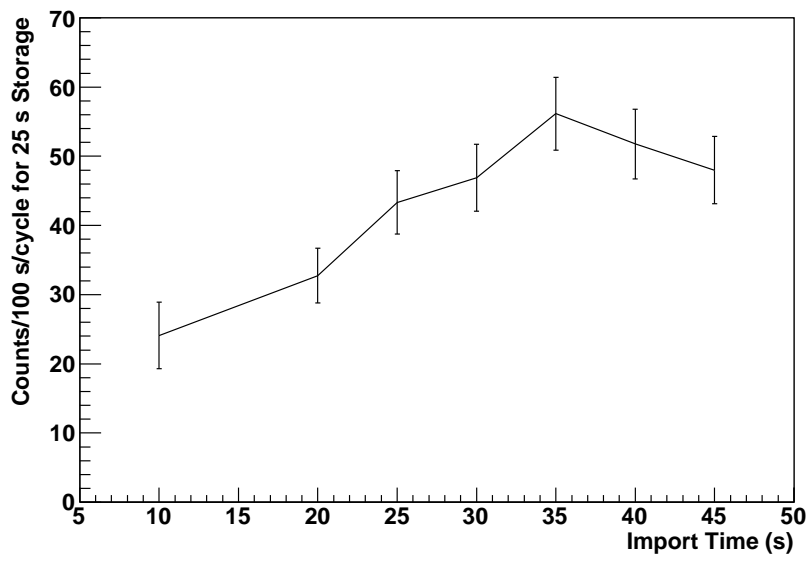irection inside the storage container. In this case, the magnitude is about the same as the relativistic magnetic field which UCNs feel in the neutron EDM experiment [84]. When the relativistic magnetic field combines with the distortion of the magnetic field, it becomes a resultant magnetic field whose contribution changes according to the direction and trajectory of the electric field.

For example, if UCN is rotating, the resultant magnetic field also rotates. In order to understand this mechanism, the time evolution (orbital dependence) of the resultant magnetic field of UCN which is translating or rotating in a cylindrical container is shown in Figure G.1 [84]. Obviously, the resultant magnetic field rotates in both cases. Therefore, the rotation period of the spin precession changes via the expression (2.12).
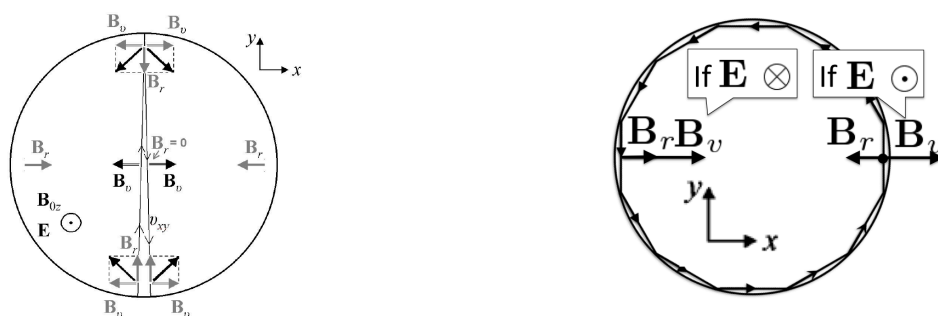
Figure.G.1 The relativistic magnetic field dependence on trajectories, the image is cited from [39]. (Left) the case of translation (Right) the case of rotational motion. The synthetic magnetic field vector is made of relativistic magnetic field and environmental magnetic field. It rotates with time and its magnitude depends on the direction of application of the electric field, which cannot be canceled by subtraction between the upper and lower electric field. Therefore, it becomes a systematic error via the expression (2.12).

The systematic error due to the distortion of a magnetic field and the relativistic magnetic field has a characteristic that it accumulates as the particle takes a specific orbit. Therefore, it is possible to statistical suppression by diffusing the trajectory of particles. However, even if the trajectory is completely diffused, systematic errors cannot be canceled as a whole. This systematic error which cannot be completely canceled is called Geometric Phase Effect (GPE).

The false neutron EDM due to GPE caused from UCNs and Hg atoms confined in a cylindrical vessel of diameter R to which uniform gradient magnetic field applies are represented as follows [84]:

$$d_{n,f} = -\frac{\hbar}{4} \frac{\frac{dB_z}{dz}}{B_z^2} \frac{v_{xy}^2}{c^2} \left[1 - \frac{\omega_r^2}{\omega_0^2}\right]^{-1} \tag{G.1}$$

$$d_{Hg,f} = \frac{\hbar}{8} \frac{dB_z}{dz} \frac{\gamma_{Hg}\gamma_n R^2}{c^2} \left[1 - \frac{\omega_0^2}{\omega_r^2}\right]^{-1} \tag{G.2}$$

where $d_{n,f}$ is false neutron EDM caused by UCNs, $d_{Hg,f}$ is false neutron EDM caused from Hg atoms, B_{0z} is the static magnetic fields used in the neutron EDM experiment, v_{xy} is the average neutron velocity on the orthogonal direction to the magnetic field, ω_r is the angular velocity, ω_0 is the Larmor precession frequency, $\frac{dB_{0z}}{dz}$ is the longitudinal magnetic field gradient in the storage container.

If assuming $B_{0z} = 1$ μT and $\frac{dB}{dz} = 1$ nT/m and $v_{xy} = 2.67$ m/s and the same condition of the ILL experiment, we can get -1.1×10^{-27} e·cm (UCNs) and 5×10^{-26} e·cm (Hg atoms) as false EDM due to GPE (see [84] for details). Hg GPE is not only 50 times larger than neutron GPE, but also cause the largest systematic error.

In the ILL experiment, GPE is effectively eliminated by using the characteristic that the expression (G.2) is linearly proportional to the vertical gradient of the magnetic field. This technique is called crossing point analysis. Specifically, the following function of R_a can be defined with vertical gradient [84].

$$R_a = \frac{\omega_n}{\omega_{Hg}} \frac{\gamma_{Hg}}{\gamma_n}$$
$$= 1 \pm \frac{\Delta h}{B_0} \frac{dB}{dz} \tag{G.3}$$

where Δh is the difference of the center of gravity between Hg and UCN, and $\pm$ sign denotes the direction to which the static magnetic field B_0 is applied (upward or downward).

In general, using formula (G.2) and (G.3), the false EDM caused by Hg GPE $d_{n,f}$ is written as follows [84]:

$$d_{Hg,f} = \pm \frac{\hbar}{8} |\gamma_n \gamma_{Hg}| \frac{R^2 B_{0z}}{\Delta h c^2} (R_a - 1) \tag{G.4}$$
$$= \pm k(R_a - 1) \tag{G.5}$$

The plot of $R_a - 1$ obtained in the ILL experiment is shown in Figure G.2. The horizontal axis is $R_a - 1$ and the vertical axis is the actual measured EDM value. On the crossing point, the contribution of GPE can be regarded as 0 (see formula (G.5) and (G.3)). Therefore, by analytically extracting neutron EDM from the crossing point, it is possible to eliminate the contribution of GPE.

This is an outline of crossing point analysis. In this study, the crossing point analysis was used to evaluate the experiment of J-PARC P33.
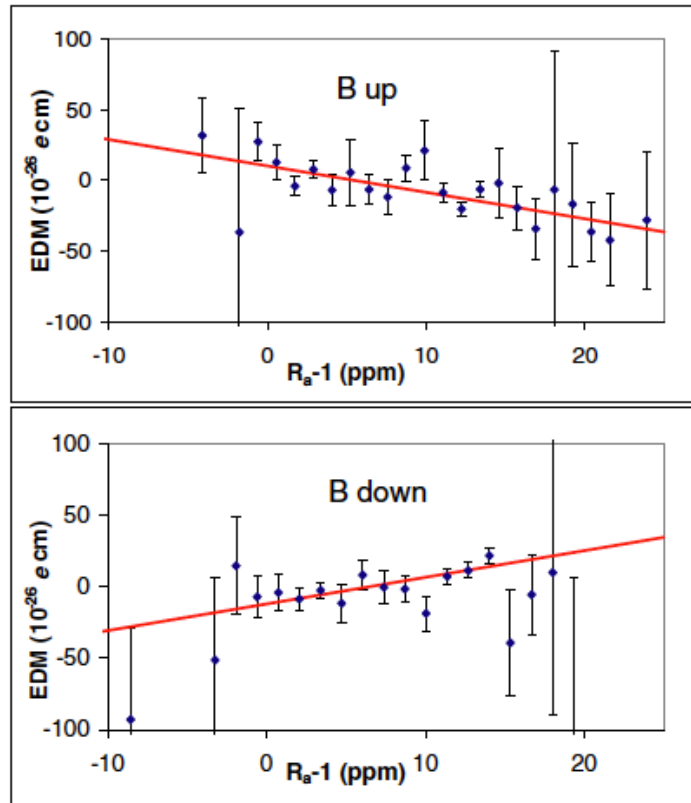
Figure.G.2   Example of the crossing point analysis, the image is cited from [41][39]. The horizontal axis is $R_a - 1$, the vertical axis is measured EDM $d_{n,meas}$ as a function of $R_a - 1$. The measured EDM at the cross point can be regarded as the value whose GPE is removed. For details see the text.

Appendix.H

Dependence Study of the Instantaneous Intensity on Cut-Out Time Width

In this thesis, the period that shutter is open after the J-PARC proton beam injection is referred to as "cut-out time". By comparing the cut-out time, we can investigate the effect of the shutter opening/closing on the instantaneous intensity of the refocused pulse UCN beams entering to the measurement cell. The higher the instantaneous intensity is, the more the rebunch efficiency improves. The aim of this appendix to show the dependence of the refocused pulsed UCN beams intensity on such a cut-out time width. In general, effectiveness of rebunch method changes depending on how the cut-time out width is synchronized with. In this study, the following extremely cases are considered as listed in Table H.1.

case/operation	What the cut-time out width is synchronized with.
case1	Not Synchronize (Shutter Always Open)
case2	Synchronize Average Beam Arrival Time
case3	Synchronize Refocused Beam Peak Arrival Time

Table.H.1   The column to explain what means each cut-out time width

The case listed of Table H.1 corresponds to the following cut-out time width:

1. the case that the shutter is always open

   This cut-out time width corresponds to the proton beam repetition period, and it is chosen to 2 s as seen in 4.1.

2. the synchronization with average beam

   This cut-out time width corresponds to the full width of time of flight of UCN beams, and it corresponds to from 1.4 s to 2.4 s as seen in Figure 4.16.

3. the synchronization with refocused beam

   This cut-out time width corresponds to the time of flight of refocused UCN beam, and it corresponds to 2.15 to 2.2 s as seen in Figure 4.16.

In this study, both effects of the shutter opening/closing and the non-specular reflection are tested. For evaluating it, transport simulation is performed in the same manner as described in chapter 4.4.3.

In this transport simulation, it was recorded the time when UCNs can reach the shutter 1 position of Figure 4.3. The transport simulation repeats 100,000 times to make the time of flight distribution. In the analysis, the number of Monte Carlo assigned in the period within the above-shown cut-out time width is compared. The obtained comparison result is shown in Figure H.1. The vertical axis is the number of Monte Carlo events normalized to 1 s, the horizontal axis is the RMS value of the surface roughness of transport guide, and the line color denotes the correlation length. Each frame corresponds to the cut-out time width, the upper left is the case that cut-out time width 0 s $\sim$ 2 s, the upper right is that the case the cut-out time width 1.4 s $\sim$ 2.4 s, and the lower left is that the case that the cut-out time width is 2.15 s $\sim$ 2.2 s. The high the instantaneous intensity is, the more effectively the UCN density in the measurement cell improves. Comparing the result of the cut-out time width 0 s $\sim$ 2 s and that of the cut-time width 1.4 s $\sim$ 2.4 s, there is two times difference in the normalized beam intensity. Comparing the result of the cut-out time width 0 s $\sim$ 2 s and that of the cut-time width 2.15 s $\sim$ 2.2 s, there is about eleven times difference in the normalized beam intensity. These result indicate that the way of synchronizing the shutter operation with UCN beams have a serious effect on the UCN density to be achieved in the experiment.
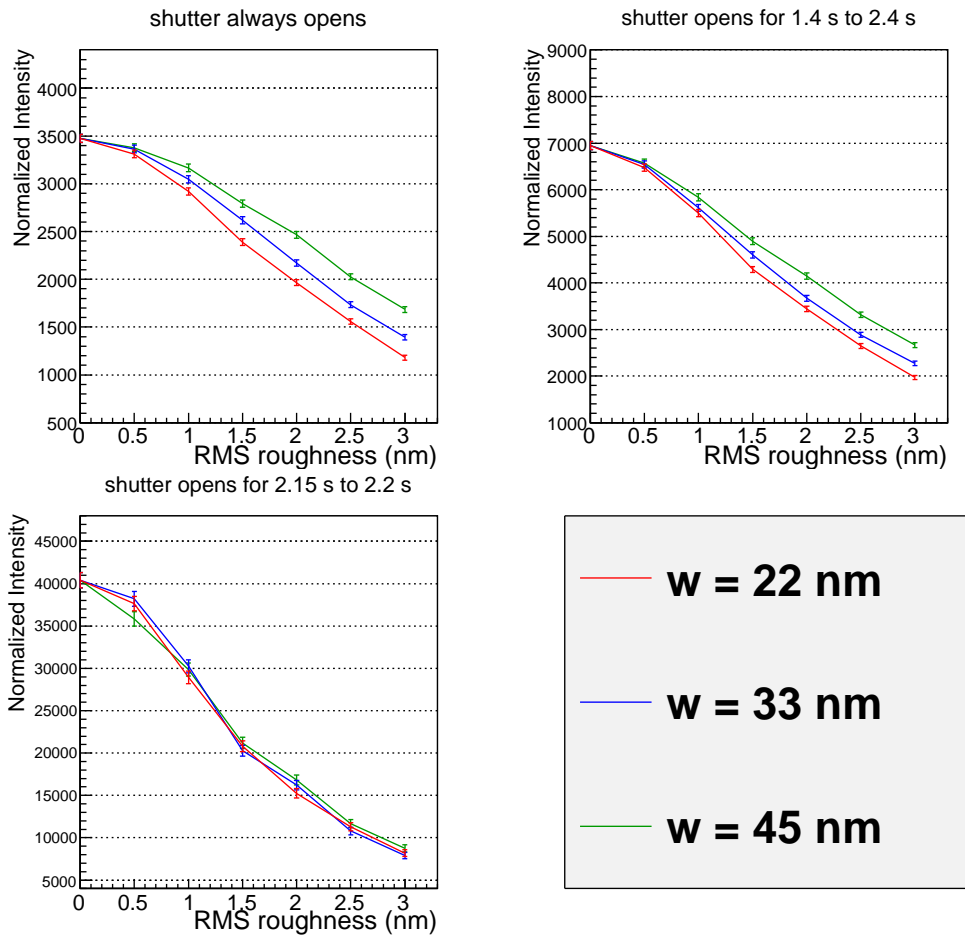
Figure.H.1 Dependence of the rebunch efficiency on the shutter opening/closing operation along with the surface roughness. The vertical axis is the number of Monte Carlo events normalized to 1 s, the horizontal axis is the RMS value of the surface roughness of transport guide, and the line color denotes the correlation length. Each frame corresponds to the cut-out time width, the upper left is the case that cut-out time width 0 s $\sim$ 2 s, the upper right is the case that the cut-out time width 1.4 s $\sim$ 2.4 s, and the lower left is the case that the cut-out time width is 2.15 s $\sim$ 2.2 s.

Appendix.I

Source is of systematic errors of UCN EDM measurements

This Appendix summarizes the source is of systematic errors of the experiments for neutron EDM measurements. Following lists are taken from the latest analysis of the ILL experiment.

I.1 Local dipoles (Door cavity dipole and Other dipole fields)

The systematic error generated by external magnetic field is called as Local dipole. In the ILL experiment, experimental setup had been surveyed from 2 cm distance by using fluxgate magnetometer with accuracy 1 nT to eliminate external magnetic fields. However, after the ILL experiment, two local dipole were found in the setup. One is called "Door cavity dipole" and the other is called "Other dipole fields" [41]. It was estimated that Local dipole existed 1.3 cm behind UCN door and its intensity was -4.2×10^{-7} A·m². ILL group succeed in reducing it by analytical technique, and finally, the door cavity dipole contribution decreased to be $(0.71 \pm 0.07) \times 10^{-26}$ e·cm[2]. It is noted that 0.71×10^{-26} e·cm is not the term regarded as an error, but correction term. On the other hand, a source of Other dipole fields was found by the magnetic field survey performed at PSI after the ILL experiment. In the ILL experiment, it was estimated that the error amount to 6×10^{-27} e · cm, which corresponded to the accuracy of the fluxgate magnetometer used in the ILL experiment [41][2].

I.2 Quadrupole difference and Earth Rotation

If magnetic field gradient is 0, GPE and Local dipole do not occur. But if $\frac{dB}{dz} = 0$, $\frac{dB}{dy} \neq 0$ and $\frac{dB}{dx} \neq 0$ is satisfied, the magnetic field is twisted in the xy plane, causing another systematic error. Such a twisting magnetic field B_q is called quadrupole field and B_q is expressed as $B_q = (-qx, qy, 0)$ [84][85] .
Indeed, by the magnetic field survey performed at PSI after the end of the ILL experiment [2], it was present in the EDM experiment setup used for the ILL experiment.

Because of Hg moving at high speed, the quadrupole field is averaged and does not contribute. On the other hand, because of UCN moving at slow speed, such a small distortion cannot be ignored and the local distortion magnetic field results in the phase shift of UCNs. As a result, the frequency ratio of Hg

to UCN changes, and $R_a - 1$ used in crossing point analysis is changed by ΔR_Q. If ΔR_Q does not depend on the direction of the static magnetic field, the crossing point does not move and can be neglected as a systematic error. However, it is actually confirmed that such quadrupole field has asymmetry depending on the applied direction of the static magnetic field, which causes the systematic uncertainty.

In general, Earth Rotation also behaves like the quadrupole effect and affects the frequency ratio of Hg to UCN. The ILL experiment estimated the systematic error caused by the sum of earth rotation and quadrupole effect as $0.33 \pm 0.14 \times 10^{-26}$ e $\cdot$ cm [2]. It is noted that 0.33×10^{-26} e·cm is not the term regarded as an error, but correction term. This thesis adopted it as evaluation of the systematic error of quadrupole effect and earth rotation.

I.3   Uncompensated B drift

The ILL experiment confirmed that the existence of a magnetic field changing according to the direction of the electric field. This is thought to be due to the hysteresis of the mu-metal according to the positive or negative of the voltage. This magnetic field has a R^{-3} dependence, while the center of gravity of Hg and UCN in the storage container differs by 0.3 cm. This generates a systematic error via Hg co-magnetometer. In the ILL experiment, this systematic error is called uncompensated B drift. This systematic error is inversely proportional to the distance from mu-metal surface [41][42][2]. In the ILL experiment, mu-metal of diameter was 1.5 m. Therefore, its systematic error can be suppressed if the diameter of mu-metal is increased.

The strength of this dipole field was estimated to be ~ 30 fT [83], and the magnitude of the systematic error was evaluated as 3.4×10^{-27} e $\cdot$ cm [2]. If the error is suppressed by using the magnetometer, a new fluxgate meter that can achieve accuracy 10 fT or better is needed.

I.4   v$\times$E (Translation)

When UCNs collectively translate and an electrostatic field is curved in the storage container, a relativistic magnetic field occurs oriented parallel/antiparallel to the static magnetic field. It depends on the direction of electric field application, so that mimic EDM signal occurs. The ILL experiment estimated it as 1×10^{-29} e $\cdot$ cm at most even if large [2].

I.5   v$\times$E (Rotation)

When UCNs collectively rotate inside the storage container to which the curving electrostatic field is applied, a relativistic magnetic field occurs behaving as mimic EDM signal. The evaluation value of this systematic error have not been determined because the magnitude of this error differs from 2×10^{-27} e $\cdot$ cm $\sim 5 \times 10^{-28}$ e·cm depending on the reference such as [41], [83] and [85]. Therefore, this study evaluates the degree of this systematic error as below.

The systematic error due to rotational motion of UCNs and distortion of the electric field can be evaluated by the phase shift of the UCN spin precession using the following expression (I.1):

$$d_{v \times E} = \frac{\hbar \Phi}{4Et} \tag{I.1}$$

where E is the strength of electric field, t is the measurement time, and Φ is the phase difference caused by the systematic error.

I.5.1 [Evaluation Condition]

Generally, this systematic error was determined by the degree of rotational motion of UCN and the degree of distortion of the electric field. In addition, a non-specular reflection diffuses the collective rotational motion inside the container and suppress systematic errors. In this study, to determine systematic errors, the degree of rotational motion, that of distortion of the electric field, and that of non-specular reflection were assumed as follows:

Rotational motion

> The rotational motion is thought to be caused by the setup misalignment. In this thesis, the rotational collective motion was created assuming that the transport guide was moved by 10 mm laterally relative to the center of ultracold neutron source.

Non-specular reflection

> In this thesis, this systematic error suppression effect was expressed by using Lambert's cosine law of formula (2.18) assuming probabilities of 0%, 1%, 5% and 10%.

Electric field distortion

> Electric field distortion can be estimated by using Finite Element Calculation (FEM). In this study, ANSYS simulation framework version 17 was used [86]. The electric field distortion was determined by the position of the edge of the electrode and the misalignment of electrodes. In this study, the degree of distortion was created as follows:

> (Edge position)

>> The container having three size electrodes of Φ 470 mm, Φ 600 mm and Φ 800 mm were assumed on the finite element calculation. The result is shown in Figure I.1. As the electrode becomes bigger, the electric field distortion decreases more.

> (Misalignment of electrodes)

>> In this study, the condition of misalignment of electrodes was assumed in as shown Table I.1. The degree of misalignment corresponds to three times of σ. which is the accuracy of the commercially available leveling unit, 0.1 mm/m. For reference, the electric field obtained from finite element calculation is shown in the Figure I.2. It can be found that the electric field distortion occurs due to the misalignment of electrodes.

I.5.2 [Simulation Study]

In this study, the non-specular reflection occurring only in the storage duration, Φ 800 mm for the electrode size, the cut-out time width from 2.15 s to 2.2 s are assumed, respectively. In addition, the

tilt ID	top lid	bottom lid
0	0	0
1	(3×0.1 mm/m×470 mm, 0)	0
2	(3×0.1 mm/m×470 mm/2, 0)	(-3×0.1 mm/m×470 mm/2, 0)
3	(3×0.1 mm/m×470 mm, 0)	(0, 3×0.1 mm/m×470 mm)

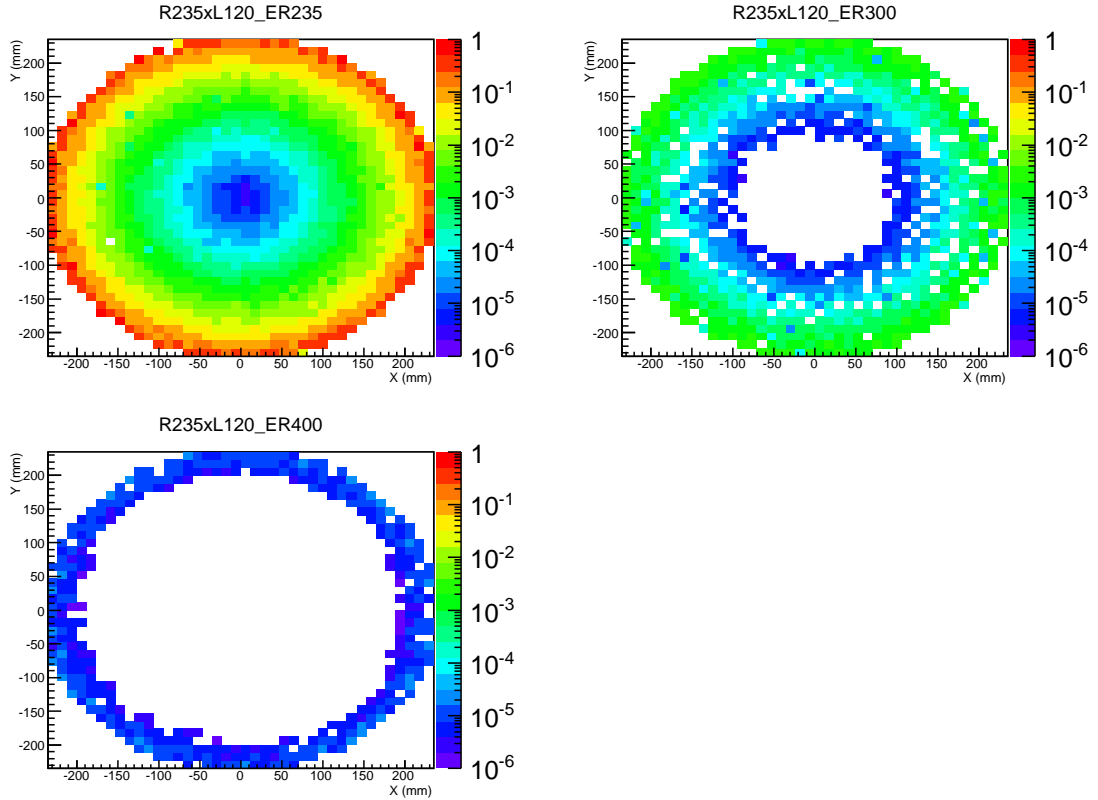Table.I.1   Non-parallelism condition of the electrode

Figure.I.1   Dependence of the radial direction component of the electric field, e_r, on the electrode radius, E_R, was calculated by ANSYS. The graph corresponds to the cross-sectional view of the storage container, and the color represents the magnitude of e_r. In this FEM calculation, the size of measurement cell is assumed to be the cylinder of 235 mm radius and 120 mm length, whereas E_R is assumed to be one of 235 mm (upper left), 300 mm(upper right), and 400 mm (lower left).

non-specular reflection probability is chosen to be one of 0%, 1%, 5% and 10%, while the degree of the misalignment of the storage container is chosen from Table I.1. In this way, the simulation to evaluate the systematic error is performed as below. First, polarized UCNs are accumulated in the container for 50 s using the rebunch storage method in same manner as chapter 4.4.4. Second, the spin precession continues to be calculated for 200 s assuming the storage region is the cylindrical configuration of Φ470 mm×L120 mm. Third, the additional spin phase shift, caused by the rotational motion and the distorted
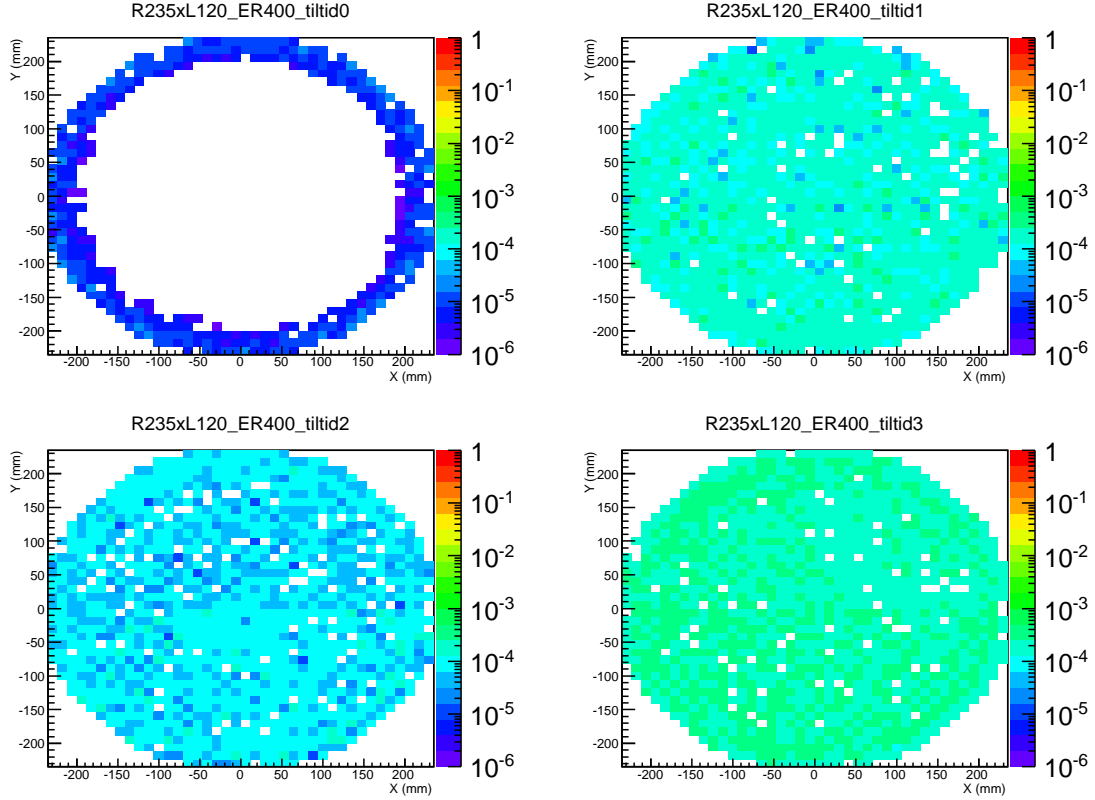
Figure.I.2 The dependence of the radial direction component of the electric field, e_r, on non-parallelism of electrodes was calculated by ANSYS. The graph corresponds to the cross-sectional view of the storage container, and the color represents the magnitude of the radial direction component of the electric field, e_r. The degree of non-parallelism is assumed to be one of ID in Table I.1. Specifically, the upper left is tilt ID0, the upper right is tilt ID1, the lower left is tilt ID2, and the lower right is tilt ID3. The size of measurement cell is assumed to be the cylinder of 235 mm radius and 120 mm length, whereas the electrode radius E_R is assumed to be 400 mm.

electric field, is evaluated at the end of 200 s storage duration. Finally, the systematic error is evaluated with the expression (I.1) by using the same method as described in the document [21][82].

The obtained result is shown in Figure I.3. The vertical axis is the systematic error evaluated, the horizontal axis is the index of the non-specular reflection probability, the black line is the average value of false EDM, and the red line is the error of the average value of false EDM. For the case that the non-specular reflection probability is 0, the systematic error amounts to $O(1 \times 10^{-26} \text{ e} \cdot \text{cm})$. On the other hand, for the other cases, it was suppressed to 1×10^{-28} e·cm or less. Therefore, systematic uncertainty due to v×E (Rotation) can be suppressed if the non-specular reflection probability of more than 1%. Figure 2.8 shows that the non-specular reflection probability can be 1% or more if surface roughness is several nm. Obviously, it is easy to satisfy this requirement. Hence, it is concluded that the systematic error of v×E (Rotation) can easily be reduced to 1×10^{-28} e·cm or less in J-PARC P33 experiment. Therefore, in this study, the magnitude of the systematic error due to v×E (Rotation) was

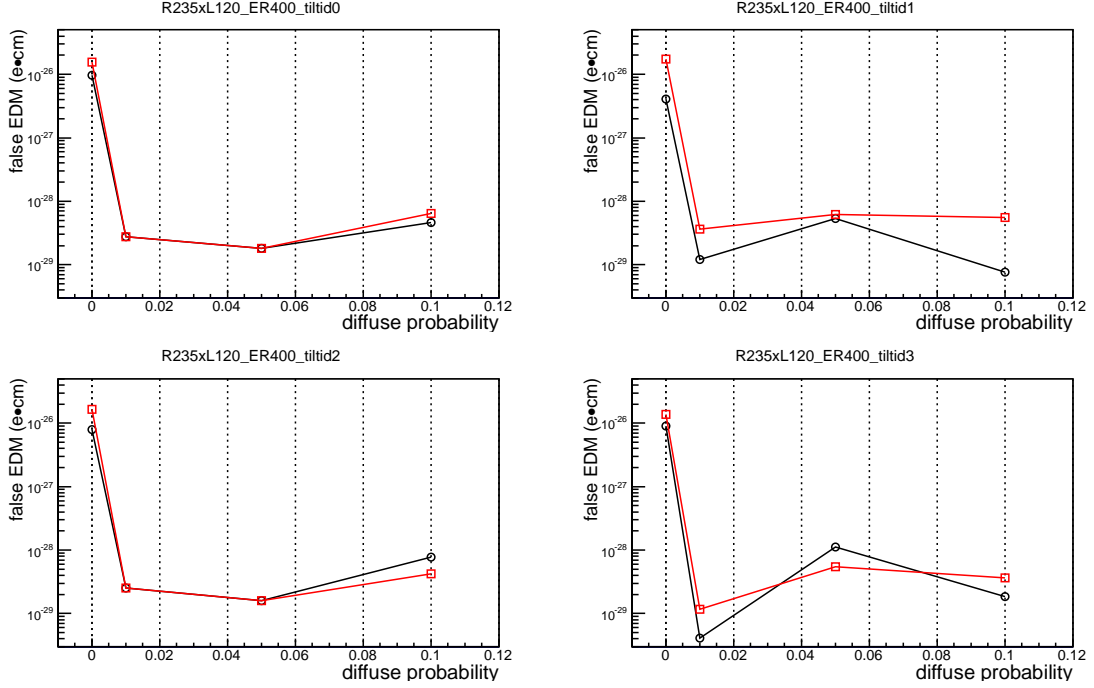evaluated as 1×10^{-28} e·cm for conservative evaluation.

Figure.I.3   Analysis result of false EDM due to v×E (rotation). The horizontal axis represents the identification number of the surface roughness, and the vertical axis represents the magnitude of the systematic error, the black circle point is the calculated systematic errors, and the red square point is the error of the calculated systematic errors. Each pad corresponds to one of the degree of non-parallelism specified in Table I.1. Specifically, the upper left corresponds to tilt ID0, the upper right corresponds to tilt ID1, the lower left corresponds to tilt ID2, and the lower right corresponds to tilt ID3. The size of measurement cell is assumed to be the cylinder of 235 mm radius and 120 mm length, whereas the electrode radius is assumed to be 400 mm.

I.6   Light shift (indirect)

When precessing ^{199}Hg is illuminated by non-resonant light, the atomic energy level shift becomes broader, which results in changing the Larmor precession frequency [87].

Generally, the above-mentioned change of the precession frequency is caused by the following fictitious magnetic field, B_{eff} [87][83].

$$\vec{B_{\mathrm{eff}}} \propto B_{\mathrm{eff}}(I,\omega)\vec{k} \qquad (I.2)$$

where, $\vec{k}$ is a unit vector of the propagation direction for incident light, and I and ω are the intensity and the frequency of incident circularly polarized light, respectively. In general, the incident light angle in the vertical plane, α, used for monitoring Hg co-magnetometer has misalignment, $d\alpha$. Therefore, at EDM measurement, ^{199}Hg atoms feel the extra magnetic field $B_{\mathrm{add}} = B_{\mathrm{eff}}\sin(d\alpha)$ applied along the vertical

direction. As a result, the magnitude of the magnetic field becomes different by B_{add} in crossing point analysis, which results in a systematic error. In the ILL experiment, this systematic error is referred to as indirect light shift. The magnitude of indirect light shift depends on the intensity of incident light.

In the ILL experiment, an indirect light shift was corrected by run-by-run by using the correspondence relation between incident light intensity and $R_a - 1$ of crossing point analysis. As a result, the systematic error can be reduced to 0.8×10^{-27} e $\cdot$ cm after the correction [41][2].

I.7   Light shift (direct)

In the ILL experiment, it was confirmed that there was a correlation between the incident light intensity of the ^{204}Hg lamp and the direction of the applied electric field. Obviously, a systematic error occurs due to the mechanism through the second term of the equation (3.2). In the ILL experiment, this systematic error is referred as to direct light shift and it was estimated to be 2×10^{-28} e $\cdot$ cm [41][2].

I.8   Hg EDM

There is room for Hg to produce EDM. If there is EDM in Hg, the precession cycle of co-magnetometer has dependence on the direction of the electric field, resulting in a systematic error. In the ILL experiment, the magnitude of this systematic error was estimated as $(2 \pm 6) \times 10^{-29}$ e $\cdot$ cm [41][2]. It is noted that 2×10^{-29} e·cm is not the term regarded as an error, but correction term.

I.9   Leakage current

When a voltage is applied between the top and bottom lids of the storage container, a systematic error occurs due to the magnetic field that a leakage current causes. In the ILL experiment, the magnitude of the systematic error was estimated to be less than to 1×10^{-28} e $\cdot$ cm [41][2].

I.10   Electric force

Because the storage container becomes squeezed by applying the electric field, the perfect parallelism of the electric field and the magnetic field lose, which result in a systematic error. In the ILL experiment, the degree of the systematic error was estimated to be 4×10^{-28} e $\cdot$ cm [41]. Actually, the magnitude of this systematic error was confirmed to be less than 3×10^{-35} e $\cdot$ cm by actual measurement using the photo detector [83].

I.11   HV AC ripple

During measurement of the neutron EDM, it is necessary to turn on and off HV. At that time alternative current by ripple generates a magnetic field and systematic error is caused. In the ILL experiment, its contribution was estimated to be 1×10^{-29} e·cm [41][2]. The magnitude of this error is proportional to the applied voltage.

Reference

[1] A.D.Sakharov, JETP-5 24-27, 1967.

[2] J. M. Pendlebury et al., Phys. Rev. D 92, 092003 (2015)

[3] J. H. Smith, E. M. Purcell, and N. F. Ramsey, Phys. Rev. 108, 120 (1957).

[4] P. D. Miller, W. B. Dress, J. K. Baird, and N. F. Ramsey, Phys. Rev. Lett. 19, 381 (1967).

[5] W. B. Dress, J. K. Baird, P. D. Miller, and N. F. Ramsey, Phys. Rev. 170, 1200 (1968).

[6] V. W. Cohen et al., Phys. Rev. 177, 1942 (1969).

[7] J. K. Baird, P. D. Miller, W. B. Dress, and N. F. Ramsey, Phys. Rev. 179, 1285 (1969).

[8] W. B. Dress, P. D. Miller, and N. F. Ramsey, Phys. Rev. D7, 3147 (1973).

[9] W. B. Dress et al., Phys. Rev. D15, 9 (1977).

[10] I. S. Altarev et al., Nucl. Phys. A341, 269 (1980).

[11] J. M. Pendlebury et al., Phys. Lett. 136B, 327 (1984).

[12] I. S. Altarev et al., JETP Lett. 44, 460 (1986).

[13] K. F. Smith et al., Phys. Lett. 234B, 191 (1990).

[14] I. S. Altarev et al., Phys. Lett. 276B, 242 (1992).

[15] P. G. Harris et al., Phys. Rev. Lett. 82, 904 (1999).

[16] R Golub and J M Pendlebury, Rep. P. Phys.42, 439 (1979)

[17] H.M.Shimizu et al., "Measurement of Neutron Electric Dipole Moment", January17, 2010, URL: http://nop.kek.jp/Zope/nEDM/publications/2009-KEK_J-PARC-PAC-Shimizu.pdf, NOTE: This is the proposal of nEDM experiment at J-PARC (P33)

[18] H.M.Shimizu et al., "Status Report for Measurement of Neutron Electric Dipole Moment (J-PARC P33)", June 14, 2010, URL: http://nop.kek.jp/Zope/nEDM/publications/2010-p33-10th-pac.pdf

[19] The J-PARC UCN Taskforce, "Summary of the J-PARC UCN Taskforce", Apr 15, 2009, URL:http://nop.kek.jp/Zope/nEDM/publications/0907.0515v1.pdf

[20] R. Golub, D.J. Richarson, S.K. Lamoreaux, Ultra-Cold Neutrons, Hilger, 1991

[21] Ryo KATAYAMA et al., "Development of a simulation for measuring neutron electric dipole moment", Journal of Physics: Conference Series 528 (2014) 012031

[22] Jackson.J.D, Classical Electrodynamics, 3rd edition, New York Wiley,1998

[23] C.-Y. Liu, A.R. Young, and S.K. Lamoreaux, Phys. Rev. B 62 (2000)

[24] E.Korobkina et al.,Phys. Rev. B 70 035409, 2004.

[25] F.Atchison et al.,Phys. Rev. C,76,4, 2007, doi:10.1103/PhysRevC.76.044001

[26] F.Atchison et al., Eur. Phys. A44 23-29, 2010.

[27] Dissertation of Stefan Heule,"Production, Characterization and Reflectivity Measurements of Diamond-like Carbon and other Ultracold Neutron Guide Materials", University Zurich (2008)

[28] S.K.Sinha et al., Phys. Rev. B38 4, 1988.

[29] A.Steyerl et al., Physica. B 173 47, 1991.

[30] A.Steyerl, Phys. Rev. C81 055505, 2010.

[31] Y.Seki et al., "Evaluation of Surface Roughness of Substrates and Mirrors for Ultra Cold Neutrons (NOTE: This is written in Japanese)", The Japan Physical Society 2012 Fall Meeting, Kyoto, September (2012)

[32] Dissertation of Kenji Mishima, "Irradiation effect of Ortho deuterium for UCN source", Osaka University, (2004)

[33] R. Golub et al., Z. Phys.B 51, 187-193 (1983).

[34] Z.-Ch. Yu, S. S. Malik, and R. Golub, Z. Phys. B 62, 137 (1986).

[35] E. Gutsmiedl, F.Böhle, A.Frei et al., Europ. Phys. Lett. 96, 62001 (2011).

[36] A.Frei et al., Eur. Phys. J. A 34, 119-127 (2007).

[37] F.Athicson et al., Phys. Rev. Lett. 95, 182502 (2005).

[38] S. Imajo et al., Prog Theor Exp Phys, 013C02 (2016)

[39] Philip Harris, "The Neutron EDM Experiment", arXiv:0709.3100

[40] http://www.rri.kyoto-u.ac.jp/neutron/optics/workshop/20120227/09_arimoto.pdf

[41] C.A.Baker et al., Phys. Rev. Lott 97 131801, 2006.

[42] Baker, C.A. et al. Nucl.Instrum.Meth. A736,184-203 (2014)

[43] http://www.icepp.s.u-tokyo.ac.jp/hecsubc/files/slides/110809_kitaguchi.pdf

[44] Dissertation of Sohei Imajo ,"Development of neutron Doppler shifter as a pulsed ultra-cold neutron source (NOTE:This is written in Japanese)", University of Kyoto (2016)

[45] https://www.psi.ch/ltp/ucn-physics

[46] Dissertation of Leonard Göltl, "Characterization of the PSI Ultra-Cold Neutron Source", ETH ZÜRICH (2012)

[47] C. A. Baker et al., "The search for the neutron electric dipole moment at the Paul Scherrer Institute", Physics Procedia 17 (2011) 159-167

[48] Bernhard Lauss, "Ultracold Neutron Production at the Second Spallation Target of the Paul Scherrer Institute", Physics Procedia 51, 2014, 98-101

[49] J.W. Martin et al., "TRIUMF Ultracold Neutron Source", March 17, 2008

[50] S.N.Balashov et al., "A Proposal for a Cryogenic Experiment to Measure the Neutron Electric Dipole Moment (nEDM)"

[51] http://www.phy.ornl.gov/nedm

[52] "Conceptual Design Report for the Neutron Electric Dipole Moment Project (nEDM) Project MIE #71RE at Los Alamos National Laboratory Los Alamos, New Mexico managed by Los Alamos National Security, LLC", URL:http://www.phy.ornl.gov/groups/neutrons/nEDM_CDR.pdf

[53] A. Kolarkar. AIP Conf. Proc. 1200 (2010) 861

[54] A P Serebrov,IOP Conf. Series: Journal of Physics: Conf. Series 798 (2017) 012206

[55] Anatolii Serebrov,"Present status and future prospects of nEDM experiment", Gatchina Physics of fundamental Symmetries and Interactions - PSI2013, URL: https://indico.psi.ch/contributionDisplay.py?contribId=61&sessionId=4&confId=2036

[56] https://phits.jaea.go.jp

[57] https://github.com/rayrios/Geant4UCN

[58] F.Maekawa et al., Nucl. Instrum. Methods Phys. Res., Sect. A 620, 159 (2010)

[59] Yasushi Arimoto et al., Phys. Rev. A 86, 023843 (2012)

[60] Manfred Daum, "R & D experiments for the PSI UCN source", International Workshop on UCN and Fundamental Neutron Physics, RCNP, Japan, April 8, 2010

[61] F. Atchison et al., Phys. Lett. B 625, 19 (2005).

[62] T. Brys et al., Nucl. Instr. and Meth. in Phys. Res. A 550, 637 (2005).

[63] P. Schmidt-Wellenburg, "The quest to find an electric dipole moment of the neutron", arXiv:1607.06609

[64] M Daum et al., Nuclear Instruments and Methods in Physics Research A741 (2014) 71-77

[65] B. Lauss, "UCN guides for the ultra cold neutron source at PSI", Workshop on Neutron Delivery Systems. Institut Laue-Langevin, France, 3, July, 2009

[66] https://www.kanagawa-iri.go.jp

[67] Master thesis of Dai Sakurai,"Evaluating neutron mirrors of deuterated diamond like carbon and clarifying the relation between its roughness and neutron reflectivity (NOTE:This is written in Japanese)", Tokyo University of Science (2012)

[68] Y.Kawabata et al., Nucl. Instr. Meth. A529 84-86 (2004).

[69] M.G.D. van der Grinten et al., Nucl. Instr. Meth. A423 421-427 (1999).

[70] http://www.nanotec-jp.com

[71] http://www.cup-kurita.co.jp

[72] http://www.onwardgiken.jp

[73] K.igi, H.kawai, Quantum Mechanics 1, Kodansha-Scientific (NOTE: This is written in Japanese)

[74] Als-Nielsen, Jens; Elements of Modern X-ray Physics (2001)

[75] Matej Mayer, "SIMNRA User's Guide", 1997-2002.

[76] http://web2.tac.tsukuba.ac.jp/uttac

[77] V.Quillet Nucl. Instr. Meth. B83 (1993)

[78] J.E.E.Baglin Nucl. Instr. Meth B64 (1992)

[79] https://www.rigaku.com/en/products/xrd/smartlab

[80] T. Ino et al., J. Phys.: Conf. Ser. 528 012039 (2014)

[81] Dissertation of Ryohei Matsumiya, "Study of He-II Spallation UCN Source", Osaka University, 2013

[82] Ryo Katayama et al., JPS Conference Proceedings Vol. 8, 026004 (2015)

[83] Dissertation of J Zenner, "The search for the neutron electric dipole moment", University of Mainz (2013)

[84] J. M. Pendlebury et al., Phys. Rev. A 70 (2004)

[85] Dissertation of M. Kuzniak, "The Neutron Electric Dipole Moment Experiment: Research and Development for the New Spectrometer", Jagiellonian University, 2008

[86] http://www.ansys.com

[87] Dissertation of M. Horras, "A highly sensitive 199Hg magnetometer for the nEDM experiment", ETH Zürich, 2012